Doctoral Dissertation
Doctoral Program in Architecture. History and Project (37th Cycle)

The Moisture Transport Properties of Cement Mortar under Salt Spray Deposition

Bing Li

* * * * * *

Supervisors

Prof. Roberto Giordano, Supervisor
Prof. Jean-Marc Tulliani, Co-Supervisor
Prof. Michele Bonino, Co-Supervisor
Prof. Qinglin Meng, Co-Supervisor

Politecnico di Torino
South China University of Technology

June 12, 2025

I hereby declare that, the contents and organisation of this dissertation constitute my own original work and does not compromise in any way the rights of third parties, including those relating to the security of personal data.

…………………………………......

Bing Li

Torino, June 12, 2025

Summary

The moisture transport properties of porous materials play a crucial role in building energy consumption and indoor thermal comfort. Due to the salt spray climate, the external boundary conditions of buildings in coastal areas differ significantly from those in inland regions. Under salt spray deposition, salt crystals accumulate and expand within the pores of building materials, which not only causes severe erosion and weathering of the envelope but also alters its moisture transport properties. Previous studies have focused extensively on the physical-mechanical properties and durability of salt-laden building materials, while the moisture transport properties and mechanisms of building materials under salt spray deposition remain unclear. To address this issue, this thesis conducted the following work:

1）Development of an accelerated salt spray test method for porous building materials. Based on international standards and relevant literature, the main control parameters and technical indicators of accelerated salt spray tests were analyzed and discussed. Combined with the core objectives and technical requirements of this study, an accelerated salt spray test method was established, particularly tailored to investigating the hygric properties of porous building materials.

2）Ion migration and crystal distribution of sodium chloride in cement mortar. The salt crystal distribution and chloride migration patterns of cement mortars with different water-cement ratios and surface evaporation conditions were determined after 120 days of semi-immersion in a 5 wt% NaCl solution. Both the clogging of internal pores by salt crystals and the sealing of external surfaces with resin significantly affect the capillarity and moisture transport properties of cement mortar.

3) Liquid transport properties of cement mortar under salt spray deposition. Vacuum saturation tests and capillary absorption tests were performed on specimens subjected to 0–35 salt spray cycles using modified methodologies. Salt spray deposits in the specimens were observed to increase apparent density while decreasing open porosity and saturated moisture content. Based on fitting formulas for salt influence factors, correction equations for the capillary absorption coefficient and capillary moisture content of cement mortar under salt spray deposition were established.

4) Vapor transport properties of cement mortar under salt spray deposition. Sorption isotherms and vapor permeability of specimens with varying salt spray deposition were measured and analyzed using standardized protocols. By correcting the equilibrium moisture content of specimens above the deliquescent humidity of NaCl via the Robinson-Stokes equation and Nielsen formula, segmented fitting equations for the equilibrium moisture content of cement mortar under salt spray deposition were derived. Additionally, correction equations for the water vapor permeability of cement mortar under salt spray deposition were established based on segmented adjustment formulas for salt influence factors.

From the perspective of moisture transport in porous building materials under coastal salt spray climates, this study investigated the influence mechanisms of salt spray deposition on the transport and storage properties of liquid water and vapor, using cement mortar—a commonly used porous construction material—as the test medium. Revised calculation equations were developed for several key hygric property parameters of cement mortar under salt spray deposition. This research lays a foundation for the accurate calculation of moisture-heat loads and energy consumption in coastal buildings.

Acknowledgment

The completion of this doctoral thesis stands as a testament to the exceptional guidance, steadfast support, and unwavering encouragement I received from numerous individuals and institutions. To all who contributed, I express my profound gratitude.

First and foremost, I am profoundly indebted to my supervisors. My sincere appreciation extends to Prof. Qinglin Meng at South China University of Technology (SCUT), my primary supervisor in China, for foundational direction on my research trajectory and enabling my engagement in academic exchanges. I am equally grateful to my Politecnico di Torino supervisors, Prof. Roberto Giordano and Prof. Jean-Marc Tulliani, for their exceptional mentorship and unwavering support throughout my joint doctoral program. Their expertise in material science and architectural technology, complemented by rigorous supervision in experimental design and data analysis, proved indispensable to this research. I also extend sincere thanks to Prof. Michele Bonino for his invaluable interdisciplinary perspectives that profoundly enhanced this work's scope.

I gratefully acknowledge the funding from the National Natural Science Foundation of China (Grant 51938006), the State Key Laboratory of Subtropical Building and Urban Science (Grants 2022ZC02, 2022KA03), and the China Scholarship Council (Grant 202206150001). This support proved indispensable for experimental resources, international cooperation, and sustained research advancement.

Essential technical support was provided by Politecnico di Torino's Interdepartmental Laboratory SISCON (Safety of Infrastructures and Constructions). Special recognition to Dr. Leonardo Lannucci for specimen support fabrication via 3D printing, Prof. Raffaella Sesana for facilitating accelerated salt spray testing access, and Mrs. Francesca Bonfante with Dr. Giuseppe Ferrara for performing XRF measurements. Their expertise and provision of critical instrumentation—TG-DTA, mercury intrusion porosimetry, and climate chambers—proved vital to experimental success.

My heartfelt gratitude extends to colleagues and friends at both South China University of Technology and Politecnico di Torino, especially junior researchers in our groups. Your generous assistance, intellectual camaraderie, and steadfast encouragement during challenging phases were invaluable. The collaborative ethos within our laboratories ultimately rendered this doctoral journey both achievable and profoundly rewarding.

Finally, above all, my deepest gratitude belongs to my family. To my spouse, parents, and sister: your unfailing love has been my sanctuary. Your quiet strength and steadfast faith formed the enduring wellspring that sustained me throughout this academic odyssey.

Bing Li
Politecnico di Torino
12 June 2025

Dedication

To the essence of dedication—
like 15th-century brick vaults in Castello del Valentino:
strength born not of stucco veneer,
but of load-bearing truth.

For my parents,
who taught me to temper lime mortar for ashlar footings before drafting Guarinian elevations.

Con sapienza costruttiva

Bing Li

Content

Terminology and abbreviations

List of abbreviations

Symbolic	Unit	Definition
$a_1 \sim a_4$	—	Fitting parameters
a_w	%	Water activity of salt solution
$A_{cap,salt}$	kg/(m^2·$s^{0.5}$)	Capillary absorption coefficient of salt-laden specimens
$A_{cap,sol}$	kg/(m^2·$s^{0.5}$)	Capillary absorption coefficient measured in saturated salt solution
$A_{cap,w}$	kg/(m^2·$s^{0.5}$)	Capillary absorption coefficient measured in deionized water
C	kg/kg	Salt content of specimens
C_s	kg/kg	Mass concentration of saturated salt solution
d_{air}	m	Thickness of air layer inside the device
E	—	Compressive elastic modulus
f_c	MPa	Compressive strength
f_f	MPa	Flexural strength
g_v	kg/(m^2·s)	Water vapor flux density
G_v	kg/s	Water vapor flux rate
G	—	Shear modulus of the material
H	m	Height of the specimen
$k_1 \sim k_4$	—	Fitting parameters
m	mol/kg	Molar concentration of salt solution in the specimen
m_0	kg	Dry weight of salt-free specimens
m_s	kg	Dry weight of salt-laden specimens
m_e	kg	Mass of external salt crystals in the specimen
m_i	kg	Mass of internal salt crystals in the specimen
m_t	kg	Total mass of salt crystals in the specimen
m_{dry}	kg	Dry weight of the specimen
m_{sat}	kg	Mass of water-saturated specimen in air
m_{sol}	kg	Mass of salt solution in saturated specimen
m_{under}	kg	Mass of saturated specimen under liquid surface
$m_{wet}(\varphi)$	kg	Equilibrium mass of the specimen at a certain relative humidity
$m_{wet}(p_c)$	kg	Equilibrium mass of the specimen at a certain capillary pressure
M_0	kg	Initial dry weight of the specimen
M_n	kg/mol	Molar mass of NaCl, 58.5 kg/mol

M_{t}	kg	Dry weight of the specimen after salt spray exposure
M_{w}	kg/mol	Molar mass of water
P_{o}	%	Open porosity
P_{c}	Pa	Capillary pressure
$p_{\mathrm{v,sat}}$	Pa	Saturated water vapor partial pressure (2 808 Pa at 23℃)
$r_{\mathrm{orig.}}$	μm	Initial pore diameter
r_{final}	μm	Final pore diameter
R_{air}	m^2•s•Pa/kg	Water vapor resistance of the air layer inside the device
R_{sample}	m^2•s•Pa/kg	Water vapor resistance of the specimen
R_{total}	m^2•s•Pa/kg	Water vapor resistance of the specimen and internal air layer of the device
u_0	kg/kg	Water-retention saturation moisture content
u_{c}	kg/kg	Equilibrium moisture content of control group specimens
$u(\mathrm{p_c})$	kg/kg	Equilibrium moisture content of the specimen at a given capillary pressure
u_{s}	kg/kg	Moisture absorption amount of salt in the specimen
u_{t}	kg/kg	Equilibrium moisture content of salt-laden specimens
$u(p_c)$	kg/kg	Water-holding equilibrium moisture content
$u_{(\varphi)}$	kg/kg	Equilibrium moisture content of the specimen at a given relative humidity
V_{b}	m^3	Apparent volume
V_{ske}	m^3	Skeleton volume
$w_{\mathrm{cap,salt}}$	kg/m^3	Capillary moisture content of salt-laden specimens
$w_{\mathrm{cap,w}}$	kg/m^3	Capillary moisture content measured in deionized water
w_{sat}	kg/m^3	Vacuum-saturated moisture content

Greek alphabet

Symbol	Unit	Definition
γ_{xy}, γ_{yz}, γ_{zx}	—	Shear strains between x-y, y-z, and z-x directions
δ_{v}	kg/ (m•s•Pa)	Water vapor permeability coefficient
$\delta_{\mathrm{v,air}}$	kg/ (m•s•Pa)	Water vapor permeability coefficient of the static air layer (2×10^{-10} kg/(m・s・Pa) under normal temperature and pressure）
$\delta_{\mathrm{v,r}}$	kg/ (m•s•Pa)	Water vapor permeability coefficient of control group specimens
$\delta_{\mathrm{v,s}}$	kg/ (m•s•Pa)	Water vapor permeability coefficient of salt-laden specimens
$\Delta_{\mathrm{Acap,w}}$	%	Rate of change in capillary absorption coefficient

$\Delta_{wcap,w}$	%	Rate of change in capillary moisture content
Δ_M	%	Rate of mass change of specimen under salt spray
Δp_v	Pa	Water vapor partial pressure difference
Δ_E	%	Rate of elastic modulus change
Δ_{fc}	%	Rate of compressive strength change
Δ_{ff}	%	Rate of flexural strength change
$\Delta_{\sigma f}$	%	Rate of ultimate stress change
ε_c	—	Compressive strain
$\varepsilon_x,\ \varepsilon_y,\ \varepsilon_z$	—	Linear strain in x,y,z axial directions
η_{Acap}	—	Influence factor of capillary absorption coefficient
η_{wcap}	—	Influence factor of capillary moisture content
η_u	—	Comprehensive influence factor of specimen equilibrium moisture content
$\eta_{u(C)}$	—	Salinity influence factor of specimen equilibrium moisture content
$\eta_{u(\varphi)}$	—	Environmental humidity influence factor of specimen equilibrium moisture content
η_{δ_v}	—	Influence factor of water vapor permeability coefficient
μ	—	Lateral contraction coefficient (Poisson's ratio)
ρ_b	kg/m^3	Apparent density of specimen
ρ_{ske}	kg/m^3	Skeletal density
$\sigma_x, \sigma_y, \sigma_z$	MPa	stress in x,y,z axial directions
$\tau_{yz}, \tau_{zx}, \tau_{xy}$	MPa	Shear stress on x+, y+, z+ planes
φ_1	%	Relative humidity (higher side)
φ_2	%	Relative humidity (lower-humidity side)
φ_{orig}	%	Initial porosity
φ_{final}	%	Final porosity
$\Phi_{(-)}$	—	Permeability coefficient of salt solution

Alphabetical Abbreviation List

Symbol	Definition
CSS	Specimens with sealed sides, salt-containing, absorbing salt solution
DRH	Deliquescence humidity of salt crystallization
EDS	Energy dispersive spectrometer
IC	Ion chromatography
MIP	Automated mercury intrusion porosimeter
NOW	Specimens with unsealed sides, salt-free, absorbing pure water

NOS	Specimens with unsealed sides, salt-free, absorbing salt solution
NSS	Specimens with unsealed sides, salt-containing, absorbing salt solution
pH	pH of aqueous solution
R^2	Coefficient of determination for fitting
RH	Relative humidity of air
RSS	Sum of squared residuals for fitting
SEM	Scanning electron microscope
TG-DTA	Thermogravimetric-differential thermal analysis
W/C	Water-cement ratio of cement mortar
XRD	X-ray diffractometer
XRF	X-ray fluorescence spectrometer

Chapter 1 Introduction

Coastal regions, islands, and peninsulas in China, under the influence of marine climates, expose building envelopes to thermal and moisture stress markedly distinct from that in inland areas; moreover, long-term intrusion and deposition of airborne salts into building materials alter their heat and moisture transfer properties as well as durability, leading to envelope erosion, increased energy consumption, significant impacts on local military and civilian production as well as daily life, and severe property damage. However, current research on heat and mass transfer in building envelopes in the unique coastal hot-humid environments—characterized by salt, high humidity, and high temperature—remains limited, with the mechanisms underlying salt-moisture coupled transfer and interaction processes in salt-laden hot-humid air for building materials still unclear. Thus, this study takes cement mortar as the experimental subject to explore the mechanisms driving changes in moisture transport properties of porous building materials in salt spray environments, aiming to provide a theoretical basis for improving building envelope performance in salt-laden hot-humid regions and to enhance building energy efficiency and indoor comfort, with the following sections presenting the research background and significance, current research status, and key focuses of the study.

1.1 Background and significance

1.1.1 Salt spray climate in coastal areas

China, located in eastern Asia and on the western coast of the Pacific Ocean, is a major maritime nation encompassing four major sea areas—the Bohai Sea, Yellow Sea, East China Sea, and South China Sea—with a total maritime area of approximately 4.73 million km^2, a mainland coastline stretching about 18,000 km, an island coastline extending roughly 14,000 km, and over 6,500 islands each exceeding 500 m^2 in area [1, 2]. Its coastal regions, distributed from north to south across mid-temperate, warm temperate, subtropical, and tropical zones, span 22 latitudinal degrees, with significant variations in climatic factors such as temperature, humidity, rainfall, and solar radiation across these zones; however, they all share the common phenomenon of salt spray climate, where marine salt spray, driven by wind, spreads inland to further expand its influence range, as illustrated in Fig. 1-1.

Fig. 1-1 Salt-laden hot-humid climatic zones in China's coastal areas

Salt spray refers to a dispersion system composed of microscopic salt-laden droplets in the atmosphere, whose formation mechanism is primarily attributed to the constant intense agitation of seawater in oceans—this causes waves to collide and impact coastal reefs, generating substantial foam. As these bubbles rise to the sea surface and rupture, they form suspended micro-droplets: most fall due to gravity, while approximately 1/4 to 1/5 remain in equilibrium with turbulent diffusion, remaining distributed over the sea surface. These droplets are then transported into the atmosphere by air currents, undergoing a series of intricate processes such as fragmentation, evaporation, and coalescence to develop into a dispersion system, thereby forming atmospheric nuclei [3, 4]. With regard to its composition, salt spray is analogous to seawater, primarily consisting of chlorides, sodium ions, and sulfate ions, with chlorides accounting for approximately 90% of the total salt content; its particles are microscopic, typically with diameters of less than 2 μm and mass ranging from 10^{-11} to 10^{-5} mg. In marine air, large primary salt nuclei have a higher ratio of sodium and chloride ions, whereas smaller particles contain a higher proportion of sulfate ions, and as a result of moisture evaporation from salt nuclei, the greater the distance from the coastline, the higher the proportion of small salt nuclei and the lower the proportion of large ones [3, 4].

Salt spray content and deposition constitute key metrics for characterizing near-surface atmospheric salt spray distribution in coastal regions, with the salt spray content in coastal atmospheres governed by two primary factors: climatic conditions (such as wind direction, wind speed, and humidity) and natural environmental conditions (including seawater tides, coastal topography, and distance from the sea) [3]. According to observations by the Guangzhou Electrical Apparatus Research Institute of the Ministry of Machinery Industry on southeastern coastal cities (see Table 1-1), the maximum NaCl content ranges from 0.024 to 1.375 mg/m³, showing a decreasing trend from the coast inland as distance increases. Coastal salt spray deposition, closely correlated with atmospheric salt spray content, is influenced by factors including seawater salinity, temperature, marine air mass characteristics, their thickness and turbulence, wind parameters, rainfall, air humidity, coastal terrain, and forest cover; observations (see Table 1-2) reveal that the maximum daily NaCl deposition per unit area ranges from 11.51 to 54.0 mg/m³·d, exhibiting a decreasing trend with increasing distance from the sea [3, 4]. Notably, Jinshanzui, Songjiang, and Qingpu are distributed longitudinally along the coastline at the confluence of the Yangtze and Qiantang River estuaries, where seawater is significantly diluted—its NaCl content is approximately one-third of the global average seawater concentration, and several kilometers of dry beaches form during low tide—so a 30 km correction was applied to the actual sea distances for these three locations [3]. Overall, analysis of salt spray content and deposition across different coastal cities confirms that China's coastal areas are generally subject to salt spray climates, with their distribution influenced by multiple factors; distance from the coastline is critical, as both salt spray content and deposition exhibit a decreasing trend with increasing distance from the coast.

Table 1-1 Observation results of airborne salt spray content at different distances from the sea [4]

Location	**Distance from the sea (km)**	**Observation result (mg NaCl/m³)**			**Number of observations**	**Open sea wind direction**
		Mean	Maximum	Minimum		
Guangzhou	50	0.017	0.024	0.008	24	SSE
Fuzhou	25	0.113	—	—	2	SE.E
Lingshui	15	0.115	0.275	0.036	18	SE
Shantou	8	0.336	0.578	0.220	135	SE.E
Haikou	7	0.279	0.440	0.151	24	N
Zhanjiang	7	0.360	0.613	0.212	120	SE
Zhoushan	4	0.530	1.375	0.264	110	SSE
Xiamen	2	0.711	—	—	4	SSE

Table 1-2 Observation results of salt spray deposition at different distances from the coast [4]

Location	**Distance from the sea (km)**	**Observation result (mg NaCl/m²·d)**			**Number of observations**	**Open sea wind direction**
		Mean	Maximum	Minimum		
Guangzhou	50	12.44	15.38	5.13	14	SSE
Baoan	45	10.43	23.28	3.42	14	SEE
Lingshui	15	14.65	17.66	11.39	12	SE
Shantou	8	31.16	58.2	9.26	68	SEE
Haikou	7	33.13	47.73	20.79	10	N

Zhanjiang	7	19.47	42.25	10.2	58	SE
Zhoushan	4	21.54	54.0	4.75	42	SSE
Jinshanju	0.1(30)	19.25	29.87	8.0	12	SSE
Songjiang	30(60)	8.22	11.51	5.41	12	SSE
Qingpu	45(75)	10.34	12.59	9.11	8	SSE

1.1.2 Status of buildings in salt-spray climate zones

Coastal areas adjacent to the ocean typically feature pleasant ecological environments, facilitated external connectivity, rapid economic development, and a dense concentration of population and resources. Sixty percent of the global population lives within 100 km of the coastline. In China, coastal regions account for 13.4% of the country’s total land area yet support 45.1% of its population and contribute 63.1% to its GDP (National Bureau of Statistics, 2021). The development of coastal areas holds particular significance for China’s economic growth. Driven by population aggregation, urban expansion, and social advancement, coastal spaces have been undergoing continuous development and construction. Since the implementation of reform and opening-up in 1978, China’s urbanization has accelerated markedly; by 2016, the urbanization rate in coastal areas had reached 64.7%, surpassing the national average of 57.35% [5]. From 1985 to 2020, the proportion of building floor area in China’s coastal regions rose from 5.98% to 10.16%, representing an increase of 5.98 percentage points [6]. Such large-scale construction and dense population in coastal areas render their unique building climate environment a critical concern.

Affected by the salt spray climate, numerous buildings and infrastructure facilities in coastal areas are subjected to severe erosion and notable challenges. As weather conditions vary, alternating wet-dry cycles driven by salt spray readily result in the formation and deposition of salt crystals within porous building materials. The continuous growth and expansion of these salt crystals in material pores exert tensile stress on pore walls—a key driver of erosion and damage to building envelope materials. Salt spray erosion not only leads to external deterioration, such as weathering, discoloration, dampness, sanding, pulverization, cracking, and peeling of wall materials [7-10], but also induces internal property changes, including stress damage, reduced bonding strength, mass loss, altered moisture transport characteristics, and diminished durability [11-14]. Long-term exposure to harsh salt spray conditions poses a significant threat to the safety, comfort, and durability of numerous coastal buildings.

To visually assess the current state of buildings in coastal salt spray climates, the Salt Spray Research Team from the Building Energy Conservation Research Center, State Key Laboratory of Subtropical Building and Urban Science, conducted a field survey in November 2020 on traditional village dwellings in Nansha District, Guangzhou (see Fig. 1-2). Situated at the southernmost tip of Guangzhou, west of the Pearl River's Humen Waterway and bordering the Lingdingyang Estuary to the south, Nansha District features a southern subtropical monsoonal marine climate, where year-round high temperature and humidity—particularly heavy rainfall and elevated air humidity in spring and summer—have caused prolonged dampness on exterior walls, leading to mold growth, discoloration, blackening, and severe contamination; some exterior wall tiles have detached due to mortar bonding failure under combined dampness and salt spray effects, white salt crystals adhere to red fired bricks and masonry mortar surfaces, and porous materials have loosened with increased internal pore volume, showing local cracking, peeling, and tile detachment, with long-term salt spray erosion reducing the aesthetics and durability of numerous village dwellings and significantly impacting residents' lives. Additionally, during the author's joint training in Italy from 2022 to 2024, surveys were conducted on historical buildings and cultural heritage sites on the main island of Venice, a coastal city in northeastern Italy's Veneto region along the Adriatic coast—surrounded by the sea, the island hosts abundant heritage including churches, galleries, museums, bell towers, monasteries, palaces, and bridges, where long-term salt spray erosion has resulted in exterior wall plaster blistering and detachment, block expansion, cracking and spalling, and masonry mortar efflorescence, sanding, and pulverization (see Fig. 1-3).

Porous materials in building envelopes are subject not only to salt spray but also to other environmental stressors such as acid rain and freeze-thaw cycles, albeit through distinct mechanisms. Acid rain—generated through nitric or sulfuric precipitation derived from pollutant gases (e.g., nitrogen oxides and sulfur dioxide) released by fossil fuel combustion—causes severe corrosion to limestone, marble, and similar materials used in buildings and statues [15, 16]. Freeze-thaw cycles involve solid-liquid phase transitions of water within porous building materials driven by temperature fluctuations; as ice occupies a larger volume than an equivalent mass of liquid water, the volumetric expansion during freezing induces expansive stress on pore walls, leading to material damage [17, 18]. In contrast, salt spray is a pervasive, non-accidental, and non-seasonal climatic phenomenon across coastal regions of diverse climate zones, exerting long-term, continuous erosive effects on buildings [8, 9]. Hence, the salt spray climate represents the most critical threat to coastal buildings and structures.

Salt crystallization is a critical driver contributing to weathering damage in coastal building materials. However, solid salt crystals cannot migrate on their own within porous materials; the root cause of such damage lies in salt migrating with moisture through porous building materials under salt spray climates, with subsequent continuous salt crystallization and deposition in material pores as moisture evaporates [10, 19, 20]. Unlike inland regions, the ocean grants coastal areas unique natural landscapes, yet the associated salt spray climate also results in severe erosion and weathering of buildings. Long-term, continuous salt spray erosion diminishes the durability and service life of coastal industrial and civil structures, induces weathering and damage to numerous precious historical architectural heritage sites, and causes significant losses of social resources and public assets in coastal areas.

Fig. 1-2 Appearance of the exterior wall of a traditional village dwelling in Nansha, Guangzhou affected by salt erosion

Fig. 1-3 Appearance of masonry structures in Venice, Italy affected by salt erosion

In 2012, China put forward the "Strategy for Building a Maritime Power" for the first time. Over the past decade or so, the country has continuously deepened ecosystem-based integrated management of coastal zones, basically established a land-sea integrated marine spatial planning system, and gradually formed an "all-round marine spatial use control system covering sea areas, islands, and coastlines" [21][22]. In 2013, President Xi proposed cooperation initiatives including the Silk Road Economic Belt and the 21st-Century Maritime Silk Road, known as the "Belt and Road Initiative". Among them, the Maritime Silk Road encompasses five coastal provinces and municipalities: Shanghai, Fujian, Guangdong, Zhejiang, and Hainan. In 2022, President Xi emphasized accelerating the building of a maritime power, which has brought new opportunities for the construction and development of China's marine and coastal areas.

Against the backdrop of the maritime power strategy, the construction of buildings and infrastructure in China's coastal and island regions is of vital significance. A large number of residents and marine workers live along the coast, and it is essential to provide them with safe, healthy, comfortable, and energy-efficient living and working spaces. Additionally, stable, reliable, and efficient military facilities must be built on islands to strengthen national defense. However, the complex and harsh marine climate in coastal areas—characterized by high humidity, salt spray, and other factors—poses severe challenges to local buildings and places higher demands on the design and technical standards of coastal construction. Therefore, mastering the heat and moisture transfer characteristics and mechanisms of porous building materials in salt spray environments, and establishing new structural technical methods for building envelopes adapted to salt spray climates, are extremely urgent tasks for China's construction industry practitioners.

1.1.3 Application of cement mortar in construction

Building mortars are categorized into cement mortar, lime mortar, and mixed mortar by their cementitious materials. Among these, cement mortar is an engineering material composed of cement, fine aggregate, and water mixed in specific proportions and subsequently hardened. It is widely used in masonry, plastering, pointing, and flooring applications for buildings and structures [23, 24]. By mixing method, cement mortar is divided into site-mixed mortar (mixed on-site) and ready-mixed mortar (manufactured by professional producers).

Cement is a hydraulic cementitious material: its paste hardens both in water and air, with even better performance in water. Based on application and performance, cement is classified into general-purpose, special-purpose, and special-type varieties. General-purpose cement, derived from Portland cement, is produced by incorporating admixtures such as slag, fly ash, and pozzolans to meet engineering and technical requirements [25-27]. Fine aggregate typically consists of well-graded, hard, and clean natural or manufactured sand with a particle size under 4.75 mm; sands are categorized by fineness into coarse, medium, fine, and extra-fine grades. Medium sand with good gradation is preferred for building mortar, as its lower void ratio reduces cement paste demand while enhancing fluidity, compactness, and strength. Mixing water for cement mortar can be drinking water, groundwater, surface water, or treated industrial wastewater meeting specifications, with national standard-compliant drinking water being preferred [24, 27]. Ordinary cement mortar has five strength grades: M15.0, M10.0, M7.5, M5.0, and M2.5. Mortar strength depends primarily on cement grade and is influenced by the water-cement ratio—generally, a higher ratio results in thinner paste, slower hardening, and lower strength [24, 26]. Unlike structural concrete, which contains coarse aggregates like gravel or cobblestones, cement mortar exhibits lower strength but better homogeneity.

Building mortars are primarily categorized into masonry mortar and plastering mortar based on function. Masonry mortar serves the functions of bonding, shimming, and force transmission, constituting a critical component of masonry works. Cement mortar is frequently used for masonry in humid environments and structures requiring higher strength—such as brick columns, brick arches, and reinforced brick lintels—typically utilizing grades M5~M10 [23, 24]. Unlike masonry mortar, plastering mortar has a larger air contact area, leading to faster water loss, which hinders cement hardening. Lime mortar is typically employed for interior wall plastering in civil buildings, but cement mortar is necessary for plastering exposed components (e.g., plinths, eaves, coping walls, railings, and outer sidewalls of door/window openings) as well as high-humidity workshops, houses, basement inner/outer walls, and concrete beams, columns, slabs, and ceilings to enhance water resistance [26]. To ensure a flat plaster surface and prevent cracking or detachment, plastering mortar is typically divided into base, middle, and surface layers. The base layer primarily functions to bond with the substrate: lime mortar is usually used for brick wall substrates (due to their high porosity), while mixed mortar or cement mortar is applied to concrete walls, beams, columns, and roof slabs. The middle layer primarily serves a leveling function, predominantly using mixed mortar or lime mortar. The surface layer is primarily decorative, mainly using mixed mortar made with fine sand, whereas cement mortar is typically used in moisture-prone or collision-prone areas such as wainscots, base surfaces, window sills, and water wells [24, 26].

Cement mortar is widely utilized in China’s industrial and civil construction projects, serving as an indispensable material in building envelope construction and playing a crucial role in safeguarding building safety, comfort, and durability. Gaining a thorough understanding of the moisture migration characteristics of cement mortar under the unique climatic conditions of high temperature, high humidity, and salt spray in coastal areas, developing calculation equations for moisture characteristic parameters of salt-laden cement mortar, and implementing effective protective and regulatory technical measures hold fundamental significance for improving the durability of coastal buildings, enhancing building energy efficiency, and optimizing indoor thermal comfort.

1.2 Literature review on related topics

1.2.1 Salt and physical-mechanical properties of building materials

Salt erosion is a prevalent cause of damage to building materials in coastal regions [10, 19, 28, 29]. The continuous accumulation of salt crystals within porous materials induces expansive stress [30-32], while the transport of chloride ions to the surface of steel bars in reinforced concrete structures triggers corrosion [29, 33, 34]—both processes significantly compromising the durability and safety of building materials and structures. Consequently, extensive prior research has examined the effects of salt on the physico-mechanical properties and durability of building materials [19, 29, 35].

Mechanical properties of building materials—including compressive strength, flexural strength, elastic modulus, and stress-strain curves—are critical metrics for assessing material durability. Numerous researchers have conducted experimental studies on the effects of salt on the mechanical properties of porous building materials (see Table 1-3). Given the extensive use of cement mortar in construction and the significance of concrete strength as a structural material, research primarily focuses on cement-based building materials [36-42]. Saline intrusion methods employed include full immersion [13, 37, 38, 43], semi-immersion [39, 40, 44, 45], wet-dry cycles [41, 46, 47], and salt spray cycles [14, 42, 48], with test durations varying significantly based on specimen size and research goals. The primary seawater salts examined are NaCl and Na_2SO_4; while the mechanisms governing the formation and growth of these two salt crystals within porous material pores differ, both induce erosive damage to building materials. Previous studies have largely centered on the effects of NaCl and Na_2SO_4—either in single or mixed forms—on the physico-mechanical properties of building materials. Due to variations in specimen specifications, experimental protocols, and building material characteristics (e.g., type, mix ratio, and porosity) across studies, specific values of different mechanical property metrics lack comparability. Thus, Table 1-3 mainly employs the percentage change of each mechanical property metric to quantify the effects of salt on the mechanical properties of building materials.

1) Compressive strength

Compressive strength denotes the maximum pressure a material can withstand per unit area when resisting external forces perpendicular to its surface, measured in MPa. It reflects a material's capacity to resist plastic deformation and serves as a critical indicator for evaluating the mechanical properties of building materials. For concrete, for instance, it is classified into cubic compressive strength and axial compressive strength based on varying specimen specifications and testing methods. Specifically, cubic compressive strength refers to the 95% guaranteed compressive strength value measured from 150 mm cube specimens per standard test protocols. Axial compressive strength, by contrast, is determined from 150 mm×150 mm×300 mm prismatic specimens following standard experimental procedures [49]. In experimental research, both types are employed, with cubic compressive strength being more frequently utilized. During the salt intrusion phase of experiments, salt solution immersion methods predominate, whereas salt spray testing methods are less common.

Table 1-3 Summary of relevant studies on the effects of salt on the physico-mechanical properties of porous building materials

Literature Source	**Material**	**Type of Salt**	Rate of change in compressive strength Δ_{fc}	**Rate of change in flexural strength Δ_{ff}**	**Rate of change in elastic modulus Δ_{E}**	**Rate of change in stress/strain $\Delta\sigma_f/\Delta\varepsilon_c$**	**Method of salt intrusion**	**Experimental Period**
Yang et al.[37]	Cement mortar	3%-9% Na_2SO_4 5%-15% NaCl	-4.2%~-13.9%	-7.5%~-22.6%	–	–	Full immersion	7-21 days
Su et al. [38]	Cement mortar	5% Na_2SO_4	–	–	-54.73% 43.6% 34.56%	-6.67% 2.70% 21.82%	Full immersion	6 months
He et al. [47]	Cement mortar	除冰盐 3%，5%，8%	–	–	-5.17% -18.07% -24.14%	–	Wet-dry cycles	120 cycles
Huang et al. [39]	Cement mortar	5% Na_2SO_4	-8%	-12%	–	–	Semi-immersion	12 days
Ma et al. [40]	Cement mortar	Na_2SO_4 15%	-40% ~ -63%	-26%	–	–	Semi-immersion	42 days

Chen et al. [41]	Cement mortar	Na_2SO_4 0.5%, 5%, 10%	3.7%	–	-6.65%	–	Wet-dry cycles	75 cycles
Wu et al. [50]	Coral aggregate concrete	–	-69%	–	-91%	–	Salt spray	30 years
Zheng et al. [14]	Mortar Brick	5% NaCl	-6.16%, -8.61%	–	-42.68%	–	Salt spray	300 cycles
Qiao et al. [42]	Reinforced concrete	13.3% NaCl, 2.27% Na_2SO_4	–	–	-25%	–	Salt spray	100 cycles
Yang et al. [46]	Concrete	20% NaCl 20% Na_2SO_4	-3% -15.04%	-2.47% -16.05	–	–	Full immersion	60 days
Yang et al. [46]	Concrete	4%, 10%, 20% NaCl, Na_2SO_4	-8% -23%	-19% -31%	–	–	Wet-dry cycles	12 cycles
Zhao et al. [48]	Asphalt mixture	5% NaCl	–	-4.2%--42.3%	–	-10%~-30%	Salt spray	12 cycles
Azevedo et al. [35]	Cement mortar (mixed with	5% NaCl	-28.98%	-24.19%	–	–	Salt spray 4+8 h	300 h

	sludge)							
Franzoni et al. [33]	Brick masonry	2% NaCl 8% Na_2SO_4	-24%	-27.5%	–	–	Wet-dry cycles	6 cycles
Borges et al. [51]	Granite	10% NaCl	-7%~ -62%	–	–	–	Salt spray 4+8 h	150 cycles
Barone et al. [52]	Natural stone	14% Na_2SO_4	-32.8%	–	–	–	Wet-dry cycles	8 cycles
Marco et al. [53]	Sandstone	10-14% NaCl	-56.5%	–	-56.4%	-25%	Wet-dry cycles	60-250 cycles

Ma et al. at Central South University[40] examined sulfate attack resistance of cement mortar specimens under varying humidity and temperature conditions via semi-immersion (20 mm depth) in 150 g/L (15%) Na_2SO_4 solution. They measured compressive strength on days 3, 7, and 28 of immersion, finding ~40%–63% reduction in compressive strength after 28 days.

Chen et al. from Hohai University[41] investigated the effects of Na_2SO_4 solutions (0.5%, 5%, and 10% concentrations) on the mechanical properties of cement mortar by exposing cubic specimens to immersion-drying cycles. They observed that compressive strength first increased then decreased with increasing cycle counts, peaking at 45 cycles.

Yang et al. from Tongji University[46] subjected prismatic concrete specimens to immersion-drying cyclic tests in 4%, 10%, and 20% Na_2SO_4 and NaCl solutions, respectively. A separate group of specimens was continuously immersed in a mixed 20% Na_2SO_4 + 20% NaCl solution to analyze chemical erosion damage. The team found that compressive strength loss rates first decreased then increased with rising salt concentration. This trend arises because initial salt crystal formation primarily fills pores to enhance compactness; once pores are saturated, however, continued crystal deposition and growth induce expansive damage. Additionally, concrete immersed in 20% NaCl solution for 30 and 60 days exhibited <3% strength loss, while 20% Na_2SO_4 immersion resulted in >5% and >15% loss over the same periods, respectively.

Huang et al. from Yangtze Normal University [39] measured compressive strength change rates of cement mortar specimens with varying nanosilica (nano-SiO_2) dosages following 12 months of semi-immersion (60 mm depth) in 5% Na_2SO_4 solution. Reference specimens exhibited 8.8% and 22.9% compressive strength loss in their immersed and dry zones, respectively, whereas nano-SiO_2 incorporation reduced such strength loss in cement mortar specimens.

Yang et al. from Yunnan Province [37] used various combinations of Na_2SO_4 solutions (3%, 6%, 9%) and NaCl solutions (5%, 10%, 15%) to compare and analyze the degree of mechanical property deterioration in cement mortar under mixed salt solution attack. They found that deterioration intensified with higher sulfate concentrations; however, at the same sulfate concentration, increasing chloride levels alleviated this deterioration. SO_4^{2-} in the solution reacts with cement hydration products to form substantial ettringite and calcium sulfate—these are the primary drivers of cement mortar performance degradation. In contrast, chloride salts do not react with cement mortar; instead, their crystal formation densifies the mortar, thus partially inhibiting sulfate attack.

Zheng et al. from Xi'an University of Architecture and Technology [14] conducted wet-dry cyclic corrosion tests on mortar, fired brick, and brick masonry specimens using 5% NaCl solution. They observed a significant decreasing trend in compressive strength with increasing number of salt spray corrosion cycles: when reaching 300 cycles, the compressive strength loss rates of mortar and brick reached 6.16% and 8.61%, respectively.

Barone et al. at the University of Catania, Italy [52] conducted immersion-drying cyclic corrosion tests on Sicilian natural stone specimens in 14% (v/v) Na_2SO_4 solution. After 8 cycles, compressive strength dropped from 6.12 MPa to 4.11 MPa, a 32.8% reduction.

Marco et al. at Portugal’s Polytechnic Institute of Setúbal [53] exposed sandstone to immersion-drying cycles in 10%–14% NaCl solutions, assessing mechanical properties at various cycle intervals. Compressive strength dropped by 50% after 60 cycles, 80% after 120 cycles, and 95% after 250 cycles.

Azevedo et al. at Brazil’s Federal University of Rio de Janeiro [35] assessed compressive strength changes in mortars with 5%, 10%, and 15% sludge content under salt spray cycles, using spray generated from 5% NaCl solution. After 300 hours of testing, the 15% sludge mortar showed the most pronounced strength loss, at ~28.98%.

Borges et al. at Portugal’s Polytechnic Institute of Portalegre [51], per EN 14147 [54] salt spray protocols, evaluated axial compressive strength of five common granite types used in building decoration in southeastern Portugal—before and after 150 salt spray corrosion cycles (75 days total). They found strength reductions ranging from 7% to 62% across the granite types.

Synthesizing these studies, salt-induced erosion typically reduces the compressive strength of porous building materials. Salt crystal deposition within material pores densifies the matrix, potentially inducing an initial increase in compressive strength during early stages of testing. However, as crystals continue to deposit and grow, they generate expansive stress in the pores, ultimately causing material degradation and a decline in compressive strength. Chloride salts primarily undergo physical changes in cement-based porous materials, whereas sulfate erosion involves both physical and chemical processes: sulfate ions react with cement hydration products to form ettringite and calcium sulfate, which readily absorb water and expand. When both chlorides and sulfates are present, chloride ions—due to their small volume and rapid diffusion—form NaCl crystals that fill surface pores (10–100 nm), densifying the surface pore structure and thereby partially inhibiting sulfate erosion [37, 44].

2）Flexural strength / Split tensile strength

Flexural strength refers to a material's ability to resist fracture under bending moments, primarily reflecting the strength of brittle materials. Expressed in MPa, it is also a key mechanical property index for building materials. The flexural strength of building materials is generally lower than their compressive strength; for example, the flexural strength of concrete is approximately 1/5 to 1/10 of its cubic compressive strength [49]. Split tensile strength is defined as the maximum load borne by a test specimen when it undergoes shear failure along a plane perpendicular to the loading direction under horizontal loading, with the unit being MPa. It is one of the important indices for evaluating the flexural performance of building materials such as concrete. Flexural strength testing methods include three-point bending and four-point bending, with the three-point bending method more commonly used in experimental research; the four-point method can also be applied to split tensile strength tests. Under salt erosion, the flexural strength of porous building materials is usually significantly affected, posing a certain threat to the durability of building structures in stressed parts of buildings.

Zhao et al. at Dalian Jiaotong University [48] used 5% NaCl solution to generate salt spray, analyzing the flexural strength of three common types of cylindrical asphalt mixture specimens under coupled salt spray and freeze-thaw cycles across four curing temperatures (5°C–45°C). After 12 cycles, the three specimen types exhibited 42.3%, 32.1%, and 18.3% reductions in flexural strength, alongside 56.5%, 53.1%, and 42.4% decreases in split tensile strength, respectively; notably, the maximum flexural strength of all three types declined significantly as curing temperature increased.

Zhang Ke et al. at Chang'an University [55] exposed asphalt mixtures to corrosion in pure water, 5% NaCl, and 10% NaCl solutions via three protocols: continuous immersion, wet-dry cycles, and freeze-thaw cycles, assessing their mechanical properties under salt-laden high-humidity conditions via split tensile strength and chloride corrosion factors. With increasing treatment cycles, specimen porosity rose progressively while split tensile strength declined: specifically, after 15 continuous immersions, strength decreases across the three solutions were 12.98%, 19.82%, and 29.43% respectively; after 15 wet-dry cycles, 9.76%, 40.08%, and 46.04%; and after 15 freeze-thaw cycles, 29.95%, 49.72%, and 54.89%.

Yang et al. at Tongji University [46] examined both the damage to concrete caused by NaCl and Na_2SO_4 salt crystallization under wet-dry cycles and the erosion of concrete immersed in 20% solutions of these salts. They found that under wet-dry cycles, specimens' flexural strength first increased then decreased, with a 19% reduction for NaCl and 31% for Na_2SO_4 after 12 cycles. In continuous immersion, flexural strength rose by 1.3% (NaCl) and fell by 7.69% (Na_2SO_4) after 30 days, and decreased by 2.47% (NaCl) and 16.05% (Na_2SO_4) after 60 days.

Ma et al. at Central South University [40] employed semi-immersion in 150 g/L Na_2SO_4 solution to investigate salt crystallization-induced physical erosion on cement mortar under varying relative humidity and temperature. After 42 days of semi-immersion, specimens with a water-cement ratio of 0.35 exhibited 67.68% residual flexural strength under 28°C and 35% RH, whereas under 35°C and 45% RH, flexural strength only dropped to 90.95%. This phenomenon stems from humidity-driven transformations between Na_2SO_4 and $Na_2SO_4 \cdot 10H_2O$ crystals, with environmental humidity fluctuations exacerbating Na_2SO_4-induced erosion of cement mortar.

Huang Qian et al. at Yangtze Normal University [39] found that after 12 months of semi-immersion in 5% Na_2SO_4 solution, nano-SiO_2-containing cement mortar showed the following flexural strength loss rates: 7.8%, 3.4%, and 2.6% for 10 nm nano-SiO_2 at dosages of 1wt%, 3wt%, and 5wt% respectively; and 4.8%, 3.2%, and 2.1% for 50 nm nano-SiO_2 at the same dosages. Nano-SiO_2 refines internal pores in the mortar and reduces pore connectivity, hindering sulfate ion migration and thus mitigating sulfate-induced damage.

Franzoni et al. at Italy's University of Bologna [33] examined the physical properties and split tensile strength of fiber-reinforced cementitious matrix (FRCM) brick masonry subjected to immersion-drying cycles in 10% Na_2SO_4 solution and deionized water. They found that after 6 cycles in the salt solution, the split tensile strength of these composite specimens decreased by approximately 27.5%. Bonding materials are critical to the strength of FRCM-masonry joints and the mechanism of salt crystal formation.

Azevedo et al. from Federal University of Rio de Janeiro, Brazil [35] conducted accelerated salt spray tests on lime mortar specimens with 0–15% sludge content using 5% NaCl solution, following relevant standards and research literature. Tests after 25 cycles (300 hours) showed that the flexural strength of specimens with 5%, 10%, and 15% sludge content decreased by 4.84%, 7.53%, and 24.19% respectively.

Synthesizing these findings, the flexural strength of porous construction materials under salt exposure is a matter of broad concern. Despite differences in salt composition, solution concentration, and cycle duration across studies, most porous construction materials show varying degrees of reduction in flexural strength following salt intrusion. This represents a key factor contributing to damage and diminished durability of such materials in seawater and salt spray environments.

3）Stress-strain curve / elastic modulus

Stress refers to the intensity of internal force at a point on the cross-section of a loaded member, where the normal component to the cross-section is normal stress (σ, MPa) and the tangential component is shear stress (τ, MPa); strain, on the other hand, is the relative change in shape and size of any point within an object caused by external forces, serving as a mechanical quantity to describe the degree of deformation at that point. Taking compressed concrete as an example, its stress-strain curve (as shown in Figure 1-4) includes segment OA, the linear elastic stage, where point A is the proportional limit—beyond A, the material enters the stable crack propagation stage, with strain increasing significantly faster than stress and exhibiting plastic characteristics, while the stress at critical point B can be used as the basis for long-term compressive strength. The CDE segment is the descending part: at point D, the specimen is macroscopically completely damaged, so the strain at D is taken as the ultimate compressive strain; beyond inflection point D, point E (with maximum curvature) is called the "convergence point," after which the main crack widens considerably, the specimen's bearing capacity becomes extremely low, and it is primarily supported by mechanical interlock and friction within the fragmented concrete [49]. In the linear elastic deformation stage, stress and strain at any point satisfy Hooke's Law (Equation 1-1), with the proportionality coefficient known as the elastic modulus (E) [56]; for specimens under unidirectional stress, their stress-strain relationships are simplified to Equations (1-2) and (1-3).

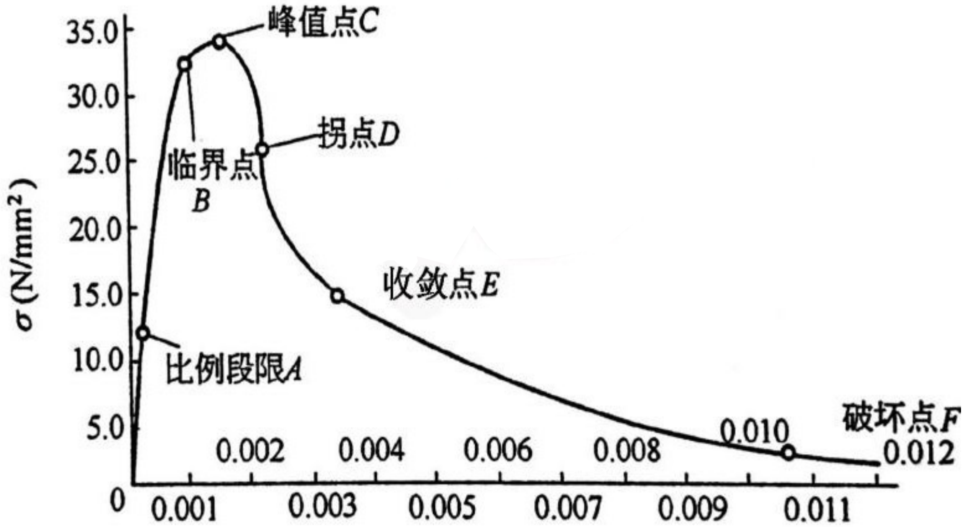

Fig. 1-4 Stress-strain curve of compressed concrete [49]

$$\begin{cases} \varepsilon_x = \frac{1}{E}[\sigma_x - \mu(\sigma_y + \sigma_z)] & \gamma_{yz} = \frac{1}{G}\tau_{yz} \\ \varepsilon_y = \frac{1}{E}[\sigma_y - \mu(\sigma_z + \sigma_x)] & \gamma_{zx} = \frac{1}{G}\tau_{zx} \\ \varepsilon_z = \frac{1}{E}[\sigma_z - \mu(\sigma_x + \sigma_y)] & \gamma_{xy} = \frac{1}{G}\tau_{xy} \end{cases} \tag{1-1}$$

$$\sigma_x = E\varepsilon_x \tag{1-2}$$

$$\varepsilon_y = \varepsilon_z = -\frac{\mu}{E}\sigma_x \tag{1-3}$$

Wherein, E is the compressive elastic modulus of the material, referred to as elastic modulus for short; G is the shear modulus of the material; μ is the lateral contraction coefficient, called Poisson's ratio.

Su et al. at Tongji University [38]] conducted uniaxial compression tests on mortar specimens with different water-cement ratios exposed to sulfate erosion over 1–6 months to obtain their stress-strain relationships. Results revealed that peak stress first increased then decreased. After 6 months of erosion, specimens with a water-cement ratio of 0.52 showed a 6.67% decrease in ultimate stress, a 60.98% increase in ultimate strain, and a 54.73% decrease in elastic modulus; those with a water-cement ratio of 0.47 exhibited a 2.7% increase in ultimate stress, a 36.96% increase in ultimate strain, and a 43.67% decrease in elastic modulus; and those with a water-cement ratio of 0.42 displayed a 21.82% decrease in ultimate stress, a 7.84% increase in ultimate strain, and a 34.56% decrease in elastic modulus.

He et al. from Xinjiang University [47] employed deicing salt solutions (3%–8% concentration) to examine mass loss and relative elastic modulus of aeolian sand cement mortar under wet-dry cyclic corrosion. The relative elastic modulus exhibited a trend of initial increase followed by decrease: it peaked at 45 wet-dry cycles, then gradually declined as the number of cycles increased. After 120 cycles, the relative elastic modulus of cement mortar immersed in 3%, 5%, and 8% salt solutions decreased by 5.17%, 18.07%, and 24.14% respectively.

Chen et al. from Hohai University[41]used Na_2SO_4 solution concentration and number of wet-dry cycles as experimental parameters, plotting and analyzing the stress-strain (σ-ε) curves of cement mortar at concentrations of 0.5%, 5%, and 10% after 20, 30, 45, and 75 wet-dry cycles. All curves were divided into three stages: linear elastic, elastoplastic deformation, and failure. The elastic modulus—derived from the linear elastic stage—exhibited a trend of initial increase followed by decrease, peaking at 45 cycles before declining with additional wet-dry cycles.

Wu et al. from the Chinese Academy of Sciences [50] drilled core samples from coral aggregate concrete in the South China Sea and tested their uniaxial stress-strain curves via a mechanical testing system. They observed that the ascending segment of the curve showed approximately linear development, with stress and strain maintaining an elastic relationship; after peak stress, the curve dropped sharply, exhibiting distinct brittle failure characteristics. Under long-term salt spray exposure, both the strength and elastic modulus of coral aggregate concrete decreased significantly—notably, the elastic modulus of core samples 0–100 mm from the surface dropped by 91%.

Qiao et al. from Lanzhou University of Technology [42] fabricated reinforced concrete specimens using four distinct concrete mix proportions and carried out accelerated salt spray-drying erosion tests, with salt spray generated from a mixed salt solution (2.29 mol/L NaCl + 0.16 mol/L Na_2SO_4). The elastic modulus of all four specimens increased in the early stage of the experiment; yet as corrosion cycles accumulated, the buildup of expansive products degraded the concrete structure, leading to a subsequent decline in their relative dynamic elastic modulus.

Marco et al. from the Polytechnic Institute of Setúbal, Portugal [53] procured four sandstone types from the exterior walls of the historic St. Leonard's Church and subjected them to accelerated salt spray testing. Uniaxial compression tests were performed to derive stress-strain curves, revealing that after 30 wet-dry cycles, the specimens exhibited no significant change in maximum strain, though their elastic modulus decreased by 26.67%. After 60 cycles, maximum strain decreased by 24.60%, and elastic modulus dropped by 56.67%.

In summary, the stress-strain curves and elastic modulus of porous building materials under salt erosion are also topics of widespread concern. Salt crystal deposition within material pores typically leads to reduced ultimate stress and increased ultimate strain. The elastic modulus—derived from the linear segment of stress-strain curves—generally exhibits a trend of initial increase followed by decrease. This is because in the early stages of cyclic testing, salt crystallization fills the pores of specimens, reducing porosity and increasing density; this reduces strain under a given stress and thus increases the elastic modulus. However, as wet-dry cycles continue to accumulate, internal erosion damage causes the elastic modulus to decrease and mechanical properties to deteriorate [41, 46, 47].

In seawater or salt spray environments, salts migrate through porous building materials alongside water, and as water evaporates, salt crystals form on material surfaces and within pores. The expansive stress generated by salt crystallization is a key driver of material erosion and diminished durability. Given that salt-induced damage impacts the safety and stability of engineering structures such as bridge piers, seawalls, and dikes, extensive, in-depth studies have been conducted on the physical and mechanical properties of cement-based materials in marine salt environments—yielding a relatively clear understanding of the patterns and mechanisms by which salts affect their mechanical properties. However, because reinforcing steel in concrete is prone to chloride-induced corrosion, and chloride ion migration and diffusion are shaped by multiple factors (including pore structure, load, climatic conditions, and ion concentration), the theoretical model of chloride ion diffusion remains under ongoing refinement and improvement [57, 58].

1.2.2 Salt and microscopic pore structure of building materials

Under different salt-induced erosion conditions, the formation of salt crystals within the pores of porous building materials alters their porosity and pore structure [13, 59]. Numerous scholars have carried out experimental investigations on various porous building materials, including limestone [45, 60, 61], sandstone [45, 60, 61], brick[43], mortar[43], and repair plaster [62]. These studies have focused on analyzing total porosity, maximum pore radius, and various alterations induced by salt erosion. Literature investigations cover a range of salts;

since the physical and chemical properties of salts themselves are key factors governing their impact on the pore structure of porous building materials, relevant research findings are reviewed below by salt type.

Table 1-4 Summary of studies on changes in pore characteristics of porous building materials induced by salt crystallization

Literature source	**Material**	**Salt**	**Initial porosity $\phi_{\mathrm{orig.}}$(%)**	**Final porosity ϕ_{final} (%)**	**Initial pore diameter r_{orig} (μm)**	**Final pore diameter r_{fin} (μm)**	**Salt intrusion method**	**Sample location**
Koniorczyk M. et al. [13]	Mortar	NaCl	23.72	14.03	0.0213	0.0382	Full immersion	Interior and surface
Rodriguez-Navarro C. et al. [11]	Limestone	Na_2SO_4 NaCl	20	18.4 10	0.5 0.2 0.07	0.4 Unchanged Unchanged	Full immersion	Interior and surface
Hendrickx R. et al. [63, 64]	Brick	Na_2SO_4 NaCl $MgSO_4$	33	31, 31. 4.29	1.7	Unchanged	Partial immersion	Interior
Espinosa-Marzal R.M. et al. [45]	Limestone	Na_2SO_4 NaCl $MgSO_4$	14.5	13.6-11.6 13.6 12.2	20	–	Partial immersion	–
Angeli M. et al. [61]	Sandstone	Na_2SO_4	3.99	4.47	0.05	Unchanged	Full immersion	Surface
Koniorczyk M. et al. [13]	Mortar	NaCl	12	9.4-6.4	0.055	0.05	Full immersion	Surface
Koniorczyk M. et al. [43]	Brick	Na_2SO_4 NaCl	28	28 28 23	0.5	Unchanged	Full immersion	Surface

		$CaCl_2$						
Koniorczyk M. et al. [43]	Mortar	Na_2SO_4 NaCl $CaCl_2$	12.5	15.4 16 16	0.05	0.055	Full immersion	Surface
Barone et al. [52]	Natural stone	Na_2SO_4	26.24	22.32	2.005	2.757	Full immersion	Surface
Lubelli B. et al. [62]	Gypsum	NaCl	58	52	250 30 0.05	Unchanged	Partial immersion	Surface

1）Effects of Na_2SO_4 and NaCl on pore structure

The most commonly used salts in research are Na_2SO_4 and NaCl, which are also the two most abundant salts in seawater [11, 13, 52]. The primary methods for salt intrusion into porous materials are full immersion or partial immersion, with full immersion being more commonly employed. To analyze changes in pore structure induced by salt crystallization, measurements of porosity and pore size distribution are performed before and after salt crystal deposition in specimens. Since sampling location significantly influences measurement results, it is essential to specify whether test samples are taken from the specimen surface or interior.

The influence of Na_2SO_4 on total porosity is limited: porosity reduction measured by mercury intrusion porosimetry (MIP) ranges from 6% [61] to 8% [60], while that detected via the gravimetric method is slightly more significant [45, 60, 61]—for limestone with smaller pores and larger pores, the respective porosity reduction rates are 2%–12% and 6%–20%. Na_2SO_4 exists in two crystalline forms: anhydrous sodium sulfate (Na_2SO_4) and mirabilite ($Na_2SO_4 \cdot 10H_2O$), whose distinct volumes govern the extent of porosity reduction in materials; owing to the coexistence of these two forms, the actual pore-filling rate of the material falls between two threshold values (approximately 10%) [45]. Some studies note that Na_2SO_4 crystallization fills larger internal pores, thereby lowering porosity [11, 60], while others propose that it distributes across pores of all scales [63, 65]. A study on brick specimens revealed that salt crystals grow along pore walls, shrinking pore sizes and generating smaller pores to alter the pore size distribution; additionally, as a corrosive salt, Na_2SO_4 can induce crack formation in materials, further contributing to increased porosity [43, 61].

NaCl exerts a more pronounced influence on the porosity of porous building materials.

Research indicates that the maximum porosity reduction in porous materials induced by NaCl crystals can reach 47% [13] and 50% [11], with the minimum reductions being approximately 4% [45] and 10% [62]. While crystallization does occur in the larger pores of the material, such a substantial reduction in porosity is primarily due to the filling of small pores. Furthermore, NaCl crystallization in brick samples alters the internal pore volume distribution: numerous pores exhibit a tendency toward reduced size. However, similar to Na_2SO_4, the quantity of salt crystals in samples is extremely small, so the alteration of the material's pore size distribution caused by salt crystallization remains limited. Experimental observations of the trend—where material porosity decreases progressively with increasing NaCl content—unveil a critical mechanism driving NaCl-induced physical erosion damage to building materials.

2）Effects of other salts on pore structure

In addition to NaCl and Na_2SO_4, studies have also examined the effects of other salts—such as $MgSO_4$, $NaNO_3$, and $CaCl_2$—on the pore structure of porous building materials[43, 60, 63-66]. Contrary to Na_2SO_4, under identical material and experimental conditions, $MgSO_4$ crystals occupy both large and small pores in the material, leading to a more pronounced reduction in porosity with a maximum decrease of 24%–28% [60, 63, 64]; its influence on the material's pore size distribution, however, is minimal. For $NaNO_3$, as salt content in the material increases, porosity decreases gradually, with a maximum reduction of 12% [57]. Similar to NaCl and Na_2SO_4, $NaNO_3$ also alters the pore size distribution of porous materials, converting pores to smaller sizes [43]. Crystallization experiments using NaCl, Na_2SO_4, and $CaCl_2$ were conducted on brick and mortar specimens. Results showed that NaCl and Na_2SO_4 had no significant effect on brick porosity, while $CaCl_2$ reduced brick porosity by 18% and modified the pore volume distribution characteristics—notably, increasing the proportion of ink bottle-shaped pores from 76% to 95%. All three salts, however, induced cracking in mortar specimens, increasing their porosity by approximately 20% [43].

Based on the above findings, the process through which salt crystallization impacts the micro-pore structure of porous building materials is complex, with distinct differences in how different salts deposit within the material's pores: some accumulate in smaller pores, while others occupy larger ones, and the underlying reasons remain unclear. This may stem from the combined influence of factors such as experimental methods, material pore structure, salt solution properties, and crystal deposition and growth characteristics [11, 60, 67. From a microscopic perspective, the complete filling of small pores by NaCl crystals and the relatively minor alterations to pore volume distribution caused by Na_2SO_4 crystals can be attributed to the distinct crystallization modes of different salts: NaCl typically forms crystals at the liquid-gas interface within pores and, with sustained salt supply, continues to grow within them until the pores are fully filled, whereas Na_2SO_4 crystals form on pore walls and gradually grow inward along their inner surfaces [11, 45, 67, 68].

Moreover, the same salt can also exert varying effects on porous materials [13, 19, 67]. For instance, in experiments with full immersion of mortar in NaCl solution, the specimen's porosity decreased by 2.6%–5.6% and pore size by 5 nm [13]; while another study showed that full immersion in NaCl solution caused a 3.5% increase in mortar porosity and a 5 nm increase in pore size [43]. Under full immersion in NaCl solution, limestone porosity decreased by 10% with no significant change in pore size distribution [11]; yet another study found that limestone porosity decreased by only 1.9% under partial immersion in NaCl solution [45]. These differences stem from variations in the properties of test materials and experimental methods, and due to the lack of unified experimental standards, different studies use different parameters depending on their research goals and focus—such as salt solution concentration, immersion/drying duration, drying temperature, and number of wet-dry cycles [11, 13, 45, 63, 64, 67, 69].

1.2.3 Salt and moisture transport properties of building materials

Moisture transport properties are extremely important physical parameters of building envelopes: they are not only closely linked to the durability of porous building materials [70-72] but also significantly affect building energy consumption and indoor thermal comfort [9, 10, 73], while acting as a key factor in analyzing risks such as biodegradation and mold growth on the inner surfaces of building components, and steel corrosion in reinforced concrete structures [74, 75].

The coupled heat and moisture transfer process is complex: the moisture transport coefficient, thermal conductivity, and heat storage coefficient all correlate with a material's moisture content and temperature, while water evaporation and water vapor condensation influence energy transfer through associated heat absorption and release [76]. Current research has developed a relatively thorough understanding of the mechanisms governing heat and moisture transport in porous materials, with multiple mathematical models proposed to describe this process [77-79]. However, in practical coastal engineering, the water within the pores of porous building materials typically contains dissolved salts. Changes in solution concentration driven by salt dissolution and crystallization alter the physical properties of pore solutions—

including density, viscosity, surface tension, and contact angle—thereby modifying heat and moisture transport processes in porous materials [67, 80].

1）Effects of salt crystallization on moisture transport properties of porous materials

The porosity and pore size distribution of porous building materials are key parameters that determine the moisture transport properties of building envelopes [10, 12, 13, 81]. When a solution contacts porous materials, it penetrates the material via capillary absorption and permeation; as moisture evaporates, salt crystals deposit on the surface or within the material [19, 62, 81]. The formation and growth of salt crystals in pores block certain pores and increase the material's density, which not only reduces the equilibrium moisture content of porous building materials in humid air but also lowers the vapor permeability coefficient [19, 69]. However, when liquid water penetrates the interior of porous materials, salt crystals redissolve, accompanied by the migration and redistribution of moisture in pores. Thus, the mechanism by which the deliquescence-crystallization changes of salt crystals under wet-dry cycles affect the moisture transport properties of building materials is remarkably complex [13, 59, 81].

There remains considerable uncertainty regarding the location and formation mechanisms of salt crystallization in porous materials, but what is certain is that the formation of salt crystals alters the porosity and pore structure of materials, in turn modifying their moisture properties. NaCl, the most abundant salt in seawater, is a primary cause of erosion damage to porous building materials: under partial seawater immersion or the capillary pressure of underground soil water, dissolved NaCl penetrates the interior of porous building materials with moisture, undergoing continuous permeation, migration, and diffusion, and when the concentration of NaCl solution in a given region reaches saturation, crystals precipitate [82-85]. Studies have shown that NaCl crystal deposition induces a linear decrease in the capillary absorption coefficient of porous materials while increasing capillary moisture content [86], and similar phenomena have been observed by numerous scholars in studies on the drying process of porous materials following saturated absorption of salt solutions [45, 87-91. Franke and Grabau [91] examined the effects of $MgSO_4$ and $CaSO_4 \cdot 2H_2O$ (gypsum) crystallization on the drying properties of ceramic tiles, finding that gypsum formed a crystalline accumulation zone 100-200 μm below the specimen surface, reducing the drying rate; additionally, the capillary absorption coefficient decreased due to the blocking effect of the crystalline layer, though once capillary water passed through this zone, the coefficient returned to its original value. In $MgSO_4$-eroded specimens, the absorption coefficient remained entirely unchanged as salt crystallization did not block internal pores, and furthermore, the water vapor permeability coefficient of gypsum-eroded specimens decreased by half, whereas that of $MgSO_4$-eroded specimens remained unchanged [87].

Espinosa et al. reported consistent findings in their studies on NaCl, Na_2SO_4, and $MgSO_4$: due to the blocking effect of salt crystal deposition zones, the permeability curves of specimens exposed to the three salts were all lower than those of control specimens [45]. Though NaCl created the narrowest blocking zones in materials with smaller pores, it imposed the greatest resistance to capillary water, a phenomenon that may stem from NaCl crystals growing progressively to fully occupy pores during evaporation [11, 68, 88], ultimately causing a significant reduction in moisture transport properties—this also indicates that surface coverage by NaCl crystal layers reduced the evaporation rate [45, 89]. However, other studies have demonstrated that salt crystals deposited on material pore walls effectively diminish pore size, thereby enhancing capillary absorption [90]. Using a different approach from the studies above, Hendrickx and Roels investigated the moisture transport properties of salt-containing materials via X-ray technology [65, 66]: they dried saturated brick specimens at 105°C to achieve uniform distribution of NaCl and $NaNO_3$ crystals within the specimens, then conducted capillary absorption experiments, and X-ray imaging revealed a linear decrease in both capillary absorption coefficient and capillary moisture content in specimens with accumulated $NaNO_3$ crystals, in contrast to the aforementioned studies showing that in specimens containing NaCl crystal deposits, measured capillary moisture content increased while the capillary absorption coefficient decreased linearly.

2） Interactive effects between salt crystal distribution and moisture transport properties

The deposition of salt crystals within porous building materials alters their porosity and pore structure, thereby changing the materials’ moisture absorption properties [10, 45, 67, 86, 91]; however, the content and distribution of salt crystals in material pores are rarely static, as the migration and crystallization of salts are dynamic processes shaped by multiple factors [36, 59, 92]. On one hand, the ongoing migration of salt solutions into the material and persistent evaporation of surface moisture drive a steady increase in pore solution concentration and gradual accumulation of salt crystals, while salt ions undergo diffusion driven by concentration gradients as they migrate toward the material surface with moisture—thus, the distribution of salt ion concentration and crystallization in porous materials results from the synergistic effect of capillary moisture absorption and ion diffusion, with the material surface evaporation rate being the most critical factor [59, 93]. On the other hand, the pore characteristics of building materials also exert a significant impact on salt migration and distribution: an open pore structure with few micropores confers superior salt solution transport and storage performance on porous materials [94], salt solutions in micropores are more prone to maintaining a supersaturated state (generating more salt crystals and exerting greater crystallization stress on pore walls) [95, 96], and as salt crystal content increases, expansion stress also develops in larger pores—when this stress exceeds the material's strength, cracking and damage occur [97]. Additionally, the migration properties of salts within porous building materials are shaped by factors including material moisture content, salt solution properties (solubility, density, viscosity, surface tension), liquid contact angle, and ambient temperature and humidity—though their underlying microscopic mechanisms remain incompletely understood [98-100].

The migration and distribution of salt crystals in porous building materials are also strongly influenced by moisture content and ambient humidity: NaCl, being highly hygroscopic, exhibits a clear trend where under identical external conditions, the higher the salt content in cement mortar, the more moisture it retains, which in turn impacts the moisture absorption properties of porous materials and leads to increased moisture content [101]. Conversely, since salts in porous materials can only migrate alongside moisture, the uneven pore size distribution and fluctuations in moisture content of porous building materials also significantly influence the localization of salt crystal accumulation [102-105]. Air humidity further shapes salt crystallization: when ambient humidity exceeds the salt's deliquescence point, salt crystals within porous building materials absorb water vapor from the air and deliquesce; once enough water vapor is absorbed, they transform into saturated salt solutions, which gradually dilute over time [10, 106, 107]. Under repeated crystallization-deliquescence cycles, even small quantities of salt can induce ongoing erosion and degradation of building materials [108]. Given the interplay between the moisture properties of porous building materials and salt crystallization, the microscopic mechanisms underlying similar erosion patterns in different materials may differ substantially [10], making the migration and distribution of salts within porous building materials remarkably complex and necessitating further exploration of the interactive effects and mechanisms between salt crystallization and material moisture properties.

The above studies provide valuable insights for better understanding the complex aspects of moisture properties in porous building materials, but a fully quantitative approach to defining the extent to which salt crystal content influences the moisture properties of porous materials remains unestablished. On one hand, discrepancies in experimental results arise from variations in factors such as the pore structure characteristics of porous materials, salt types, salt solution concentrations, salt immersion methods, and measurement techniques [98-100]; on the other hand, the deposition of salt crystals alters the pore structure, thereby changing liquid water transport and storage properties (e.g., capillary absorption coefficient, capillary moisture content, and saturated moisture content) and water vapor transport and storage properties (e.g., water vapor permeability coefficient and equilibrium moisture content) [19, 67, 69, 98]. In turn, shifts in the moisture properties of porous materials affect the migration of salt solutions within pores, which in turn governs the migration and distribution of salt crystals in pores, meaning the deposition of salt crystals and changes in moisture properties form a mutually interactive process that further complicates moisture migration challenges in porous building materials in coastal areas.

1.2.4 Related research work from the laboratary team

Guided by China's maritime power strategy and the development initiatives for the Guangdong-Hong Kong-Macau Greater Bay Area, and addressing the harsh climatic challenges faced by buildings in China's coastal regions and South China Sea islands, the research team at the Building Energy Conservation Research Center has carried out the following studies in recent years. These efforts are supported by projects including the Major Project of the National Natural Science Foundation of China—"Heat and Mass Transfer and Thermal Performance Index System of Envelopes in Extreme Hot-Humid Climate Zones" (No. 51590912), the Key Prjoectof the National Natural Science Foundation of China—"Research on Coupled Heat and Mass Transfer and Energy Conservation in Buildings under Saline Hot-Humid Climatic Conditions" (No. 51938006), and projects from the State Key Laboratory of Subtropical Building and Urban Science (No. 2022ZC02, No. 2022KA03).

In 2018, Xu [109] used red ceramic permeable bricks as test specimens and replicated the typical summer daytime climatic conditions of five sites—four reefs in the South China Sea (Dongsha Island, Xisha Island, Nansha Island, Yongshu Reef) and one coastal city (Sanya)—via thermal-humidity climate wind tunnel experiments. The study examined the heat transfer coefficients of building materials under dry, wet, and salt spray conditions, finding that the effect of salt spray on the heat transfer coefficients of dry or wet specimens was most pronounced during the hours around midday, while its impact on the evaporative heat transfer coefficients was minimal.

In 2018, Pan [110] replicated the extreme hot-humid conditions of South China Sea islands in a dynamic thermal-humidity climate wind tunnel. He experimentally analyzed the effects of salt-laden humid air, meteorological factors, and salt solutions on the evaporative cooling mechanism of ceramic porous materials, proposing a dynamic evaporation correction equation and factor-specific correction equations for the conditions studied. This work confirmed that both fresh water and salt solutions yield substantial evaporative cooling benefits in extreme hot-humid climates.

In 2019, Huang [111] investigated the effects of various climatic factors (temperature, relative humidity, wind speed) on salt concentration in humid air using dynamic thermal-humidity climate wind tunnel experiments. He found that wind speed is the dominant factor influencing salt concentration in the wind tunnel’s humid air. Through experiments simulating the actual atmospheric conditions of typical meteorological days on South China Sea islands, he proposed salt spray concentration control strategies for different wind speed scenarios.

In 2019, Li [112] addressed technical challenges in wind tunnel control parameters through theoretical analysis, numerical simulation, and experimental testing. She designed and constructed an all-weather dynamic thermal-humidity climate wind tunnel, developed methods to achieve multiple wind tunnel parameters, and successfully replicated seven meteorological parameters (wind speed, temperature, humidity, solar radiation, sky long-wave radiation, rainfall, and salt spray) in the wind tunnel. A correction model for sky long-wave radiation in the wind tunnel was also established.

In 2022, Zhou [113] conducted accelerated salt spray corrosion aging tests and wind tunnel experiments using ultraviolet weathering chambers and salt spray corrosion chambers, with water-based polyurethane coatings, water-based acrylic coatings, and solvent-based coatings as test subjects. He explored the relationships between wind speed, radiation, and various heat transfer coefficients, and by replicating the climatic conditions of typical summer meteorological days, analyzed the variation patterns of convective and radiative heat transfer coefficients of building coatings after surface salt spray corrosion.

In 2022, Mao [114] focused on glass (a transparent building envelope material), analyzing the effects of salt deposition on glass surface temperature, heat flux, surface heat transfer coefficient, and the variation laws of visible light transmittance, reflectance, emissivity, and shading coefficient with deposition amount via accelerated salt spray tests and climate wind tunnel experiments. Additionally, through simulations of typical coastal office buildings, he examined the influence of salt deposition on glass surfaces on indoor light-thermal environments, envelope heat transfer, and building energy consumption.

In 2023, Zhao Heyang [115] focused on sampling high-altitude salt-laden air in coastal areas. Using a multi-rotor UAV equipped with a sampling pod to collect air samples, he analyzed sources of sampling system errors, corrected and experimentally validated salt spray concentration measurements, and established an effective spatial sampling system and experimental method for near-surface salt-laden air.

In 2023, Xiang [116] addressed chloride deposition on building surfaces in coastal areas, proposing an efficient sampling method by optimizing the biological swab technique. She compared and selected analytical methods for chloride ion concentration in samples, then used this method to test chloride deposition characteristics on typical building surfaces in the Pearl River Estuary (Guangzhou), analyzing correlations between offshore distance, building height, and chloride deposition quantity.

In 2023, Tang You [117] focused on air salt spray concentration in coastal areas, developing a method to determine salt spray concentration in air samples. Through field measurements and investigative studies, he analyzed the influence of factors such as meteorological conditions, offshore distance, and building shielding on air salt spray concentration distribution. He found that a single building’s shielding can reduce leeward salt spray concentration by up to 121.49μg/m^3, while enclosed building clusters can lower central salt spray concentration to 36.79μg/m^3.

In 2023, He Jian [118] used full immersion in salt solution to achieve varying salt contents in aerated concrete specimens, then tested their isothermal moisture absorption curves and water vapor permeability coefficients. He found that salt enhances the air equilibrium moisture absorption performance of aerated concrete, while its effect on water vapor permeability varies with moisture content: it enhances the coefficient at higher moisture contents yet inhibits it at lower moisture contents.

To summarize, the team’s studies on building properties under special coastal climatic conditions fall into two categories: one focuses on analyzing interactions among coastal climatic parameters, replicating hot-humid environments, and establishing experimental platforms; the other involves analyzing how salt content affects thermal properties of building materials (e.g., evaporative cooling capacity, surface heat transfer coefficient, shading coefficient, heat transfer coefficient) through field investigations, salt spray collection, measurement, and accelerated salt spray tests. Conducting in-depth studies on heat transfer mechanisms of building envelope materials under coastal salt spray climates using established experimental methods holds significant practical value for developing building thermal performance systems and advancing energy conservation in extreme coastal climates.

While heat transfer occurs in building envelopes, moisture transport concurrently takes place. The moisture transport properties of building materials significantly affect the durability of building structures and building energy consumption. However, the completed work above primarily focuses on the heat transfer and photothermal properties of building materials, without exploring their moisture transport properties under coastal salt spray climates. Building on existing research, the team will continue to focus on investigating the moisture transport properties of porous building materials in salt spray environments, aligned with practical issues of building thermal performance and energy conservation in coastal areas, as well as the objectives of the aforementioned projects.

1.2.5 Summary and Evaluation

1）Physicomechanical properties

In coastal regions, under seawater or salt spray conditions, salts readily permeate into porous building materials alongside moisture, inducing erosion damage and posing a severe threat to the safety and durability of structures. Consequently, the physicomechanical properties of salt-laden porous building materials have long been a central focus of prior research. In earlier experimental studies, the primary salts examined were NaCl and Na_2SO_4, with research subjects encompassing common construction materials such as concrete, cement mortar, bricks, asphalt, and natural stone. Methods employed to induce salt ingress into porous materials included full immersion, partial immersion, immersion-drying (wet-dry cycles), and salt spray cycling. Key mechanical performance metrics tested included compressive strength, flexural strength (splitting strength), stress-strain curves, and elastic modulus. Core findings can be summarized in two aspects:

First, salt-induced erosion leads to the deterioration of mechanical properties in porous building materials. Generally, higher salt solution concentrations and more frequent cycling result in a greater rate of decline in material performance. That said, during the early stages of experiments, salt crystal deposition may fill pores—enhancing material compactness—and in some cases, improve properties like compressive strength and elastic modulus. However, as salt continues to infiltrate and accumulate, the mechanical properties of these materials will ultimately degrade.

Second, NaCl primarily undergoes physical processes within porous building materials: its erosion mechanism arises from the growth and expansion of NaCl crystals in pores. When the resulting expansion stress exceeds the material’s tensile strength, localized cracking and damage occur. In contrast, Na_2SO_4 undergoes both physical and chemical changes in cement-based materials: sulfate ions react with cement hydration products to form ettringite and calcium sulfate, a critical driver of degradation in such materials. Notably, adding NaCl to Na_2SO_4 solutions can effectively mitigate the chemical erosion of cement-based materials.

In summary, extensive prior studies have carried out comprehensive and in-depth analyses of how salts affect the physicomechanical properties of building materials, largely clarifying the patterns of mechanical property changes and erosion mechanisms under salt exposure. This body of work holds substantial theoretical value for assessing durability and ensuring the safety of buildings and infrastructure in coastal areas.

2）Pore structure and moisture transport properties

As salt crystals accumulate within the internal pores of building materials, they typically modify the materials' porosity and pore size distribution. Since moisture properties—among the most critical characteristics of porous building materials—are closely tied to their pore structure, the moisture behavior of porous materials under salt exposure has also emerged as a key research focus. When salt solutions permeate materials, moisture evaporation causes their concentration to rise until saturation, at which point salt crystals precipitate. The resulting pore blockage by these crystals reduces porosity and pore connectivity, often leading to reductions in moisture-related parameters such as capillary absorption coefficient, capillary moisture content, and water vapor permeability coefficient.

The mechanism by which salt crystallization affects the moisture properties of porous materials is notably complex. On one hand, the moisture absorption process of porous materials is influenced by multiple factors: material pore structure, salt solution properties, ambient humidity, and the deliquescence and moisture absorption of salt crystals. Even with the same salt, results measured under specific experimental conditions can vary significantly. On the other hand, the distribution of salt crystals in porous building materials and their moisture transport properties interact reciprocally: salt crystallization impacts moisture absorption by altering porosity characteristics, while salts can only migrate alongside moisture in pores—meaning that under wet-dry cycles, the moisture transport properties of porous materials govern salt migration and distribution.

To recap, from varied research objectives and analytical perspectives, previous studies have established a valuable foundation for understanding the moisture properties of salt-laden porous building materials. Yet, given the complexity of interactions between salt crystallization and moisture transport in porous materials, the microscopic mechanisms underlying changes in the moisture properties of salt-containing materials remain incompletely elucidated and warrant further investigation. Additionally, prior research exhibits limitations in experimental methodologies and systematic inquiry:

(1) Most studies have utilized immersion, partial immersion, or wet-dry cycles to induce salt ingress into porous building materials, then analyzed how varying salt contents affect moisture properties. These methods, though, are only applicable to the actual environments of concrete structures such as seawalls, marine embankments, and bridge piers. In contrast, most

building envelopes in coastal areas are air-exposed and primarily affected by salt-laden air conditions. Consequently, salt solution immersion does not replicate the real-world environment of buildings, nor can it truly reflect how salt spray climates impact building materials.

(2) Some studies have employed artificially accelerated salt spray tests to introduce salt into building materials—an approach consistent with the actual conditions of coastal buildings. However, in the absence of unified experimental standards, significant discrepancies exist in experimental methods and control parameters across studies: salt solution concentration for spray generation, specimen dimensions and placement angles, durations and ratios of salt spray to drying phases, drying temperatures, and cycle periods, among others. As a result, even findings from the same material in different studies are not comparable.

(3) The migration of salt ions and distribution of salt crystals in porous building materials are influenced not only by pore structure but also significantly by surface moisture evaporation conditions. Previous studies have overlooked analyzing and comparing the combined effects of these two variables on salt and moisture transport. Additionally, conducting capillary absorption experiments with pure water can dissolve salt crystals bound in pores, altering the material's original salt-laden pore structure—and this also conflicts with the boundary conditions of salt solutions formed when surface-deposited salt crystals deliquesce in salt spray environments.

(4) In salt spray climates, salt intrusion induces simultaneous changes in multiple moisture transport and storage properties of porous building materials. Comprehensively understanding these moisture property parameters is crucial to calculating building thermal-moisture loads and energy consumption. Most prior studies have focused on capillary water transport and salt crystal deposition in materials under salt solution immersion and drying conditions, while neglecting systematic research on liquid water and water vapor transport properties. A fully quantitative method to define how salt crystal content influences the moisture properties of porous materials has yet to be proposed.

Guided by national and regional development strategies, the Building Energy Conservation Research Team of the State Key Laboratory of Subtropical Building and Urban Science has carried out a series of studies in recent years—encompassing experimental observations, numerical simulations, and mechanistic analyses—focused on the unique climatic challenges confronting buildings in China's coastal regions and South China Sea islands, alongside building thermal performance metrics. The team has developed a robust multi-parameter dynamic thermal-humidity climate experimental platform and supporting methodologies, elucidated the laws governing how salt spray influences key thermal parameters of building materials and structures, and provided a vital theoretical foundation for thermal engineering and energy-efficient design of coastal buildings. Building upon the team’s established experimental methods and findings, future research will focus on investigating the moisture transport properties and their underlying mechanisms in building materials under salt spray climates, continuing to advance the development of building thermal-moisture index systems, and aiming to contribute to China’s coastal urban development and public welfare.

1.3 Outline of this dissertation

Building on the research tasks of three projects—the Key Program of the National Natural Science Foundation of China (No. 51938006) titled "Research on Coupled Heat and Mass Transfer and Energy Conservation in Buildings under Saline Hot-Humid Climatic Conditions", the International Cooperation Project of the State Key Laboratory of Subtropical Building Science (No. 2022ZC02) entitled "Research on Erosion Mechanism and Durability of Building Structures in Salt Spray Environments", and the Key Project of the State Key Laboratory of Subtropical Building Science (No. 2022KA03) named "Mechanism and Prevention of Salt Spray Thermophysical Corrosion Catastrophes on Building Envelopes in Tropical and Subtropical Maritime Regions"—this dissertation employs a combination of experimental observation and theoretical analysis to systematically investigate how coastal salt spray climates influence the moisture transport properties of porous building materials.

Beyond these three funding sources, the author has also received support from the China Scholarship Council’s International Joint Training Program for Innovative Talents (No. 202206150001). With a focus on the research content, multiple thematic seminars and academic exchanges have been conducted with the LINCE Laboratory at Politecnico di Torino (Italy). The experimental work for this dissertation was conducted sequentially in laboratories at South China University of Technology and Politecnico di Torino, leveraging the strengths of international collaborative research and interdisciplinary platforms.

1.3.1 Research objectives

Guided by the prominent challenges faced by buildings in China’s coastal regions under unique climatic conditions, the goal of enhancing the thermal and moisture performance of building envelopes, and the major limitations of prior studies in this field identified through literature review, the research objectives of this dissertation are established as follows:

(1) Given that most studies on the moisture properties of building materials have relied on experimental methods involving immersion in salt solutions—an approach misaligned with the

salt spray environments where coastal buildings are exposed—this dissertation will develop effective accelerated salt spray experimental methods. These methods will be based on existing standards, diverse experimental approaches employed in existing literature, and the research goals pertaining to the moisture properties of porous building materials.

(2) To address the interactive effects between salt crystal distribution and moisture migration, cement mortar specimens with varying water-cement ratios and lateral evaporation conditions will undergo long-term partial immersion in NaCl solutions. The impacts of differences in internal pore structure and external evaporation conditions on salt solution migration and salt crystal distribution will be compared, and the mechanism governing salt and moisture migration and distribution in cement mortar will be analyzed.

(3) To address the issue of salt crystal dissolution in porous materials during liquid water absorption, saturated NaCl solution will replace pure water in vacuum saturation and capillary absorption experiments. This will enable effective measurement of the pore characteristics and moisture absorption properties of cement mortar under salt-laden conditions. A correction equation will be developed based on the variation patterns of its capillary moisture absorption parameters under salt spray exposure.

(4) To tackle the lack of systematic research and quantification of moisture property parameters in porous building materials under salt spray conditions, specimens subjected to varying salt spray cycle durations will undergo systematic testing and analysis of liquid water transport parameters and water vapor transport parameters under standardized experimental conditions. Moisture property parameters under salt spray exposure will be quantified using influencing factors and correction equations.

Based on the above research objectives and the significance of moisture properties in porous building materials for building envelope performance, the liquid water transport parameters of porous building materials under salt spray conditions to be studied include the capillary absorption coefficient, capillary moisture content, saturated moisture content, and water retention curve, among others. The water vapor transport parameters primarily include equilibrium moisture content, isothermal moisture absorption curve, and water vapor permeability coefficient.

1.3.2 Research content

The primary research methods employed in this dissertation include field investigations, experimental observations, and mechanistic analysis. Based on the established research objectives, the specific research content encompasses the following aspects:

Firstly, through an extensive literature review, this study synthesizes and evaluates experimental methods adopted in relevant domestic and international research, as well as salt spray test standards in related fields. Key technical parameters—such as the concentration of salt solutions used to generate salt spray, salt spray cycling protocols, salt spray deposition rates, temperature, specimen specifications, and placement angles—are analyzed. Integrated with the focus on the moisture transport properties of experimental materials, an accelerated salt spray test method for porous building materials will be developed.

Secondly, cement mortar, a typical porous building material, is chosen as the experimental material. Specimens with controlled water-cement ratios and lateral sealed treatments are subjected to long-term partial immersion in a specified NaCl solution. The effects of differences in internal pore structure and external evaporation conditions on chloride ion migration and salt crystal distribution patterns in cement mortar are analyzed. Additionally, capillary absorption tests under four sets of external environmental conditions are conducted on different specimen groups to compare and examine the moisture transport properties of salt-laden cement mortar under varying evaporation conditions.

Thirdly, cement mortar specimens are subjected to salt spray tests with varying durations, employing the established accelerated salt spray method. Saturated salt solutions are used as the absorbing medium to conduct vacuum saturation tests, capillary absorption tests, and water retention tests on specimens exposed to different salt spray cycles. Basic parameters—including open porosity, apparent density, and saturated moisture content of cement mortar under different salt-laden states—are determined. The influence of salt content on the capillary absorption curves and water retention curves of cement mortar is examined, and the calculation equations for capillary absorption parameters are revised based on salt spray influence factors.

Fourthly, isothermal moisture absorption tests and water vapor permeability tests will be performed on cement mortar specimens exposed to different salt spray cycles. The effects of salt spray on the equilibrium moisture content and isothermal moisture absorption curves of the specimens are evaluated. A fitting equation for the equilibrium moisture content of salt-laden cement mortar in humid air will be developed, considering the interaction factors of ambient humidity and salt content on isothermal moisture absorption curves, integrated with the critical deliquescence and moisture absorption principles of salt crystals. Furthermore, the calculation equation for the water vapor permeability coefficient of salt-laden cement mortar will be adjusted based on the salt content influence factors governing water vapor permeability coefficient calculations.

1.3.3 Thesis framework

Based on the above research objectives and content, this dissertation follows the technical route shown in Fig. 1-5: The introduction analyzes the current status of salt spray erosion on coastal buildings and the research landscape through investigations, selecting cement mortar as the experimental subject. Chapter 2 establishes an accelerated salt spray test method for porous materials by defining key parameters and control protocols. Chapter 3 explores the mechanism of salt-moisture migration under varying pore structures and evaporation conditions through observations of chloride distribution, microstructural characteristics, and comparative capillary absorption tests. Chapter 4 studies liquid water transport properties, analyzing test data under salt spray cycles to develop correction equations for capillary moisture parameters. Chapter 5 investigates water vapor transport properties, developing segmented fitting equations for equilibrium moisture content and water vapor permeability based on test results and fundamental principles, with SEM, MIP, XRD, and IC techniques employed to reveal microscopic mechanisms. Finally, the dissertation summarizes key conclusions, novel contributions, limitations, and prospects for future research.

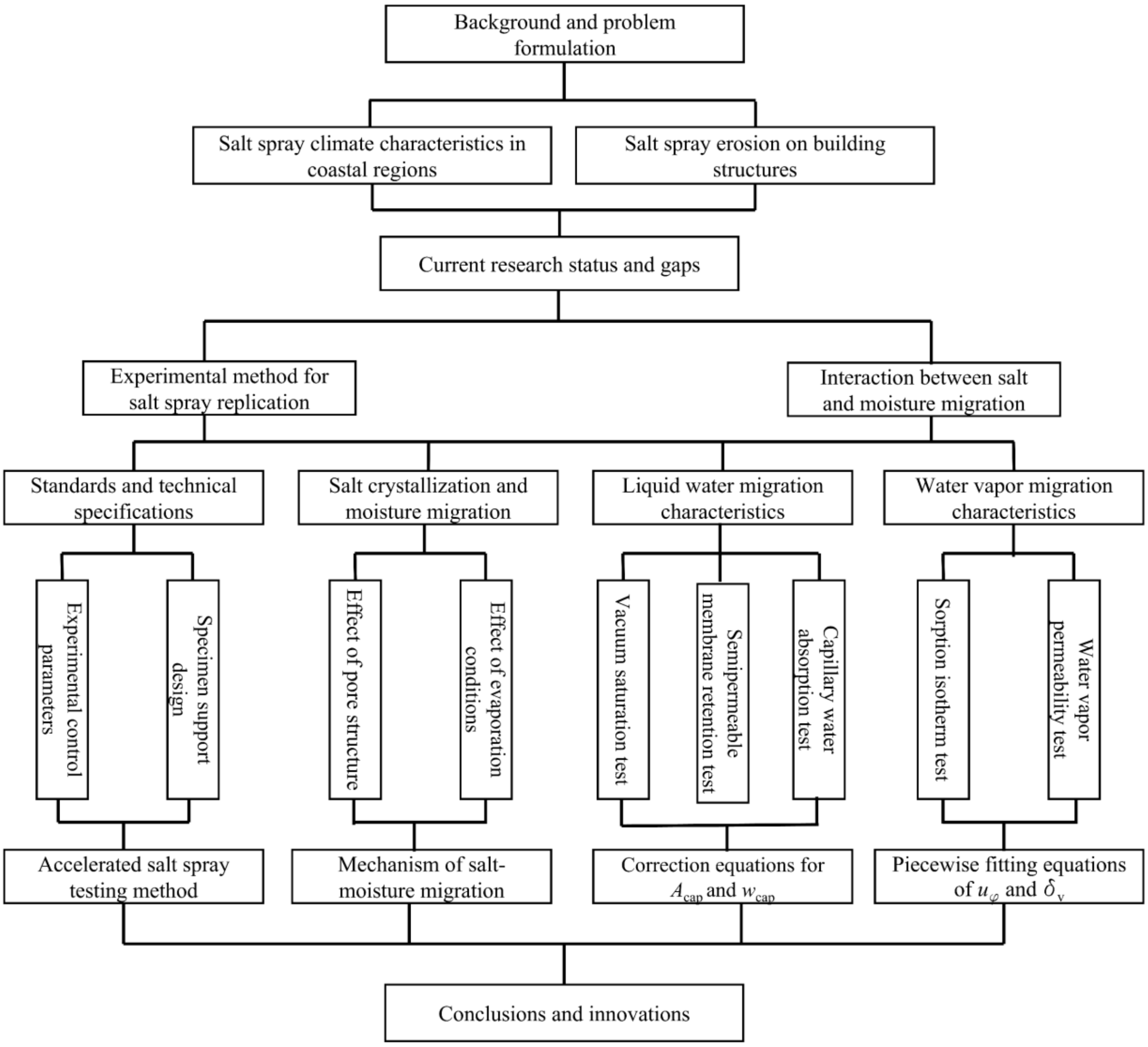

Fig. 1-5 Technical route of this dissertation

1.4 Chapter Summary

China has an extensive coastline and dense coastal cities, where numerous buildings in coastal regions and on islands experience severe erosion of their envelope materials due to long-term exposure to marine salt spray climates. This chapter synthesizes the current state of research domestically and internationally across three dimensions: the physicomechanical properties, microscopic pore structures, and moisture transport properties of building materials under salt exposure. It also traces the research trajectory of the laboratory's team in the field of building thermal engineering under the extreme hot and humid climates of coastal areas and South China Sea islands, analyzes the notable progress and theoretical achievements of prior studies, and identifies the shortcomings and gaps in previous research—particularly regarding salt spray experimental methods for porous building materials and the research framework for moisture property parameters. Building on this, the research objectives, content, and technical route of this dissertation are established.

Chapter 2: Accelerated salt spray test methods for porous building materials

2.1 Introduction

Unlike marine concrete structures, which endure seawater immersion, partial submersion, and alternating wet-dry scouring, many coastal buildings do not directly contact seawater but are instead exposed to a saline hot-humid atmosphere. Artificial salt spray testing thus provides an effective method to replicate the erosive environment experienced by building materials in coastal regions [10, 12, 35, 119]. Accelerated salt spray tests—characterized by controllable environmental parameters and short durations—serve as the primary approach for durability research in salt spray environments globally. While numerous well-developed salt spray test standards exist with detailed technical specifications, most are tailored to fields such as metal protective coatings, electrical engineering, and electronics, rendering them incompletely applicable to porous building materials [120-122]. In studies focusing on building materials, experimental methods and control parameters vary significantly due to differing research motivations and objectives.

This chapter will first analyze and synthesize the technical requirements and characteristic parameters of accelerated salt spray tests, drawing on existing industry-specific standards and relevant research literature. Based on subsequent research objectives regarding the moisture properties of porous building materials and the capabilities of available experimental facilities, it will then resolve key technical challenges in experimentation, define critical control parameters and salt spray cycling protocols, and develop an accelerated salt spray testing protocol tailored to studying the moisture properties of porous building materials in salt spray climate zones.

2.2 Analysis of salt spray test parameters

2.2.1 Experimental materials

Porous building materials studied in accelerated salt spray tests are diverse, with concrete being the most prevalent. This includes ordinary concrete and composite concretes incorporating fly ash, slag powder, and coral aggregates [42, 50, 123, 124]. Other materials encompass natural stones such as granite, marble, and limestone [7, 73, 125, 126]; glass fiber and carbon fiber composites [127, 128]; waterproofing materials like petroleum asphalt and

SBS-modified asphalt [48]; as well as mortar specimens, sintered bricks, and masonry assemblies [13, 14, 35, 43]. Concrete and mortar specimens typically undergo 28 days of standard curing after demolding before testing. Studies often fabricate specimens with varied mix proportions—by controlling parameters such as water-cement ratio and admixture content—to examine how material composition influences salt spray resistance [42, 124].

Most experiments utilize single-material specimens, yet in practical engineering, building materials are often integrated into assemblies (e.g., mortar and blocks in masonry structures). To investigate material interactions and overall durability under salt spray, some studies employ composite specimens composed of different materials [129, 130]. Beyond laboratory-fabricated specimens, field sampling is another approach [7, 50]. While field sampling accurately reflects material weathering in real salt spray environments and facilitates comparisons of erosion levels across different building locations or orientations, natural salt spray weathering is a slow, prolonged process. Single-time-point sampling thus limits the ability to track long-term changes in material properties over time.

2.2.2 Specimen dimensions

The shape of salt spray test specimens is generally dictated by the experimental evaluation method. Common forms include prismatic specimens, cubic specimens, cylindrical specimens, and plate-shaped specimens. For instance, cubic or prismatic specimens are routinely employed in compressive strength and stress-strain tests—cubic for cube compressive strength measurements, prismatic for axial compressive strength—whereas prismatic specimens are favored for flexural strength tests [9, 35, 50, 131]. Cylindrical specimens are frequently used in mechanical property tests to avoid stress concentration and edge effects, and they enable volumetric analysis at a specific resolution during dynamic X-ray observation [132].

Specimen sizes vary considerably across studies. For instance, the Standard for Test Method of Basic Properties of Construction Mortar (JGJ/T 70-2009) specifies 70.7 mm×70.7 mm×70.7 mm cubic specimens for compressive strength and freeze-thaw resistance tests, and 40 mm×40 mm×160 mm prismatic specimens for shrinkage tests [23]. According to research literature, cubic specimens employed in salt spray tests also encompass dimensions including 100 mm×100 mm×100 mm, 250 mm×30 mm×35 mm, 365 mm×240 mm×746 mm, 6.8 mm×6.8 mm×10 mm, and 300 mm×90 mm×10 mm [8, 14, 42, 48, 50, 124]. Cylindrical specimens include sizes such as Φ100 mm×350 mm, Φ50 mm×100 mm, and Φ150 mm×57 mm [48, 50]. Employing smaller specimens that satisfy experimental requirements not only conserves materials but also shortens the time needed for moisture absorption and thorough drying, thereby reducing the test cycle [133].

Standards for testing porous materials generally prescribe the minimum number of specimens for different experiments. For example, JGJ/T 70-2009 requires 3 specimens per group for cubic compressive strength and freeze-thaw resistance tests of construction mortar, while for tensile bond strength tests, it requires at least 10 specimens per mortar sample [23]. In research literature, the number of specimens used is typically limited to 3 or fewer, though more may be employed when destructive testing is needed to examine internal chloride ion content or erosion [7, 134]. The number of specimens is determined by the type of performance under test, technical methods, and requirements for controlling measurement errors.

2.2.3 Specimen placement angle

The natural stone salt spray test standard BS EN 14147-2003(E) [54] does not specify the placement angle of specimens within the salt spray chamber. In such chambers, salt mist is generated by nebulizing salt solution into fine droplets via nozzles using compressed air; these droplets disperse throughout the chamber and settle vertically under gravitational force. When specimens are placed horizontally, salt deposition and corrosion during the initial stage occur almost exclusively on their upward-facing surfaces, which does not align with real-world environmental conditions. Furthermore, the inclination angle of the specimen surface exerts a significant impact on salt deposition and corrosion effects [122, 135]. Studies by May and Alexander indicate that corrosion reaches its maximum when the specimen surface forms a 30°–80° angle with the horizontal plane, with relatively consistent corrosion effects observed within this range [122].

Salt spray test standards for metal materials and electrical/electronic devices across multiple countries specify specimen placement angles. For instance, China’s standard for tropical electrical products (JB/T 4159-1999) and ASTM B117-11(E) by the American Society for Testing and Materials both stipulate an angle of 15°–30° relative to the vertical. Other national standards—including ASTM B117-64 (USA), JIS Z 2371-1963 (Japan), BS 1224-1970 (UK), NFX 41-002-1996 (France), and DIN 50907-1952 (West Germany)—also specify either 20° or a 15°–30° range relative to the vertical [120, 122, 136], which is consistent with May and Alexander’s findings. In specific experiments, the optimal specimen placement angle should be determined by research objectives, taking into account factors including the material’s actual service environment, standard requirements, and the space utilization efficiency of the salt spray chamber.

2.2.4 Salt spray solution preparation

Seawater comprises complex salt components, with NaCl being the most abundant and the primary salt responsible for corrosion in porous materials. NaCl solutions are thus commonly used for salt spray preparation [35, 119, 134, 136-138]. Typically, higher salt concentrations accelerate corrosion rates in salt spray tests; however, excessively high concentrations can lead to salt crystal formation, which clogs nozzles and disrupts experimental procedures [120, 122, 136]. Additionally, the average global seawater salinity is approximately 3.5%, so concentrations close to this value better reflect real-world coastal salt spray conditions. Accordingly, salt spray test standards for electrical and electronic products worldwide typically specify NaCl solutions with concentrations ranging from 3% to 5%. With growing focus on the reliability and reproducibility of experimental results, most standards have gradually adopted 5 wt.% NaCl solutions [120, 122]. For instance, standards including ASTM B117-64 (USA), BS 1224-1970 (UK), NF A91-101-1966 (France), DIN 50907-1952 (West Germany), TGL 9209-1970 (East Germany), and JIS Z 2371-1963 (Japan) either specify or, following revisions, adopt 5% NaCl solutions for salt spray preparation, as detailed in Table 2-1.

Table 2-1 Comparison of commonly used salt spray test standards across countries [120-122]

Standard No.	**Scope of Application**	**Saline Solution**		**Experimental Conditions**		**Atomization Method**	**Experimental Duration/h**
		Concentration	pH	Temperature /°C	Deposition Amount ml /80 cm^{2}h		
International Electrotechnical Commission IEC 68-2-11	Samples with identical structures and protective layers	（5±1）% by weight	6.5~7.2	35±2	1~2	Continuous	16, 24, 48, 96, 168, 336, 672
International Organization for Standardiz	Metal coatings Material coatings	（50±5）g/L	6.5~7.2	35±2	1~2	Continuous	2, 6, 24, 48, 96, 240, 480, 720

ation ISO 3768-1976							
American Society for Testing and Materials ASTM B17-73	Metal coatings Material coatings	（5±1）% by weight	6.5~7.2	35±（-1.1~1.7）	1~2	Continuous	Selected according to the series
United States Military Standard MIL-STD-S10D-83	Equipment in salt spray environments	（5±1）% by weight	6.5~7.2	35	0.5~3	Continuous	48 or relevant regulations
United States Military Standard MIL-STD-202F	Components of electronic equipment	5%，20%	6.5~7.2	35±（1.1~1.7）	0.5~3	Continuous	48, 96
British Standard BS 2011	Quality and uniformity of protective layers	（5±0.1）% by volume	6.5~7.2	35±2	1~2	Continuous	According to the requirements of the test samples
French Standard NF C20-511	Quality and uniformity of protective layers	5% by weight	6.5~7.2	35±2	1~3	Continuous	24,48，96
West German Standard DIN 50021-75	Material components and equipment	（5±0.1）% by weight	6.5~7.2	35±1	15±0.5	Continuous	Same as ASTM

Japanese Standard JIS C5028-75	Electronic components, metal materials, and inorganic or organic coatings	（20±2）% by weight	6.5~7.2	35±2	0.5~3	Continuous	16±1, 24±2, 48±4, 96±4
Japanese Standard JIS H8681-80	Anodic oxide films of aluminum and aluminum alloys	（5±1）%	3.0±0.2	50±1	1~2	Continuous	4,8,16,72
Chinese Standard GB 2423.17-81	Electrical and electronic products	（5±0.1）%by weight	6.5~7.2	35±2	1~2	Continuous	16,24,48,96,168,336,672

Numerous studies have demonstrated that in salt spray environments generated using 5 wt.% NaCl solutions, significant chloride ion migration takes place in porous building materials such as concrete [35, 119, 134, 137, 138][120]. This migration induces changes in the pore structure characteristics and macroscopic physical properties of such porous building materials [119, 134, 137]. Additionally, some experimental studies have employed higher-concentration salt solutions prepared via mass-volume ratios, such as 165 g/L [9], 180 g/L [8], and (100 ± 10) g/L [139] NaCl solutions, for salt spray preparation.

2.2.5 Salt spray test control parameters

Accelerated salt spray tests can be classified by control protocols into continuous spraying [35, 127, 134], intermittent spraying [8, 34, 140], and salt spray-drying cycles [14, 42, 124, 131, 141]. All salt spray test standards for metals, electrical, and electronic products from various countries listed in Table 2-1 employ the continuous spraying mode. However, research on salt spray tests of porous building materials differs. Because alternating cycles of salt spray and drying better simulate the natural salt spray climatic environment of building locations, this mode is used in most experimental studies. Nevertheless, specific studies show significant variations in the set durations, ratios, cycle periods, and frequencies of salt spray and drying processes [120][124, 141]. Statistics on salt spray test control parameters from relevant domestic and international studies are detailed in Table 2-2.

Table 2-2 Statistics on process control parameters of salt spray tests

Literature Source	**Material**	**Temperature in Salt Spray Chamber℃ (Humidity)**	**Spray Duration/h**	**Drying Temperature ℃**	**Drying Duration/h**	**Cycle Period/h**	**Number of Cycles**	**Measurement Interval**	**Total Duration/d**
Song Guanghui [142]	Concrete with mineral admixtures	35	6	55	6	12	150	30	75
		35	12	55	12	24	150	30	150
		35	8	55	16	24	150	30	150
		35	24	55	24	48	150	30	300
Zhao Lihua et al. [48]	Asphalt mixture	15	24	-18	24	48	12	–	24
		25	24	-18	24	48	12	–	24
		35	24	-18	24	48	12	–	24
		45	24	-18	24	48	12	–	24
Li Bing et al.[131]	Concrete with mineral admixtures	*（75%~80%）	12	*	12	24	270	80	270
Wang Jianmin et al. [124]	Concrete with mineral admixtures	35	8	55	16	24	150	30	150
Liu Jianhua et al.[127]	Glass fiber resin-based composite material	35	24	–	–	24	60	8~24	60
Wang Qi et al. [128]	Carbon fiber epoxy resin-based composite material	35	24	*	24	48	5	1	10
Zheng Shansuo et	Mortar, brick and	45（90%）	3	60	2	6	300	50/100	75

al.[14]	masonry								
Qiao Hongxia et al.[42]	Reinforced concrete	*	16	60	8	24	100	20	100
López-Arce P. et al. [143]	Granite	*	4	35	8	12	150	60/75	75
Azevedo A.R.G. et al.[35]	Sludge-blended mortar	*	24	–	–	24	300	–	300
Silva Z.S.G. [8]	Limestone and silicate rock	*	12(+36)	60	24	11	5	–	10+1
Silva Z.S.G.[134]	Joint concrete	*	24	–	–	24	40	–	40

Note 1: In the table, "*" indicates that information in the literature is unspecified; "—" indicates that this item is not set in the experiment.

Song's comparative study on different salt spray cycle modes showed that when the duration ratio of drying to salt spray was 2:1, the chloride ion content in samples measured under the same environmental conditions was the highest [142]. Additionally, several studies have adopted the "16+8" wet-dry salt spray cycle, finding that this mode effectively facilitates salt penetration into porous building materials and accelerates salt spray corrosion [42, 124, 142]—notably, this 2:1 wet-dry duration ratio aligns with the specifications of the international standard BS EN 14147-2003 [54]. Salt spray tests involve the coupled action of environmental parameters like temperature, humidity, and salt spray on the tested materials, making the experiment's temperature and humidity conditions equally critical. In salt spray test studies on building materials, the set temperature for the salt spray mode is typically 35℃, while that for the drying mode generally ranges from 55–60℃; since salt spray fills the chamber during the spray phase, tests have shown that relative humidity is nearly saturated, so it is generally not controlled in the salt spray mode.

2.2.6 Measurement and evaluation methods

1）Chloride ion content

Chloride ion content is one of the most critical test items in salt spray experiments. By determining chloride ion content, the deposition amount of salt spray and the degree of salt intrusion into specimens can be quantitatively evaluated. The main existing testing techniques include titration, test paper method, ion chromatography, spectrophotometry, and potentiometric titration.

（1） Titration method

Titration methods can be further categorized into Mohr's method and mercurimetric method based on different indicators [116, 144]. Mohr's method uses potassium chromate (K_2CrO_4) as an indicator to determine chloride ion content in samples via titration with $AgNO_3$ solution. When chloride ions completely react with $AgNO_3$ to form white AgCl precipitate, the remaining $AgNO_3$ reacts with K_2CrO_4 to form red silver chromate (Ag_2CrO_4), indicating the titration endpoint. The mercurimetric method employs diphenylcarbazone ($C_{13}H_{12}N_4O$) as an indicator, which reacts with residual mercury nitrate ($Hg(NO_3)_2$) to form a purple complex, marking the titration endpoint. Since operational procedures significantly affect measurement results, titration is suitable for solutions with chloride ion concentrations > 5 mg/L. Additionally, $AgNO_3$, K_2CrO_4, and $Hg(NO_3)_2$ are all toxic substances; thus, proper protective measures should be implemented during testing, and waste liquids must be treated afterward.

（2） Test paper method

The test paper method relies on the reaction of mercury ions with organic chromogenic reagents to form colored complexes on fibrous filter paper. If the reflection wavelength of both the chromogenic reagent and the formed complex falls within the visible light range, the color change before and after the chemical reaction can be visually identified. This method is simple, rapid, and low-cost, typically completing the entire test in 3–5 minutes. As a semi-quantitative analysis technique, it has a detection range of tens to hundreds of mg/L [145, 146].

（3） Ion chromatography

Ion chromatography is a technique that separates and quantifies various ions in a sample based on the principle that ions exhibit different distribution coefficients between the stationary and mobile phases [146]. First, ions in the test sample are exchanged onto the chromatographic column, followed by separation of different ion types using an eluent. Corresponding ion chromatographic peaks are obtained by continuously monitoring the eluent's conductivity, with ion types identified by peak order. The detection limit is 0.2 μg/L. This technique is simple, rapid, and highly sensitive but requires relatively expensive equipment with high maintenance costs [116].

（4） Spectrophotometry

Spectrophotometry is a technique that converts measured absorbance intensity into ion concentration by continuously irradiating a sample solution of a specific concentration with light of varying wavelengths, based on the principle that different analytes absorb light at specific wavelengths. It offers high detection sensitivity and accuracy, but ion concentration and absorbance are non-linear at high concentrations, necessitating dilution prior to measurement. Moreover, it has strict requirements for sample purity; the presence of particulate impurities can compromise the accuracy of detection results [116, 147].

（5） Potentiometric titration

Potentiometric titration is based on titration principles, where the titration endpoint is determined by changes in solution potential during titration, allowing calculation of chloride ion content in the solution [146]. At the start of titration, silver ion concentration and solution potential are low; as titrant is added, silver ion concentration gradually increases, and solution potential rises. When chloride ions are fully reacted with the titrant, the solution potential peaks. This method has a detection range of 5–300 mg/L [116]. Currently, an automated potentiometric titrator with user-friendly operation and high detection accuracy has been developed based on this technique.

Chloride ion content in porous building materials may be unevenly distributed. Typically, test samples are prepared by drilling cores at different depths of the specimen; these samples are ground into fine powder, all sieved through a 0.63 mm mesh, then dissolved in a fixed volume of solvent, shaken thoroughly, and tested for chloride ion content [148]. In research, comparative analyses are typically performed on chloride ion content at different depths of the same specimen and at the same depth of different specimens [124, 142. For flexural members subjected to the combined action of salt spray and load, cores are taken from the pure bending section of the specimen to investigate the influence of bending stress and strain on chloride ion concentration [7].

2）Mass change rate

The mass change rate can macroscopically reflect the extent of erosion of specimens caused by salt spray weathering. Typically, specimen mass is measured using an electronic balance before and after the salt spray experiment: first, the initial dry weight of the specimens is measured and recorded. After different salt spray cycles, the specimens are removed from the salt spray chamber and placed in a drying oven. Once surface moisture has fully evaporated, the specimens are weighed, and their mass change rate ΔM is calculated using the following formula [54, 127]:

$$\Delta_M = \frac{M_t - M_0}{M_0} \times 100\% \tag{2-1}$$

where M_0 is the initial dry weight of the specimen (kg); M_t is the dry weight of the specimen after exposure to different salt spray cycles (kg).

In salt spray experiments, salt deposits on the specimen surface and migrates/diffuses into the interior with water, resulting in the formation of salt crystals within the material’s pores—this initially increases specimen mass. However, the gradual growth of these salt crystals in the pores generates expansive stress, inducing cracking, decomposition, and eventual damage to the material. Thus, long-term salt spray weathering ultimately leads to mass loss of the specimens [8, 35, 139].

Depending on the specific objective of measuring the mass change rate, post-cycle specimen treatment involves two approaches: cleaning and non-cleaning. For assessing salt spray-induced corrosion and the extent of damage (e.g., local cracking, pulverization, or spalling), specimens are removed from the salt spray chamber and soaked in deionized water in a container—with water volume 2–3 times the total volume of all specimens; soaking is gradual, requiring daily water replacement until all salt is leached out, which is verified when the conductivity of the solution in contact with the specimens does not exceed twice that of clean deionized water, after which specimens are dried to constant weight at 70°C, cooled to room temperature, and their dry weight M_t is recorded [54]. In the second case, for determining the mass of salt crystals deposited in specimens under salt spray exposure, specimens need not be cleaned with deionized water post-experiment; instead, they are directly dried to constant weight in a drying oven, and Mt is measured after cooling to room temperature.

3）Physico-mechanical properties

The physico-mechanical properties of porous building materials are key indicators that determine their service functions and durability. In salt spray experiments, mechanical indicators such as compressive strength, flexural strength, splitting tensile strength, and elastic modulus are typically tested. Moreover, strength loss rates and stress-strain curves can be used to analyze changes in material mechanical properties [14, 35, 50, 131, 139]. Testing equipment includes electronic universal testing machines and microcomputer-controlled electro-hydraulic servo pressure testing machines. Loads applied to specimens can be controlled through pressure sensors, while generated strains are monitored via data acquisition instruments. Specimens' mechanical properties are typically tested at different salt spray cycles to analyze the variation patterns of material mechanical properties under salt spray exposure.

Based on the literature review in Section 1.2.1 of Chapter 1 regarding salt's influence on the physico-mechanical properties of building materials, prismatic specimens measuring 40×40×160 mm^3 are predominantly used in mechanical property experiments on cement-based building materials. First, specimens are positioned horizontally on the roller supports of the press for flexural strength testing using the "three-point method"; the fractured specimens are then removed and placed on the press base plate for compressive strength testing. Typically, the loading rate for flexural strength tests is (50±10) N/s, while that for compressive strength tests is (500±50) N/s or (1±0.5) MPa/s [35, 139].

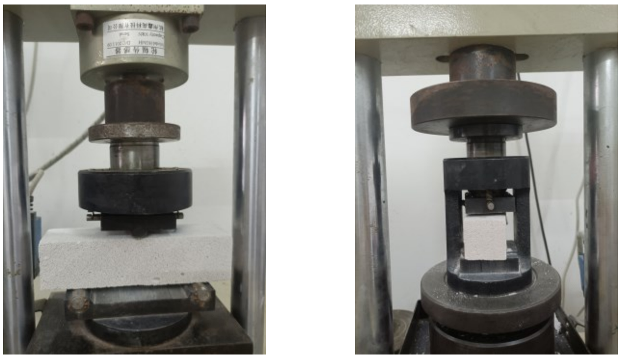

a) Flexural strength test **b) Compressive strength test**

Fig. 2-1 Mechanical property tests on prismatic specimens

4）Microstructural analysis

To characterize changes in porous building materials before and after salt spray erosion, or across different erosion stages, from a microscopic perspective, analyses of specimens' microtopography, pore structure, and chemical composition are typically performed. Common analytical techniques include Scanning Electron Microscopy (SEM), Mercury Intrusion Porosimetry (MIP), X-ray Diffraction (XRD), and X-ray Fluorescence (XRF).

SEM employs a focused, high-energy electron beam (narrow in diameter) to scan samples. Interactions between the beam and the material excite various physical signals, which are collected, amplified, and re-imaged to characterize the material's microtopography [149]. MIP is a method for measuring the pore size distribution of mesopores and macropores. Its core principle is that mercury is non-wetting to most solids; external pressure must be applied to force it into pores, with higher pressure enabling penetration into smaller-radius pores. By quantifying mercury intrusion under varying external pressures, the volume of pores corresponding to each size can be determined [150]. XRD is a technique for structural analysis that leverages X-ray diffraction in crystalline materials: when X-rays of a defined wavelength irradiate crystalline substances, they scatter upon interacting with regularly arranged atoms or ions within the crystal. The scattered X-rays undergo phase reinforcement in specific directions, producing characteristic diffraction patterns unique to the crystal structure. XRF is a method for determining trace element types and contents in substances: it uses primary X-ray photons or other microparticles to excite atoms in the test material, inducing the emission of secondary characteristic X-rays, which are then used for compositional analysis and chemical state investigation.

In research, combining multiple analytical techniques allows simultaneous observation of microtopography and micro-area compositional analysis. For instance, MIP can analyze the microscopic pore structure of porous materials under different salt conditions, measuring sample porosity and pore size distribution. SEM (at both low and high magnifications) can then observe pore connectivity and distribution, material density, interface cracks between components, corrosion products, and salt deposition patterns [7,42,131,139]. Further integration with XRD and XRF enables identification and analysis of crystal types and chemical compositions in the material. Based on experimental research requirements, such multi-technique combinations can provide accurate, reliable conclusions for qualitative and quantitative evaluation of physicochemical changes and microscopic pore structure alterations in porous materials during salt spray tests—ultimately offering a foundation for elucidating the mechanisms underlying macroscopic property changes in porous building materials under salt spray exposure.

2.3 Accelerated salt spray test method

Based on the above analysis and discussion of salt spray test standards in various fields, as well as the test methods and technical parameters in relevant research literatures, focusing on the research objective of this paper—studying the mechanism of changes in liquid water and water vapor moisture migration characteristics of cement mortar in a salt spray environment—and combined with the existing facilities and technical equipment in the laboratory, an accelerated salt spray test scheme for porous building materials suitable for this study is established.

2.3.1 Salt spray testing equipment

The salt spray chamber is a commonly used equipment for accelerated salt spray experiments, capable of simulating the salt spray climatic conditions in coastal areas by setting specific environmental parameters and cycling protocols. In this study, a CEAST 5050 salt spray test chamber (as shown in Figure 2-2) of Italian manufacture will be used. The chamber primarily comprises a solution storage tank, a salt spray generation compartment, and a control panel. The solution storage tank holds the prepared salt solution, which is sucked into the nozzle via compressed air and atomized into a fine mist. The control panel is equipped with knobs and buttons for setting the compartment temperature and salt spray cycling mode. A transparent sight glass on the exterior of the solution storage tank displays the liquid level, while the tank is fitted with a solution inlet at the top—where a glass funnel can be placed to enable timely replenishment of the salt solution. The salt spray generation compartment is capped with a four-sided pyramidal transparent lid to direct condensed water to the edges. A circular transparent window on the front face of the compartment facilitates real-time monitoring of salt spray conditions and specimen changes inside.

The salt spray generation compartment houses a spraying device, a salt spray collector, and a sample stage (as shown in Fig. 2-3). To prevent direct impingement of salt spray onto specimens in front of the nozzle and ensure uniform distribution of salt spray within the compartment, a spray diffuser (7) is installed outside the nozzle. A graduated cylinder beneath the salt spray collector (9) is used to measure the salt spray deposition rate. Referring to international standards BS EN 14147-2003(E) [54] and ASTM B117-11(E) [151], the average salt spray deposition rate is typically specified as 1–2 mL/(80 $cm^2 \cdot h$). An inclined baffle (17) above the saturation tower (5) and sprayer (6) inside the compartment prevents excessive salt spray deposition in this area—such deposition could otherwise lead to salt crystallization blocking the salt spray generation device and interfering with the continuous operation of the experiment. A water trough (18) at the interface between the compartment top and the lid collects condensed water flowing down the inner wall of the lid (2) (to prevent dripping onto specimens) and drains it from the compartment through an overflow port (20) once the water level reaches a specific height. Additionally, the water in the trough provides a seal around the edge of the top lid.

Fig. 2-2 CEAST 5050 salt spray test chamber

2.3.2 Test parameter settings

Based on salt spray test standards in various fields and numerous studies on salt spray experiments of porous building materials (Section 2.2), and considering the need to control salt solution concentration to avoid excessive salt crystallization that might block nozzles—combined with the main salt components and concentrations of seawater in China's coastal areas—this study employs a 5wt.% NaCl solution (prepared by mixing deionized water with analytical reagent (AR grade) NaCl crystals) for salt spray generation, with specific parameters referenced to international standards BS EN 14147-2003[54] and ASTM B117-11[151]. Notably, the salt spray is neutral, with the pH of collected condensed salt spray solution (measured at 23℃) ranging from 6.5 to 7.2; the salt solution added to the chamber's solution tank must be free from suspended undissolved salt crystals to prevent clogging of solution pipes and nozzles. For clean compressed air, sufficient pressure must be maintained before injection into the internal air saturation tower, ensuring that during the 35℃ salt spray phase, the saturation tower's top pressure exceeds 83 kPa and temperature exceeds 46℃.

Prior to the experiment, salt spray deposition rate is tested using two collectors: after 16 hours of continuous spraying with the prepared solution, the average deposition rate is calculated, with each collector yielding 1–2 mL/(80 cm²·h). Temperature control in the salt spray generation chamber is achieved via an immersion electric heater at the chamber bottom, with real-time monitoring by upper and lower internal temperature sensors; the salt spray mode is controlled at 35℃, and the drying mode at 55℃. Since humid air in the chamber is nearly saturated during the salt spray mode, relative humidity in this mode is not controlled.

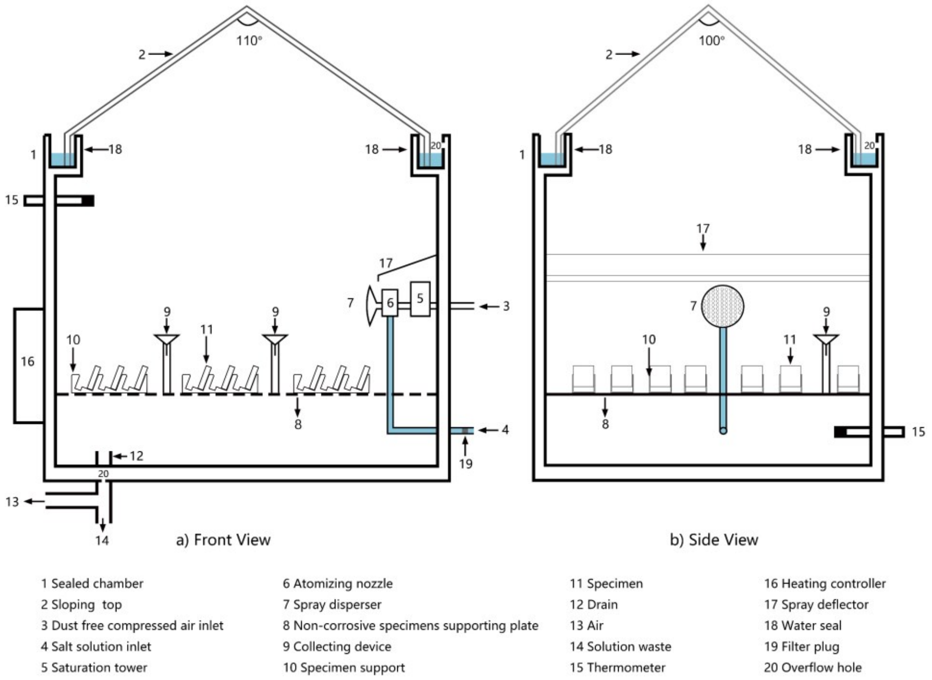

Fig. 2-3 Schematic diagram of the internal compartment structure of the salt spray test chamber

2.3.3 Design of specimen support

In Section 2.2.3, salt spray test standards and research literature across various fields commonly specify a specimen placement angle of 15°–30°. Considering specimen dimensions, placement angle, spacing, and the salt spray chamber's space utilization, cement mortar specimens will be placed with their front surfaces inclined at 20° to the vertical.

First, a suitable support structure must be designed to position and secure specimens on the chamber's sample stage. The design adheres to the principle of material efficiency while satisfying strength and experimental technical requirements. Following preliminary design and iterative optimization, six distinct schemes were developed, each with a 3D model (Fig. 2-4). These support models were additively manufactured using a 3D printer (WASP Delta 2040, Italy) from the DISAT Cultural Heritage Diagnosis Laboratory (Figure 2-5a). The raw material is polylactic acid (PLA), a novel biodegradable material exhibiting good gloss, solvent resistance, and thermal stability, widely used in multiple European manufacturing sectors. 3D printing offers advantages such as integrated fabrication, high plasticity, precise dimensional control, and high material utilization—attributes that align well with the support fabrication requirements of this experiment. Some finished supports are shown in Fig. 2-5b.

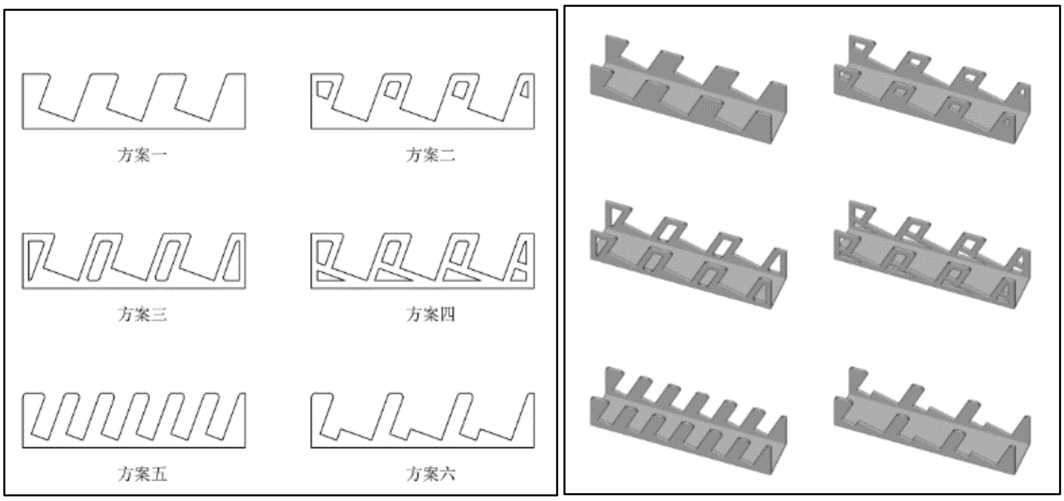

a) Design schemes **b) 3D models**

Fig. 2-4 Design and modeling of salt spray specimen supports

Scheme 1 is structurally robust but material-intensive. Schemes 2–4 incorporate hollowing of specimen backing plates and bases with varied geometric patterns to reduce material consumption; however, their relatively wide backing plates (20 mm) create confined spaces between specimens, partially blocking salt spray circulation around the rear surfaces of specimens. Thus, Scheme 5 narrowed the backing plates to 10 mm, doubling the number of placeable specimens but reducing inter-specimen spacing. Given the three specimen dimensions to be fabricated in Chapters 4 and 5 (40mm×40mm×10mm, 40mm×40mm×20mm, and 70mm×70mm×20mm), Scheme 6—building on Scheme 5—adjusted by removing three backing plates at intervals, widening the remaining backing plates to 22 mm, and increasing front-rear specimen spacing to improve air circulation, thereby enabling salt spray to permeate around specimens. Following multiple design iterations and refinements, Scheme 6 was selected as the final specimen support for the salt spray experiment, with its detailed geometry and dimensions illustrated in Fig. 2-5 c.

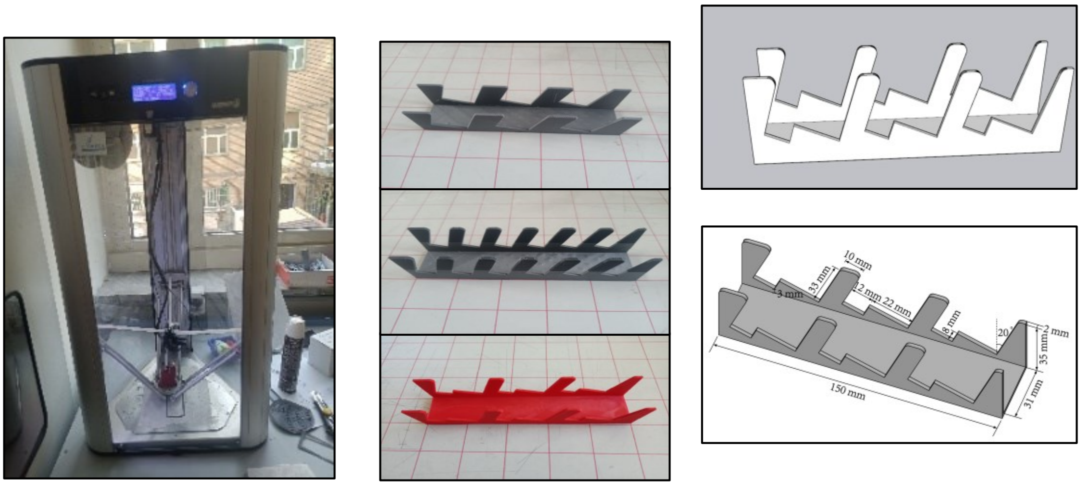

a) 3D printer (WASP Delta) **b) Printed products** **c) Selected model and dimensions**

Fig. 2-5 3D printing fabrication of salt spray specimen supports

2.3.4 Salt spray cycling procedure

To simulate the alternating weather conditions in coastal areas and the climatic characteristics of wet-dry salt spray cycles, this study adopts a salt spray-drying alternating cycle regime, drawing on relevant procedures from international standards BS EN 14147-2003[54] and ASTM B117-11[151]. Each 24-hour cycle comprises 8 hours of continuous salt spray (35°C) and 16 hours of constant-temperature drying (55°C).

After calibrating the salt spray deposition rate within the chamber, specimens from each group are placed on the internal supports. Following lid closure, the salt spray cycle experiment proceeds per the preset protocol, as illustrated in Fig. 2-6. Every 7 cycles serve as a test node, with one group of specimens retrieved for testing and analysis after 7, 14, 21, 28, and 35 cycles sequentially.

Fig. 2-6 Placement of cement mortar specimens inside the salt spray chamber

Consistent with the research objectives on moisture migration characteristics of porous building materials under salt spray deposition, five distinct moisture property experiments were conducted. The salt spray cycle durations for each specimen group in these experiments are presented in Tables 2-3 and 2-4. For each experiment, 6 specimen groups were prepared: 5 groups of salt-loaded specimens exposed to 7–35 salt spray cycles (one group per cycle count) and 1 group of salt-free control specimens. Specifically, for the vacuum saturation test, capillary water absorption test, water retention curve test, and water vapor permeability test, each group included 4 parallel specimens (Table 2-3). For the isothermal moisture adsorption curve test—which requires 5 distinct air humidity environments—6 specimen groups were prepared for each humidity level, with 3 parallel specimens per group (Table 2-4). Beyond the aforementioned specimen groups for moisture migration characteristic tests, an additional group was prepared to be retrieved at each salt spray cycle node for chloride ion content detection, SEM microtopography observation, MIP pore structure analysis, and other related analyses.

Table 2-3 Salt spray cycle durations of specimen groups in hygric properties experiments

Hygric properties experiments	0 cycle	7 cycles	14 cycles	21 cycles	28 cycles	35 cycles
Vacuum saturation experiment	$1O_1$, $1O_2$, $1O_3$, $1O_4$	$1A_1$,$1A_2$, $1A_3$, $1A_4$	$1B_1$, $1B_2$, $1B_3$, $1B_4$	$1C_1$, $1C_2$, $1C_3$, $1C_4$	$1D_1$, $1D_2$, $1D_3$, $1D_4$	$1E_1$, $1E_2$, $1E_3$, $1E_4$
Capillary absorption experiment	$2O_1$, $2O_2$, $2O_3$,$2O_4$	$2A_1$,$2A_2$, $2A_3$, $2A_4$	$2B_1$, $2B_2$, $2B_3$, $2B_4$	$2C_1$, $2C_2$, $2C_3$, $2C_4$	$2D_1$, $2D_2$, $2D_3$, $2D_4$	$2E_1$, $2E_2$, $2E_3$, $2E_4$
Water retention curve experiment	$4O_1$, $4O_2$, $4O_3$,$4O_4$	$4A_1$,$4A_2$, $4A_3$, $4A_4$	$4B_1$, $4B_2$, $4B_3$, $4B_4$	$4C_1$, $4C_2$, $4C_3$, $4C_4$	$4D_1$, $4D_2$, $4D_3$, $4D_4$	$4E_1$, $4E_2$, $4E_3$, $4E_4$
Water vapor permeability experiment	$5O_1$, $5O_2$, $5O_3$, $5O_4$	$5A_1$,$5A_2$, $5A_3$, $5A_4$	$5B_1$, $5B_2$, $5B_3$, $5B_4$	$5C_1$, $5C_2$, $5C_3$, $5C_4$	$5D_1$, $5D_2$, $5D_3$, $5D_4$	$5E_1$, $5E_2$, $5E_3$, $5E_4$

Table 2-4 Salt spray cycle durations of specimen groups in sorption isotherm experiments

Ambient humidity	0 cycle	7 cycles	14 cycles	21 cycles	28 cycles	35 cycles
33%	3O1-1, 3O2-1, 3O3-1	3A1-1, 3A2-1, 3A3-1	3A1-2, 3A2-2, 3A3-2	3A1-3, 3A2-3, 3A3-3	3A1-4, 3A2-4, 3A3-4	3A1-5, 3A2-5, 3A3-5
53%	3O1-2, 3O2-2, 3O3-2	3B1-1, 3B2-1, 3B3-1	3B1-2, 3B2-2, 3B3-2	3B1-3, 3B2-3, 3B3-3	3B1-4, 3B2-4, 3B3-4	3B1-5, 3B2-5, 3B3-5
75%	3O1-3, 3O2-3, 3O3-3	3C1-1, 3C2-1, 3C3-1	3C1-2, 3C2-2, 3C3-2	3C1-3, 3C2-3, 3C3-3	3C1-4, 3C2-4, 3C3-4	3C1-5, 3C2-5, 3C3-5
84%	3O1-4, 3O2-4, 3O3-4	3D1-1, 3D2-1, 3D3-1	3D1-2, 3D2-2, 3D3-2	3D1-3, 3D2-3, 3D3-3	3D1-4, 3D2-4, 3D3-4	3D1-5, 3D2-5, 3D3-5
95%	3O1-5, 3O2-5, 3O3-5	3E1-1, 3E2-1, 3E3-1	3E1-2, 3E2-2, 3E3-2	3E1-3, 3E2-3, 3E3-3	3E1-4, 3E2-4, 3E3-4	3E1-5, 3E2-5, 3E3-5

2.3.5 Methods of analysis and evaluation

To analyze salt deposition and changes in basic physical properties of specimens during accelerated salt spray cycles, mass change rate, chloride ion content, and micropore structure were measured and evaluated for specimen groups exposed to varying salt spray cycle durations. Unlike the procedure specified in BS EN 14147:2003—where specimens are cleaned with deionized water and dried to constant weight post-test to determine corrosion-induced mass loss—this study aimed to quantify salt crystals formed within specimens. Thus, specimens were directly dried to constant weight and weighed after salt spray exposure.

Chloride ion content was measured using a chromatographic analyzer or Chlorimeter C-Cl 3000. When a 3g sample was fully dissolved in an acidic solution to induce an electrochemical reaction, chloride ion concentration was determined via voltage changes in the analyzer's probe electrode. Detailed methods and procedures are provided in Chapter 4, Section 4.2.3. For analyzing material composition, microtopography, and pore structure of cement mortar, X-ray diffraction (XRD), scanning electron microscopy (SEM), and mercury intrusion porosimetry (MIP) were used to characterize microstructural changes induced by varying salt spray cycles. Specific protocols for SEM, MIP, and XRD adhere to international standards ISO 21466:2019 [149], ISO 15901-1:2016 [150], and BS EN 13925-2:2003 [152], respectively.

Methods for measuring moisture migration-related properties of cement mortar under salt spray deposition are detailed in Chapters 4 and 5. Basic physical properties (saturated moisture content, apparent density, open porosity) and liquid water migration properties (capillary absorption coefficient, capillary moisture content, water retention curve) are described in Chapter 4, Section 4.3. Measurements of isothermal equilibrium moisture adsorption curves and water vapor permeability coefficients under salt spray deposition are presented in Chapter 5, Section 5.3.

2.4 Chapter summary

To establish an accelerated salt spray testing method applicable to porous building materials in coastal salt spray zones, this chapter reviewed domestic and international standards for salt spray testing across various fields, along with relevant experimental research literature. Key technical requirements and experimental parameters for salt spray testing—including specimen specifications, salt solution concentration, specimen placement angle, salt spray cycling regime, and measurement and evaluation methods—were compared and analyzed.

Based on the research objectives and available experimental equipment, the primary control parameters for the salt spray test were determined. Specimen supports meeting technical requirements were designed and fabricated, and a salt spray cycling regime and measurement/evaluation methods suitable for porous building materials were established. The accelerated salt spray testing method developed in this chapter provides a critical foundation for the investigations in Chapters 4 and 5, which examine the liquid water and water vapor migration characteristics of cement mortar under salt spray deposition, respectively.

Chapter 3 Chloride migration and crystal distribution in cement mortars

3.1 Introduction

Under the perennial influence of salt spray climates, salt crystallization readily forms and deposits within the pores of building envelope materials in coastal areas due to the continuous migration of salt and moisture. This phenomenon not only degrades the durability of building materials [19, 153] but also alters the hygrothermal transfer properties of the envelope structures, thereby impacting building energy consumption [72, 154, 155]and indoor thermal comfort [72, 156, 157]. Salt cannot independently penetrate building materials; instead, it dissolves in water and migrates into the material through capillary action alongside moisture. This process determines the deposition location and distribution pattern of salt crystallization [13, 19, 36, 59]. To understand the migration mechanisms and crystallization characteristics of salt in porous building materials, capillary absorption tests under semi-immersion in salt solutions were conducted prior to accelerated salt spray testing.

This chapter focuses on cement mortar, a porous building material widely used in building envelope engineering. Specimens with varying water-to-cement ratios (W/C) and surface evaporation conditions were subjected to partial immersion in a 5% NaCl solution to induce salt absorption and crystallization. Advanced analytical techniques, including Ion Chromatography (IC), Scanning Electron Microscopy with Energy Dispersive Spectroscopy (SEM-EDS), X-ray Diffraction (XRD), and Mercury Intrusion Porosimetry (MIP), were employed to investigate chloride ion distribution, salt crystallization patterns, and pore structure characteristics. Additionally, comparative capillary absorption tests in saturated NaCl solutions were conducted to study the hygroscopic behavior of salt-containing cement mortar. This research provides a theoretical foundation for further analyzing the mechanisms of salt crystallization deposition and hygrothermal property changes in cement mortar under salt spray climate conditions.

3.2 Experimental materials and methods

3.2.1 Materials and specimen preparation

To investigate the salt migration mechanisms in cement mortar specimens with varying water-to-cement ratios (W/C) under different evaporation conditions, six groups of specimens were prepared. Four groups were used for capillary water absorption experiments (detailed in Section 3.2.3), while the remaining two groups were designated for measuring chloride ion (Cl^-) concentrations after immersion in NaCl solutions. Each group included specimens with W/C ratios of 0.4, 0.6, and 0.8. The cement mortar specimens were prepared using locally sourced Portland cement (PO 42.5 grade), deionized water, and natural sand. The sand had an apparent density of 2580 kg/m^3, a fineness modulus of 2.19, and a well-graded particle size distribution. Based on sieve analysis results, the sand particles exhibited a continuous size distribution, with each size fraction occupying a specific proportion, as shown in Fig. 3-1.

The uniformly mixed paste was thoroughly vibrated in steel molds to achieve full compaction. The molded specimens were then steam-cured in a constant temperature and humidity chamber for 24 hours. After demolding, prismatic specimens with dimensions of 40 mm × 40 mm × 160 mm were obtained. These specimens were subsequently cured in a controlled curing chamber (20 ± 2°C, relative humidity (RH) > 95%) for 28 days. To analyze the potential influence of evaporation conditions on salt crystallization deposition in porous materials [60, 62, 68, 98], two out of the six specimen groups were coated with an epoxy resin layer on their four lateral surfaces (above 6 cm in height) to inhibit surface moisture evaporation. This modification allowed for comparative capillary absorption tests under different surface evaporation conditions.

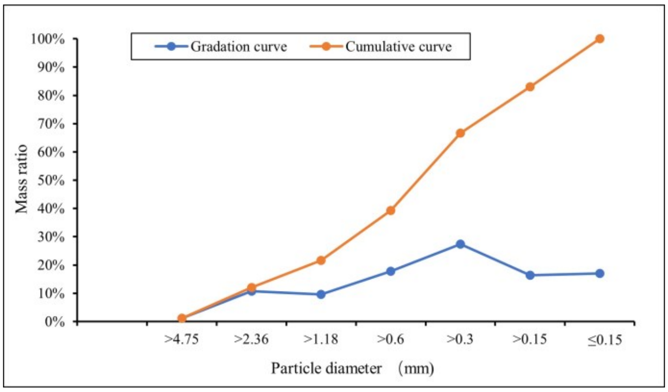

Fig. 3-1 Grading curve of natural sand

3.2.2 Salt induction

Prior to salt absorption, all cement mortar specimens were oven-dried at 70°C until reaching constant mass (defined as a weight variation of ≤0.1% between measurements taken at 24 ± 2-hour intervals) [158]. The dried specimens were then partially immersed in glass containers filled with a 5 wt.% NaCl solution (6 cm depth, Fig. 3-2) to facilitate capillary-driven salt infiltration. This NaCl concentration was selected based on experimental standards (B117–

11 [151], B.S.1224-1970, NFA91-101-1966 [120, 122, 136]), previous studies on chloride salt erosion in porous building materials [35, 119, 134, 136-138], and natural seawater salinity. Each specimen was elevated on a 5-mm stainless steel support to ensure full contact between its base and the solution. The experiments were conducted over 120 days in a controlled environment (23 ± 0.5°C, RH 60 ± 5%), with periodic replenishment of the solution to maintain a constant liquid level and complete replacement of the solution every 14 days to ensure stable concentration.

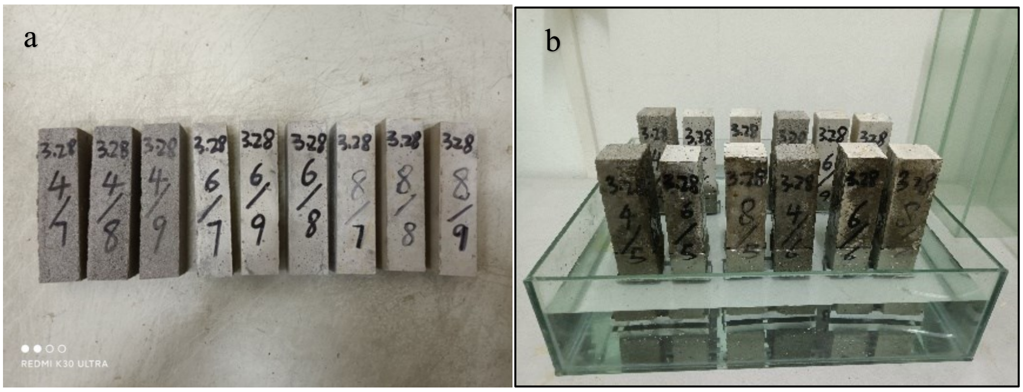

Fig. 3-2 Specimens partially immersed in NaCl 5 wt.% solution for 120 days

3.2.3 Test and analysis methods

1）Salt crystallization distribution

As the salt solution continuously infiltrates the specimen through capillary action, water evaporates from the unsealed surfaces exposed to air, leading to solution supersaturation. Salt crystals are partially deposited within the specimen and partially accumulated on its surface [59], resulting in an increase in total specimen mass. The mass balance is expressed as:

$$m_f - m_0 = m_t \tag{1}$$

$$m_t - m_e = m_i \tag{2}$$

where m_0 is the initial dry mass of the specimens, m_f is the dry mass of the specimens after soaking in NaCl 5 wt% solution for 120 days, m_t is the total mass of salt crystals in or on the specimens, m_e is the mass of the external salt crystals scraped off from the surface of specimens, and m_i is the mass of internal salt crystals.

2）Chloride ion concentration analysis

To analyze the migration and distribution of salt in cement mortar specimens, chloride ion (Cl^-) concentrations at different heights and depths were measured using an ICS-900 Ion

Chromatography System (instrument parameters listed in Table 3-1). Each specimen was vertically sectioned into five segments along its height: segments S1–S4 (30 mm height each) and S5 (40 mm height). During the initial immersion phase, segments S1–S3 were exposed above the salt solution surface, while S5 remained fully immersed. A 5-mm-thick horizontal slice was then cut from the top of each segment. From each 40 mm × 40 mm × 5 mm slice, a 20-mm-diameter core sample was drilled from the center, leaving a hollow rim sample (Fig. 3-3). Both core and rim samples were individually pulverized into fine powder using an agate mortar. For Cl⁻ concentration testing, 1 g of powder from each sample was dissolved in 20 ml of deionized water. The solution was vigorously shaken to ensure homogeneity and allowed to settle at room temperature for 30 minutes prior to analysis.

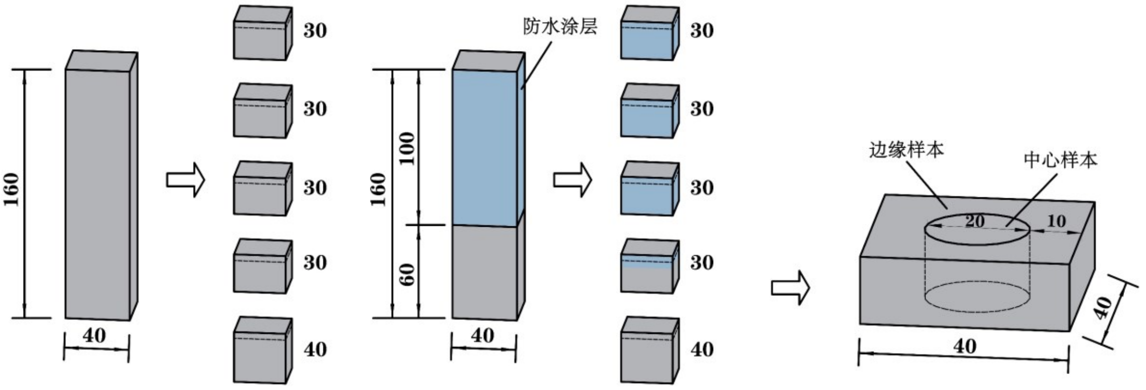

Fig. 3-3 Sample preparation for determining Cl- concentration

3）Microstructural analysis

To observe salt crystallization-induced changes in cement mortar, microstructural analyses were conducted using a Hitachi S-3700N scanning electron microscope coupled with energy-dispersive X-ray spectroscopy (SEM-EDS) and a Bruker D8 X-ray diffractometer (XRD) for qualitative and semi-quantitative characterization of crystal morphology and composition [13, 159, 160]. Additionally, pore structure evolution (porosity and pore size distribution) in salt-laden specimens was analyzed via mercury intrusion porosimetry (MIP, AutoPore IV9500) following ISO 15901-1 [150], utilizing dry, non-corrosive nitrogen gas as the intrusion medium. Instrument parameters are summarized in Table 3-1.

Table 3-1. Specifications of Analytical Instruments

Instruments	Manufacturer	Model	Precision	Measurement range
Ion chromatograph	Diane Co. USA	ICS-900	Infusion pump flow density <0.1%	0~10,000 uS/cm

Scanning electron microscope (SEM)	Hitachi Co. Japan	S-3700N	Resolution 3 nm	Magnification 5x-300,000x
Energy Dispersive X-ray detector (EDS)	Bruker Co. Germany	Quantax400	—	The element 4Be~92U
X-ray diffractometer (XRD)	Bruker Co. Germany	D8 ADVANCE	Angular accuracy≤0.01°	2θ Scale 0～150°
Automatic mercury porosimeter (MIP)	Micromeritics Co. USA	AUTOPORE IV 9500	0.001 cm^3	Pore size range $3.6\times10^{-3} \sim 400$ μm

4）Capillary absorption characteristics

Capillary absorption tests were conducted to investigate the effects of salt crystallization on the moisture migration in cement mortar [161]. Prismatic specimens (40 mm × 40 mm × 160 mm) were sealed with transparent plastic film on their four lateral surfaces and top surface, with two holes punctured in the top film to allow air escape (Fig. 3-4a). The bottom 1 cm of the lateral surfaces remained unsealed to avoid interference from film-liquid contact. Specimens were positioned on stainless steel supports in glass containers, with the liquid level maintained 2–5 mm above the support top. During testing, the solution (pure water or saturated NaCl) was periodically replenished to ensure a constant liquid level (Fig. 3-4b). Specimen dry mass was measured following the method described in Section 3.2.2. The capillary absorption coefficient (Acap) was determined in accordance with international standard BS EN 1925:1999 [162].

a) b)

Fig. 3-4 Capillary absorption test (a. Schematic diagram; b. Test scenario).

While capillary absorption tests typically use pure water as the absorption medium [161, 163], pure water infiltrating salt-laden porous materials can dissolve pre-existing salt crystals within the pores, leading to salt migration and redistribution that alter the initial capillary absorption behavior [13, 62, 164]. To address this, saturated NaCl solution was employed as the absorption medium in this study. However, differences in density, viscosity, and surface tension between saturated NaCl solution and pure water may influence the measured capillary absorption coefficient (A_{cap}) [6, 28, 29]. To quantify this effect and determine the capillary absorption coefficient ratio ($A_{\mathrm{cap,sol}}/A_{\mathrm{cap,w}}$), two groups of specimens were tested: one in deionized water (labeled NOW) and the other in saturated NaCl solution (labeled NOS), as shown in Fig. 3-4b. Based on the results and calculated $A_{\mathrm{cap,sol}}/A_{\mathrm{cap,w}}$, comparative capillary absorption tests were conducted between salt-contaminated specimens with uncoated lateral surfaces (labeled NSS) and those coated with epoxy resin on lateral surfaces (labeled CSS), both immersed in saturated NaCl solution. Pretreatment and testing conditions for all groups are summarized in Table 3-2.

Table 3-2 Pretreatment and test conditions of specimens for capillary absorption test at 23 ± 2 °C)

Group symbol	Amount of specimens	Water cement ratio(W/C)	Lateral sides treatment （Epoxy）	Partial immersion treatment (5 wt% NaCl solution, 120d）	Liquid for capillary absorption
NOW	1 1 1	0.4 0.6 0.8	No	No	Pure water
NOS	1 1 1	0.4 0.6 0.8	No	No	Saturated NaCl solution
NSS	1 1 1	0.4 0.6 0.8	No	Yes	Saturated NaCl solution
CSS	1 1 1	0.4 0.6 0.8	Yes	Yes	Saturated NaCl solution

3.3 Observation and measurement Rresults

3.3.1 Salt crystal distribution

Salt crystals on the surfaces of cement mortar specimens accumulated progressively with immersion time, exhibiting reduced growth rates after 90 days. Post-120-day immersion, white salt crystals were predominantly observed on lateral surfaces above the solution level, with their density increasing vertically. Distinct crystallization patterns emerged depending on the water-to-cement ratio (W/C): specimens with W/C = 0.4 displayed thick, clustered salt crystal layers in upper regions, whereas those with W/C = 0.6 and 0.8 exhibited thin, uniformly distributed layers along the height (Fig. 3-5). These differences stem from matrix material characteristics, where denser matrices (lower W/C) suppressed crystal growth, while porous matrices (higher W/C) facilitated thicker deposits [165]. Notably, epoxy resin-coated specimens showed significantly fewer surface crystals, appearing as isolated spots or patches.

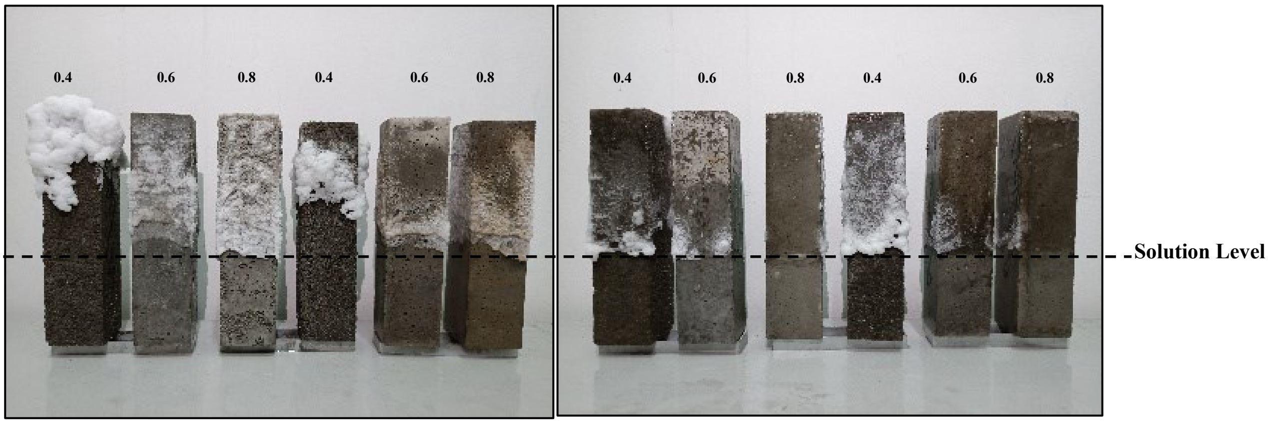

Fig. 3-5. Salt crystal distribution patterns on upper lateral surfaces of cement mortar specimens

Significant differences in internal versus external salt crystal mass distribution were observed among cement mortar specimens with varying water-to-cement ratios (W/C) (Fig. 3-6). For uncoated specimens: $m_{i0.4} < m_{e0.4}$, $m_{i0.6} < m_{e0.6}$, and $m_{i0.8} > m_{e0.8}$ (respective differences of 28.80 g, 5.09 g, and 24.07 g). In contrast, epoxy-coated specimens exhibited reversed trends: W/C 0.4: $m_{i0.4} > m_{e0.4}$, $m_{i0.6} > m_{e0.6}$, and $m_{i0.8} > m_{e0.8}$ (differences of 1.88 g, 4.18 g, and 38.22 g).

These results indicate that epoxy coating reduced total salt crystal mass (m_t) and surface-deposited mass (m_e), while increasing internal deposition (m_i). The impermeable epoxy resin suppressed lateral moisture evaporation, thereby minimizing salt migration toward surfaces. Notably, under prolonged immersion, salt crystallization-induced expansive stresses degraded the epoxy coating on specimens, eventually allowing salt crystals to form on coated surfaces.

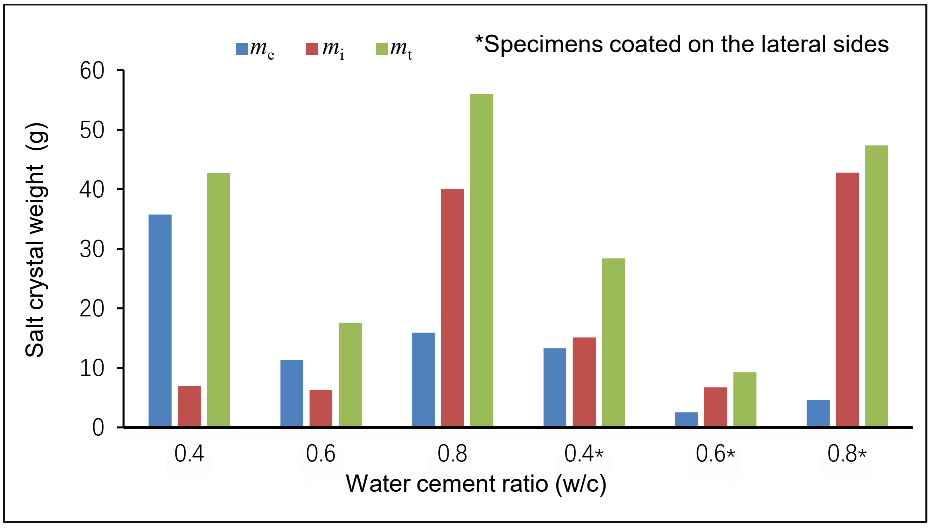

Fig. 3-6. Mass distribution of salt crystals in cement mortar with varying water-to-cement (W/C) ratios

3.3.2 Chloride ion concentration

Chloride ion (Cl^-) concentrations in cement mortar specimens exhibited heterogeneous distributions. For uncoated specimens (Fig. 3-7a), Cl^- concentrations in edge regions exceeded those in core regions at all heights. In W/C 0.4 specimens, the highest Cl^- concentrations were observed in the top segment (S1), with core and edge values of 30.89 mg/g and 51.06 mg/g, respectively, decreasing progressively from S2 to S5. W/C 0.6 and 0.8 specimens showed comparable core Cl^- concentrations across heights (averages: 9.60 mg/g and 13.30 mg/g, respectively). However, edge concentrations in W/C 0.6 specimens fluctuated vertically, while W/C 0.8 specimens displayed a gradual decline from S1 to S5, akin to W/C 0.4.

In epoxy-coated specimens (Fig. 3-7b), Cl^- concentrations in both core and edge regions were reduced across all segments (except S1) compared to uncoated specimens. For W/C 0.4 and 0.8, S1 exhibited elevated Cl^- concentrations, while S2–S5 segments showed nearly uniform values. W/C 0.6 specimens exhibited minimal Cl^- concentrations in S1–S3 (core: <0.75 mg/g; edge: <2.28 mg/g), with a gradual increase from S3 to S5. These trends suggest that Cl^- distribution under capillary absorption is governed by both lateral evaporation conditions and pore structure (influenced by W/C).

Two critical observations emerge: (1) Surface evaporation-driven crystallization: Uncoated specimens experienced continuous moisture evaporation and salt solution migration to surfaces, promoting salt accumulation near evaporation fronts [76, 166], thus explaining their higher Cl^- levels. (2) S5 segment behavior: Minimal Cl^- concentration differences between coated and uncoated groups in S5 arose because this segment remained fully immersed, lacking lateral evaporation, which altered salt transport mechanisms compared to S1–S4.

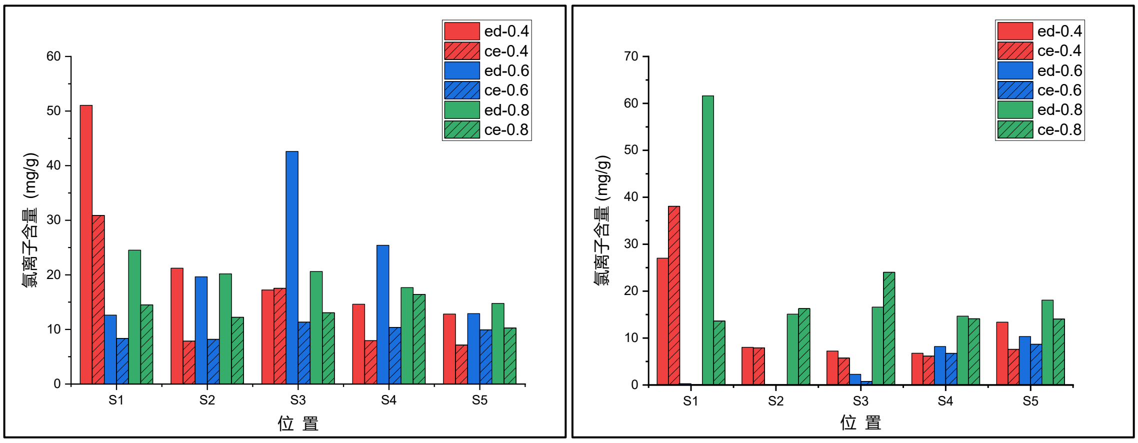

a) Uncoated lateral surfaces **b) Epoxy-coated lateral surfaces**

Fig. 3-7. Cl^- concentration distribution at varying heights and depths in cement mortar specimens

3.3.3 Microscopic morphology

To microscopically identify chemical elements and crystalline phases in salt solution-immersed cement mortar, selected specimens were analyzed via SEM-EDS and XRD. Fig. 3-8 shows EDS spectra of specimens with water-to-cement ratios (W/C) of 0.4 and 0.8. Characteristic X-ray energy peaks revealed major elements in SEM-observed regions, including C, O, Si, Na, Cl, Ca, Al, and Mg. In addition to primarementitious elements (e.g., Ca, Si), distinct Na and Cl peaks confirmed NaCl crystallization. XRD analysis (Fig. 3-9) further identified crystalline phases such as $CaCO_3$, $CaSO_4·2H_2O$, SiO_2, CaO, $NaCl$, and $3CaO·Al_2O_3·3CaSO_4·32H_2O$ in both W/C 0.4 and 0.8 specimens, corroborating NaCl deposition and distribution within the mortar matrix.

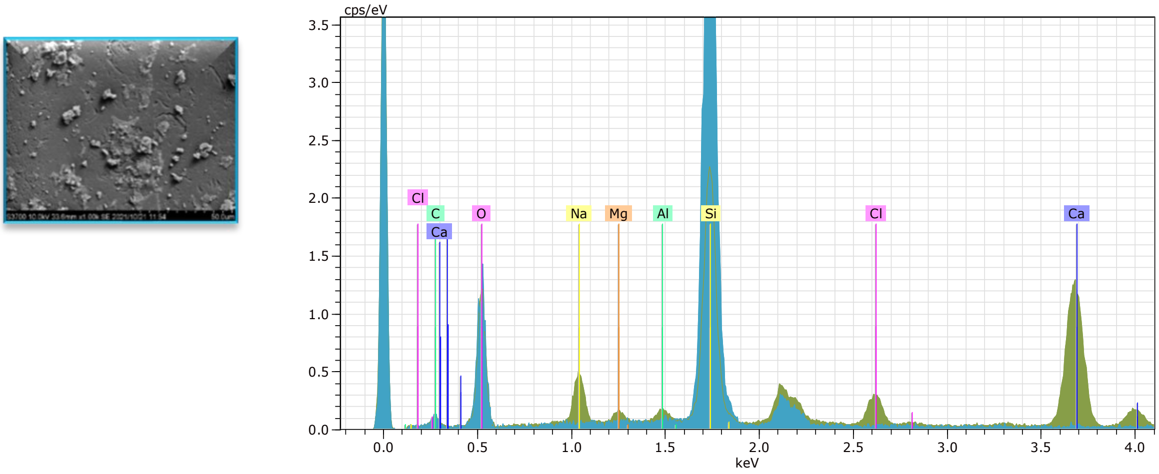

a) W/C = 0.4

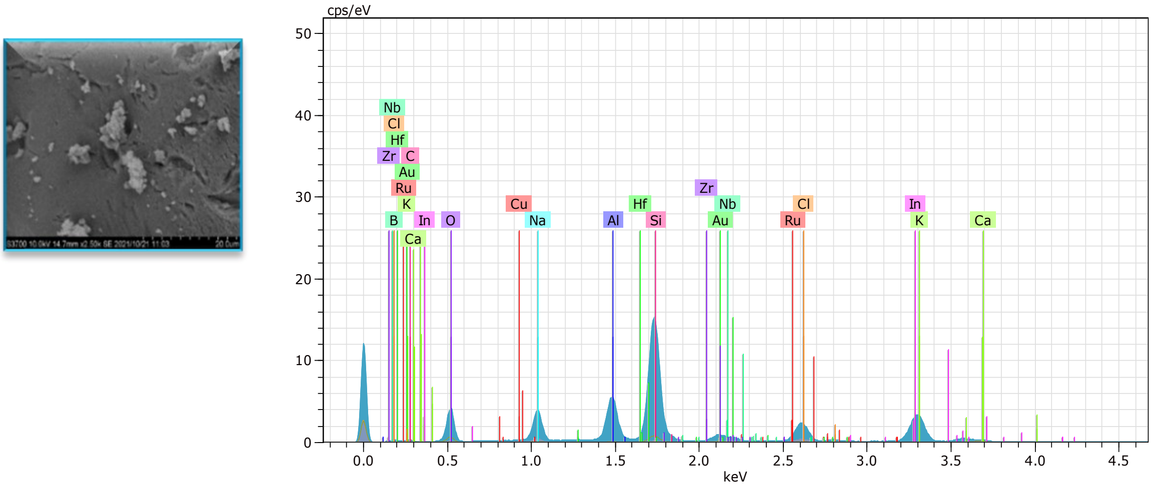

b) W/C = 0.8

Fig. 3-8. EDS spectra of cement mortar specimens sampled after immersion in 5 wt% NaCl solution:

To analyze the distribution patterns of NaCl crystals within cement mortar pores, scanning electron microscopy (SEM) was employed to observe salt crystallization in specimens, with comparisons to pristine NaCl crystals prior to dissolution (Fig. 3-10). The upper row (a–c) displays SEM images of pristine NaCl crystals used in solution preparation, characterized by regular cubic shapes, smooth surfaces, and isolated particles. In contrast, the lower row (d–f) shows NaCl deposits in specimens after 120-day immersion in 5 wt% NaCl solution and drying to constant mass in a forced-air oven. Post-immersion crystals exhibited smaller, irregular morphologies with blurred boundaries and clustered aggregates, indicating that pore-confined salt solutions underwent evaporation-induced supersaturation and recrystallization, with crystal morphology constrained by the internal pore structure. These microscopic observations align with the macroscale salt distribution trends reported in Section 3.3.1, confirming that crystallization patterns are governed by pore architecture and moisture transport properties of porous materials.

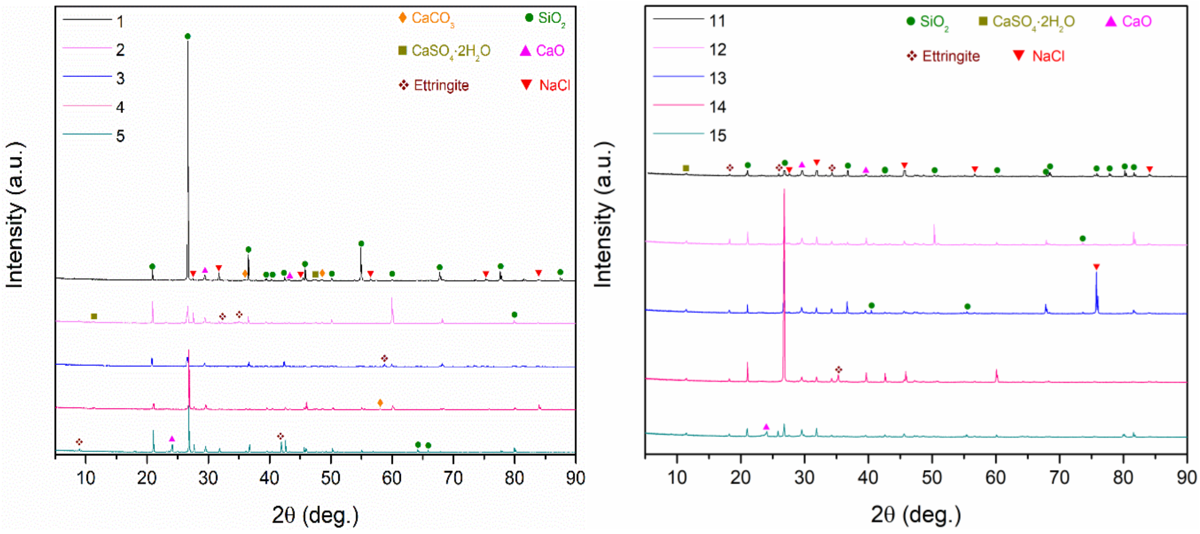

a) W/C = 0.4 **b) W/C = 0.8**

Fig. 3-9. XRD patterns of cement mortar specimens at varying heights

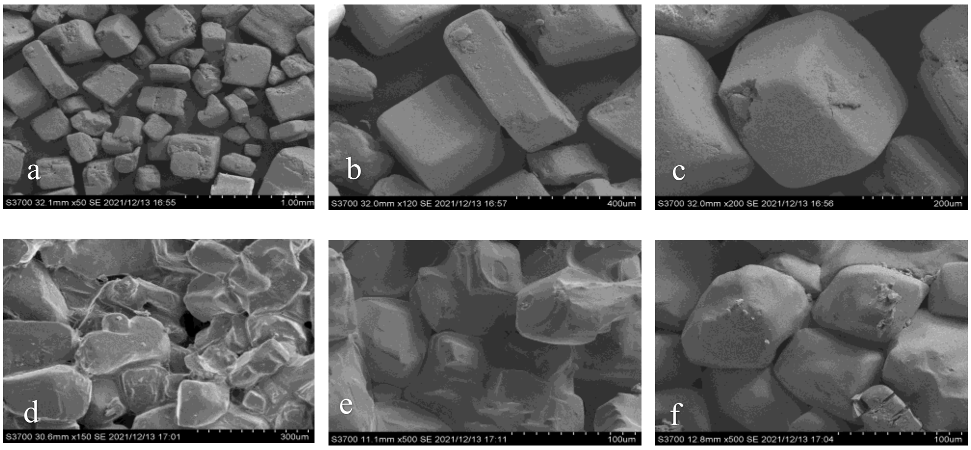

Fig. 3-10. SEM images of NaCl crystals before and after intrusion into cement mortar pores: (a–c) Pristine NaCl crystals; (d–f) NaCl crystals within pores

3.3.4 Pore structure characteristics

Mercury intrusion porosimetry (MIP) tests on specimens after 120-day salt solution immersion revealed porosity and pore size distributions for W/C = 0.4, 0.6, and 0.8 specimens (Fig. 3-11, Table 3-3). Despite similar porosity, distinct average pore diameters were observed: 161.3 nm (W/C = 0.4), 60.9 nm (W/C = 0.6), and 40.3 nm (W/C = 0.8). The difference between apparent and bulk densities, reflecting open pore volume, was highest for W/C = 0.4 (0.26), followed by W/C = 0.8 (0.23) and 0.6 (0.20). The larger open pore volume in W/C = 0.4 specimens likely stems from air entrapment during mixing due to high viscosity and poor workability of low W/C pastes. This enhanced capillary uptake and surface evaporation, aligning with significant surface salt deposition observed in Fig.3-5.

Fig. 3-11 further compares cumulative and incremental mercury intrusion volumes across pore size ranges: 0–100 nm: $V_{0.8} > V_{0.6} > V_{0.4}$. 100–1000 nm: $V_{0.6} > V_{0.8} > V_{0.4}$. 10^3–10^5 nm: $V_{0.4} \approx V_{0.6} \approx V_{0.8}$. W/C = 0.4 specimens exhibited ~30% pore volume in pores >10^5 nm, compared to ~10% for W/C = 0.6 and 0.8. This suggests W/C = 0.4 specimens possess more large pores and fewer small pores, deviating from conventional trends where porosity increases with W/C [167]. The anomaly may arise from insufficient water and lack of superplasticizers in W/C = 0.4 mixes, leading to dry, viscous pastes with poor workability, reduced compactness, and incomplete cement hydration under low W/C and high sand content conditions [168].

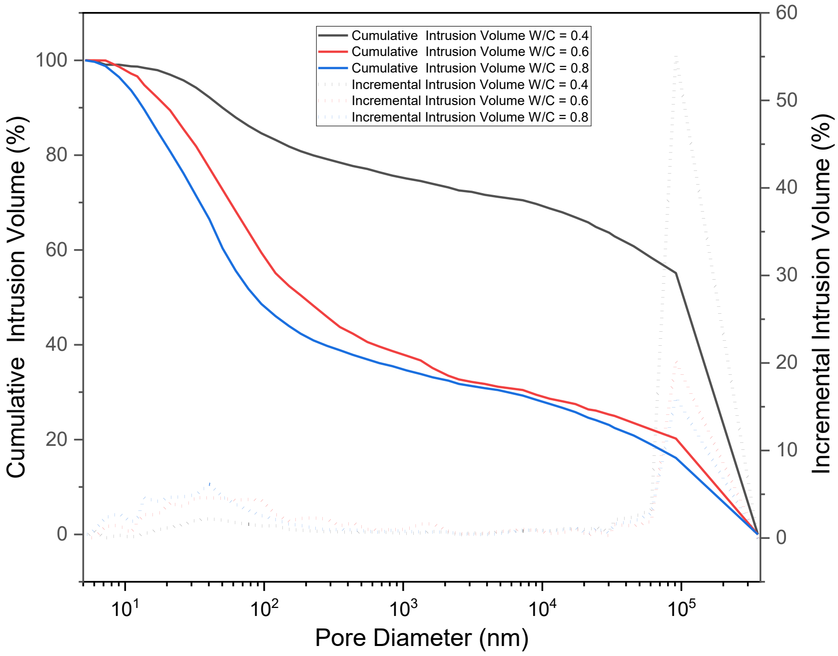

Fig. 3-11. Pore size distribution of cement mortar specimens with water-to-cement (W/C) ratios of 0.4, 0.6, and 0.8

Table 3-3 Pore structure data of target specimen

Pore parameters	w/c = 0.4	w/c = 0.6	w/c = 0.8
Porosity	12.65%	10.17%	11.38%
Average Pore Diameter（nm）（4V/A）	161.3	60.9	40.3
Permeability（mdarcy）	113.67	56.27	56.27
Bulk Density (0.51 psia) (g/mL)	1.82	1.75	1.81
Apparent Density (g/mL)	2.08	1.95	2.04

3.3.5 Capillary absorption curves

The capillary absorption curves of NOW (deionized water) and NOS (saturated NaCl solution) specimen groups shown in Fig. 3-12 exhibit two distinct phases: a rapid initial rise (Phase I) followed by a gradual plateau (Phase II). For pure water absorption (NOW), Phase I corresponds to capillary pore filling, while Phase II reflects slow moisture uptake into smaller pores and air voids [169]. During Phase I, the capillary absorption coefficient ($A_{\mathrm{cap,NOS}}$) of NOS specimens was lower than that of NOW specimens ($A_{\mathrm{cap,NOW}}$). Calculated ratios $A_{\mathrm{cap,NOS}}/A_{\mathrm{cap,NOW}}$ for W/C = 0.4, 0.6, and 0.8 specimens were 0.79, 0.90, and 0.98, respectively. This reduction in A_{cap} under NaCl solution arises from its higher density, surface tension, and viscosity compared to pure water [80, 170], which impede capillary flow [67]. In Phase II, NOS specimens with W/C = 0.6 and 0.8 achieved higher moisture contents than their

NOW counterparts, whereas the inverse trend was observed for W/C = 0.4 specimens.

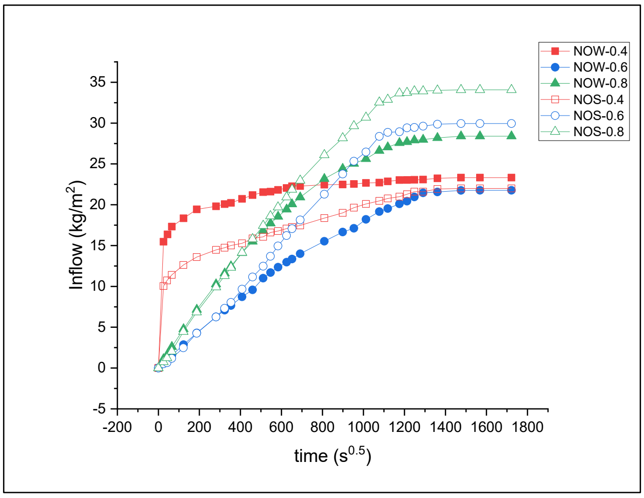

Fig. 3-12. Capillary absorption curves of NOW and NOS specimen groups

The hygroscopic behavior of porous materials is influenced by pore structure. Liquid water enters pores via capillary action, permeation, or both. Capillary action dominates in pores sized 100–10^5 nm [171], while permeation occurs in pores >10^5 nm [172]. As shown in Fig. 3-11, W/C = 0.4 specimens exhibit the highest proportion of pores >10^5 nm (30%), leading to enhanced permeation-driven moisture uptake during Phase I and distinct capillary absorption curve morphology compared to W/C = 0.6 and 0.8 specimens.

Fig. 3-13 compares capillary absorption curves of uncoated specimens in saturated NaCl solution (NSS group) with salt-free specimens (NOS group). The NSS group exhibited lower $A_{\mathrm{cap,w}}$ values. Using the $A_{\mathrm{cap,NOS}}/A_{\mathrm{cap,NOW}}$ ratio (see Section 3.3.5), $A_{\mathrm{cap,sol}}$ values were normalized to $A_{\mathrm{cap,w}}$ (Table 3-4). Compared to NOS, NSS specimens showed A_{cap} changes of +101.26% (W/C = 0.4), -45.72% (W/C = 0.6), and -60.82% (W/C = 0.8), with corresponding w_{cap} changes of +21.42%, -56.39%, and -56.34%, indicating salt crystallization alters salt solution absorption and transport.

For W/C = 0.6 and 0.8 specimens, salt crystals predominantly fill smaller pores, reducing pore volume and suppressing capillary absorption (A_{cap} and w_{cap} decline) [67, 86]. Conversely, W/C = 0.4 specimens, with larger open pores, facilitate salt solution permeation and surface migration, forming abundant external crystals but fewer internal deposits. Partial pore blockage by limited internal crystals enhances capillary action (A_{cap} increases), while hygroscopic surface crystals elevate w_{cap} [90].

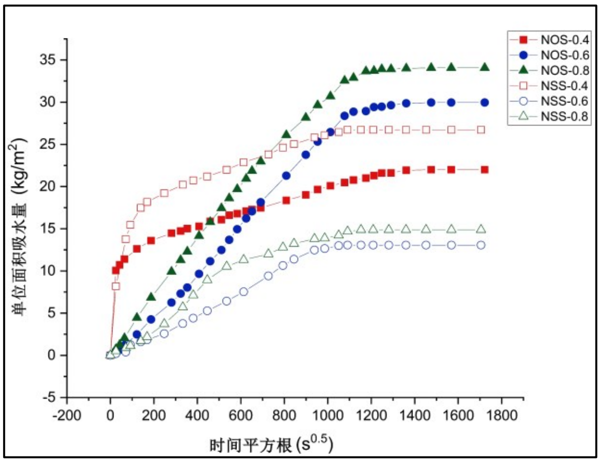

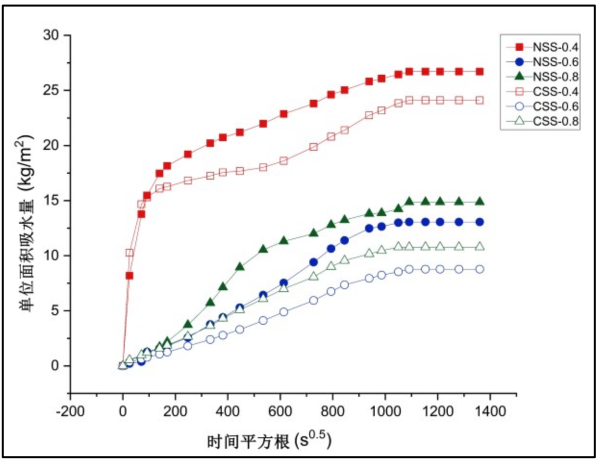

Fig. 3-13. Capillary absorption curves of NOS and NSS specimen groups (Left)

Fig. 3-14. Capillary absorption curves of NSS and CSS specimen groups (Right)

A comparison of capillary absorption curves between NSS and CSS specimen groups reveals that epoxy coating on lateral surfaces reduced both A_{cap} and w_{cap}, as shown in Fig. 3-14. Compared to the NSS group, CSS specimens with W/C = 0.4, 0.6, and 0.8 exhibited normalized $A_{cap,w}$ reductions of −22.92%, −36.13%, and −28.55%, respectively, and $w_{cap,w}$ reductions of −9.76%, −32.82%, and −27.52% (Table 3-4). These reductions primarily stem from suppressed lateral moisture evaporation, which decelerated salt solution uptake from the specimen base and diminished total absorption capacity.

Table 3-4 The values of A_{cap} and w_{cap} for target specimens（t = 20 ℃, RH = 60%）

Sample group	C/w	$A_{cap,sol}$（$kg \cdot m^{-2}s^{-0.5}$）	$A_{cap,w}$（$kg \cdot m^{-2}s^{-0.5}$）	w_{cap}（$kg \cdot m^{-3}$）	Δ $A_{cap,w}$（%）	Δ w_{cap} (%)
NOW	0.4	0.043	/	145.750	/	/
	0.6	0.022	/	136.050	/	/
	0.8	0.037	/	177.469	/	/
NOS	0.4	0.034	0.043	137.500	-21.08	-5.66
	0.6	0.020	0.022	187.188	-9.83	+37.59
	0.8	0.036	0.037	212.930	-0.96	19.98
NSS	0.4	0.069	0.087	137.500	+101.26	+21.42
	0.6	0.011	0.012	187.188	-45.72	-56.39
	0.8	0.014	0.015	212.930	-60.82	-56.34
CSS	0.4	0.053	0.067	150.664	-22.92	-9.76
	0.6	0.007	0.008	54.848	-36.13	-32.82
	0.8	0.010	0.010	67.383	-28.5 5	-27.52

3.4 Mechanism analysis and application

3.4.1Mechanisms of salt migration and distribution

1) Salt crystallization deposition

The migration mechanisms of chloride ions in cement mortar are inferred from salt crystallization patterns and Cl^- distribution. Salt crystallization reflects the outcome of salt migration, while Cl^- concentrations trace the transport pathways of salt solutions. The water-to-cement ratio (W/C) critically influences salt content in partially immersed specimens. For uncoated specimens, W/C = 0.4 exhibited the highest surface salt crystal mass (m_e), approximately double that of W/C = 0.6 and 0.8 (Fig. 3-6). Conversely, W/C = 0.8 specimens showed the highest internal salt crystal mass (m_i), nearly five times greater than W/C = 0.4 and 0.6. These distinctions arise from variations in porosity and pore size distribution.

W/C = 0.4 specimens, with a higher proportion of large pores ($\geq 10^5$ nm, Table 3-3), allowed rapid salt solution permeation. Subsequent evaporation led to progressive salt accumulation on surfaces with abundant open pores [10, 59]. In contrast, W/C = 0.6 and 0.8 specimens relied on capillary action in smaller pores. Weak surface evaporation limited salt migration to surfaces, while slow evaporation in large pores drove solution supersaturation and crystallization in smaller pores [173]. W/C = 0.8 specimens, with the smallest average pore diameter and highest microporosity (0–100 nm, Fig. 3-11), thus exhibited the largest m_i.

Epoxy-coated specimens showed reduced total (m_t) and surface (m_e) salt crystal masses compared to uncoated counterparts, with m_e decreasing by >50% while m_i remained relatively stable (Fig. 3-6). In porous materials, salt migration is water-mediated [14]. Coating suppressed lateral evaporation, hindering both salt solution uptake and transport. For W/C = 0.4, epoxy clogged surface open pores, trapping more salt crystals internally ($m_e\downarrow$, $m_i\uparrow$). Additionally, salt crystal morphology—thin layers on dense matrices versus thick clusters on porous, moist surfaces—is governed by material properties, solution chemistry, evaporation rates, and moisture content [165, 174].

2）Chloride ion distribution

Cl^- concentration profiles across heights and depths of cement mortar specimens reveal key patterns in salt migration. For uncoated specimens (Fig. 3-7a), edge regions consistently exhibited higher Cl^- concentrations than cores at all heights, indicating evaporation-driven salt transport toward surfaces. Notably, W/C = 0.4 specimens showed elevated Cl^- concentrations in the top segment (S1), driven by combined permeation through large pores and intense evaporation at the upper surface. In contrast, coated specimens (Fig. 3-7b) displayed smaller vertical Cl^- gradients (except in S1), as epoxy coating suppressed lateral evaporation and redirected salt migration vertically via capillary action.

Vertical Cl^- distributions differed significantly between coated and uncoated specimens, except in the immersed S5 segment and upper S1. This highlights the interplay between vertical and horizontal salt transport. However, inhomogeneous pore distribution and localized epoxy cracking (caused by salt crystallization stresses) may introduce measurement uncertainties. For W/C = 0.6 coated specimens, Cl^- concentrations decreased with height (Fig. 3-7b), attributed to low porosity, poor pore connectivity, and weak capillary action, which hindered upward salt migration from the base.

All specimens, regardless of W/C or coating, exhibited similar Cl^- concentrations in the fully immersed S5 segment. Here, Cl^- levels depended solely on permeation and diffusion within internal pores, as surface evaporation was absent.

3.4.2 Mechanisms of capillary absorption behavior

1) NOW vs. NOS Comparison

The trend of the capillary absorption curves was determined both by the pore characteristics of the material and the properties of the absorbed solution. For the pore characteristics, the capillary absorption was affected by the porosity and pore size distribution of the materials. Intense evaporation of the specimen with the W/C of 0.4 occurred on its rough surfaces with multiple open pores. Its large internal pores also further promoted infiltration, resulting in the rapid initial stage of capillary absorption. Conversely, for the specimens with ratios of 0.6 and 0.8, moisture was absorbed relatively slowly through capillary action, given their smooth surfaces and small internal pores. Since the specimen with the W/C of 0.8 demonstrated a higher water content than that with a ratio of 0.6 during preparation, its higher porosity correspondingly led to a higher rate of capillary absorption ($A_{\mathrm{cap},0.8} > A_{\mathrm{cap},0.6}$). Based on the results of the NOW and NOS test (Fig. 3-12), the $A_{\mathrm{cap,\ sol}}$ of the three specimens in the saturated NaCl solution decreased compared to $A_{\mathrm{cap,w}}$ in the pure water, because of that the density and surface tension of the saturated NaCl solution were slightly higher than that of pure water at 21°C and its viscosity coefficient was twice that of pure water. Meanwhile, given the higher density of the saturated NaCl solution, the specimen could demonstrate a large increase in weight by drawing in the same volume of the salt solution. Thus, the $w_{\mathrm{cap,\,sol}}$ was higher than the $w_{\mathrm{cap,w}}$ [80, 98, 170].

2) NOS vs. NSS Comparison

Through the capillary absorption test in the saturated NaCl solution, the effects of salt crystallization on the hygric property of the cement-mortar specimens were analyzed. For the NSS specimens with W/Cs of 0.6 and 0.8, both the A_{cap} and w_{cap} were found to decrease, based on the capillary absorption curves of the NOS and NSS groups (Fig. 3-13). This finding was attributed to not only the dense surfaces of the two specimens, but also their small average size of the pores (Table 3-3), which could be completely occluded by the salt crystals [67, 175]. This finding further corroborated with the effect of $NaNO_3$ crystals on the hygric properties of natural stone and ceramic tiles, but differed from that of NaCl crystals [30]. This might be due to the different material types and solution properties. Conversely, for the NSS specimen with the ratio of 0.4, both the A_{cap} and w_{cap} increased (Fig. 3-14 and Table 3-4). This finding was attributed to its internal and external salt contents (Fig. 3-6) and its pore characteristics (Fig. 3-11, Table 3-3). Firstly, given the relatively large average internal pore diameter of the specimen (161.3 nm), the salt crystals formed on the pore wall could not easily occlude the internal pores. Secondly, the reduced pore size enhanced the capillary force, thus elevating $A_{\mathrm{cap},0.4}$. Lastly, the salt crystals deposited in large amounts on the sides of the specimen were strongly hygroscopic [90, 176]; water in the specimen was absorbed by them through open pores, thus increasing both $A_{\mathrm{cap},0.4}$ and $w_{\mathrm{cap}.0.4}$ [86, 101].

3) NSS vs. CSS Comparison

Comparison between the NSS and CSS groups (Fig. 3-14, Table 3-4) showed that their A_{cap} and w_{cap} of the side-coated specimens decreased to different extents, highlighting the effects of surface evaporation on capillary absorption. The salt crystals deposited in porous materials could reduce the hygroscopicity through their occlusion of the internal pores of the specimens [45, 67, 176]. However, the m_{e} on the coated specimens was significantly lower than that of the uncoated ones, whereas the m_{i} remained almost unchanged (Fig. 3-6). This observation indicated that salt crystallization in the specimens did not contribute to the difference. Moreover, w_{cap} varied with the W/C of the specimens. The w_{cap} of the specimens with the ratios of 0.6 and 0.8 were respectively reduced by 32.82% and 27.52%, which represented a threefold difference compared to the specimen with the ratio of 0.4 (9.76%). This could be attributed to the difference in their porosity and pore size distribution (Fig. 3-14, Table 3-3). By contrast, the specimen with the ratio of 0.4 was associated with a larger average pore size and more connected macrospores. These features enabled the relatively rapid migration of water to reach the top of the specimen by the infiltration and capillary absorption, followed by intense evaporation. This explained the minimal effect of coating on its moisture content. To sum up, the side-coated specimens were associated with not only diminished areas for evaporation, but also a lowered rate of evaporation, both of which were the main factors underlying the decrease of their A_{cap} and w_{cap}.

3.4.3Engineering application recommendations

To enhance the salt corrosion resistance of cement-based materials in coastal environments, optimizing the water-to-cement ratio (W/C) and incorporating supplementary additives (e.g., slag, silica fume, fly ash, limestone powder) are recommended. These additives reduce porosity and pore size through filler effects, yielding denser matrices with lower capillary absorption coefficients (A_{cap}) and chloride diffusion coefficients [170, 180-182]. Such modifications minimize internal salt crystallization and chloride ingress, mitigating expansion-induced damage from pore-deposited salts.

Applying waterproof coatings (e.g., acrylic, epoxy, polyurethane, polyurea, styrene-butadiene rubber) on cement mortar surfaces further improves durability. These organic polymer coatings form impermeable barriers that inhibit both external saltwater intrusion and internal moisture evaporation, effectively reducing chloride migration and salt deposition [177-182]. This dual mechanism supports their use in enhancing hygrothermal performance and salt resistance of building envelopes in coastal and island regions.

3.5 Chapter summary

This chapter investigated epoxy-coated and uncoated cement mortar specimens with water-to-cement ratios (W/C) of 0.4, 0.6, and 0.8 under partial immersion in 5 wt% NaCl solution for 120 days. Salt crystal deposition, chloride ion (Cl^-) distribution, and capillary absorption characteristics were systematically analyzed. Key conclusions are as follows:

Crystallization Dynamics: The specimens with larger pores (e.g., W/C = 0.4) exhibited thick, clustered external salt layers on upper surfaces due to enhanced permeation and evaporation. Conversely, the specimens with smaller pores (e.g., W/C = 0.6/0.8) formed thin, uniform external layers but accumulated more internal crystals, driven by capillary confinement and slow evaporation.

Salt migration Mechanisms: Uncoated specimens showed higher Cl^- concentrations in edge regions at all heights, reflecting evaporation-driven horizontal salt migration. While coated specimens displayed reduced lateral Cl^- gradients, as epoxy suppressed evaporation and redirected transport vertically.

Capillary absorption Behavior: Replacing pure water with saturated NaCl solution reduced capillary absorption coefficients (A_{cap}) due to higher fluid density, viscosity, and pore-clogging by salt crystals. Side-coating further decreased A_{cap} and moisture content (w_{cap}) by limiting evaporation-driven capillary action.

Anti-Salt Corrosion Strategies: Crystallization-induced expansive stresses from NaCl deposition are a primary degradation driver. Mitigation requires: (1) Enhanced matrix density: Achieved by optimizing W/C and incorporating mineral additives (e.g., slag, silica fume). (2) Surface impermeability: Waterproof coatings (e.g., epoxy, polyurethane) reduce salt ingress and evaporation, improving durability of coastal building envelopes.

Chapter 4 Liquid water transport properties of cement mortar with salt deposition

4.1 Introduction

Investigating moisture transport properties of porous building materials is critical for hygrothermal analysis of building envelopes, energy consumption prediction, and indoor environmental regulation [74, 158-161]. Moisture transport in porous materials primarily involves liquid water and vapor phases. In China's humid coastal and island regions, liquid water transport dominates due to persistent high humidity and salt-laden air. Under long-term coastal saline environments, salt crystallization forms on building envelope surfaces. These crystals cannot migrate independently but are transported and redistributed with liquid water into material interiors [13, 19, 36, 59]. Salt deposition alters porosity and pore size distribution, thereby modifying liquid moisture transport behavior. Consequently, salt crystallization and liquid water transport in porous materials constitute a complex, interdependent process [36, 59, 92]. However, the mechanisms governing liquid moisture transport dynamics in coastal salt spray climates remain poorly understood.

This chapter employs the accelerated salt spray testing methodology established in Chapter 2 to replicate coastal salt spray climatic conditions. Focusing on cement mortar—a widely used porous building material—we investigate: (1) Physicochemical evolution: Changes in open porosity, apparent density, and salt content under varying salt spray cycles. (2) Liquid moisture behavior: Impacts of salt deposition on saturated moisture content (w_{cap}), capillary absorption coefficient (A_{cap}), capillary moisture storage, and water retention curves. (3) Model refinement: Modified equations for capillary absorption parameters based on salt-induced pore structure alterations. (4) Microstructural insights: SEM and MIP analyses to link macroscopic transport phenomena to pore-scale salt-matrix interactions. The experimental workflow is illustrated in Fig. 4-1.

4.2 Sample and salt spray test methods

4.2.1 Material and specimens

Cement mortar specimens were prepared using CEM II/B-LL 32.5R cement, CEN-standard sand (BS EN 196-1:2016), and deionized water with a water-to-cement ratio (W/C) of 0.5 and sand-to-cement ratio (S/C) of 3. The homogenized mixture was cast into 40 mm × 40 mm × 160 mm steel molds, vibrated for compaction, and cured for 24 hours in a controlled chamber (23°C, 95% relative humidity). After demolding, specimens were water-cured at 23°C for 28 days. Subsequently, they were cut into two sizes using a CNC cutting machine: (1) 40 mm × 40 mm × 10 mm: For vacuum saturation and water retention curve tests. (2) 40 mm × 40 mm × 20 mm: For capillary absorption tests. All specimens were rinsed with deionized water, oven-dried to constant mass, labeled, and grouped for subsequent experiments.

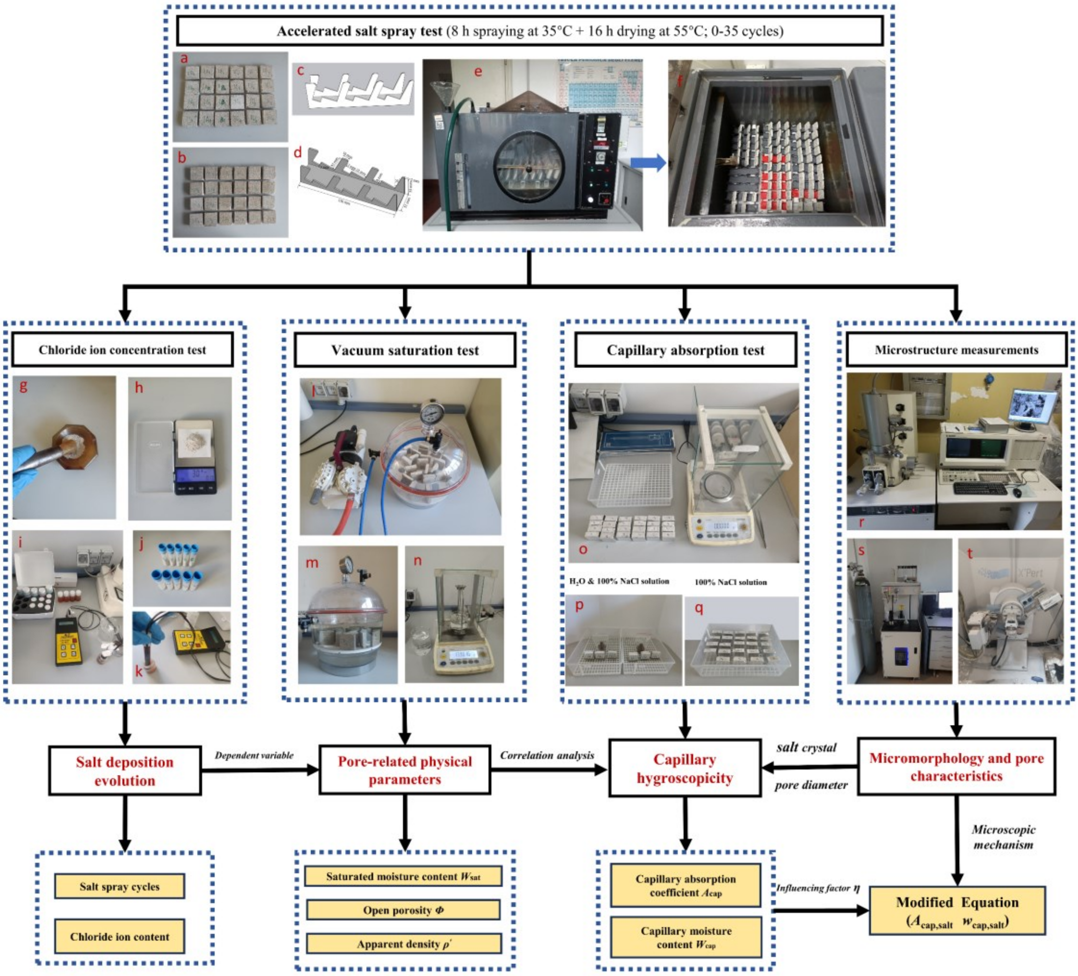

Fig. 4-1. Experimental workflow for hygric properties of cement mortar under salt spray environments

4.2.2 Accelerated salt spray test

To replicate coastal salt spray climates and observe liquid moisture transport evolution in cement mortar under varying salt exposure durations, accelerated salt spray tests were conducted using a CEAST 5050 salt spray chamber (Italy). A 5 wt.% NaCl solution was atomized with a deposition rate of 2 mL/(80 cm²·h). Specimens were positioned at a 20° tilt from the vertical axis, spaced 47 mm apart (Fig. 4-2). Each 24-hour cycle comprised 8 hours of continuous spraying at 35°C and 16 hours of drying at 55°C.

The chamber configuration and parameter settings align with Chapter 2.3. For each hygric property test (capillary absorption, vacuum saturation, water retention), six specimen groups were prepared: Control group (0 cycles) and test groups (7, 14, 21, 28, and 35 salt spray cycles). Each group included four replicates to calculate mean values and standard deviations (Table 4-1).

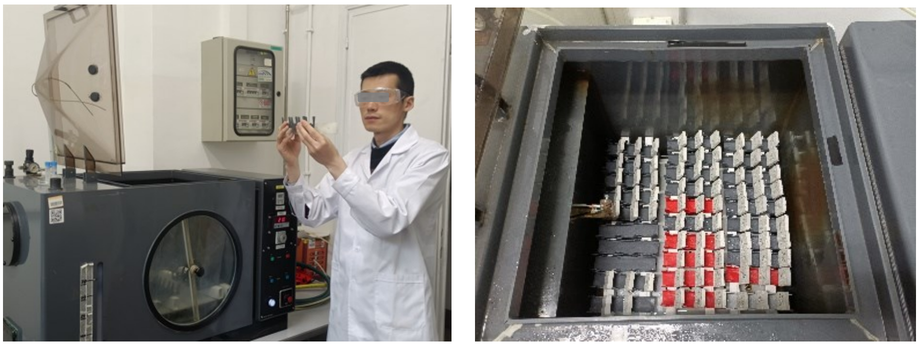

Fig. 4-2. Accelerated salt spray chamber and interior specimen arrangement

Table 4-1. Group numbering of specimens subjected to different salt spray cycles

Control group	**Vacuum saturation Tests**	**Capillary absorption tests**	**Water retention curve tests**
7 cycles	1O1, 1O2, 1O3, 1O4	2O1, 2O2, 2O3, 2O4	4O1, 4O2, 4O3, 4O4
14 cycles	1A1,1A2, 1A3, 1A4	2A1,2A2, 2A3, 2A4	4A1,4A2, 4A3, 4A4
21 cycles	1B1, 1B2, 1B3, 1B4	2B1, 2B2, 2B3, 2B4	4B1, 4B2, 4B3, 4B4
28 cycles	1C1, 1C2, 1C3, 1C4	2C1, 2C2,2C3, 2C4	4C1, 4C2, 4C3, 4C4
35 cycles	1D1, 1D2,1D3, 1D4	2D1, 2D2, 2D3, 2D4	4D1, 4D2,4D3, 4D4
Control group	1E1, 1E2, 1E3, 1E4	2E1, 2E2, 2E3, 2E4	4E1, 4E2, 4E3, 4E4

4.2.3 Chloride ion concentration test

To quantify salt ingress and analyze its impact on the hygric properties of cement mortar, chloride ion (Cl^{-}) concentrations in specimens subjected to varying salt spray cycles were measured using a Chlorimeter C-Cl 3000 system (Fig. 4-3a). This system employs electrochemical principles: Cl^{-} ions dissolved in an acidic solution generate voltage changes detected by a probe equipped with electrodes and a temperature sensor. The voltage, adjusted for temperature effects, is converted to Cl^{-} concentration and displayed on the instrument screen (Fig. 4-3b). The Chlorimeter C-Cl 3000 is specifically calibrated for Cl^{-} detection in concrete and cement-based materials.

Prior to testing, the instrument was calibrated using five solutions with Cl⁻ concentrations of 0.005%, 0.01%, 0.05%, 0.1%, and 0.3%. Electrodes were rinsed with deionized water and dried with lint-free cloth between each solution. Calibration was confirmed when the screen displayed a stabilized voltage and "OK" prompt. Post-calibration measurements were completed within 2 hours to ensure accuracy.

a) Sampling, calibration, and measurement components b) Chlorimeter C-Cl 3000 device

Fig. 4-3. Chloride ion (Cl⁻) concentration measurement system

To comprehensively assess chloride ion (Cl⁻) concentrations across specimen depths, full-thickness samples were extracted from dried 40 mm × 40 mm × 10 mm cement mortar specimens and ground into fine powder using an agate mortar (Fig. 4-4a). A 3 g powder sample was weighed using an electronic balance (0.001 g precision) and immediately transferred to a bottle containing 20 mL of acidic solution (Fig. 4-4b). The bottle was capped and vigorously shaken for 1 minute, followed by a 2-minute settling period to stabilize the solution. The cap was then loosened slowly to release internal pressure (Fig. 4-4c). After 2–4 minutes, the probe was inserted into the solution, and the Cl⁻ mass percentage (relative to the 3 g sample) was displayed on the instrument's LCD screen.

All measurements were conducted at 23°C. Key precautions included: (1)Electrode maintenance: Electrodes were kept clean, dry, and free of scratches or liquid residues prior to immersion. (2)Probe positioning: The sensor probe was slightly angled within the bottle to avoid contact with settled residues at the bottom, preventing electrode abrasion (Fig. 4-4d).

a) Grinding **b) Weighing** **c) Dissolving** **d) Detection**

Fig. 4-4. Measurement procedure for chloride ion (Cl$^-$) concentration in cement mortar specimens

4.3 Experimental methods for liquid water transport characterization

4.3.1 Vacuum saturation test

The vacuum saturation apparatus (Fig. 4-5) measures key hygric properties of porous building materials, including apparent density, open porosity, and saturated moisture content. While this method, originally developed for natural stone and aligned with the European standard BS EN 1936:2006 [183], has been widely applied to characterize hygric parameters in various porous materials [65, 67, 184, 185], its use in salt-contaminated cement mortar is limited. When salt-laden specimens are exposed to distilled water, pore-deposited salt crystals dissolve and migrate, altering the original porosity and pore size distribution under salt-crystallized conditions.

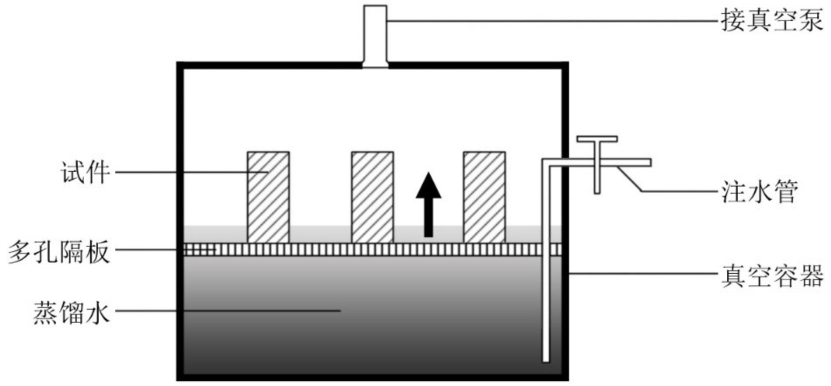

Fig. 4-5 Schematic diagram of the vacuum saturation experimental setup

To address this limitation, saturated NaCl solution (density: 1199 kg/m^3 at 23°C) replaced deionized water as the absorption medium in vacuum saturation tests. Cement mortar specimens (Fig. 4-6a) were first oven-dried at 55°C to constant mass, cooled in a desiccator (Fig. 4-6b), and weighed（m_{dry}）using an analytical balance. Specimens were then placed on a porous rack within a vacuum chamber (Fig. 4-6c). Pressure was gradually reduced to 2.0 ± 0.7 kPa and maintained for 2 ± 0.2 hours to evacuate air from open pores (Fig. 4-6d). Saturated NaCl solution was slowly injected into the chamber under continued vacuum, ensuring full immersion over ≥15 minutes. After immersion (liquid level ≥20 mm above specimens), atmospheric pressure was restored, and specimens remained submerged for 24 ± 2 hours (Fig. 4-6e).

Following Archimedes' principle, the submerged weight (m_{under}, kg) was measured using a hydrostatic balance in saturated NaCl solution (Fig. 4-6f). Specimens were then removed, surface-blotted with damp cloths, and weighed for saturated mass (m_{sat}, kg) in air.

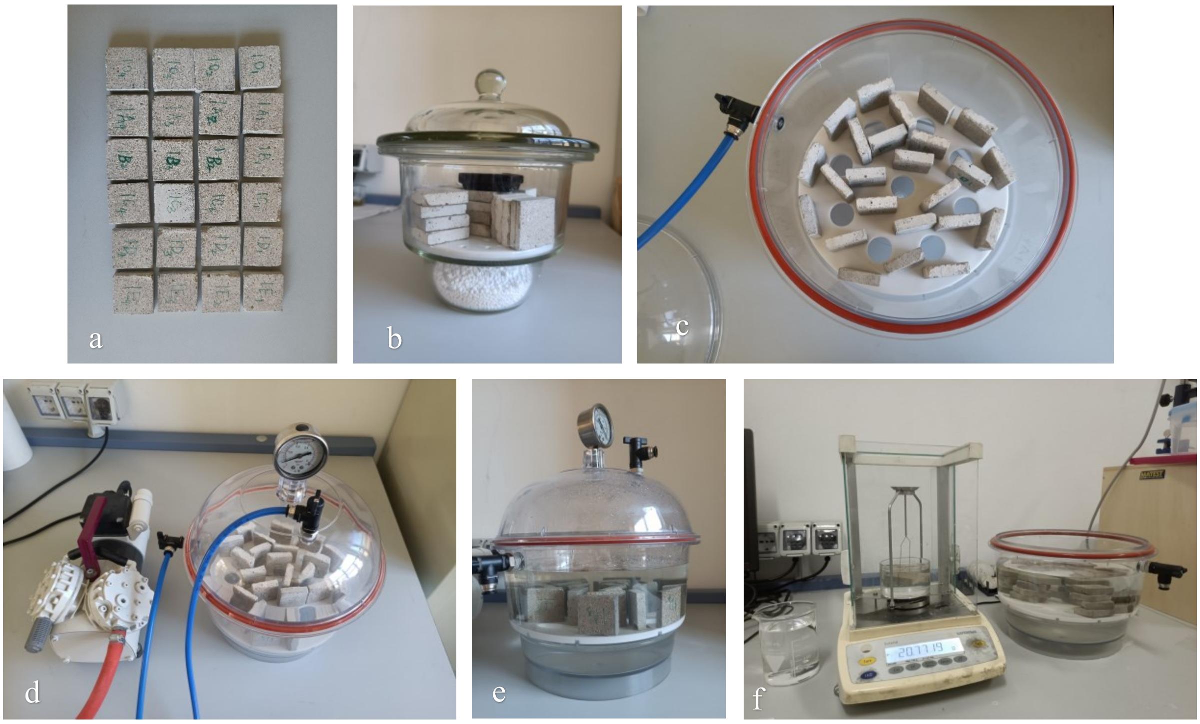

Fig. 4-6 Vacuum saturation experimental setup and procedure

Based on the measurement results from the above vacuum saturation test, the apparent density ρ_{b}(kg/m^3), open porosity P_{o} (%), saturation moisture content w_{sat} (kg/m^3), and skeletal density ρ_{ske}(kg/m^3) of each group of cement mortar specimens subjected to different salt spray cycles were calculated using the following formulas (4-1) to (4-6).

$$\boldsymbol{m_{sol} = m_{sat} - m_{\text{dry}}} \tag{4-1}$$

$$V_b = \frac{m_{sat} - m_{under}}{\rho_{sol}} \tag{4-2}$$

$$\rho_b = \frac{m_{dry}}{V_b} = \frac{m_{dry} \cdot \rho_{sol}}{m_{sat} - m_{under}} \tag{4-3}$$

$$P_o = \frac{m_{sol}}{\rho_{sol} \cdot V_b} = \frac{m_{sat} - m_{dry}}{m_{sat} - m_{under}} \times 100\% \tag{4-4}$$

$$w_{sat} = \frac{m_{sol}}{V_b} = \frac{(m_{sat} - m_{dry}) \cdot \rho_{sol}}{m_{sat} - m_{under}} \tag{4-5}$$

$$\rho_{ske} = \frac{m_{dry}}{V_{ske}} = \frac{m_{dry}}{V_b \cdot (1 - P_0)} = \frac{\rho_b}{1 - P_0} = \frac{m_{dry} \cdot \rho_{sol}}{m_{sat} - m_{under}} \cdot \frac{m_{dry} - m_{under}}{m_{sat} - m_{under}} \tag{4-6}$$

In the above equations, m_{sat} is the weight of the specimen in the water-saturated state (kg); m_{under} is the submerged weight of the specimen under the liquid surface (kg); m_{sol} is the weight of the NaCl solution in the water-saturated specimen (kg); m_{dry} is the dry weight of the specimen (kg); ρ_{sol} is the density of the saturated NaCl solution, taken as 1199 kg/m³; V_{b} is the apparent volume of the specimen (m³).

4.3.2 Capillary absorption test

To determine the capillary absorption coefficient A_{cap} (kg/m^3) and capillary moisture content w_{cap} (kg/m^{2}s$^{0.5}$) of cement mortar specimens, capillary absorption tests were performed in compliance with EN ISO 15148 and ASTM C1585 standards [161, 186]. ASTM C1585 permits the use of resin coatings, non-adhesive plastic films, or self-adhesive aluminum tapes as sealing materials. However, for small specimens, resin coatings were found to penetrate 1–1.5 mm into the substrate, thereby reducing the effective cross-sectional area for capillary absorption and resulting in systematic underestimation of A_{cap} and w_{cap} [163]. Preliminary trials with non-adhesive plastic films revealed two critical issues: (1) interfacial gaps between the film and specimen surface triggered anomalous capillary absorption, and (2) a 10 mm unsealed zone at the lower sidewall absorbed solution during bottom-up imbibition, both introducing significant measurement errors. To address these limitations, the final experimental protocol employed self-adhesive aluminum tape to fully encapsulate the specimen sidewalls, while a centrally positioned vent hole on the top surface facilitated air release during water uptake (see Fig. 4-7).

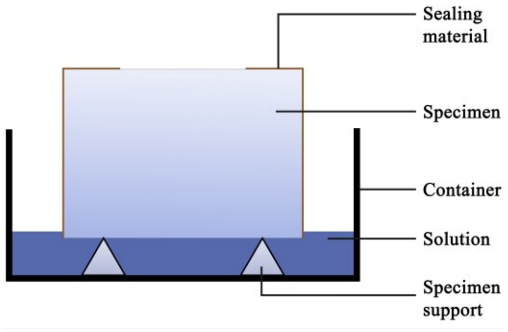

Fig. 4-7 Capillary absorption setup schematic [187]

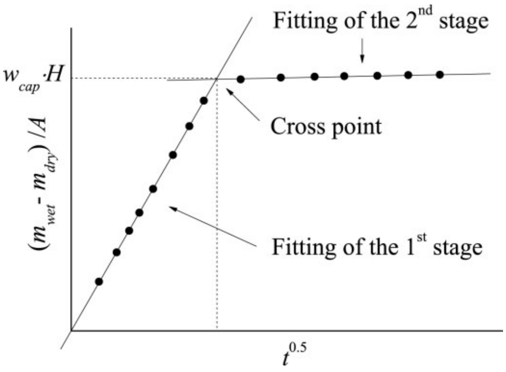

Fig. 4-8 Capillary moisture content w_{cap} determination [163]

To prevent the dissolution of salt crystals within the specimens during capillary absorption, saturated NaCl solution was employed as the absorption medium instead of deionized water. However, the density, viscosity, and surface tension of saturated NaCl solution are higher than those of water [67, 80], which may influence the measured values of A_{cap} and w_{cap} [98]. To evaluate and quantify this effect, two reference specimen groups were tested in parallel using deionized water and saturated NaCl solution for capillary absorption experiments (Fig. 4-9a).

Fig. 4-9 Capillary absorption experimental setup and procedure

Based on the measurement results, the ratio of capillary absorption coefficients under two conditions ($A_{\mathrm{cap,sol}}/A_{\mathrm{cap,w}}$) was calculated. Salt-containing specimens subjected to salt spray cycles were then tested in saturated NaCl solution (Fig. 4-9 b,c), and the measured capillary absorption coefficient was corrected. The cumulative moisture flow (m_{wet}-m_{dry}/A, kg/m^2) was determined by subtracting the dry weight (m_{dry}, kg) from the wet weight (m_{wet}, kg) at different time points and dividing by the specimen's cross-sectional area A. The capillary absorption curve [161, 186] was plotted by correlating the cumulative moisture flow with the square root of time ($t^{0.5}$, s$^{0.5}$), which exhibited two distinct phases: a rapid initial phase followed by a gradual second phase (as shown in Fig. 4-8). The A_{cap} was determined using the single-tangent (linear regression) method, widely adopted in studies [163, 188, 189] and recommended by international standards ISO 15148 [161], ASTM C1585 [186], and BS EN 1925 [162]. By fitting the first-phase data points to Equation (4-7), A_{cap} was obtained. Although standards do not explicitly define the calculation method for w_{cap}, this parameter is frequently referenced in research as a critical moisture characteristic of porous materials. It is typically defined as the moisture content corresponding to the transition point between the first and second phases of the capillary absorption curve [189, 190]. Following ASTM C1585, the second phase of the curve was linearly fitted, and its intersection with the first-phase fitting curve was calculated. Finally, w_{cap} was derived by dividing the cumulative moisture flow at the intersection point by the specimen height H (Eq. 4-8).

$$\frac{m_{sat}-m_{dry}}{A} = A_{cap} \cdot t^{0.5} + k_1 \qquad (4\text{-}7)$$

$$w_{cap} = \frac{m_{wet}-m_{dry}}{A}\Big|_{cross} \cdot \frac{1}{H} \qquad (4\text{-}8)$$

In the equation, k_1 is the fitting parameter.

During the testing process, the ambient temperature was controlled at 18–28°C with a relative humidity of 40%–60%. The liquid level in the tank was maintained constant and positioned (5 ± 2) mm above the specimen's bottom surface. Timing commenced immediately upon immersion of the specimen into the solution. After 5 minutes, the specimen was removed, surface moisture was absorbed using a wrung-out damp cloth, and the specimen was weighed on an analytical balance. This procedure was repeated at intervals of 10 minutes, 20 minutes, 30 minutes, 1 hour, 2 hours, 4 hours, 6 hours, 9 hours, 12 hours, 18 hours, 24 hours, 36 hours, and 48 hours. Additional weightings were performed as needed based on curve trend observations to obtain a series of wet mass values (m_{wet}) at different time points. The entire operation cycle (removal → drying → weighing → reimmersion) for each specimen was completed within 20 seconds. The weighing accuracy was maintained at ±0.1% of the specimen mass. The edge length of cubic specimens was measured using a vernier caliper, with cross-sectional area errors controlled within 1%. Typical random operational errors in m_{wet} measurements were ±5%, and the standard deviation of the capillary absorption curve slope was approximately ±4%.

4.3.3 Water retention curve test

The water retention curve, a key moisture characteristic of porous building materials, defines the upper limit of water storage capacity via the moisture content–capillary pressure relationship [191, 192]. Standard measurement methods include pressure plate [65, 193], pressure membrane [192, 194], hanging water column [194, 195], and mercury intrusion porosimetry (MIP) [150, 196]. These methods, however, lack full coverage of the supersorption range. Feng Chi (2019) introduced two alternatives: the semi-permeable membrane and chilled-mirror dew-point methods, validated up to -1×10^5 Pa for sorption/desorption in materials like calcium silicate boards and aerated concrete [197]. Given the dew-point instrument's cost and unavailability, this study employs the semi-permeable membrane method for its cost efficiency and simplicity.

This method isolates specimens from solution via a semi-permeable membrane while maintaining hydraulic contact. Specimens equilibrate under osmotic pressure (equal to capillary pressure in magnitude but opposite in sign [198]), allowing contamination-free moisture exchange. Post-equilibrium, moisture content is measured (Fig. 4-10). Experiments used a Dow Filmtec BW30XFRLE membrane (305 × 305 mm^2).

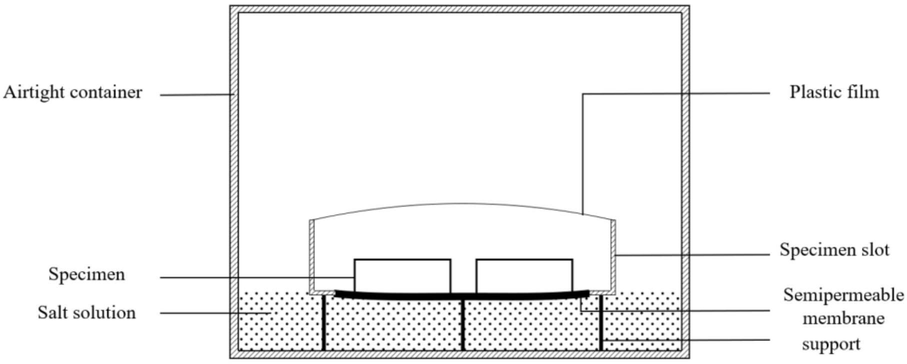

Fig. 4-10 Schematic diagram of the semi-permeable membrane experimental setup [198]

A 27 × 18 cm² opening was cut at the base of a small plastic container (37.9 × 26.5 × 13 cm³) and sealed with Bostik black liquid rubber along the edges, adhering the semi-permeable membrane with its smooth side facing inward and rough side outward. After preliminary curing of the rubber (48 hours), the container was floated in deionized water for 30 minutes to verify membrane sealing integrity. A white plastic mesh frame (10 mm height) was placed inside a larger container (52.5 × 37 × 30.5 cm³), and the small sealed container was positioned atop this mesh. The larger container was filled with K_2SO_4 solution (capillary pressure: -5×10^6 Pa), ensuring the solution level exceeded the mesh top by 3–5 mm to fully contact the membrane.

Following ISO 12570:2000(E) [158], six cement mortar specimens were oven-dried to constant mass (m_{dry}) in a forced convection oven. Specimens were then placed on the membrane (Fig. 4-11a), and both containers were sealed (Fig. 4-11b) and stored in a 23°C constant-temperature chamber (Fig. 4-11c). After one week, specimens were individually weighed. Moisture equilibrium was assumed when three consecutive weighings (≥24-hour intervals) showed ≤0.1% relative variation, with the mean value recorded as m_{wet}. The procedure was repeated at capillary pressures of -2.66×10^6 Pa, -1.5×10^6 Pa, -8×10^5 Pa, and -5×10^5 Pa by adjusting K_2SO_4 solution concentration.

Fig.4-11 Experimental setup and procedure for water retention curve measurement via the semi-permeable membrane method

According to the standard T/CECS 10292-2023 [198], the relationship between capillary pressure p_c(Pa) and K_2SO_4 solution concentration C (kg/kg) within the range of 0.01–0.1 kg/kg can be approximated by Equation 4-9. The equilibrium moisture content $u(p_c)$ of specimens is calculated using Equation 4-10, and the water retention curve is fitted to experimental data across capillary pressures via Equation 4-11.

$$p_c = -2.88 \times 10^7 \cdot C - 3.43 \times 10^5 \qquad (4\text{-}9)$$

$$u(p_c) = \frac{m_{wet}(p_c) - m_{dry}}{m_{dry}} \qquad (4\text{-}10)$$

$$u(p_c) = u_0 \cdot \sum_{i=1}^{n} k_1^i \left[1 + (k_2^i \cdot p_c)^{k_3^i}\right]^{(1-k_3^i)/k_3^i} \qquad (4\text{-}11)$$

Nomenclature: u（p_c）is equilibrium moisture content at capillary pressure p_c (mass fraction, %); p_c is capillary pressure (Pa); C is K_2SO_4 solution concentration (kg/kg); m_{dry} is dry mass of specimen (kg); m_{wet} (p_c) is equilibrium mass of specimen at capillary pressure p_c (kg); k_1^i、k_2^i、k_3^i are fitting parameters, constrained by $0 \le k_1^i \le 1 \le 1$ and $\sum_{i=1}^{n} k_1^i = 1$; u_0 is saturated moisture content of the specimen (kg/kg).

4.3.4 Techniques of observation and measurement

To analyze the moisture evolution mechanisms in cement mortar specimens under salt deposition from a microscopic perspective, mercury intrusion porosimetry (MIP) and scanning electron microscopy (SEM) were conducted. Given the heterogeneous salt distribution caused by inward migration during salt spray-drying cycles, prismatic subsamples containing cross-sections from the surface to the core were extracted to comprehensively evaluate pore structure and microscopic morphology at varying depths under different cycle durations.

First, samples were dried to constant mass in a 50°C oven. For MIP analysis, 3–4 g subsamples were tested using an Autopore IV instrument (USA) with a maximum pressure of 2000 bar, resolving pores down to 6 nm via the Washburn equation. Duplicate MIP tests per specimen ensured data reliability. For SEM, dried samples were sputter-coated with gold (SPI sputter coater, USA) and imaged using a Hitachi S4000 SEM (Japan). Detailed procedures followed ISO 15901:2005 [150] (MIP) and ISO 21466:2019 [149] (SEM).

a) MIP (Autopore V) mercury intrusion porosimeter b) SEM (Hitachi S4000) scanning electron microscope

Fig. 4-12 Analytical instruments (Lince Laboratory)

4.4 Effect of salt spray deposition on material porosity

4.4.1 Salt spray deposition and saturated moisture content

Based on chloride ion concentration measurements across the full thickness of cement mortar specimens, the salt deposition (characterized by chloride content) under varying salt spray cycles is shown in Fig. 4-13. The salt content in specimens increased progressively with the number of cycles, rising from 0.9% after 7 cycles to 2% after 35 cycles. Notably, chloride concentration grew rapidly between 7–21 cycles but slowed thereafter, indicating NaCl deposition and gradual salt crystal accumulation within the specimens during salt spray-drying cycles. The deceleration in later stages likely stems from salt crystals partially clogging surface and subsurface open pores, hindering further salt migration.

Conversely, the saturated moisture content (w_{sat}) decreased with increasing cycles (Fig. 4-13). Control specimens (no salt) exhibited w_{sat} =202 kg/m^3. After 21 cycles, w_{sat} dropped to 187 kg/m^3 (7.56% reduction), further declining to 164 kg/m^3 (18.7% reduction) after 35 cycles (Table 4-2). The reduction rate accelerated in later stages, correlating with chloride trends. This suggests that salt crystals progressively fill open pores, reducing pore volume and porosity. Despite undissolved salt crystals during vacuum saturation with NaCl solution (Section 4.3.1, Fig. 4-6), NaCl's inherent hygroscopicity likely mitigated early-stage w_{sat} reductions [81, 101].

For all tested groups, chloride content standard deviations ranged from 1.02% to 3.57%, while w_{sat} deviations spanned 0.84%–4.37%. These variations primarily arose from heterogeneous pore volume distributions and salt deposition patterns. However, deviations remained orders of magnitude smaller than measured values, rendering specimen heterogeneity negligible in this study.

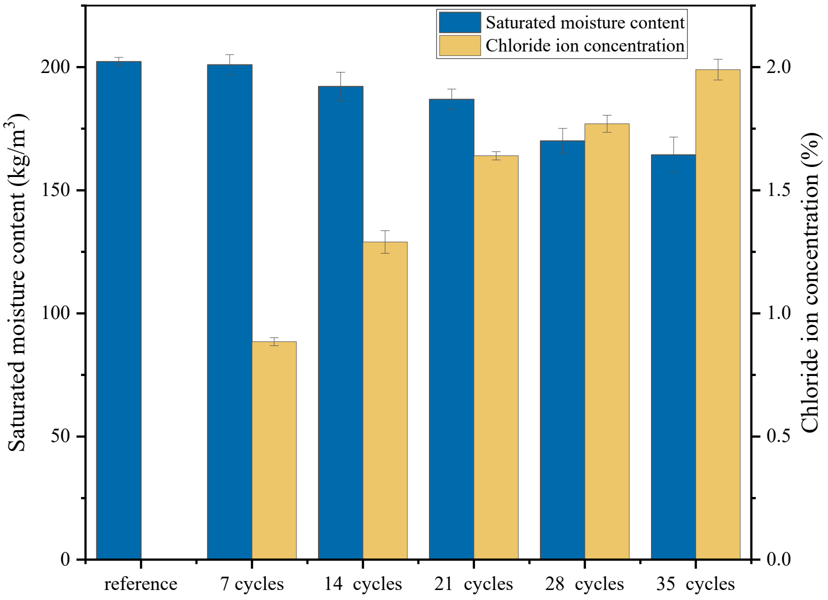

Fig. 4-13 Chloride ion concentration and saturated moisture content of cement mortar under varying salt spray cycles

4.4.2 Open porosity and apparent density

As shown in Fig. 4-14, the open porosity and apparent density of cement mortar exhibited opposing trends during salt spray cycles. With increasing cycles, the open porosity gradually decreased, while the apparent density increased nearly linearly. Combined with the observed reduction in saturated moisture content (w_{sat}), this suggests that salt crystals formed during the cycles partially occluded open pores, thereby reducing the vacuum-saturable pore volume. The control group (no salt) had an apparent density (ρ_b) of 2136 kg/m³. After 7 cycles, ρ_b increased to 2151 kg/m³, rising further to 2173 kg/m³ at 21 cycles and 2219 kg/m³ at 35 cycles. This increase aligns with the density of dry NaCl crystals (2163 kg/m³ [199]), which is slightly higher than the initial mortar density (2133 kg/m³) and significantly exceeds the density of air (1.168 kg/m³) under standard conditions (p_0 =10^5 Pa, T=25 °C) [200]. Thus, salt crystal deposition within pores directly contributes to the elevated ρ_b.

For all tested groups, the standard deviation of open porosity ranged from 0.84% to 2.62%, while that of apparent density varied between 0.19% and 0.42%. These deviations, attributed to material heterogeneity, were orders of magnitude smaller than the measured values and thus deemed negligible.

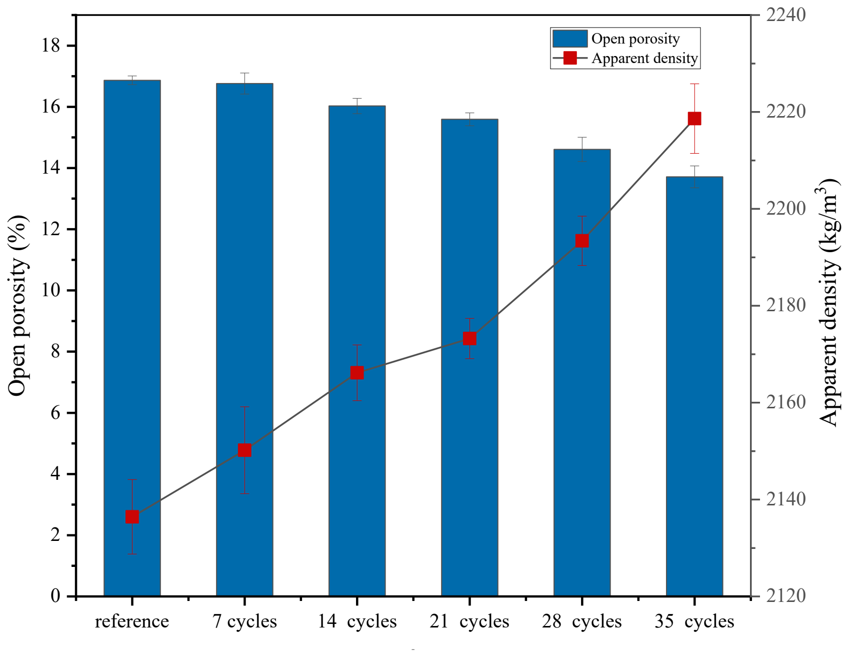

Fig. 4-14 Open porosity and apparent density of cement mortar under varying salt spray cycles

4.5 Effect of salt spray deposition on the transport properties of liquid water

4.5.1 Capillary absorption coefficient and capillary moisture content

As shown in Fig. 4-15, the relationship between cumulative moisture flow ($(m_{\mathrm{wet}} - m_{\mathrm{dry}})/A$) and $t^{0.5}$ illustrates the capillary absorption processes of one reference specimen and five experimental groups. These six curves align with the hypothesized trajectory in Fig. 4-8, exhibiting a steep initial linear phase followed by a gradual secondary linear phase. However, the slopes determined from the first phase and the cumulative moisture flow values in the second phase differ across groups. During the initial 112 $\mathrm{s}^{0.5}$ (210 minutes), salt-containing specimens absorbed moisture faster than the reference group, particularly those subjected to 14, 21, and 28 salt spray cycles. This accelerated absorption likely stems from NaCl's inherent hygroscopicity [81, 101]. Subsequently, absorption rates in salt-containing groups gradually decreased and were overtaken by the reference group, marking the transition to the second phase. At this stage, the moisture content ranked as: Reference > 7 cycles > 14 cycles > 21 cycles > 28 cycles > 35 cycles, consistent with the w_{sat} order observed in Fig. 4-13.

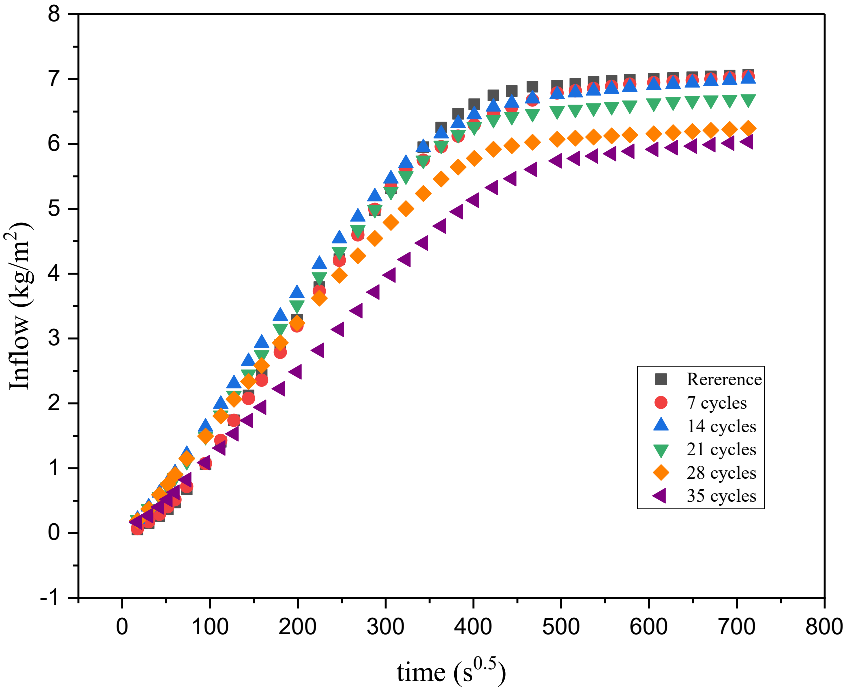

Fig. 4-15 Characteristic curves of capillary absorption of cement mortar subjected to different salt spray cycles

The capillary absorption coefficients $A_{\mathrm{cap,w}}$ (in deionized water) and $A_{\mathrm{cap,sol}}$ (in saturated NaCl solution) of the reference cement mortar specimen were calculated using Equation 4-7. The ratio $A_{\mathrm{cap,sol}}/A_{\mathrm{cap,w}} = 0.871$ was slightly lower than the theoretical value of 0.891 [101, 201] and the experimental value of 0.882 reported by J. Todorovic for ceramic tiles [67]. This discrepancy may arise from differences in material properties and pore structure. By applying this ratio (0.871) to correct $A_{\mathrm{cap,sol}}$ derived from the first-phase fitting curves of salt-containing specimens in Fig. 4-15, the corrected $A_{\mathrm{cap,w}}$ values for all six specimen groups are shown in Fig. 4-16. Following the method in Fig. 4-8, the two-phase curves in Fig. 4-13 were linearly fitted, and their intersection points were identified to calculate $w_{\mathrm{cap,sol}}$ using Equation 4-8. The measured density of saturated NaCl solution (ρ_{sol} =1199kg/m^3) and deionized water (ρ_w = 998kg/m^3) at standard temperature and pressure (25°C, 10^5 Pa) in the Building and Foundations Laboratory (sub-laboratory of Lince Lab, Politecnico di Torino) were used to adjust $w_{\mathrm{cap,sol}}$ based on the density ratio $\rho_{\mathrm{w}}/\rho_{\mathrm{sol}}$. As evident in Fig. 4-16, both A_{cap} and w_{cap} decreased with increasing salt spray cycles.

For all groups, the standard deviations of A_{cap} and w_{cap} ranged from 0.92%–1.25% and 1.1%–6.19%, respectively. These variations, primarily caused by material heterogeneity and uneven salt crystal distribution in pores, were orders of magnitude smaller than the measured values, thus deemed negligible.

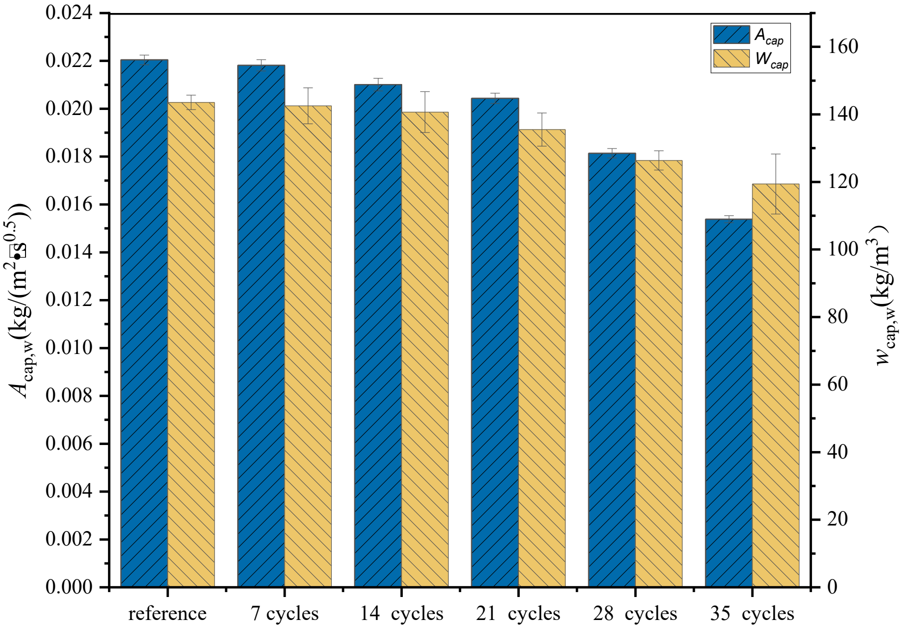

Fig. 4-16 Capillary absorption properties of cement mortar exposed to 0 to 35 salt spray cycles

Salt spray exposure significantly impacts the open porosity (*P*o) of cement mortar. As shown in Table 1, *P*o progressively decreased with increasing salt spray cycles, exhibiting an 18.7% reduction after 35 cycles. Multiple studies have reported NaCl-induced porosity reductions in building materials: limestone (−6.12% to −6.21%) [45], masonry bricks (−4.85%) [63], gypsum (−10.34%) [62], mortar (−21.67% to −46.67%) [13], and ceramic tiles (−21.6%) [67]. Notably, these studies employed full immersion [13, 45] or partial immersion [62, 67] in NaCl solutions, which differ significantly from accelerated salt spray testing. While experimental methods and material properties influence results, NaCl consistently reduces porosity by crystallizing at pore walls until complete occlusion [68, 88].

After 7 cycles, reductions in P_o, w_{sat}, $w_{cap,w}$, and $A_{cap,w}$ were minimal. By 14 cycles, $w_{cap,w}$ decreased less markedly than *P*o and w_{sat} (Fig. 4-2), suggesting additional factors beyond pore volume govern capillary moisture content. A plausible explanation is NaCl's strong hygroscopicity: increased salt deposition elevates capillary moisture content, partially offsetting porosity-driven reductions [81, 101]. However, $A_{cap,w}$ declined more sharply than $w_{cap,w}$, particularly after 28–35 cycles, indicating greater sensitivity of absorption rate to salt spray effects. This phenomenon relates not only to porosity reduction and hygroscopicity but also to altered pore size distribution induced by salt crystallization.

Table 4-2 Mean and standard deviation of hygric property parameters for the reference sample and samples treated with 7, 14, 21, 28 and 35 salt spray cycles

Salt spray cycles	**Reference**	**7**	**14**	**21**	**28**	**35**
P_o **[%]**	16.9± *0.142*	16.8 ± *0.343*	16.0 ± *0.251*	15.6 ± *0.213*	14.2 ± *0.397*	13.7 ± *0.359*
w_{sat} **[kg/m^3]**	202.240	200.962	192.167	186.946	175.159	164.413
Reduction of P_o **and** w_{sat} **[%]**		0.63	4.98	7.56	13.39	18.70
$w_{cap,w}$ **[kg/m^3]**	144 ± *1.78*	143 ± *4.42*	141± *5.04*	136± *4.10*	126± *1.39*	119± *7.37*
Reduction of $w_{cap,w}$ **[%]**		0.7	2.1	5.6	12.5	17.4
$A_{cap,w}$ **[kg/m^2·s$^{0.5}$]**	0.0220 ± *2.03E-04*	0.0218 ± *2.36E-04*	0.0210 ± 2.63E-04	0.0204 ± 2.13E-04	0.0181 ± 1.95E-04	0.0154 ± 7.46E-04
Reduction of $A_{cap,w}$ **[%]**		0.9	4.6	7.3	17.7	30.0

4.5.2 Salinity influence factors and modified equations

Under salt spray deposition, salt crystallization alters the porosity and pore structure of cement mortar, leading to significant changes in liquid water transport properties such as the capillary absorption coefficient (A_{cap}) and capillary moisture content (w_{cap}). Traditional moisture characteristic equations fail to provide accurate predictions under these conditions. To quantify the influence of salt content on capillary absorption parameters in salt-spray-exposed cement mortar, salinity influence factors were calculated based on experimental data. These factors were then fitted to empirical curves, enabling the modification of capillary absorption equations originally derived for salt-free porous materials.

Using the salt content growth trend (Fig. 4-13) and capillary parameter variations (Table 4-2) across salt spray cycles, the ratios of $A_{cap,w}$ and $w_{cap,w}$ between salt-containing and reference specimens were computed for each cycle. These ratios define the salinity influence factors $\eta_{A\mathrm{cap}}$ (for A_{cap}) and $\eta_{w\mathrm{cap}}$ (for $w_{cap,w}$). Fig. 4-17 plots these factors against salt content, establishing empirical relationships to guide equation modification.

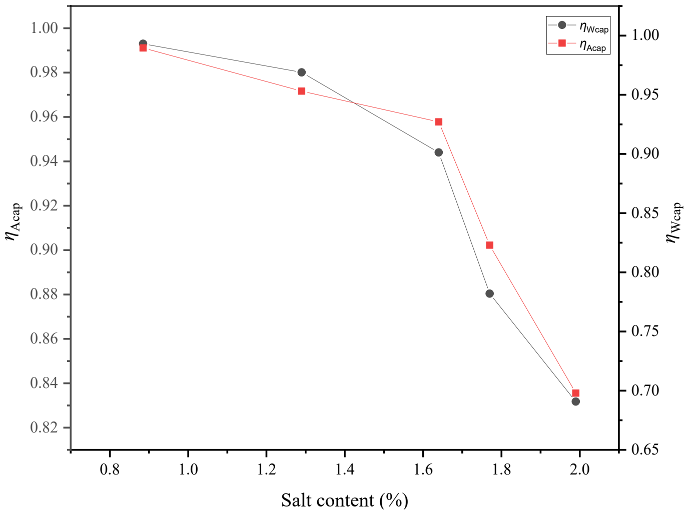

Fig. 4-17 Variation of the influencing factors η_{Acap} and η_{wcap} with salt content in the cement mortar

Based on the salinity influence factors η_{Acap} and η_{wcap} for cement mortar specimens in Fig. 4-17, polynomial equations were fitted to characterize their relationships with chloride concentration (C_{Cl}), as follows:

$$\eta_{A_{cap}} = -0.362{C_{Cl}}^2 + 0.791C_{Cl} + 0.56 \qquad R^2 = 0.95 \qquad (4\text{-}12)$$

$$\eta_{w_{cap}} = -0.181{C_{Cl}}^2 + 0.373C_{Cl} + 0.8 \qquad R^2 = 0.97 \qquad (4\text{-}13)$$

The above equations mainly reflect the impact of chloride ion content in the cement mortar on the capillary absorption parameters A_{cap} and w_{cap} , which is limited to salt spray conditions. The applicable chloride concentration range is 0.8 to 2.0 wt%. It can be concluded that the functions of capillary absorption coefficient $A_{\mathrm{cap,salt}}$ and capillary moisture content $w_{\mathrm{cap,salt}}$ of cement mortar with salt contamination in salt spray environment are as follows:

$$A_{cap,salt} = A_{cap,w}(-0.362{C_{Cl}}^2 + 0.791C_{Cl} + 0.56) \qquad (4\text{-}14)$$

$$w_{cap,salt} = w_{cap,w}(-0.181{C_{Cl}}^2 + 0.373C_{Cl} + 0.8) \qquad (4\text{-}15)$$

4.5.3 Equilibrium water content and water retention curves

The equilibrium moisture content of reference specimens (u_0) and salt-spray-cycled specimens (u_1~ u_5, 7–35 cycles), measured via the semi-permeable membrane method, is shown in Figure 4-18a. Water retention curves for the six specimen groups, plotted using averaged equilibrium moisture content values from four replicates, are presented in Figure 4-18b. As the capillary pressure of the salt solution beneath the membrane increased (from -5×10^6 Pa to -2×10^5 Pa), the equilibrium moisture content of all groups increased. However, at any given capillary pressure, salt-containing specimens exhibited lower equilibrium moisture content than the reference group, with further reductions observed as salt spray cycles increased. This indicates that salt crystal deposition in cement mortar pores does not alter the general trend of the water retention curve with capillary pressure but reduces equilibrium moisture content at all pressure levels. These findings align with the trends in saturated moisture content (w_{sat}) under salt deposition (Section 4.4.1, Fig. 4-13) and capillary moisture content (w_{cap}) (Section 4.5.1, Fig. 4-16).

For all groups in Figure 4-18, measurement standard deviations remained below 0.5%: Control group: 0.40%–0.42%，7 cycles: 0.40%–0.46%，14 cycles: 0.29%–0.33%，21 cycles: 0.19%–0.23%，35 cycles: 0.21%–0.29%. These deviations, orders of magnitude smaller than the measured values, confirm negligible experimental error.

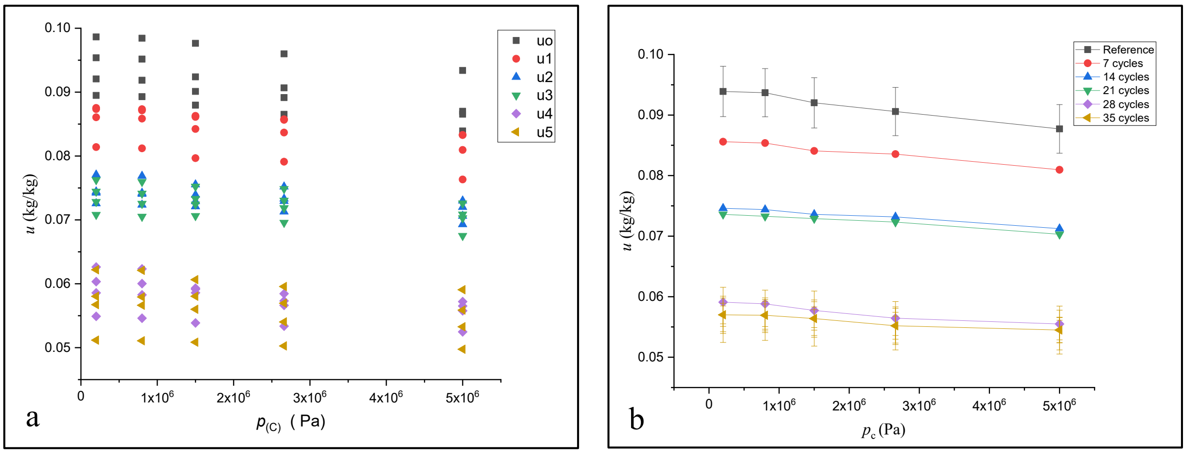

Fig. 4-18 Water retention curves of cement mortar under varying salt spray deposition

The macroscopic measurements collectively reveal that prolonged salt spray deposition and the associated reduction in open porosity (Fig. 4-14) lead to diminished liquid water transport and storage capacities. Key parameters, including saturated moisture content (w_{sat}), capillary absorption coefficient (A_{cap}), capillary moisture content (w_{cap}), and equilibrium moisture content (u), decrease with increasing salt content. This suppression of liquid water dynamics is primarily attributed to NaCl crystal deposition within pores, which reduces accessible pore volume and open porosity.

For building envelope systems, reduced moisture content in porous materials increases air-filled pore volume, lowering thermal conductivity and enhancing insulation performance—beneficial for energy efficiency. Additionally, diminished hygroscopic stress due to lower moisture content improves material durability. Thus, accurately quantifying liquid water transport and storage properties of salt-contaminated porous materials in coastal climates is critical for energy-efficient design and indoor thermal comfort predictions.

4.6 Pore structure and microscopic morphology

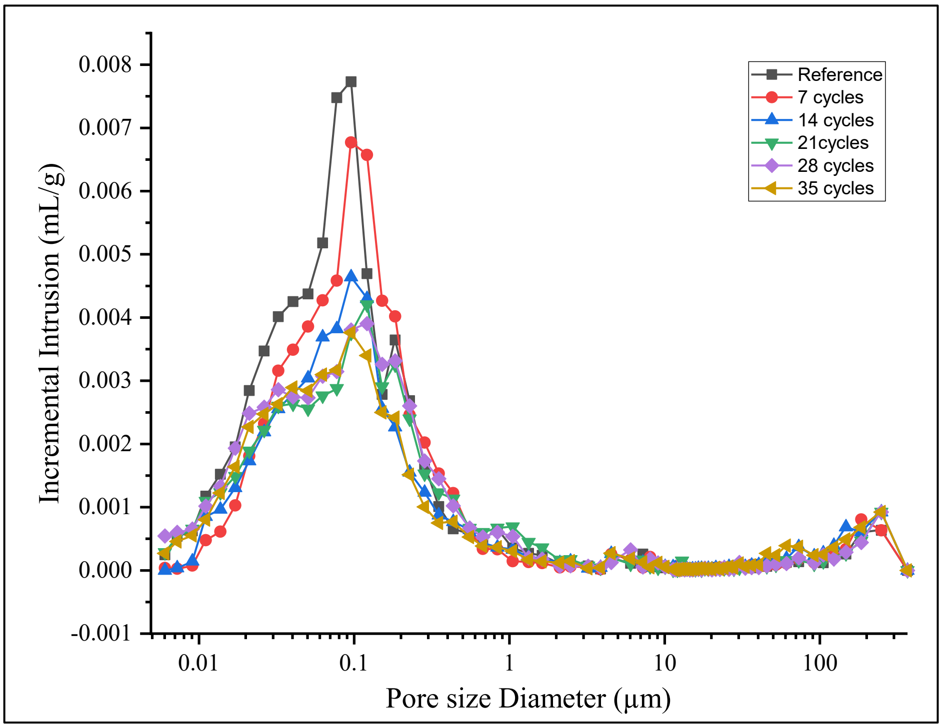

a) Incremental Intrusion vs Pore size

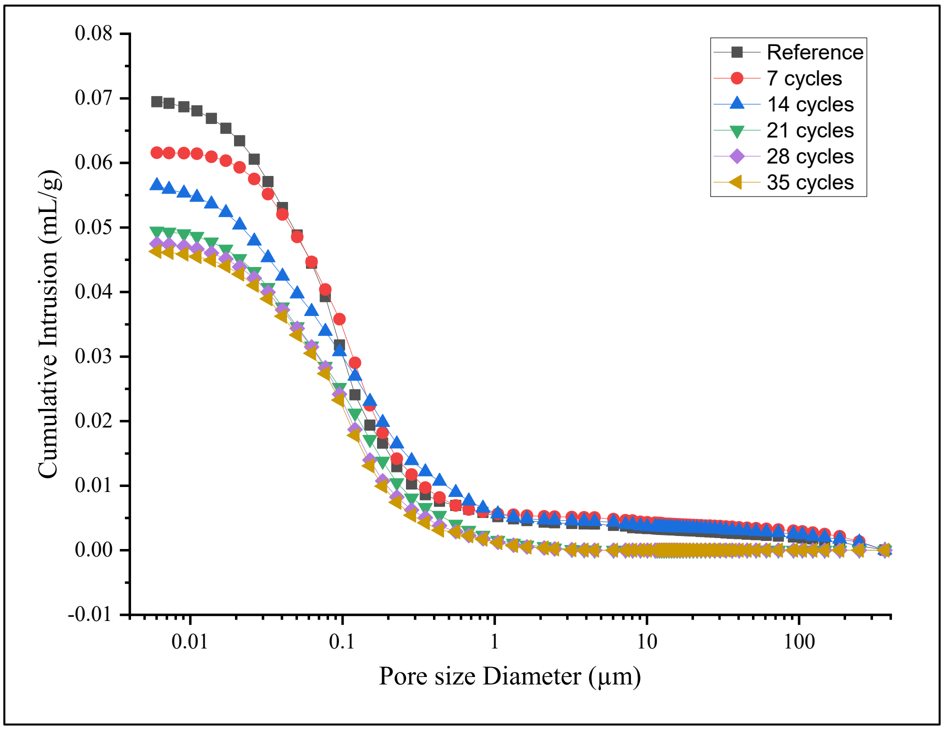

b) Cumulative Pore Area vs Pore size

Fig. 4-19 Pore volume distribution of cement mortar after different salt spray cycles (including reference group)

To explore the mechanisms underlying salt spray-induced changes in pore size distribution and capillary absorption properties of cement mortar at the microscale, mercury intrusion porosimetry (MIP) was performed on five salt-spray-cycled (7–35 cycles) groups and one reference group. As shown in Fig. 4-19a, all six specimens exhibited peak mercury intrusion volumes near a pore diameter of 0.1 μm. Compared to the reference, salt-spray-exposed specimens showed significant reductions in pore volume within the 0.02–0.12 μm range, while pores larger than 0.12 μm remained largely unaffected.

This aligns with prior findings that porosity reductions in porous building materials primarily result from salt crystal deposition in smaller pores, such as 0.01–0.08 μm pores in cement mortar [13] and 0.01–0.12 μm pores in limestone [11]. Capillary absorption predominantly occurs in pores of 0.1–100 μm, whereas permeation can occur in pores as small as 0.01 μm [202]. The reduced pore volume in the 0.02–0.12 μm range in salt-contaminated specimens directly explains their diminished capillary absorption coefficients (A_{cap}) observed in Fig. 4-15 and Fig. 4-16.

To further investigate microstructural evolution and salt crystal distribution under salt spray, surface and subsurface specimens were analyzed via scanning electron microscopy (SEM) (Fig. 4-20). After 7 cycles, cubic NaCl crystals appeared on the surface but not subsurface. At 14–35 cycles, surface crystals grew, aggregated, and fused into dense salt clusters (Fig. 4-20 2a–5a), which clogged surface open pores, contributing to the significant open porosity reduction (Section 4.14). Subsurface samples revealed a matrix of calcium silicate hydrate (CSH) and needle-like ettringite ($C_3A\cdot 3CaSO_4\cdot 32H_2O$) (Fig. 4-20 1b). With increasing cycles, cubic salt crystals nucleated within pores between these phases, adhering to pore walls and densifying the microstructure. This microscale densification mechanistically explains the macroscale trends of decreasing saturated moisture content (w_{sat}) and increasing apparent density (ρ_b) with cycle progression (Fig. 4-13 and Fig. 4-14).

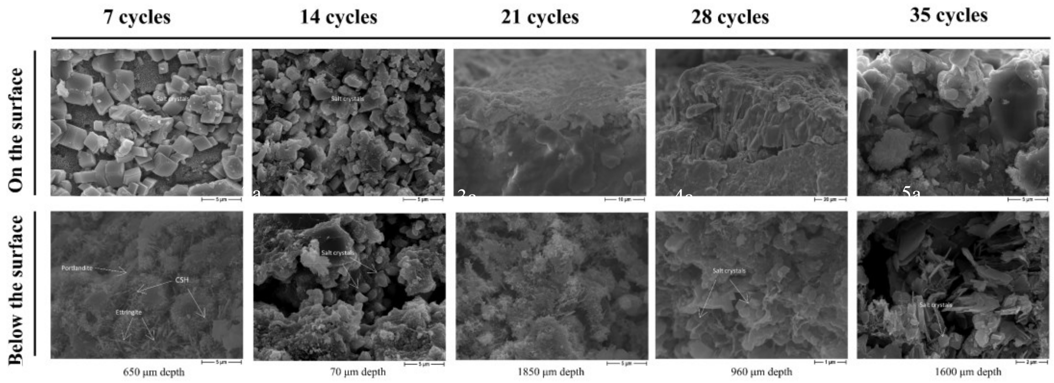

Fig. 4-20 SEM images of cement mortar samples at different depths after 7–35 cycles of salt spray testing.

4.7 Chapter summary

To investigate the impact of coastal salt spray on liquid water transport in porous building envelope materials, this chapter conducted accelerated salt spray tests and related analyses on cement mortar specimens. After 7–35 accelerated salt spray cycles, measurements included chloride ion concentration, vacuum saturation, capillary absorption, and semi-permeable membrane water retention experiments. A novel measurement technique and computational method were developed and validated to accurately quantify water sorption properties of cement mortar in salt-contaminated states. Key findings are summarized as follows:

(1) Increasing salt spray cycles promoted NaCl crystal deposition and inward migration in cement mortar, reducing open porosity (P_o) and increasing apparent density (ρ_b). After 35 cycles, average chloride mass concentration reached 1.99%, P_o and saturated moisture content (w_{sat}) decreased by 18.7%, ρ_b increased by 3.85% (vs. control group).

(2) Comparative capillary absorption tests in deionized water and saturated NaCl solution yielded a capillary absorption coefficient ratio $A_{cap,sol}/A_{cap,w}$=0.871. This ratio accounts for the combined effects of absorption medium density, surface tension, and viscosity, enabling correction of A_{cap} for salt-containing specimens. Modified equations for $A_{cap,salt}$ and $w_{cap,salt}$ were established using salinity influence factors η_{Acap} and η_{wcap}.

(3) Both $A_{cap,w}$ and $w_{cap,w}$ decreased progressively with salt spray cycles. After 35 cycles, $A_{cap,w}$ declined by 30% and $w_{cap,w}$ declined by 17.4%. The reduction primarily resulted from salt crystal occlusion of 0.02–0.12 μm pores, diminishing porosity and capillary/permeation effects. However, NaCl’s hygroscopicity partially offset the $w_{cap,w}$ reduction.

This study provides a comprehensive understanding of liquid water dynamics in salt-contaminated porous building materials, establishing a basis for accurate parameterization in coastal building envelope design. Chapter 5 further explores water vapor permeability and isothermal moisture equilibrium under salt spray conditions.

Chapter 5 Water vapor transport properties of cement mortar with salt deposition

5.1 Introduction

The water vapor permeability coefficient (δ) represents the mass of water vapor transmitted through a unit area of material per unit time under a unit vapor pressure gradient [203]. Equilibrium moisture content (u) is defined as the moisture content at which dynamic equilibrium occurs between a material and its environment, with no further weight change [204]. Under constant temperature and pressure, the moisture storage curve (or sorption isotherm) describes a material's water retention capacity by plotting equilibrium moisture content against relative humidity [203, 205]. These vapor transport properties critically govern heat and moisture transfer in building envelopes [204, 206], indoor environmental comfort [206], and building energy consumption [207, 208], making accurate quantification of δ and u essential for hygrothermal modeling and energy-efficient design.

In coastal salt spray climates, salt crystallization within material pores significantly alters equilibrium moisture content [10, 73, 209] and water vapor permeability [9, 13, 210]. While current Chinese standards for climatic zoning (GB 50178-1993) [211] and building thermal design (GB 50176-2016) [212] fail to adequately address salt spray effects, thereby constraining hygrothermal performance optimization in these regions. Consequently, elucidating water vapor transport mechanisms in salt-affected porous building materials presents an urgent research priority.

This chapter employs accelerated salt spray cycling to simulate coastal conditions, using cement mortar as a representative material. Through equilibrium sorption tests and vapor permeability measurements across varying salt exposure cycles, we quantify salinity influence factors on δ and u. Complementary MIP/SEM analyses reveal microscale mechanisms driving these changes. Collectively, this work establishes a theoretical foundation for improving hygrothermal simulations and energy-efficient designs in salt-affected coastal environments.

5.2 Samples and salt spray test methods

5.2.1 Material and samples

Cement mortar was prepared using CEM II/BLL 32.5R cement (Italy), CEN standard sand (UNI EN 197-1:2011), and tap water. This cement is widely employed in wall construction [25], with a clinker content of 65–79%, limestone content of 21–35%, and gypsum additive content of 0–5%. The chemical composition, determined by X-ray fluorescence (XRF, Rigaku NEX CG), is listed in Table 5-1. Loss on Ignition (LOI) was measured via TG-DTA. The raw materials were mixed at a mass ratio of cement:sand:water = 1:3:0.5. After thorough mixing, the paste was cast into 40 × 40 × 160 mm³ molds in layers, compacted by vibration, and cured for 24 hours in a constant climate chamber (23°C, 95% RH). Demolded specimens were then water-cured at room temperature for 28 days.

Tabel 5-1 Chemical composition (wt%) of cement CEM II/BLL 32.5R determined by XRF analysis

Component	CaO	MgO	SO_3	Al_2O_3	Fe_2O_3	K_2O	Na_2O	TiO_2	SrO	P_2O_5	LOI	Others
Content	60.2	3.56	3.46	3.12	2.19	1.12	1.05	0.185	0.147	0.104	12.8	0.19

To accelerate isothermal sorption equilibrium tests, smaller specimens are typically used [213, 214]. However, thin cement mortar specimens proved difficult to mold directly while ensuring paste compactness and surface flatness. Therefore, 40 × 40 × 160 mm³ specimens were first prepared using the aforementioned method and subsequently cut into 40 × 40 × 10 mm³ slices. The sliced specimens were cleaned sequentially with compressed air and deionized water to remove adherent particles, preventing open pore blockage. Cleaned specimens were labeled, grouped, and dried in a forced convection oven at 55°C. According to ISO 12570:2000(E) [158], constant mass was confirmed when three successive 24-hour weighings showed mass variations ≤0.1% of specimen mass. Theoretically, cutting larger specimens may damage pore structures and increase porosity, potentially affecting equilibrium moisture content. However, since moisture sorption at 0–97% RH is dominated by micropores—which remain minimally disturbed during cutting [191, 215]—this method negligibly impacts equilibrium moisture measurements.

a）CNC cutting　b） Cleaning and labeling　c）Constant-temperature drying

Fig. 5-1 Processing and drying of specimens for sorption isothermal tests

Water vapor permeability tests employed specimens of a different size. Unlike concrete, cement mortar contains no coarse aggregates and was thoroughly vibrated during molding to eliminate air bubbles, rendering it a relatively homogeneous material. Per ISO 12572:2016(E) [216], which governs vapor permeability measurements via the dry/wet cup method, homogeneous materials require a minimum specimen thickness of 20 mm. While thicker specimens prolong test duration, a 20 mm thickness was selected to balance experimental rigor and efficiency. Post-curing, 70 × 70 × 70 mm^3 cubes were cut into 70 × 70 × 20 mm^3 specimens using the method illustrated in Fig. 5-1a (result shown in Fig. 5-2). Specimens were cleaned sequentially with compressed air and deionized water to remove adherent particles and prevent open pore occlusion. Finally, cleaned specimens were labeled and dried to constant mass at 55°C [158].

a) 70×70×70 mm^3 cube specimen **b) 70×70×20 mm^3 specimen**

Fig. 5-2 Specimens for water vapor permeability testing

5.2.2 Accelerated salt spray test

Salt deposition and erosion on building materials is a slow process influenced by uncontrollable climatic factors. Accelerated salt spray testing was employed to simulate coastal conditions for studying vapor transport in porous materials. Current standards predominantly target electrical/metallic industries [120-122], while existing stone standards (BS EN 14147:2003 [54], B117-11 [151]) focus on durability. Aligned with Chapter 2's methodology, specimens underwent cyclic testing in a CEAST 5050 chamber (Italy; full parameters in Section 2.3). Key settings: 5 wt.% NaCl solution; specimens tilted 20° from vertical with 47 mm spacing (Figure 5-3); cyclic 8-h spray (35°C) + 16-h drying (55°C); average deposition 2 mL/(80 $cm^2\cdot h$); humidity uncontrolled during spraying (chamber near saturation).

For equilibrium sorption tests, 90 specimens were divided into five humidity groups (33%, 53%, 75%, 84%, 93% RH). Each group comprised six subgroups (0 [control], 7, 14, 21, 28, 35 cycles) with triplicates for mean/SD calculations (Table 5-2). For vapor permeability tests, 24 specimens formed groups 5O, 5A, 5B, 5C, 5D, 5E (corresponding to 0, 7, 14, 21, 35 cycles) with quadruplicates (e.g., 5A1–5A4) (Table 5-2). Post-exposure, all specimens were conditioned to constant mass at 23°C/50% RH [216] to eliminate moisture interference.

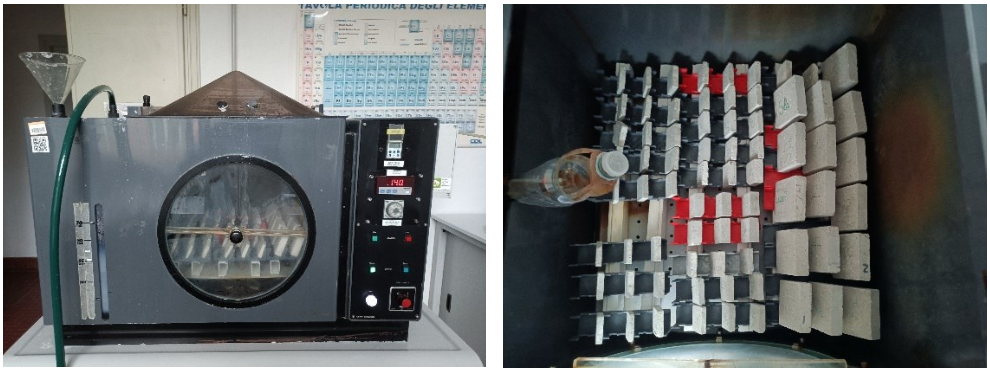

Fig. 5-3 Salt spray chamber and specimen placement (20° from vertical)

Table 5-2 Grouping of cement mortar specimens by salt spray cycles and humidity conditions

Ambient RH (%)	Reference	7 Cycles	14 Cycles	21 Cycles	28 Cycles	35 Cycles
33	3O1-1, 3O2-1, 3O3-1	3A1-1, 3A2-1, 3A3-1	3A1-2, 3A2-2, 3A3-2	3A1-3, 3A2-3, 3A3-3	3A1-4, 3A2-4, 3A3-4	3A1-5, 3A2-5, 3A3-5
53	3O1-2, 3O2-2, 3O3-2	3B1-1, 3B2-1, 3B3-1	3B1-2, 3B2-2, 3B3-2	3B1-3, 3B2-3, 3B3-3	3B1-4, 3B2-4, 3B3-4	3B1-5, 3B2-5, 3B3-5
75	3O1-3, 3O2-3, 3O3-3	3C1-1, 3C2-1, 3C3-1	3C1-2, 3C2-2, 3C3-2	3C1-3, 3C2-3, 3C3-3	3C1-4, 3C2-4, 3C3-4	3C1-5, 3C2-5, 3C3-5
84	3O1-4, 3O2-4, 3O3-4	3D1-1, 3D2-1, 3D3-1	3D1-2, 3D2-2, 3D3-2	3D1-3, 3D2-3, 3D3-3	3D1-4, 3D2-4, 3D3-4	3D1-5, 3D2-5, 3D3-5
93	3O1-5, 3O2-5, 3O3-5	3E1-1, 3E2-1, 3E3-1	3E1-2, 3E2-2, 3E3-2	3E1-3, 3E2-3, 3E3-3	3E1-4, 3E2-4, 3E3-4	3E1-5, 3E2-5, 3E3-5
Water vapor permeability	$5O_1$, $5O_2$, $5O_3$, $5O_4$	$5A_1$,$5A_2$, $5A_3$, $5A_4$	$5B_1$, $5B_2$, $5B_3$, $5B_4$	$5C_1$, $5C_2$, $5C_3$, $5C_4$	$5D_1$, $5D_2$, $5D_3$, $5D_4$	$5E_1$, $5E_2$, $5E_3$, $5E_4$

5.3 Test methods for water vapor transport properties

5.3.1 Sorption isotherms experiment

1）Experimental setup

Isothermal equilibrium hygroscopicity tests adhered to ISO 12571:2013(E) [205] and ASTM C1498-04a [217]. As shown in Fig. 5-4a, specimens were placed on perforated support plates (≥30% open area) within sealed plastic containers. Saturated salt solutions maintained specific relative humidity (RH) levels, with stainless steel stands elevating specimens when necessary to prevent airflow obstruction through plate apertures.

Five RH levels (33%, 53%, 75%, 85%, 93% at 23°C) were selected using saturated solutions of $MgCl_2{\cdot}6H_2O$, $Mg(NO_3)_2{\cdot}6H_2O$, $NaCl$, KCl, and KNO_3. This selection satisfied ISO's requirement for ≥4 uniformly distributed RH points (30–95% range) and reflected coastal humidity patterns (e.g., Xiamen: 70–86% RH; Venice: 71–81% RH). Measured RH values deviated <1% from theoretical standards (Table 5-3).

Visible salt crystals ensured continuous saturation. Miniature fans enhanced humidity homogeneity and moisture exchange (Fig. 5-4b). Pre-experiment, all containers underwent 23°C equilibration in a climate chamber, with RH/temperature calibrated using testo 174H sensors (temperature range: -20 to +70°C, accuracy ±0.1°C; RH range: 0–100%, accuracy ±0.1% RH) (Fig. 5-4c).

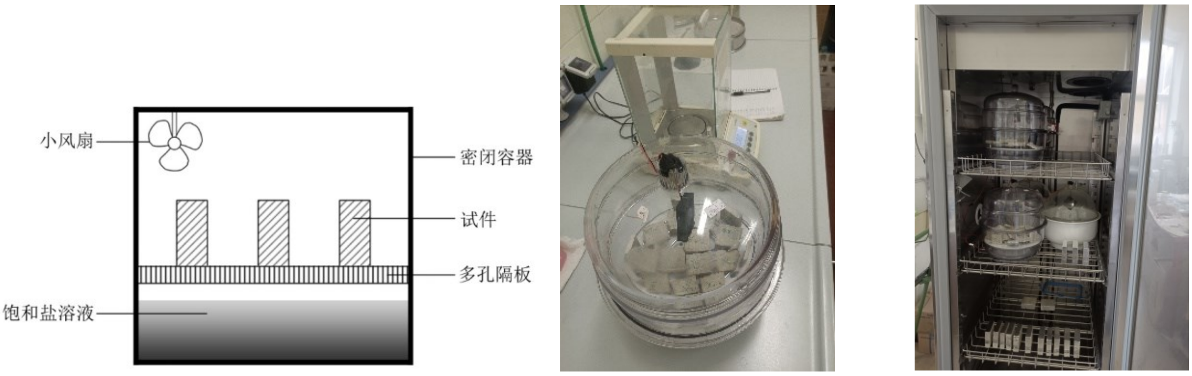

a) Schematic[187] **b) Physical assembly** **c) 23°C climate chamber**

Fig. 5-4 Experimental setup for sorption isothermal tests

Table 5-3 Calibration of saturated salt solutions: Theoretical vs. Measured (RH) at 23°C [205]

NO.	**Saturated Salt Solution**	**Relative Humidity (RH, %)**		**Relative Deviation（%）**
		Theoretical Value	Measured Value	
1	$MgCl_2{\cdot}6H_2O$	33	32.9	－0.30
2	$Mg(NO_3)_2{\cdot}6H_2O$	53	53.5	0.94
3	$NaCl$	75	75.2	0.27
4	KCl	85	84.9	－0.12
5	KNO_3	93	93.6	0.65

2）Experimental procedures

Following ISO 12570:2000(E) [158], cement mortar specimens underwent salt spray cycles (0–35 days) and were dried to constant mass (criteria: non-monotonic mass change over three consecutive weightings with SD <0.1%). Specimens were then distributed across sorption chambers at 33%–97% RH in a full-factorial design: *each salt spray group* (0d, 7d, 14d, 21d, 28d, 35d) was exposed to *all humidity levels*. For example, 7-cycle specimens were allocated as: 3A1-1~3A3-1 (33% RH), 3B1-1~3B3-1 (53% RH), 3C1-1~3C3-1 (75% RH), 3D1-1~3D3-1 (85% RH), 3E1-1~3E3-1 (97% RH). The 33% RH chamber contained six subgroups ($3O_{1-1}$ ~ $3O_{3-1}$, $3A_{1-1}$ ~ $3A_{3-1}$, $3A_{1-2}$ ~ $3A_{3-2}$, $3A_{1-3}$ ~ $3A_{3-3}$, $3A_{1-4}$ ~ $3A_{3-4}$, $3A_{1-5}$ ~ $3A_{3-5}$) (Fig. 5-2; Table 5-2).

After five weeks of isothermal sorption equilibrium testing, triplicate specimens per group were weighed using a sealed transfer protocol (Fig. 5-5): subgroups were extracted, immediately sealed in non-hygroscopic containers, individually weighed (±1 mg precision; air exposure <10 s), and returned to chambers. Equilibrium was confirmed when three consecutive 24-h mass measurements varied ≤0.1%. Crucially, NaCl dissolution above 75% RH caused salt redistribution at 95% RH, altering original crystallization patterns. Therefore, analysis focused exclusively on sorption curves to preserve salt-deposited microstructural integrity.

Fig. 5-5 Glass container for sealed specimen weighing

3）Isothermal sorption curve fitting

The equilibrium moisture content $u_{(\varphi)}$ for each group was calculated using Equation 5-1. Mean values from triplicate specimens per salt spray cycle at each relative humidity (RH) were used to plot sorption isotherms.

$$u_{(\varphi)} = \frac{m_{wet}(\varphi)-m_{dry}}{m_{dry}} \qquad (5\text{-}1)$$

Nomenclature: $u(\varphi)$ is the equilibrium moisture content at particular RH (kg/kg, %), $m_{\mathrm{wet}(\varphi)}$ is the equilibrium mass at particular RH (kg).

Sorption isotherms were plotted with RH (33%, 53%, 75%, 85%, 93%) as the x-axis and $u(\varphi)$ as the y-axis. Curve slope variations were analyzed to assess salt spray impacts on hygroscopicity. For salt-free materials, $u(\varphi)$ depends solely on RH. For salt-contaminated specimens, it is a bivariate function of both RH and salt content.

Existing sorption isotherm models for porous materials are summarized in Table 5-4. The optimal model was selected based on control specimens (0 cycles). To quantify salinity effects, the influence factor η_u is defined as:

$$\eta_u = \frac{u_s}{u_c} \tag{5-2}$$

Nomenclature: u_s is equilibrium moisture content of salt-sprayed specimens (kg/kg), u_c is equilibrium moisture content of salt-free control specimens (kg/kg) (both at identical RH conditions).

Table 5-4 Classical Fitting Equations for Sorption Isotherms

Equation	Formula
BET[218]	$u = k_1\varphi/[(1+k_2\varphi)(1-k_3\varphi)]$
Oswin[219]	$u = k_1[\varphi/(1-\varphi)]^{k_2}$
Caurie[220]	$u = \exp(k_1 + k_2\varphi)$
Henderson[221]	$u = \{[\ln(1-\varphi)]/k_1\}^{k_2}$
Peleg[222]	$u = k_1\varphi^{k2} + k_3\varphi^{k4}$
GAB[223]	$u = k_1k_2k_3\varphi/[(1-k_1\varphi)(1-k_2\varphi+k_2k_3\varphi)]$
Feng[191]	$u = \ln\left[(100\varphi+1)^{k_1}/(1-\varphi)^{k_2}\right] + k_3\exp(100\varphi)$
Exponential	$u = k_1 + k_2e^{k_3x}$

5.3.2 Water vapor permeation test

1）Experiment setup

A custom apparatus (Fig. 5-6) compliant with ISO 12572:2016(E) [216] established water vapor pressure gradients by sealing 70×70×20 mm³ specimens with self-adhesive aluminum membrane on all sides to prevent sealant intrusion (Fig. 5-7a), then mounting them centrally in a 72×72 mm² lid opening with symmetric 10 mm protrusion above/below the lid plane. BOSTIK liquid rubber (Italy) was uniformly applied along specimen edges; after initial curing, reverse-side application ensured complete pore filling and rigid bonding (Fig. 5-7b), enabling controlled moisture flow through specimens under vapor pressure differentials.

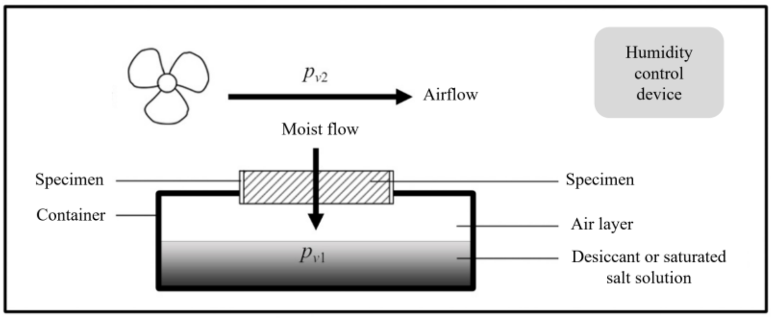

Fig. 5-6 Schematic diagram of water vapor permeability test device [187]

Given the critical impact of plastic container seal integrity on vapor permeability measurement accuracy [191, 216], seal quality verification was conducted 24 hours post-assembly by positioning the assembled lid with its inner surface facing upward, filling it with deionized water to submerge the perimeter sealant while maintaining a 2–3 mm clearance below the specimen surface to prevent water ingress (Fig. 5-7c). After three hours of static observation, components showing no leakage were validated, whereas leaking units underwent sealant reapplication; finally, all validated assemblies were conditioned at (23 ± 2)°C and (50 ± 2)% RH in a constant climate chamber prior to formal testing.

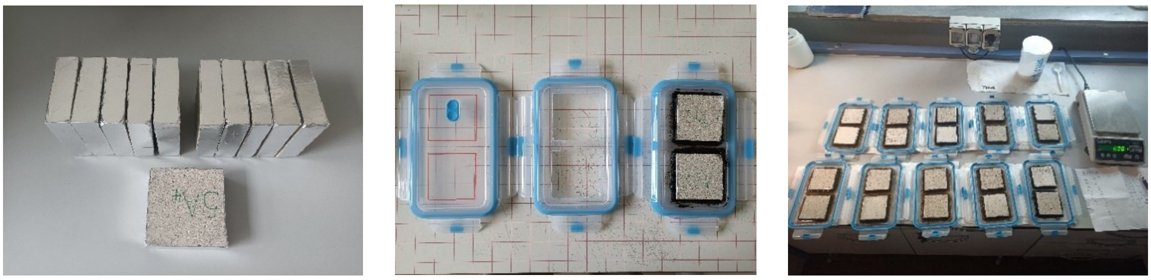

a) Perimeter sealing **b) Sealant embedding** **c) Leak test**

Fig. 5-7: Assembly and seal verification of water vapor permeability specimens

2）Methodology rationale

Water vapor permeability testing employed dry-cup and wet-cup methods per ISO 12572 [161, 216], where the dry-cup method quantifies vapor diffusion under low humidity (0–50% RH) while the wet-cup method assesses combined vapor/liquid transfer under high humidity (50–94% RH), as partial pore saturation enhances capillary flow but reduces vapor permeation; consequently, dry-cup tests preceded wet-cup tests for all specimens to comprehensively characterize cement mortar behavior across humidity gradients.

For dry-cup tests (23°C, 0/50% RH; Table 5-5), silica gel desiccant maintained 0±2% RH inside plastic boxes, with assemblies placed in a 23°C/50±2% RH climate chamber; for wet-cup tests (23°C, 50/94% RH; Table 5-5), saturated K_2SO_4 solution (with excess crystals ensuring sustained saturation) provided 94±2% RH internally, while the climate chamber controlled external humidity at 50±2% RH, with critical 20 mm (specimen-to-desiccant) and 50 mm (specimen-to-solution) air gaps standardized across all assemblies via equal-mass adjustment of desiccant/solution to ensure identical air layer thicknesses (Fig. 5-8b).

Table 5-5 Environmental conditions for water vapor permeability measurement via dry-cup/wet-cup method [216]

Experimental method	Tmeperature °C	Relative Humidity (RH) %	
		Dry state	Wet state
Dry cup	23 ± 0.5	0 ± 2	50 ± 2
Wet cup	23 ± 0.5	50 ± 2	98 ± 2

Before commencing the experiment, test components were conditioned in a constant temperature/humidity chamber at (23 ± 0.5)°C and (50 ± 2)% RH until moisture equilibrium was achieved. Constant mass was confirmed when three consecutive daily mass measurements varied by ≤ 5% (Fig. 5-8a). The stabilized top components were then sealed onto containers holding equal masses of desiccant or saturated salt solution to form test assemblies (Fig. 5-8b). All assemblies were simultaneously transferred to the environmental chamber to initiate testing. The chamber's internal fan was activated to maintain ≥100 mm/s air velocity across specimens' upper surfaces (Fig. 5-8c). Ambient temperature and humidity were continuously recorded using a Testo 174H data logger. After four weeks, assemblies were sequentially weighed in a 23 ± 2°C controlled environment, with weighing times recorded. Subsequent mass measurements occurred at 48-hour intervals until water vapor transmission reached steady state, defined as ≤5% variation across five consecutive readings relative to their mean value.

a) Conditioning **b) Specimen assembly** **c) Water vapor transmission permeability**

Fig. 5-8 Specimen Preparation and Testing for Water Vapor Permeability

3）Experimental data processing

The total mass of the dry/wet cup assembly was regressed against weighing time using linear fitting to determine the water vapor flux rate through the cement mortar specimen, G_v (kg/s). The coefficient of determination (R^2) for the linear fit must be ≥0.99. Water vapor flux density was calculated as:

$$g_v = \frac{G_v}{A} \tag{5-3}$$

Where g_v is water vapor flux density [kg/(m²·s)], A is specimen's exposed surface area (m²).

The water vapor partial pressure differential was calculated by:

$$\Delta p_v = p_{v,sat} \cdot |\varphi_1 - \varphi_2| \tag{5-4}$$

Where Δp_v is vapor pressure differential (Pa); $p_{v,sat}$ is saturated vapor pressure (2,808 Pa at 23°C).

Total vapor transfer resistance (specimen + air layer) ($m^2 \cdot s \cdot Pa/kg$):

$$R_{total} = \frac{\Delta p_v}{g_v} \tag{5-5}$$

Air layer resistance R_{air} ($m^2 \cdot s \cdot Pa/kg$):

$$R_{air} = \frac{d_{air}}{\delta_{V,air}} \tag{5-6}$$

Where d_{air} is air layer thickness (m); $\delta_{V,air}$ is vapor permeability coefficient of stagnant air [2×10^{-10} kg/(m·s·Pa)].

Specimen resistance R_{air} ($m^2 \cdot s \cdot Pa/kg$)：

$$R_{sample} = R_{total} - R_{air} \tag{5-7}$$

Specimen vapor permeability coefficient δ_v [(kg/ (m · s · Pa)]:

$$\delta_v = \frac{H}{R_{sample}} \tag{5-8}$$

Where H is specimen thickness (m).

5.3.3 Microscopic measurement and analysis methods

1）Chloride ion content

Salt crystallization in porous building materials progressively accumulates under salt spray exposure, though its natural deposition kinetics remain poorly characterized [7-9]. To quantify salt deposition in cement mortar specimens during accelerated testing, chloride content was measured after varying salt spray cycles. Given the 5 wt% NaCl spray solution (Section 5.2.2), deposited salts comprised exclusively NaCl crystals, enabling specimen salt content determination through Cl^- concentration analysis. Measurements employed a chloride testing system (C-CL-3000, James Instruments, USA; specifications in Section 4.2.3), which calculates Cl^- mass concentration via voltage changes from electrochemical reactions in acidic solutions (Fig. 4-3). Prior to testing, electrodes were calibrated using five standard solutions (0.005%, 0.001%, 0.05%, 0.1%, and 0.3% Cl^-).

Full-thickness specimens were homogenized by grinding to integrate depth-dependent salt distribution. From this powder, 3 g aliquots were dissolved in 20 mL acidic solution (Fig. 4-4a,b). Solutions were capped, vigorously shaken, and stabilized for 2 minutes before degassing by loosening caps. Measurements commenced after 2-4 minutes (Fig. 4-4c,d) at 23°C ambient temperature. All samples remained desiccated pre-weighing, with batch measurements completed within 2 hours post-calibration.

2）Micro-morphology and pore characteristics

To elucidate microstructural evolution and moisture transport mechanisms in cement mortar under salt spray exposure, specimens subjected to varying salt spray cycles were analyzed using: X-ray diffraction (XRD; PANalytical X'Pert PRO, Netherlands), scanning electron microscopy (SEM; Hitachi S4000, Japan), and mercury intrusion porosimetry (MIP; Micromeritics Autopore V, USA) as illustrated in Fig. 5-9. Mid-depth cross-sections representing full-thickness microstructure and material composition were extracted from cubic specimens. For XRD analysis, samples were pulverized and sieved through a 0.25-mm mesh to remove aggregate particles. Due to rapid carbonation susceptibility of fine cementitious powders in ambient air [224, 225] prepared samples were stored in sealed vials to prevent deterioration and maintain dryness prior to testing. XRD spectra were acquired between 10° and 70° 2θ (copper cathode, 0.003° step size, 21.42 s/step).

a) Scanning Electron Microscopy (SEM)

b) X-Ray Diffraction (XRD)

c) Mercury Intrusion Porosimetry (MIP)

Fig. 5-9 Analytical Test Equipment

SEM specimens encompassed fracture surfaces from exposed faces to mid-depths, enabling depth-resolved microstructural characterization. Samples underwent desiccation followed by gold sputter-coating (SPI Supplies, USA) before imaging. For MIP analysis, specimens were first dried to constant mass at 50°C. Triplicate 3-4 g aliquots per group were analyzed at maximum pressures of 2,000 bar, resolving pores ≥6 nm via the Washburn equation. All analytical specimens were maintained in anhydrous conditions throughout preparation. SEM and MIP procedures adhered to ISO 21466:2019 [149] and ISO 15901-1:2016 [150] respectively.

5.4 Sorption isotherms and fitting equations

5.4.1 Salt spray cycles and salt deposition

Chloride concentration measurements from full-thickness cement mortar specimens reveal increasing salt content with extended salt spray cycles (Fig. 5-10). Specimen salt content rose progressively from 0.885 wt% after 7 cycles to 1.99 wt% following 35 cycles, demonstrating cumulative salt ingress under cyclic salt spray-drying conditions. Comparative studies show: Bai et al. [69] reported 0.175-0.724 wt% chloride concentrations in cement mortar after 12-hour immersion in 2.5-10% NaCl solutions. He et al. [226] documented 0.06-0.87 wt% salt content in aerated concrete following 12-hour immersion in 0.2-2% NaCl solutions. Despite methodological and material differences, the salt content after 7 cycles in this study (0.885 wt%) approximates the maximum values in these immersion experiments. Whereas immersion achieves rapid salt penetration, cyclic salt spray enables slower but ultimately greater accumulation - reaching nearly double the maximum literature values at 35 cycles. Measurement uncertainties (SD range: 0.51-1.78 wt%) were orders of magnitude below reported salt content values, confirming negligible impact on experimental conclusions.

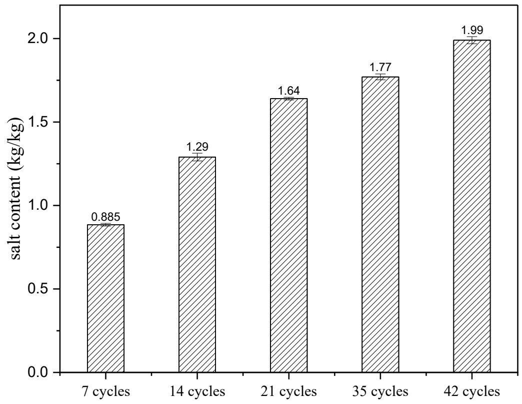

Fig. 5-10 Salt content of cement mortar specimens under cyclic salt spray exposure

When NaCl-laden moisture infiltrates cement mortar pores, chloride ions may chemically bind to hydration products due to their adsorptive capacity—a distinct state from crystalline salt deposits. Specimens were fully dried and pulverized prior to chloride quantification, resulting in measurements encompassing both adsorbed ions and crystalline salt-derived chlorides. The primary objective is determining total salt deposition under cyclic salt spray exposure to analyze its impact on pore structure and hygric properties; thus, no distinction was made between these states. However, microstructural characterization remains necessary to differentiate crystalline NaCl from chemically bound chlorides within the material.

5.4.2 Sorption isotherms and influence factors

1) Specimen appearance changes

Following hygroscopic equilibrium attainment in humidity-controlled containers (Fig. 5-11R), cement mortar specimens exhibited humidity-dependent surface transformations across 33-93% RH environments (Figs. 5-11a-d). All specimens maintained dry surfaces at ≤75% RH. However, distinct liquid water films formed exclusively on salt-deposited specimens above this threshold: Group 3D1-1 to 3D3-5 at 84% RH and Group 3E1-1 to 3E3-5 at 93% RH. Crucially, salt-free reference specimens (3O1-4/5, 3O2-4/5, 3O3-4/5) retained dry surfaces under identical high-humidity conditions. This demonstrates that salt crystallization induces surface wetting in cement mortar specifically above 75% RH, indicating humidity-dependent modification of hygroscopic behavior that requires further mechanistic investigation.

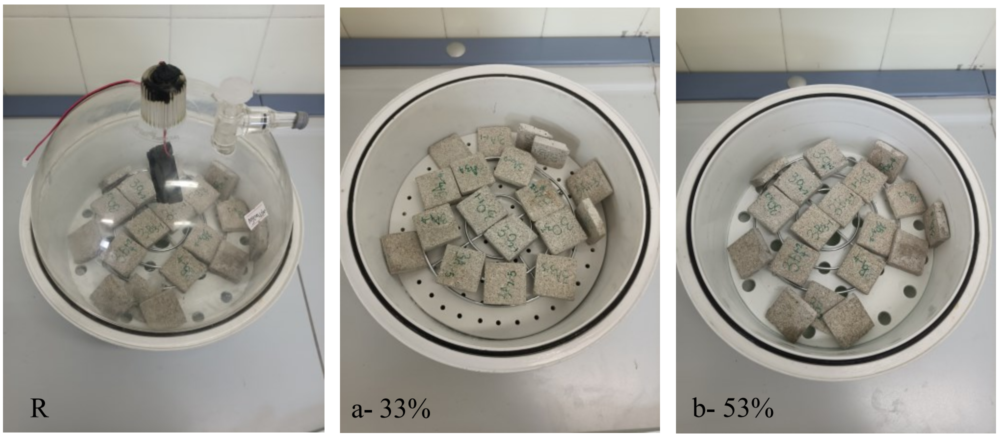

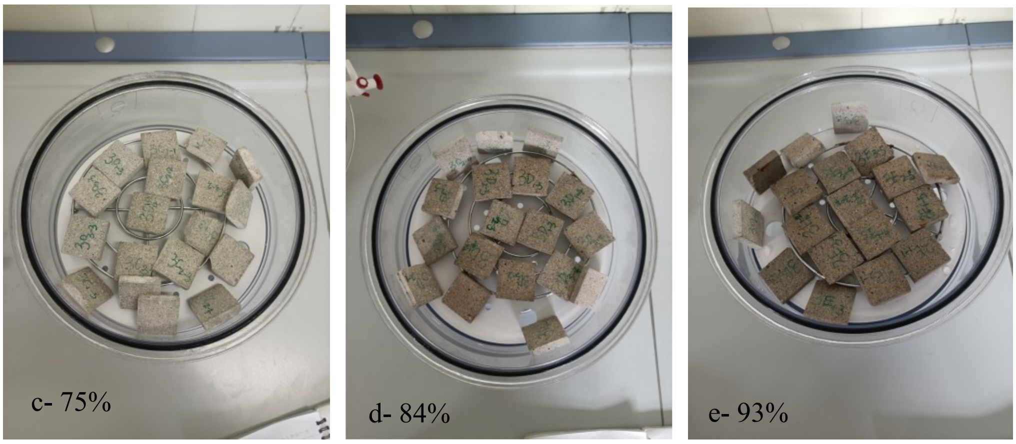

Fig. 5-11 Morphological State of Cement Mortar Specimens at Hygroscopic Equilibrium Under 33–93% RH

2) Sorption Isotherms and Influencing Factors

Fig. 5-12 presents equilibrium moisture content (EMC) of specimens subjected to 7-35 salt spray cycles versus reference groups across humidity levels. Salt-contaminated specimens consistently exhibited higher EMC than salt-free references throughout 33-93% RH, with EMC increasing proportionally to cycle count. This demonstrates that NaCl deposition enhances moisture retention capacity. As Fig. 5-13 illustrates, EMC augmentation was moderate at low humidity (33-55% RH) but increased progressively toward higher humidity, with particularly pronounced enhancement at 85-95% RH - indicating humidity-dependent salt crystallization effects.

Below 75% RH, all isotherms showed gentle slopes with modest EMC increases. Above this threshold, curves exhibited sharp inflection where EMC surged dramatically. Critically, salt-contaminated specimens demonstrated significantly greater EMC increments than references, proportional to deposition density. This suggests NaCl's deliquescence behavior (75% RH at 20°C [106]) governs moisture response: below 75% RH, NaCl remains crystalline; above it, hygroscopic dissolution occurs. The resulting EMC amplification becomes especially pronounced >85% RH (Fig. 5-12).

These findings align with Professor Feng's observations of steep EMC rises >85% RH in aerated concrete, calcium silicate boards, and ceramics [191]. Our cement mortar references similarly exhibited abrupt EMC increases at 85% RH, confirming that minor humidity fluctuations in damp environments trigger substantial moisture uptake in porous materials - an effect amplified by salt deposition. Measurement uncertainties (SD magnitude lower than EMC values) were negligible.

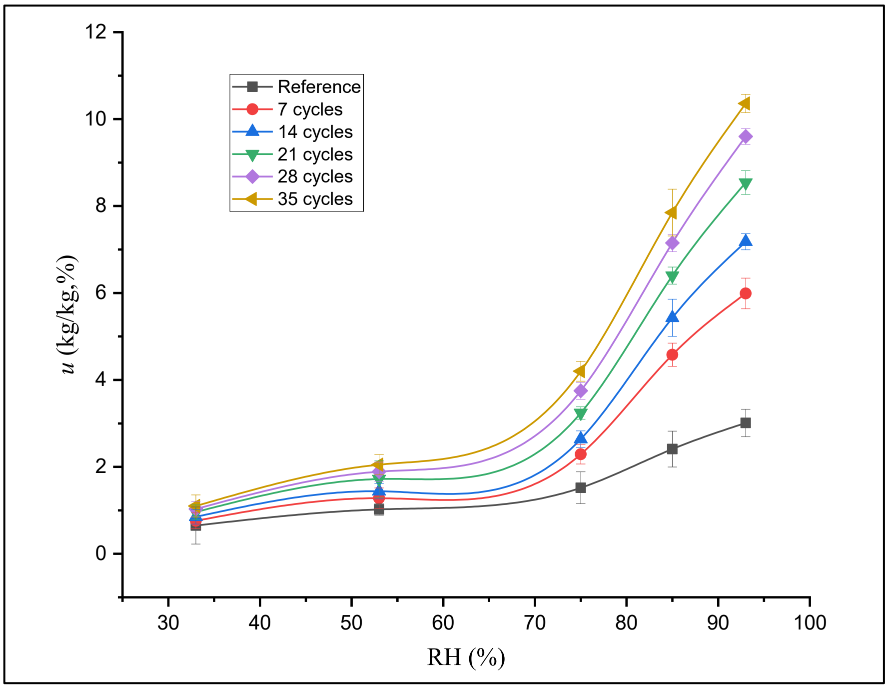

Fig. 5-12 Sorption isotherms of cement mortar specimens under varying salt spray cycles

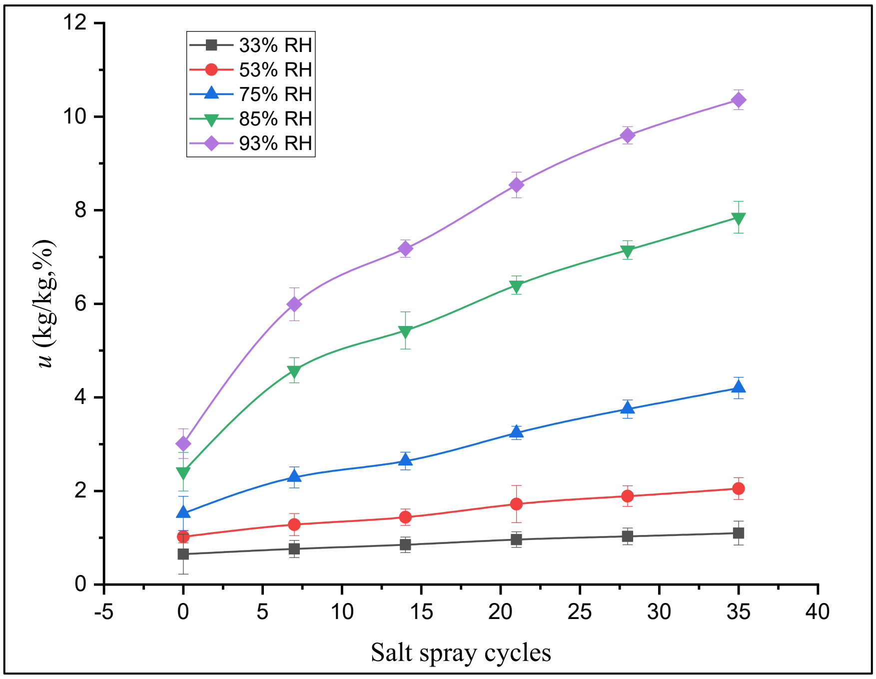

Fig. 5-13 Variation of equilibrium moisture content with salt spray cycles at discrete humidity level

To further analyze the influence of salt content (C, kg/kg dry basis) and ambient humidity on equilibrium moisture content (φ, %), two influence factors were quantified: Humidity influence factor $\eta_{u(\varphi)}$ was calculated using 32% RH as the reference (Fig. 5-14). Salt content influence factor $\eta_{u(C)}$ was derived relative to salt-free reference specimens (Fig. 5-15).

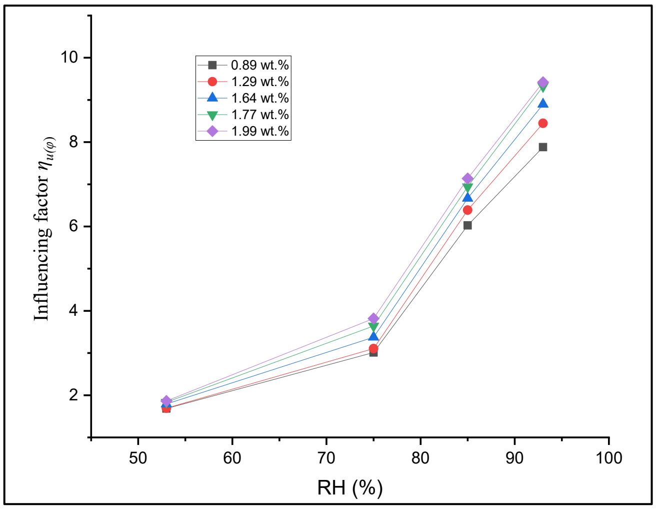

Fig. 5-14 Influence factor of air humidity on equilibrium moisture content across salt spray cycles

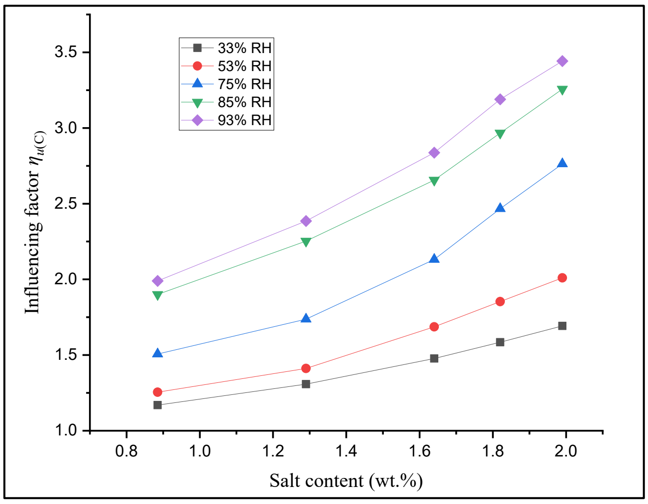

Fig. 5-15 Influence factor of salt content on equilibrium moisture content across humidity levels

As evidenced in Fig. 5-14, the humidity influence factor $\eta_{\mathrm{u}(\varphi)}$ exhibits consistent enhancement with increasing relative humidity across all salt spray exposure groups, demonstrating marginal elevation corresponding to extended cycling durations. Crucially, all $\eta_{\mathrm{u}(\varphi)}$ profiles display a distinct inflection at 75% RH, demarcating initial gradual ascent from subsequent rapid acceleration. This behavioral shift is mechanistically attributed to NaCl deliquescence phenomena - crystalline NaCl initiates vapor sorption above its 75% RH deliquescence threshold at 23°C [107], progressively transitioning into saturated solution through continuous moisture absorption. Below this critical humidity, NaCl maintains crystalline stability while solutions undergo dehydration until crystal precipitation occurs [90, 227].

Fig. 5-15 reveals progressive but moderate increases in salt content influence factor $\eta_{\mathrm{u(C)}}$ across humidity gradients. Comparative analysis demonstrates $\eta_{\mathrm{u(C)}}$ manifests substantially lower absolute values and reduced sensitivity to independent variables relative to $\eta_{u(\varphi)}$: quantitative evaluation shows $\eta_{u(\varphi)}$ for 35-cycle specimens escalates from 1.86 (53% RH) to 9.42 (93% RH; Δ=7.56), whereas $\eta_{u(C)}$ at 95% RH increases merely from 1.99 (7 cycles) to 3.44 (35 cycles; Δ=1.45). This establishes ambient humidity as the principal governing factor for moisture equilibrium in porous matrices, with salt deposition (0.885-1.99 wt%) exerting secondary influence due to its comparatively limited concentration range.

Salt deposition significantly elevates equilibrium moisture content (u_t), particularly above the 75% RH threshold, inducing critical pore structure transformations: increased water volume concurrently reduces air-filled porosity. This microstructural alteration directly enhances thermal conductivity while degrading insulation capacity, ultimately elevating building HVAC energy demands. Such compounded effects present substantial operational challenges for coastal structures in high-humidity environments, where synergistic salt-humidity interactions exacerbate energy consumption penalties during both heating and cooling seasons.

5.4.3 Segmented curve theory and fitting equations

1) Factor modification method

The equilibrium moisture content (EMC) of cement mortar exhibits distinct phase-transition behavior: it increases progressively with salt content but demonstrates a pronounced inflection point at 75% RH (Figs. 5-12, 5-14). This critical humidity corresponds to NaCl deliquescence onset, where salt-driven moisture sorption mechanisms fundamentally diverge below and above this threshold. Consequently, the influence factor η_u is defined as a piecewise function of ambient humidity:

$$\eta_u = \begin{cases} (a_1 C \times 10^2 + a_2)(a_3\varphi + a_4) & \varphi \leq 0.75 \\ (a_5 C \times 10^2 + a_6)(a_7\varphi + a_8) & \varphi > 0.75 \end{cases} \tag{5-9}$$

Where φ is the ambient relative humidity (%), C is the salt content (kg/kg), a_1-a_8 are the fitting parameters. Following Bai et al.'s modification approach for salt-contaminated cement mortar [69], η_u adjusts the salt-free EMC expression f(φ):

$$u_t = \eta_u f(\varphi) \tag{5-10}$$

Eight sorption isotherm models (Table 5-4) were fitted to salt-free specimen data. Only five models plus an exponential function yielded valid fits ($R^2 > 0.97$), while Henderson and GAB models failed due to non-convergence (Table 5-6). Beyond R^2, residual sum of squares (RSS) and residual distribution were evaluated. Randomly distributed residuals across all models confirm symmetrical data dispersion about fitted curves. The BET, Peleg, and

Exponential models achieved near-identical maximum R² values, with the Exponential function exhibiting minimal RSS for optimal performance.

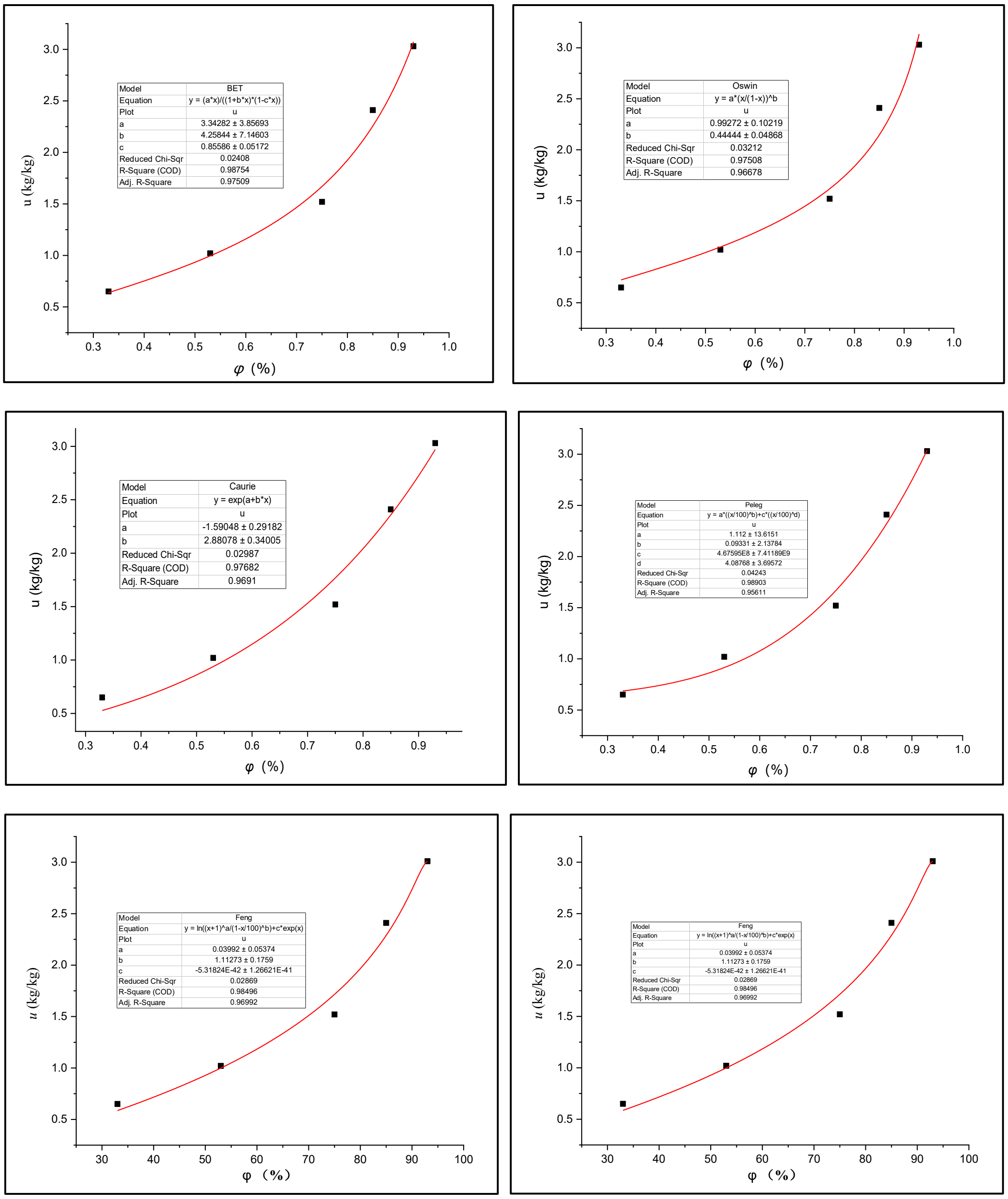

Fig. 5-16 Six Distinct types of sorption isotherm fitting curves for cement mortar

Table 5-6 Fitted parameters of sorption isotherm equations for control cement mortar specimens

Equation	k_1	k_2	k_3	k_4	R^2	RSS	Residual Distribution
Oswin	0.99272	0.44444	/	/	0.975	0.09635	Random

Caurie	-1.5905	2.88078	/	/	0.977	0.08962	Random
BET	3.34282	4.25844	0.85586	/	0.988	0.04817	Random
Peleg	1.112	0.09331	4.67595	4.08768	0.989	0.04243	Random
Feng	0.0399	1.1127	-5.3182		0.985	0.05737	Random
Exponential	0.49834	0.04305	0.04387	/	0.989	0.04102	Random

Based on the parameters determined from the five sorption isotherm models in Table 5-6, five distinct piecewise equations for equilibrium moisture content were derived through Equations (5-9) and (5-10). The functional relationships for the first segment ($\varphi \leq 0.75$) are presented in Table 5-7, while those for the second segment ($\varphi > 0.75$) appear in Table 5-8.

Table 5-7 Factor- modified sorption isotherm equations for salt-contaminated cement mortar (φ ≤75%)

Fitting Equations	Equation Forms	R^2
Modified BET Equation	$u_t = (0.787C \times 10^2 + 92.234)(0.0052\varphi + 0.0054)\frac{3.343\varphi}{(1+4.258\varphi)(1-0.856\varphi)}$	0.974
Modified Oswin Equation	$u_t = (0.158C \times 10^2 + 18.529)(0.04\varphi + 0.0178) \times 0.993\left(\frac{\varphi}{1-\varphi}\right)^{0.444}$	0.974
Modified Caurie Equation	$u_t = (0.163C \times 10^2 + 19.066)(0.002\varphi + 0.0409) \times \exp(-1.59 + 2.881\varphi)$	0.974
Modified Peleg Equation	$u_t = (0.141C \times 10^2 + 16.465)(0.02\varphi + 0.0196)(1.112\varphi^{0.093} + 4.676\varphi^{4.088})$	0.968
Modified Feng Equation	$u_t = (0.071C \times 10^2 + 8.392)(-0.021 + 4.9228) \times \ln\frac{(100\varphi+1)^{0.04}}{(1-\varphi)^{1.113}} - 5.32\exp(100\varphi)$	0.970
Modified Exponential Equation	$u_t = (0.213C \times 10^2 + 25.228)(0.1778\varphi - 0.032)(0.498 + 0.043e^{0.0439\varphi})$	0.951

Table 5-8 Factor--modified sorption isotherm equations for salt-contaminated cement mortar (φ >75%)

Fitting Equations	Equation Forms	R^2
Modified BET Equation	$u_t = (0.812C \times 10^2 + 66.838)(0.0139\varphi + 0.0018)\frac{3.343\varphi}{(1+4.258\varphi)(1-0.856\varphi)}$	0.981
Modified Oswin Equation	$u_t = (0.203C \times 10^2 + 16{,}752)(0.055\varphi + 0.0074) \times 0.993\left(\frac{\varphi}{1-\varphi}\right)^{0.444}$	0.974
Modified Caurie Equation	$u_t = (0.205C \times 10^2 + 16{,}872)(0.06\varphi + 0.0029) \times \exp(-1.59 + 2.881\varphi)$	0.978
Modified Peleg Equation	$u_t = (0.182C \times 10^2 + 14.965)(0.042\varphi + 0.0048)(1.112\varphi^{0.093} + 4.676\varphi^{4.088})$	0.985
Modified Feng Equation	$u_t = (0.131C \times 10^2 + 10.813)(-0.03\varphi + 0.0087) \times \ln\frac{(100\varphi+1)^{0.04}}{(1-\varphi)^{1.113}} - 5.32\exp(100\varphi)$	0.935
Modified Exponential Equation	$u_t = (0.317C \times 10^2 + 26.49)(0.294\varphi - 0.096)(0.498 + 0.043e^{0.0439\varphi})$	0.870

Based on coefficient of determination (R^2) analysis, the BET, Oswin, and Caurie models demonstrated optimal performance for the first segment ($\varphi \leq 0.75$), each achieving $R^2 = 0.974$. The BET function was selected for this segment (Table 5-7) due to its minimal residual sum of squares (RSS) among these candidates. For the second segment ($\varphi > 0.75$), both Peleg and BET models attained the highest R^2 values, with the Peleg function exhibiting superior RSS in Table 5-6. Consequently, the piecewise equation (5-11a) was formulated using: BET function for $\varphi \leq 0.75$ and Peleg function for $\varphi > 0.75$. Complementarily, a fully BET-based piecewise equation (5-11b) was developed following Bai's methodology [69]. All models incorporated experimental salt content values (*C*) ranging 0-2 wt%.

$$u_t = \begin{cases} \left(0.787C \times 10^2 + 92.234\right)(0.0052\varphi + 0.0054)\frac{3.343\varphi}{(1+4.258\varphi)(1-0.856\varphi)} & \varphi \leq 0.75 \\ (0.182C \times 10^2 + 14.965)(0.042\varphi + 0.0048)(1.112\varphi^{0.093} + 4.676\varphi^{4.088}) & \varphi > 0.75 \end{cases} \qquad \text{（5-11a）}$$

$$u_t = \begin{cases} (0.787C \times 10^2 + 92.234)(0.0052\varphi + 0.0054)\frac{3.343\varphi}{(1+4.258\varphi)(1-0.856\varphi)} & \varphi \leq 0.75 \\ (0.812C \times 10^2 + 66.838)(0.0139\varphi + 0.0018)\frac{3.343\varphi}{(1+4.258\varphi)(1-0.856\varphi)} & \varphi > 0.75 \end{cases} \quad （5\text{-}11b）$$

2）Robinson–Stokes equation method

Most salts exhibit solubility not only in liquid water but also through deliquescence below 100% RH. When ambient humidity exceeds the water activity (a_w) of a saturated salt solution, the solution absorbs atmospheric moisture. This critical humidity varies with salt species and temperature. Above this threshold, crystalline salts dissolve into saturated solutions that progressively dilute with increasing humidity. At RH approaching 100%, salt concentrations approach zero [90]. The relationship between solution molality and humidity is governed by the Robinson-Stokes equation [228]:

$$ln\varphi = lna_w = -n\phi \cdot M_w \cdot m \quad (5\text{-}12)$$

Where φ is the relative humidity (%); a_w is the water activity, ν is the number of ionic species (-), ϕ is the osmotic coefficient (-), M_w = molar mass of water (0.018 kg·mol^{-1}), m is the solution molality (mol·kg^{-1}).

For porous materials with salt deposits, the salt content relates to solution concentration through:

$$mu_sM_N = C \quad (5\text{-}13)$$

Where u_s is the moisture content due to salt dissolution (kg·kg^{-1}), M_N is the molar mass of NaCl (0.0585 kg·mol^{-1}), C is the salt content (kg·kg^{-1}).

Adapting He et al.'s methodology for salt-contaminated aerated concrete [226], substitution of Equation (5-12) into (5-13) yields the moisture absorption model:

$$u_s = \frac{kC}{-ln\varphi} \quad (5\text{-}14)$$

This formulation quantifies NaCl moisture absorption in cement mortar above 75% RH. Combined with Table 5-6 parameters for salt-free isotherms, five composite EMC equations were derived (Table 5-9).

Fig. 5-9 Robinson-stokes adjusted sorption isotherm equations for salt-contaminated cement mortar (RH >75%)

Fitting Equations	Equation Forms	R^2
BET-based Equation	$u_t = \frac{3.343\varphi}{(1+4.258\varphi)(1-0.856\varphi)} + \frac{0.00289C \times 10^2}{-ln\varphi}$	0.944

Oswin-based Equation	$\boldsymbol{u_t = 0.993\left(\frac{\varphi}{1-\varphi}\right)^{0.444} + \frac{0.00289C \times 10^2}{-ln\varphi}}$	0.935
Caurie-based Equation	$\boldsymbol{u_t = \exp(-1.59 + 2.881\varphi) + \frac{0.00291C \times 10^2}{-ln\varphi}}$	0.952
Peleg-based Equation	$\boldsymbol{u_t = (1.112\varphi^{0.093} + 4.676\varphi^{4.088}) + \frac{0.00206C \times 10^2}{-ln\varphi}}$	0.933
Exponential-based Equation	$\boldsymbol{u_t = (0.498 + 0.043e^{0.0439\varphi}) + \frac{0.00419C\times10^2}{-ln\varphi}}$	0.853

Based on fitting results, the Caurie model demonstrated optimal performance in the RH >75% range (R^2 = 0.952). Consequently, the segmented equation (5-15) for salt-contaminated cement mortar was established using: Caurie function for $\varphi > 0.75$ and Influence factor modification method (Eqs. 5-10/5-11) for $\varphi \leq 0.75$.

$$u_t = \begin{cases} (0.787C \times 10^2 + 92.234)(0.0052\varphi + 0.0054)\frac{3.343\varphi}{(1+4.258\varphi)(1-0.856\varphi)} & \varphi \leq 0.75 \\ \exp(-1.59 + 2.881\varphi) + \frac{0.00291C\times10^2}{-ln\varphi} & \varphi > 0.75 \end{cases} \tag{5-15}$$

3）Nielsen formula method

Given the hygroscopicity of salt crystals in saline porous building materials, the moisture uptake of salt crystals in air above their deliquescence relative humidity (DRH) can be calculated using the Nielsen formula (Eq. 5-16) [227]. The total equilibrium moisture content (u_t) combines matrix (u_m) and salt contributions (u_s).

$$u_s = \frac{c}{c_s} \times \frac{1-\varphi_s}{1-\varphi} \tag{5-16}$$

$$u_t = u_m + u_s = f(\varphi) + \frac{c}{C_s} \times \frac{1-\varphi_s}{1-\varphi} \tag{5-17}$$

Where u_s [kg/kg] the salt-derived hygroscopic moisture content, C [%] the material salt content, C_s [kg/kg] the solubility of saturated salt solution, φ [%] the ambient relative humidity and φ_s [%] the relative humidity above the saturated salt solution.

For NaCl at 23°C, C_s = 0.36 kg/kg and φ_s = 0.75 [107]. Substituting these values and integrating parameters from salt-free models (Table 5-6), five distinct equations for u_t at RH > 75% were derived (Table 5-10).

Table 5-10 Nielsen- Adjusted Sorption Isotherm Equations for Salt-Contaminated Cement Mortar (RH >75%)

Fitting Equations	**Equation Forms**	R^2

BET-based Equation	$u_t = \dfrac{3.343\varphi}{(1+4.258\varphi)(1-0.856\varphi)} + \dfrac{0.00394C\times10^2}{0.359}\times\dfrac{1-0.75}{1-\varphi}$	0.949
Oswin-based Equation	$u_t = 0.993\left(\dfrac{\varphi}{1-\varphi}\right)^{0.444} + \dfrac{0.00394C\times10^2}{0.359}\times\dfrac{1-0.75}{1-\varphi}$	0.939
Caurie-based Equation	$u_t = \exp(-1.59+2.881\varphi) + \dfrac{0.00397C\times10^2}{0.359}\times\dfrac{1-0.75}{1-\varphi}$	0.957
Peleg-based Equation	$u_t = (1.112\varphi^{0.093}+4.676\varphi^{4.088}) + \dfrac{0.00279C\times10^2}{0.359}\times\dfrac{1-0.75}{1-\varphi}$	0.930
Exponential-based Equation	$u_t = (0.498+0.043e^{0.0439\varphi}) + \frac{0.00571C\times10^2}{0.359}\times\frac{1-0.75}{1-\varphi}$	0.866

According to the fitting results, the equilibrium moisture content under RH ≤ 0.75 was modeled using the BET equation from Table 5, while the Caurie model from Table 8 governed the high-humidity regime (RH > 0.75). This yielded the segmented sorption isotherm equation (5-18) for salt-deposited cement mortar.

$$u_c = \begin{cases} (0.787C\times10^2+92.234)(0.0052\varphi+0.0054)\frac{3.343\varphi}{(1+4.258\varphi)(1-0.856\varphi)} & \varphi\le 0.75 \\ \exp(-1.59+2.881\varphi)+\frac{0.00397C\times10^2}{0.359}\times\frac{1-0.75}{1-\varphi} & \varphi > 0.75 \end{cases} \qquad (5-18)$$

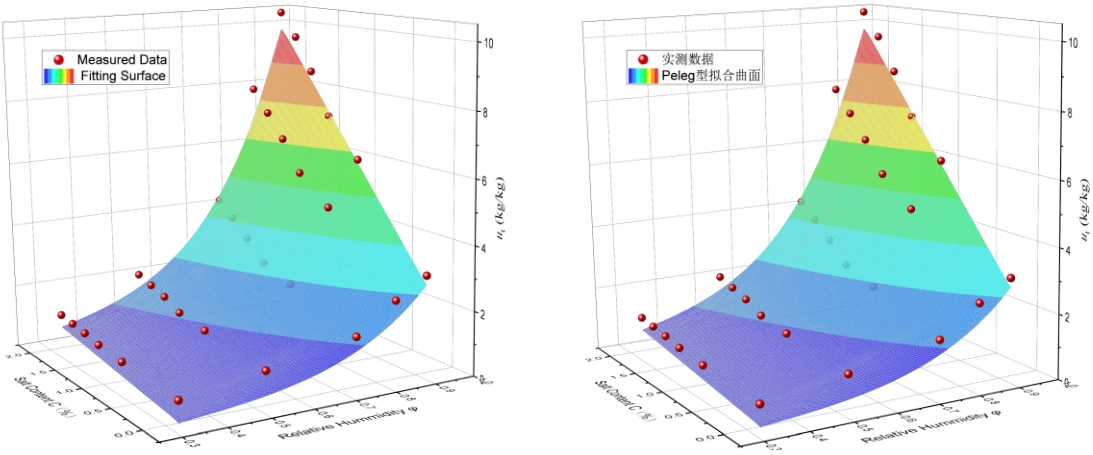

a）Equation 5-11a（R^2 =0.985)　　b）Equation 5-11b (R^2 =0.981)

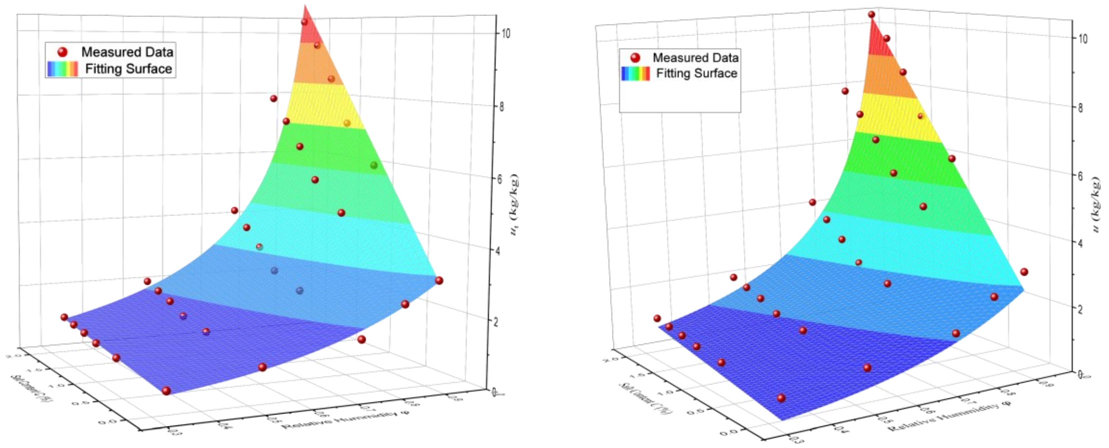

c) Equation 5-15 (R^2 =0.952) **d) Equation 5-18(R^2 =0.957)**

Fig. 5-17 Sorption isothermal fitted surfaces and experimental data of cement mortar under salt spray deposition

Three distinct formulations for predicting equilibrium moisture content in salt-contaminated cement mortar were developed based on isothermal sorption characteristics under varying salt deposition levels (Figs. 5-12, 5-13), accounting for interactive effects between salt content and ambient humidity. These include the influence factor-based formulations (5-11a/b), Robinson-Stokes equation-derived function (5-15), and Nielsen formula-based function (5-18). Given NaCl's deliquescence at 75% RH (23°C), all models adopt piecewise structures reflecting fundamentally different moisture sorption mechanisms below and above this critical threshold, consistent with the characteristic inflection observed at 75% RH in experimental sorption curves [90, 107].

Formulations 5-11a/b employ modified BET functions for the first segment (≤75% RH) and Peleg/BET modifications for the second segment (>75% RH), selected for optimal coefficient of determination. While effectively capturing the combined influence of salt content and humidity through empirical modifications, these lack explicit mechanistic foundations. In contrast, formulations 5-15 and 5-18 maintain modified BET functions for the initial segment but implement mechanistic superposition for the second segment: combining matrix moisture absorption (u) with salt-derived moisture (u_s). The Robinson-Stokes approach (5-15) models solution concentration-humidity relationships, whereas the Nielsen method (5-18) provides a more direct expression of salt hygroscopicity, reducing parametric dependencies.

Compared to Bai et al.'s immersion-based BET model [69], the present piecewise formulations significantly improve humidity response accuracy through deliberate incorporation of the 75% RH deliquescence threshold. Relative to He et al.'s segmented approach for aerated concrete [226], the influence factor modification in Segment 1 achieves superior goodness-of-fit, while the Nielsen formulation in Function 5-18 establishes a more physically transparent relationship between salt’s moisture uptake and humidity with fewer computational parameters. This represents a methodological progression toward mechanism-driven predictions.

Accurate isothermal sorption curves are essential for building energy simulations, particularly in coastal regions where aerosol-deposited salts alter porous materials' hygric behavior through pore structure modification and deliquescence-driven moisture uptake. The proposed models enable efficient EMC prediction across humidity gradients based solely on salt content measurements - circumventing the protracted experimental determination required for dense materials at high RH. Unlike prior models derived from immersion studies [69, 226], these formulations specifically address salt deposition via atmospheric exposure. While complete desorption isotherms could not be obtained due to salt dissolution effects in saturated specimens, the sorption experiments successfully quantified salt deposition impacts, fulfilling the study's primary objective of establishing predictive frameworks for salt-laden building materials in marine environments.

5.5 Water vapor permeability coefficient and modified equations

5.5.1Water vapor permeability coefficient measured by dry/wet cup method

Dry cup (0%/50% RH) and wet cup (50%/98% RH) measurements of cement mortar specimens (Figs. 5-18-19) revealed distinct linear mass trends: dry cup assemblies exhibited progressive mass gain due to vapor absorption by silica gel desiccant, while wet cup assemblies showed consistent mass loss due to vapor dissipation from saturated K_2SO_4 solution chambers through specimens into the lower-humidity environment. Minor initial mass variations among reference specimens and salt-sprayed samples (7-35 cycles) resulted from inherent material heterogeneity and thickness tolerances (±0.3 mm) during specimen preparation, yet these variations do not compromise experimental validity as the analysis focuses exclusively on mass change rates. Measurement uncertainties (0.01%-0.03%), attributable primarily to heterogeneous pore structures and salt crystal distribution, remained negligible relative to vapor transmission magnitudes.

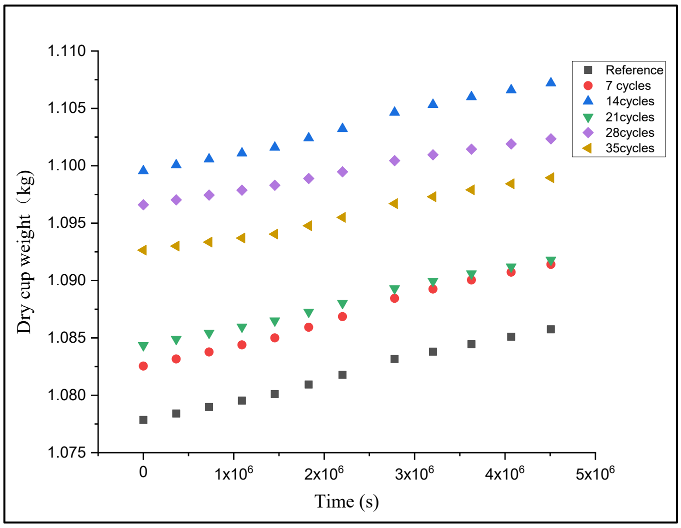

Fig. 5-18 Mass of dry cup assemblies at various times during water vapor transmission test

Linear fitting determined the water vapor flux rates G_v (derived from mass change rates in Figs. 5-18 and 5-19) as summarized in Tables 5-11 and 5-12. For dry cup assemblies, all linear fits achieved coefficients of determination $R^2 > 0.98$ with residual sum of squares (RSS) < 6.00332×10^{-7}. The reference specimens exhibited the highest G_v, with values decreasing progressively with increasing salt spray cycles (Table 5-11). Wet cup assemblies demonstrated $R^2 > 0.99$ and RSS < 5.88554×10^{-5}, where reference specimens showed the lowest G_v values, increasing sequentially with salt spray exposure (Table 5-12).

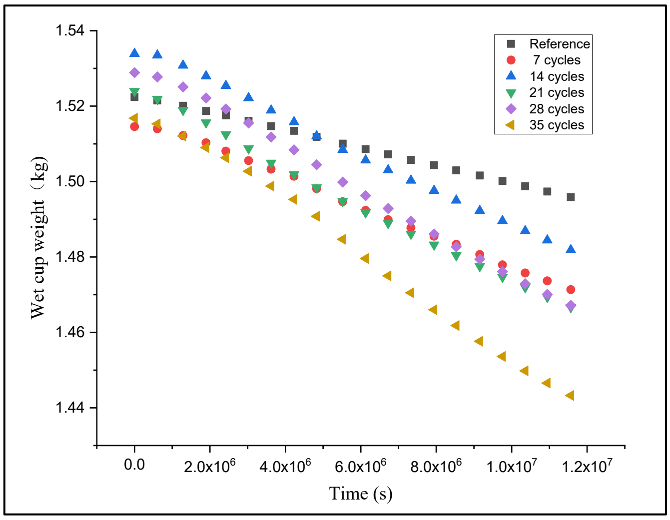

Fig. 5-19 Mass of wet cup assemblies at various times during water vapor transmission test

Table 5-11 Linear fitting results of water vapour flow rate (G_v) for cement mortar under salt spray deposition (dry cup method, 0–50% RH)

Salt Spray Cycling	Dry Cup Assembly	G_v (kg/s)	R^2	RSS
Reference	$5O_1 \sim 5O_4$	2.06783×10^{-9}	0.990	6.00332×10^{-7}
7 Cycles	$5A_1 \sim 5A_4$	1.82618×10^{-9}	0.992	3.49465×10^{-7}

14 Cycles	$5B_1 \sim 5B_4$	1.79315×10^{-9}	0.988	5.3501×10^{-7}
21Cycles	$5C_1 \sim 5C_4$	1.72146×10^{-9}	0.993	2.75475×10^{-7}
28 Cycles	$5D_1 \sim 5D_4$	1.49543×10^{-9}	0.981	5.83101×10^{-7}
35 Cycles	$5D_1 \sim 5D_4$	1.32698×10^{-9}	0.993	1.55235×10^{-7}

Table 5-12 Linear fitting results of water vapour flow rate (G_v) for cement mortar under salt spray deposition(wet cup method, 50–98% RH)

Salt Spray Cycling	Wet Cup Assembly	G_v (kg/s)	R^2	RSS
Reference	$5O_1 \sim 5O_4$	-2.34299×10^{-9}	0.999	6.85676×10^{-7}
7 Cycles	$5A_1 \sim 5A_4$	-3.94800×10^{-9}	0.997	1.04771×10^{-5}
14 Cycles	$5B_1 \sim 5B_4$	-4.75102×10^{-9}	0.997	1.42988×10^{-5}
21Cycles	$5C_1 \sim 5C_4$	-5.09070×10^{-9}	0.998	1.47054×10^{-5}
28 Cycles	$5D_1 \sim 5D_4$	-5.66033×10^{-9}	0.998	1.75064×10^{-5}
35 Cycles	$5D_1 \sim 5D_4$	-6.83262×10^{-9}	0.995	5.88554×10^{-5}

Water vapor permeability coefficients (δ_v) and associated process parameters were calculated for all cement mortar specimen groups using Equations 5-3 to 5-8 (Tables 5-13 and 5-14). Consistent specimen length and width dimensions, guaranteed by mold-controlled fabrication with near-zero dimensional error, ensured uniform exposed surface area A for vapor flux density (g_v) computations. To address thickness variations (±0.15 mm) from cutting operations, the thickness parameter H incorporated the mean of six vernier caliper measurements taken at distinct positions per specimen, thereby mitigating preparation-induced uncertainties while maintaining experimental rigor.

Under dry cup conditions (Table 5-13), reference specimens exhibited maximum permeability (5.95×10^{-12} kg/(m·s·Pa)), with δ_v decreasing progressively to 4.09×10^{-12} kg/(m·s·Pa) after 35 salt spray cycles. Conversely, wet cup measurements (Table 5-14) revealed higher baseline permeability in references (8.25×10^{-12}kg/(m·s·Pa)) that increased incrementally to 2.80×10^{-11} kg/(m·s·Pa) following equivalent cycling. This demonstrates salt deposition's dichotomous impact: it reduces vapor permeability in low-humidity environments (0-50% RH) while enhancing it under high-humidity conditions (50-98% RH), attributable to humidity-driven phase transitions of NaCl deposits within pore networks.

Table 5-13 Water vapour permeability (δ_v) and process parameters of cement mortar under salt spray deposition (dry cup method, 0–50% RH)

Salt Spray Cycling	**G_v (kg/s)**	**g_v [kg/(m².s)]**	**Δp_v (Pa)**	**R_{total} (m²·s·Pa/kg)**	**R_{air} (m²·s·Pa/kg)**	**R_{sample} (m²·s·Pa/kg)**	**δ_v [kg/(m·s·Pa)]**
Reference	2.07×10^{-9}	4.22×10^{-7}	1404	3.33×10^{-9}	1×10^{8}	3.23×10^{9}	5.95×10^{-12}

7 Cycles	1.83×10^{-9}	3.73×10^{-7}	1404	3.77×10^{-9}	1×10^{8}	3.67×10^{9}	5.78×10^{-12}
14 Cycles	1.79×10^{-9}	3.66×10^{-7}	1404	3.84×10^{-9}	1×10^{8}	3.74×10^{9}	5.66×10^{-12}
21Cycles	1.72×10^{-9}	3.51×10^{-7}	1404	4.00×10^{-9}	1×10^{8}	3.90×10^{9}	5.17×10^{-12}
28 Cycles	1.50×10^{-9}	3.05×10^{-7}	1404	4.60×10^{-9}	1×10^{8}	4.50×10^{9}	4.54×10^{-12}
35 Cycles	1.33×10^{-9}	2.71×10^{-7}	1404	5.18×10^{-9}	1×10^{8}	5.08×10^{9}	4.09×10^{-12}

Table 5-14 Water vapour permeability coefficient (δ_v) and process parameters of cement mortar under salt spray deposition (wet cup method, 50–98% RH)

Salt Spray Cycling	G_v (kg/s)	g_v [kg/(m^2·s)]	Δp_v (Pa)	R_{total} (m^2·s·Pa/kg)	R_{air} (m^2·s·Pa/kg)	R_{sample} (m^2·s·Pa/kg)	δ_v [kg/(m·s·Pa)]
Reference	-2.34×10^{-9}	4.78×10^{-7}	1347.84	2.82×10^{-9}	2.5×10^{8}	2.57×10^{9}	8.25×10^{-12}
7 Cycles	-3.95×10^{-9}	8.06×10^{-7}	1347.84	1.67×10^{-9}	2.5×10^{8}	1.42×10^{9}	1.340×10^{-11}
14 Cycles	-4.75×10^{-9}	9.70×10^{-7}	1347.84	1.39×10^{-9}	2.5×10^{8}	1.14×10^{9}	1.88×10^{-11}
21Cycles	-5.28×10^{-9}	1.08×10^{-6}	1347.84	1.25×10^{-9}	2.5×10^{8}	1.00×10^{9}	2.10×10^{-11}
28 Cycles	-5.66×10^{-9}	1.16×10^{-6}	1347.84	1.17×10^{-9}	2.5×10^{8}	9.17×10^{8}	2.38×10^{-11}
35 Cycles	-6.83×10^{-9}	1.39×10^{-6}	1347.84	9.67×10^{-9}	2.5×10^{8}	7.17×10^{8}	2.80×10^{-11}

Xie et al. [210] documented cement mortar vapor permeability coefficients (δ_v) within the range of 2.66×10^{-12} to 4.02×10^{-12} kg/(m·s·Pa) at 43-97.6% RH, registering marginally lower values than our measurements—a divergence attributable to differences in cement composition and mix proportions. Crucially, their results demonstrate salt's humidity-dependent influence: inhibiting vapor transport under low-humidity/high-salinity conditions while enhancing permeability at elevated humidity and salt concentrations, corroborating our experimental trends (Tables 5-13, 5-14; Fig. 5-20).

The humidity-mediated permeability response originates fundamentally from NaCl's deliquescent properties. Below the 75% RH threshold at 23°C [107], crystalline salts reduce porosity and obstruct pore connectivity [10, 45, 67, 86, 91], causing progressive δ_v reduction as salt deposition increases. Conversely, above 75% RH, dissolved NaCl migrates via capillary-driven penetration [59, 67, 81, 93], while at the wet cup's 50% RH interface, vapor release induces recrystallization [90, 227]. This liquid-phase transport significantly elevates δ_v, with salt's intrinsic hygroscopicity (Eqs. 5-14, 5-16) [227, 228] further amplifying moisture migration at higher concentrations through intensified dissolution-recrystallization cycling within pore networks.

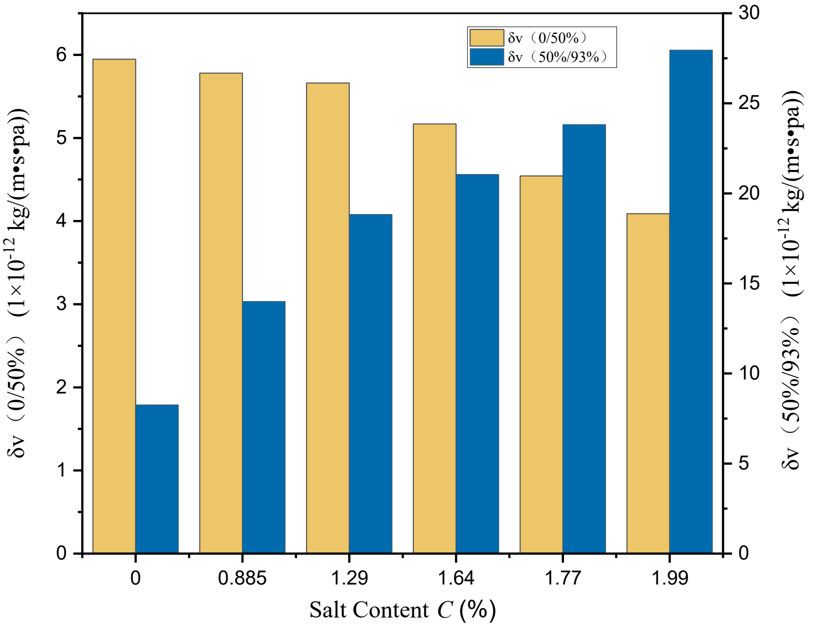

Fig. 5-20 Water vapor permeability of cement mortar under varying salt contents

The impact of salt deposition on the vapor permeability coefficient (δ_v) of cement mortar is dual in nature: when ambient humidity is below 75%, δ_v decreases with increasing salt content; whereas above 75% humidity, δ_v increases with higher salt concentration. Elevated vapor permeability not only intensifies moisture transfer through building envelopes but also indirectly enhances heat transfer across these structures. Consequently, building thermal loads increase and energy consumption rises. Thus, salt deposition proves particularly detrimental to buildings in high-temperature, high-humidity coastal regions.

5.5.2 Salt influence factors and modified equations

To further analyze and quantify the influence of salt content on the water vapor permeability coefficient (δ_v) of cement mortar under salt spray conditions, the correction factor η_{δ_v} was calculated for both dry-cup ($\varphi \leq$ 0.75) and wet-cup ($\varphi >$ 0.75) methods using Equation (5-19). This calculation integrates the mechanistic analysis of NaCl crystallization (below 75% RH) and deliquescence (above 75% RH) on vapor transport properties. Polynomial regression models were established to express η_{δ_v} as a function of salt content for sub-critical ($\varphi \leq 0.75$) and super-critical ($\varphi > 0.75$) humidity regimes, yielding coefficients of determination (R^2) exceeding 0.96 and 0.95, respectively (as illustrated in Fig. 5-2 a and b). This dual-phase model aligns with the crystallographic and hygroscopic transitions of NaCl, validating its role in modulating vapor transport across humidity gradients.

$$\eta_{\delta_v} = \frac{\delta_{v,s}}{\delta_{v,r}} \tag{5- 19}$$

where $\delta_{\mathrm{v,s}}$ denotes the water vapor permeability coefficient of salt-containing specimens kg/(m·s·Pa), and $\delta_{\mathrm{v,r}}$ represents the water vapor permeability coefficient of salt-free reference specimens kg/(m·s·Pa).

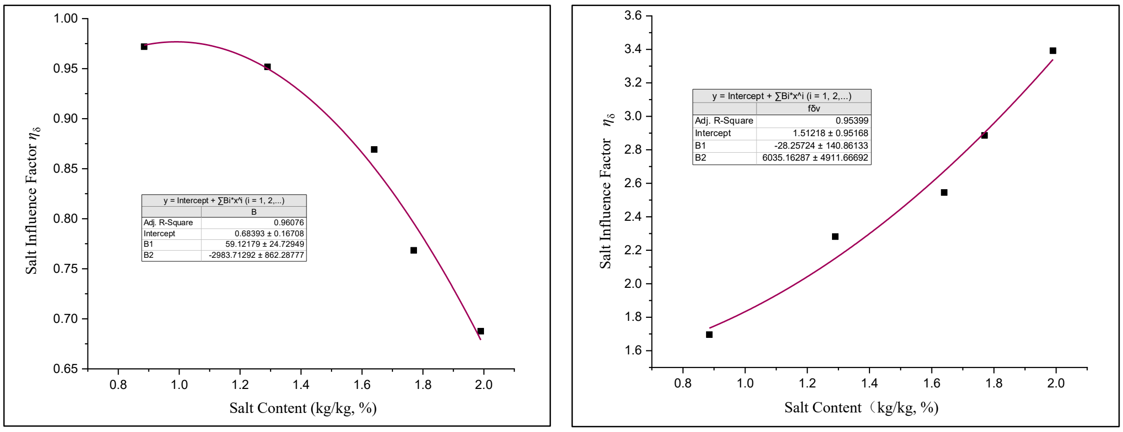

a) $\varphi_1 \leq 0.75$ **b) $\varphi_1 > 0.75$**

Fig. 5-21 Influence factor (η_{δ_v})for water vapor permeability of cement mortar as a function of salt content

The water vapor permeability coefficient for salt-free porous materials ($\delta_{v,r}$) was derived from Equations (5-3) – (5-8) and expressed in Equation (5-20), where all symbols and units align with those defined in Section 2.3. To account for salt deposition effects, $\delta_{v,r}$ was adjusted using the polynomial fit for the influence factor η_{δ_v} (Fig. 5-21), yielding the modified permeability coefficient $\delta_{v,s}$ for NaCl-containing cement mortar in Equation (5-21):

$$\delta_{v,r} = \frac{H}{\frac{p_{v,sat} \cdot A \cdot |\varphi_1 - \varphi_2|}{G_v} - \frac{d_{air}}{\delta_{v,air}}} \tag{5-20}$$

$$\delta_{v,s} = \begin{cases} (-2983.71C^2 + 59.12C + 0.68)\dfrac{H}{\frac{p_{v,sat} \cdot A \cdot |\varphi_1 - \varphi_2|}{G_v} - \frac{d_{air}}{\delta_{v,air}}} & \varphi_1 \leq 0.75 \qquad R^2 = 0.96 \\ (6035.16C^2 - 28.26C + 1.51)\dfrac{H}{\frac{p_{v,sat} \cdot A \cdot |\varphi_1 - \varphi_2|}{G_v} - \frac{d_{air}}{\delta_{v,air}}} & \varphi_1 > 0.75 \qquad R^2 = 0.95 \end{cases} \tag{5-21}$$

The water vapor permeability coefficient (δ_v) is a critical parameter for evaluating hygrothermal transfer in building envelopes and calculating energy consumption. Accurate determination of δ_v for salt-laden porous building materials under coastal salt spray conditions holds significant practical importance. Traditional testing of δ_v across diverse materials is labor-intensive and time-consuming. However, the correction factor method (Equation 5-21) enables efficient adjustment of pre-measured δ_v values for varying salt contents, eliminating the need for extensive repetitive testing.

Cement mortar, a widely used porous material in building envelopes, exhibits no chemical reactivity with NaCl [67, 81, 229]. Its salt-moisture transport and physical alterations are predominantly governed by pore structure characteristics. Consequently, this study's findings offer valuable insights for other porous construction materials, including artificial masonry blocks and natural stones. Current research is limited to NaCl, the predominant salt in seawater; the effects of other seawater salts (e.g., $MgCl_2$, $CaSO_4$) and compound salts on δ_v remain unexplored and warrant future investigation to enhance predictive models for coastal building energy performance.

5. 6 Pore structure and micro-morphology analysis

5.6.1 MIP pore structure analysis

To investigate the microstructural evolution of cement mortar under salt spray exposure, pore size distributions of specimens subjected to 7–35 salt spray cycles were systematically compared with reference specimens (Figs. 5-22 a–e). The dominant pore volume peak in cement mortar was observed at 0.1 μm. Under cyclic salt spray conditions, pore volumes within the 0.02–0.12 μm range exhibited a progressive decline with increasing cycles, accompanied by a distinct rightward shift in the pore volume peak. This observation demonstrates that NaCl crystallization preferentially occupies smaller pores (<0.1 μm), corroborating prior studies on NaCl deposition patterns in cement mortar (0.01–0.08 μm) [13] and limestone (0.01–0.12 μm) [11]. Given that gas diffusion primarily occurs in pores > 10^{-3} μm [202], the accumulation of salt crystals progressively impedes vapor transport in dry-cup tests, resulting in a systematic reduction of permeability coefficients (Table 5-13, Fig. 5-20). In contrast, wet-cup testing revealed a counteractive mechanism: deliquescence of salt crystals under high humidity alleviated pore blockage, while concurrent brine-vapor migration through interconnected pores enhanced moisture transport efficiency, leading to increased water vapor permeability coefficients (Table 5-14, Fig. 5-20). This humidity-dependent duality highlights NaCl's dual role — pore occlusion via crystallization under low humidity (dry-cup) versus transport enhancement via deliquescence under high humidity (wet-cup).

For comparative analysis with immersion-based methodologies [69, 210], specimens immersed in 2.39 wt% NaCl solution (simulating seawater salinity) for 48 h were analyzed (Fig. 5-22f). Immersion-induced pore volume reduction in the 0.02–0.12 μm range mirrored that of 7-cycle salt spray specimens (Fig. 5-22a), suggesting analogous pore-filling mechanisms between salt spray deposition and solution immersion. This equivalence persists despite divergent salt delivery pathways (surface deposition vs. bulk infiltration), reinforcing the universality of NaCl-induced pore modification in porous matrices.

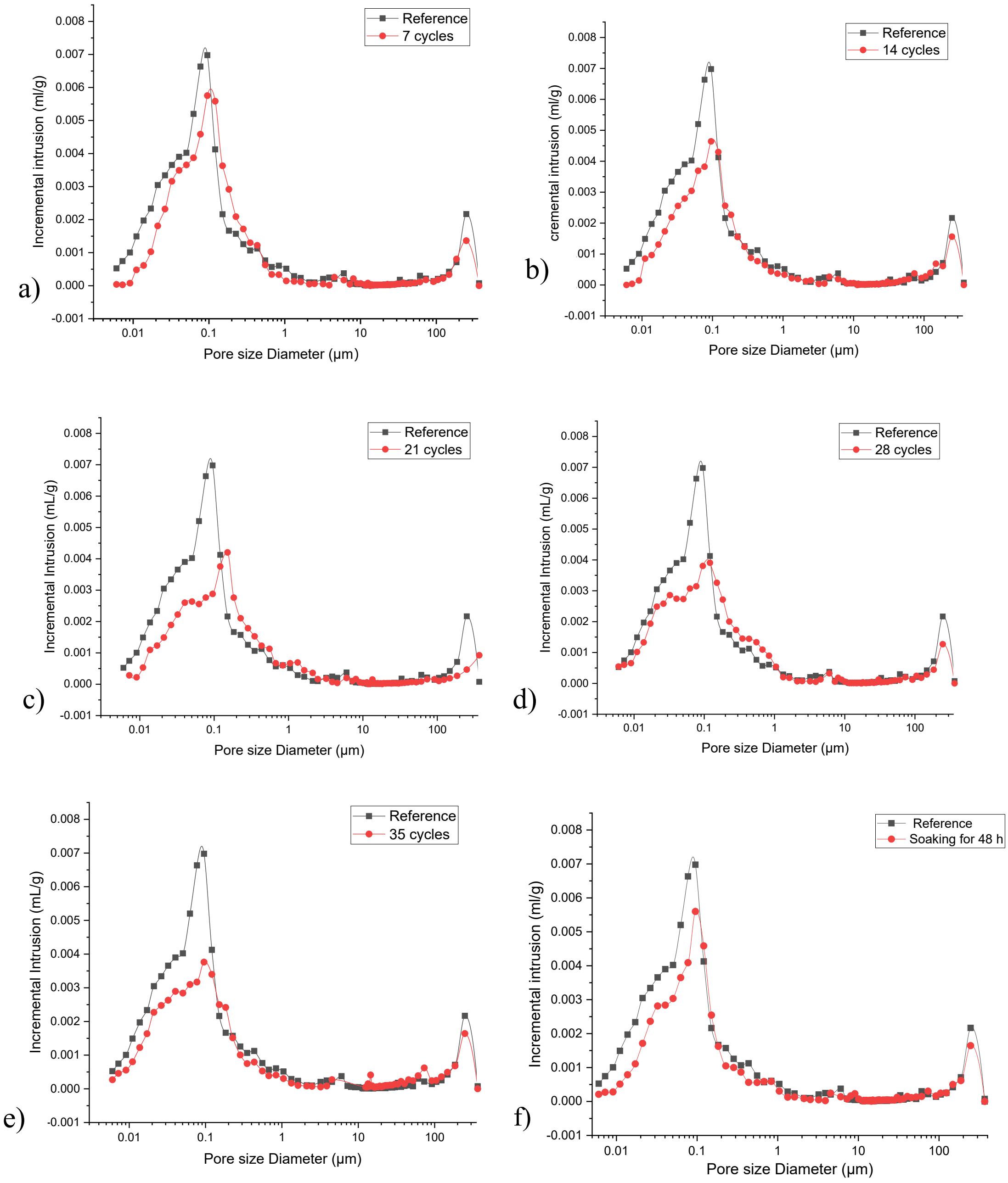

Fig. 5-22 Pore Size Distribution of Cement Mortar under NaCl Deposition

(a– e: 7–35 Salt Spray Cycles; f: 48 h Salt Solution Immersion)

Specific surface area refers to the total surface area per unit mass of a material. For porous materials, it encompasses both external and internal specific surface areas, with its magnitude dependent on pore morphology and surface characteristics. Specific surface area and pore volume distribution collectively characterize the material's microstructure, significantly influencing its macroscopic properties [230, 231]. To further analyze pore structure evolution in cement mortar under salt spray exposure, cumulative pore volume and cumulative specific surface area were measured via mercury intrusion porosimetry (MIP) for reference specimens and those subjected to 7-35 salt spray cycles (Fig. 5-23). Reference specimens exhibited maximum cumulative pore volume and specific surface area (0.069 m³/g, 5.218 m²/g), both of which decreased progressively with increasing salt spray cycles. As established in prior analysis, this reduction is attributable to significant filling of 0.02-0.12 μm diameter pores by deposited NaCl crystals (Fig. 5-22).

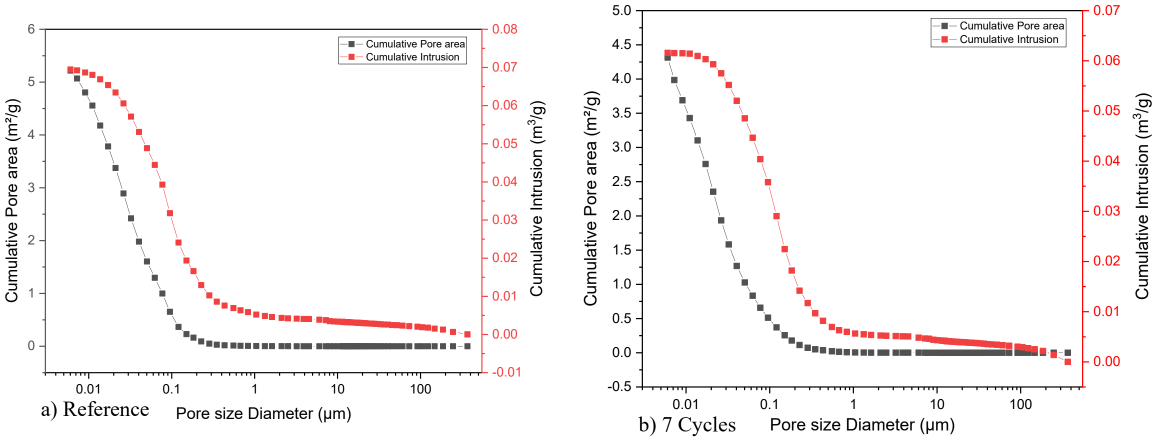

a) Reference

b) 7 Cycles

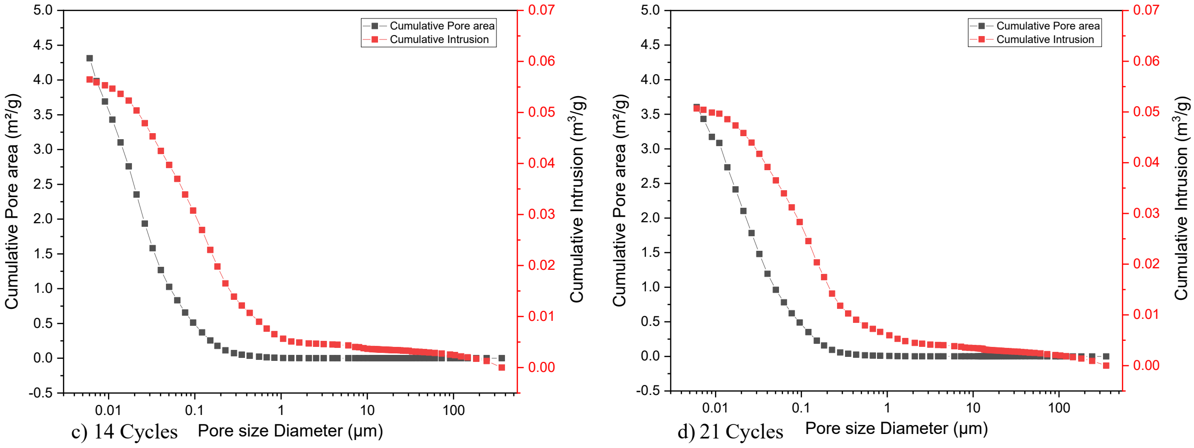

c) 14 Cycles

d) 21 Cycles

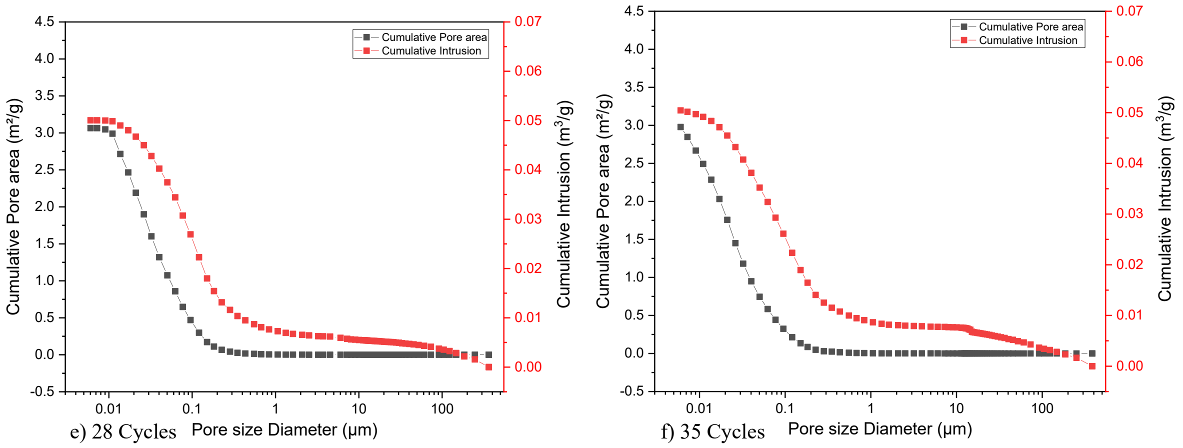

e) 28 Cycles

f) 35 Cycles

Fig. 5-23 Cumulative pore volume and specific surface area of cement mortar subjected to varying salt spray cycles

The decrease in specific surface area of salt-containing specimens results from two primary mechanisms: First, partial filling of micropores by salt crystals converts them into dense structures, reducing internal surface area. Second, unlike Na_2SO_4 crystals forming on pore walls, NaCl crystals nucleate at liquid-gas interfaces within pores and grow toward pore walls [11, 45, 67, 68]. During growth, these crystals don't cover the internal surface area until contacting the pore walls. While salt crystal formation increases material's internal surface area, it simultaneously increases specimen mass. At standard atmospheric pressure and 23°C, dry NaCl crystals exhibit a density of 2163 kg/m^3 [199], slightly higher than the measured density of cement mortar (2133 kg/m^3). Given NaCl's greater density and non-porous nature compared to porous mortar, its deposition reduces the composite material's overall specific surface area.

Despite reducing specific surface area (m^2/g), NaCl deposition increases the absolute external surface area per unit volume (m^2/m^3) within pores. This expanded interface enhances gas molecule contact, thereby boosting material adsorption capacity. This phenomenon accounts for the observed increase in equilibrium moisture content with rising salt content below 75% RH (Figs. 5-11, 5-12), where deposited salt crystals remain undissolved and enhance moisture retention through surface adsorption mechanisms.

5.6.2 Observation by optical microscopic

To investigate salt deposition and distribution on cement mortar under accelerated salt spray testing, optical microscopy was employed to capture surface morphology of dried specimens subjected to 7–35 salt spray cycles at specific magnifications (Fig. 5-24). White NaCl crystals were observed on all surfaces (front, back, and sides) of the 40 × 40 × 20 mm^3 specimens. After 7–14 cycles, sparse salt crystals preferentially adhered to the cement matrix regions (non-sand areas), forming discontinuous thin layers. With increasing cycles (21–35), salt deposits became denser (coverage >85%), filled surface pores, and evolved into continuous layers exceeding 50 μm thickness, ultimately achieving full surface coverage.

Salt deposition on cement mortar specimens produces extensive surface salt crystallization, forming overgrowths that occlude surface-connected pores. This reduces open porosity, accounting for the declining open porosity with increasing salt spray cycles previously observed in Fig. 4-14 (Section 4.4.2). The pore occlusion simultaneously impedes airflow penetration into specimens. This constitutes a primary mechanism for the observed reduction in vapor permeability coefficient (δ_v) with rising salt content below 75% RH (Table 5-13, Fig. 5-20), where salt crystals remain undissolved. Additionally, during sorption isotherm testing above 75% RH, surface salt deposits undergo deliquescence and absorb moisture. This phenomenon further intensifies the progressive increase in equilibrium moisture content with extended salt spray cycles (Figures 5-12, 5-13).

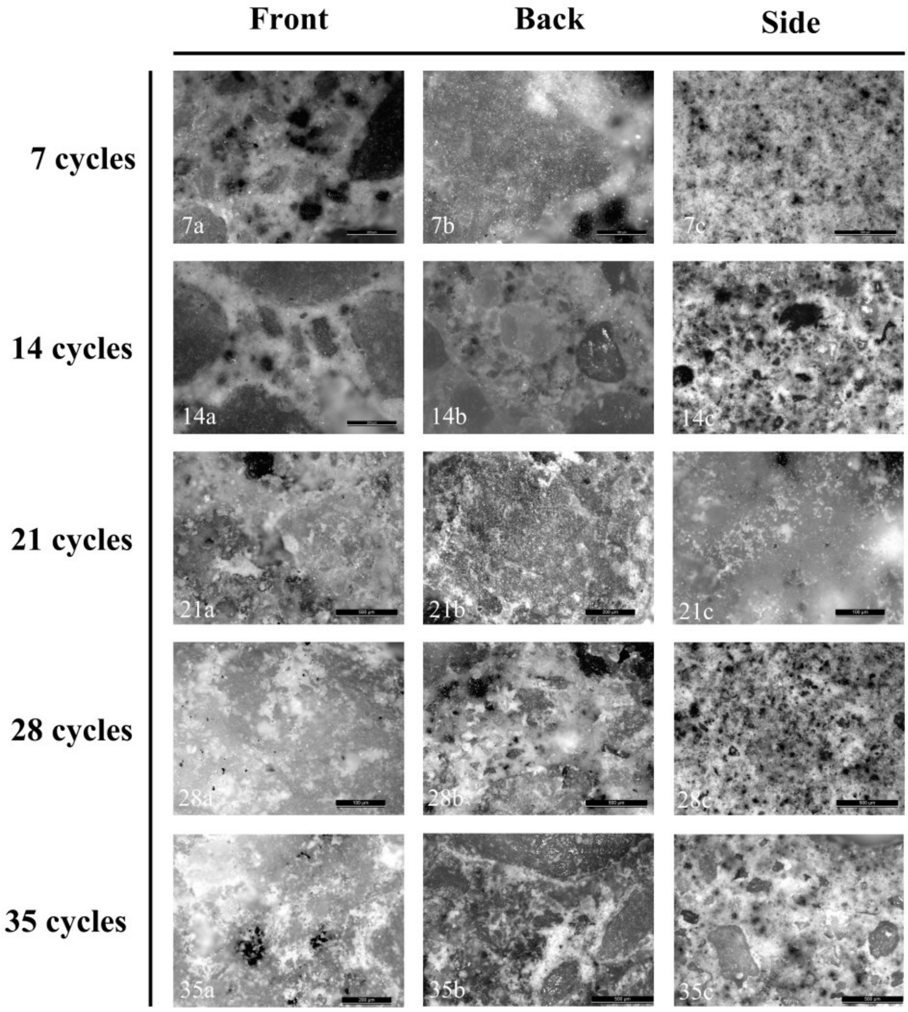

Fig.5-24 Optical microscopy of cement mortar surfaces subjected to salt spray cycling

5.6.3 Micro-morphology analysis by SEM

To visualize the microstructural evolution of salt crystallization on cement mortar surfaces under cyclic salt spray, scanning electron microscopy (SEM) was conducted on all specimen groups (Fig. 5-25). After 7 cycles, cubic NaCl crystals densely covered the surface (Fig.5-25 7a, 7b), inducing surface roughening (Fig.5-25 7c). At 14 cycles, crystal density increased with irregular shapes and reduced particle sizes, forming thicker coatings (Fig.5-25 14a–14c). By 21 cycles, granular crystals transitioned to interconnected flake-like layers (Fig.5-25 21a–21c). Prolonged cycling (28 cycles) produced fused crystalline clusters (Fig. 5-25 28a–28c), while 35 cycles revealed inward salt diffusion into subsurface pores, with smaller crystals adhering to larger molten clusters (Fig. 5-25 35a–35c). This progression—sparse-to-dense coverage and thin-to-thick crystallization—demonstrates how NaCl deposition progressively occludes surface pores, reducing open porosity and impeding vapor transport [67, 81]. These microstructural alterations corroborate the declining water vapor permeability coefficients observed in dry-cup tests (Table 5-13, Fig.5-18), linking morphological changes to macroscopic transport inhibition.

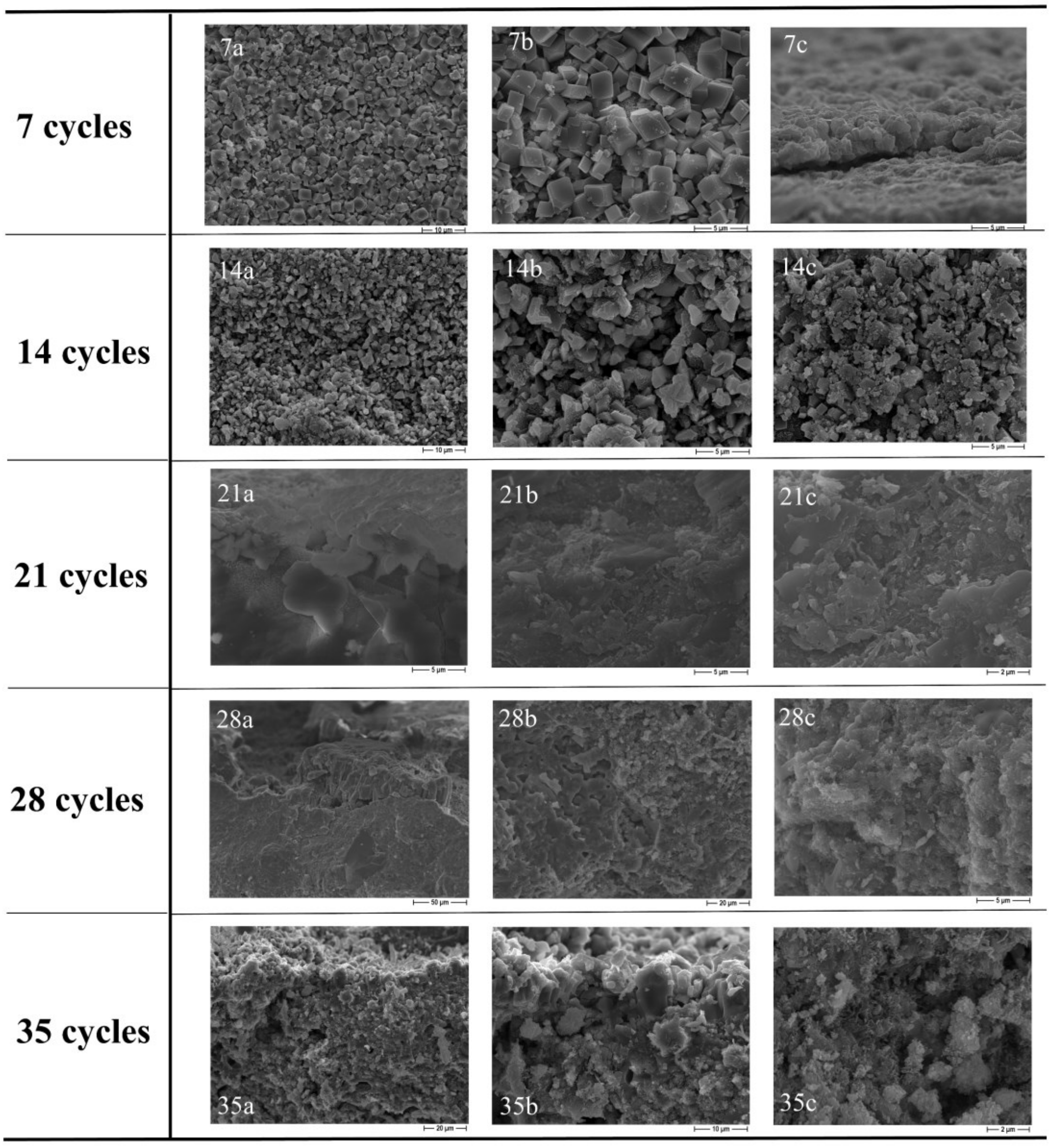

Fig. 5-25 Surface morphology of cement mortar under varying salt spray cycles (SEM)

To comprehensively evaluate salt spray-induced microstructural alterations in cement mortar, cross-sectional morphologies at varying depths were analyzed and compared with reference specimens (Fig. 5-26). Reference samples (Ra–Rd) exhibited characteristic cementitious phases, including C-S-H gel networks, needle-like ettringite ($3CaO \cdot Al_2O_3 \cdot 3CaSO_4 \cdot 32H_2O$), and rod/plate-shaped calcium aluminate hydrate (C-A-H). Following 7–14 salt spray cycles, sparse yet dense NaCl crystals emerged within interphase voids (Fig. 5-267a–14c). Progressive cycling (21–35 cycles) triggered salt cluster proliferation, occluding micropores while generating larger macropores with smoothed surfaces (Figs. 5-26 28c–35c). These observations confirm that salt deposition penetrates both surface and subsurface pore networks. NaCl migration operates through humidity-driven dissolution-recrystallization dynamics: deliquescence under humid conditions enables brine infiltration into deep pores via capillary action [59, 81], while drying cycles drive internal brine toward shallow regions, culminating in recrystallization and pore architecture modification (Fig. 5-26 5 a-f). The progressive accumulation of salt crystals accounts for the sustained reduction in 0.02–0.12 μm pore volumes observed during salt spray testing (Fig. 5-22). Furthermore, higher salt content amplifies hygroscopic moisture uptake and liquid-phase transport under elevated humidity. Repeated crystallization-dissolution cycles dynamically reconfigure pore networks, mechanistically explaining the divergent water vapor permeability trends quantified in dry/wet-cup experiments (Tables 5-13, 5-14).

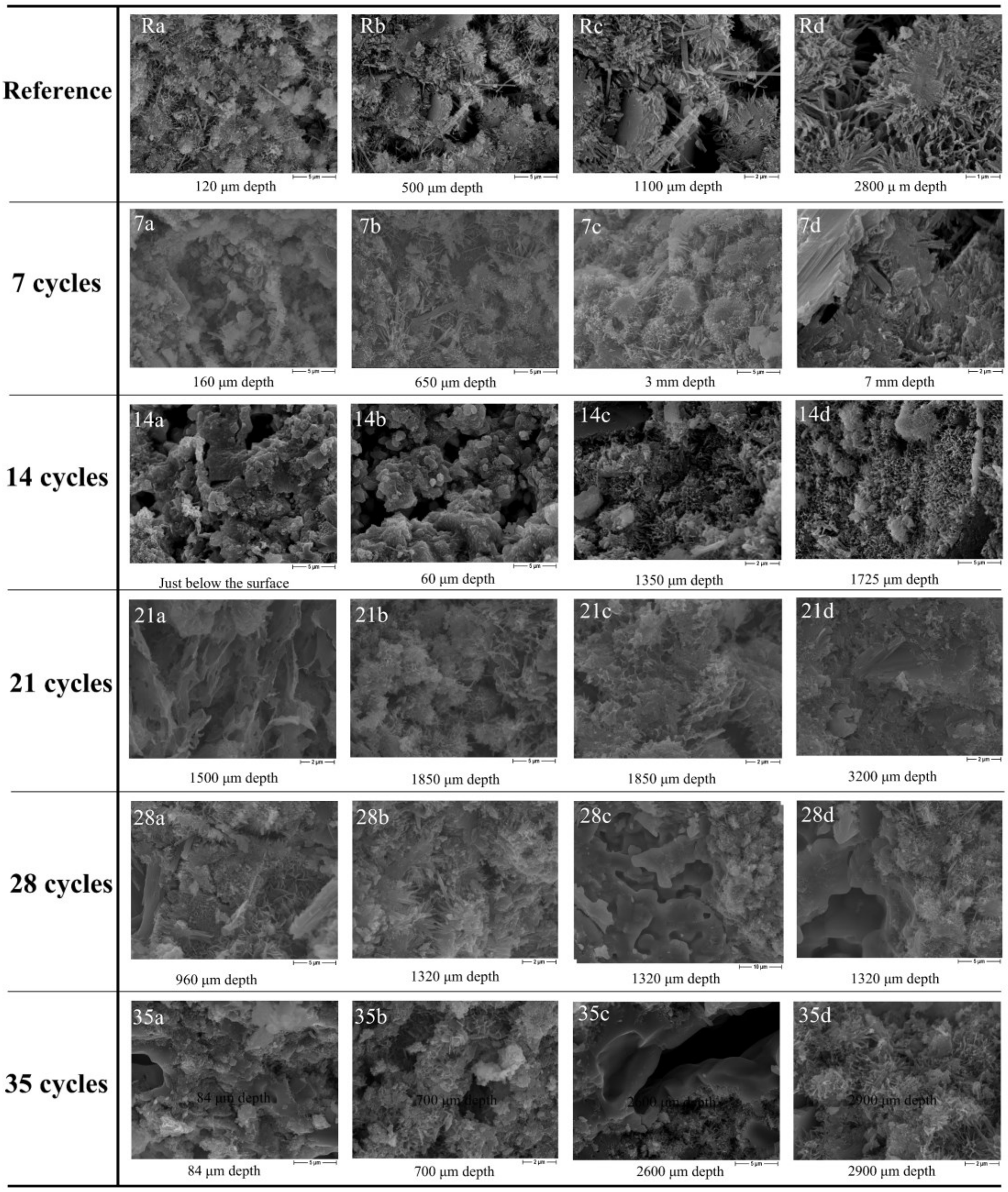

Fig. 5-26 Internal morphology of cement mortar under varying salt spray cycles (SEM)

5.7 Chapter summary

This chapter presents a comprehensive investigation into the effects of coastal salt spray environments on moisture transport and storage characteristics in porous building materials. Utilizing the accelerated salt spray testing methodology established in Chapter 2, we conducted systematic experimental analyses of isothermal sorption curves and vapor permeability coefficients in cement mortar under salt deposition conditions. The principal research findings are summarized below:

(1) Salt deposition was found to significantly increase the EMC of cement mortar. At relative humidity levels below 75%, salt-contaminated specimens demonstrated moderately higher EMC compared to reference samples. When RH reached or exceeded 75%, the deliquescence of NaCl crystals caused a marked increase in sorption isotherm slopes, with EMC showing a proportional relationship to salt content. These results clearly demonstrate the combined influence of environmental humidity and salt concentration on moisture retention properties.

(2) Three distinct piecewise mathematical models (Eqs. 5-11a-b, 5-15, and 5-18) were developed to characterize EMC behavior. These models were derived by applying: (i) the influence factor method, (ii) Robinson-Stokes equation, and (iii) Nielsen formula to modify the optimal fitting equations obtained from salt-free reference specimens, with particular emphasis on the critical 75% RH transition point.

(3) The study revealed a dualistic effect of salt deposition on vapor permeability coefficients (δ_v). In dry/wet cup tests where the high-humidity side maintained RH below 75%, increasing salt content resulted in decreased permeability due to pore blockage by salt crystals. Conversely, when the high-humidity side exceeded 75% RH, permeability increased with salt content as a consequence of enhanced liquid water transport through deliquesced salt solutions.

(4) Through quantitative analysis of salt content effects, we established humidity-specific correction factors for vapor permeability. These factors were systematically incorporated into modified calculation equations, yielding segmented models that accurately describe permeability variations under salt spray exposure conditions.

(5) Salt crystallization was observed to primarily occur in surface and near-surface regions (0.02-0.12 μm pore range). While increasing the absolute surface area and consequently enhancing moisture adsorption (leading to higher EMC), the physical pore filling simultaneously reduced vapor permeability in dry cup test configurations.

While the experimental scope was necessarily limited to cement mortar specimens (0-35 salt spray cycles) to ensure controlled conditions and comparable results, the fundamental physical mechanisms identified - particularly the pore structure-dependent processes of salt crystallization, deliquescence, and migration - provide valuable insights for other porous building materials. The predominantly physical (rather than chemical) nature of these interactions suggests broad applicability of the findings, though material-specific variations should be considered. Future research will extend this investigation to additional porous materials, with the ultimate goal of developing robust theoretical frameworks for hygrothermal performance assessment and energy efficiency optimization in coastal building applications. This chapter has established significant groundwork for understanding moisture transport phenomena in salt-contaminated building materials, while also identifying key areas for further investigation to support sustainable construction practices in marine environments.

Conclusions and outlook

Main conclusions

Building envelopes serve as critical boundaries between indoor spaces and outdoor environments, playing a pivotal role in protecting against harsh weather conditions (wind, cold, heat, humidity, and radiation) while maintaining safe, healthy, and comfortable indoor environments. The moisture transport properties of porous building materials significantly influence not only the durability of building envelopes but also building energy consumption and indoor thermal comfort. Coastal regions face substantially different environmental challenges compared to inland areas due to persistent salt spray exposure, yet the moisture transport characteristics of porous materials under such conditions remain poorly understood. Current Chinese building climate zoning and thermal design standards notably lack consideration for salt spray climate conditions.

Building envelope materials exposed to salt spray environments are particularly susceptible to erosion damage. Most existing research has primarily focused on material durability and mechanical performance. On one hand, continuous salt deposition fills internal pores with NaCl and Na_2SO_4 crystals, generating expansive stresses that exceed material strength limits, leading to internal degradation (reduced strength, mass loss) and external deterioration (cracking, spalling). On the other hand, for reinforced concrete structures, salt penetration initiates chloride-induced steel corrosion, compromising structural integrity.

While some studies have examined moisture transport in salt-contaminated porous materials, the research remains underdeveloped. Porosity and pore structure fundamentally govern moisture transport processes, yet salt crystallization alters these mechanisms by reducing pore connectivity and increasing material density, thereby modifying both liquid and vapor transport behaviors. Furthermore, subsequent moisture ingress can dissolve and redistribute salt crystals, creating complex interactions between salt deposition and moisture dynamics. Crucially, most previous studies employed immersion or wet-dry cycling methods that poorly replicate actual coastal salt spray conditions, highlighting the need for more representative experimental approaches.

Addressing these research gaps, this dissertation systematically investigates cement mortar (a common porous building material) through accelerated salt spray testing. First, we established an optimized salt spray methodology by analyzing parameters from various standards and studies. Second, through immersion experiments (5 wt.% NaCl solution for 120 days), we characterized salt crystallization patterns, chloride ion distribution, and capillary absorption behaviors across different water-cement ratios. Third, vacuum saturation, capillary absorption, and water retention experiments elucidated salt deposition effects on liquid transport, enabling development of modified equations for capillary absorption coefficients and moisture content. Finally, isothermal sorption and vapor permeability tests revealed salt impacts on vapor transport, leading to segmented equilibrium moisture content (EMC) models and corrected permeability equations. The key findings are detailed as follows:

1）Salt spray testing of porous materials exhibits significant methodological and parametric variations due to the absence of standardized protocols, where specimen materials and dimensions are typically selected based on research objectives and post-exposure evaluation methods. Given gravity-driven vertical salt deposition, specimen surface inclination critically influences salt accumulation and corrosion, with industry standards (e.g., ASTM B117) and experimental studies recommending a 15–30° tilt angle relative to the vertical plane. While elevated salt concentrations accelerate corrosion, they risk nozzle clogging from salt crystallization that may terminate testing prematurely; considering seawater composition (3.5% salinity average) and cross-industry standards, a 5 wt.% NaCl solution is recommended for spray generation. Compared to continuous or intermittent spray regimes, cyclic wet-dry alternation induces more pronounced weathering corrosion in porous materials, with global parameter analyses confirming that a 1:2 wet-to-dry duration ratio optimizes accelerated corrosion—aligning with BS EN 14147:2003. Post-exposure evaluations employ diverse metrics including chloride ion penetration depth, mass change rate, physical/mechanical properties, and microstructural evolution, tailored to specific research goals.

2）Based on critical parameter analysis for salt spray testing, this study established an accelerated experimental protocol utilizing a CEAST 5050 salt spray chamber to regulate environmental parameters and cyclic programs. The spray solution comprised 5 wt.% NaCl (pH 6.5–7.2), yielding an average sedimentation rate of 1–2 mL/80 cm^2·h after 16 hours of continuous spraying. Specimens were positioned at 20° to the vertical plane, optimizing spatial efficiency while accommodating dimensions, spacing, and angular requirements. Cost-effective specimen holders meeting mechanical and technical criteria were designed and fabricated via 3D printing (PLA material). The 24-hour cyclic regime consisted of 8-hour continuous salt spray (35°C) and 16-hour dry phase (55°C), with humidity unregulated during spraying due to chamber near-saturation. Aligned with research objectives on moisture transport under salt deposition, specimen groups were extracted after every 7 cycles (7, 14, 21, 28, 35 cycles) for hygric characterization, mass variation assessment, and chloride concentration measurements, complemented by microstructural analyses (XRD, MIP, SEM) of salt-laden specimens' pore morphology and crystallization patterns.

3）The water-cement ratio (W/C) and surface evaporation conditions critically govern NaCl crystallization distribution in cement mortar under partial immersion. Specimens with W/C=0.4 exhibited approximately double the external crystal mass (m_e) compared to W/C=0.6 and W/C=0.8 specimens, while maximum internal crystallization (m_i) occurred in W/C=0.8 specimens—fivefold higher than W/C=0.4 and W/C=0.6 counterparts. This divergence stems from dominant transport mechanisms: W/C=0.4 specimens' abundance of pores $>10^5$ nm facilitated permeation-driven solution uptake from the base, with rapid surface evaporation concentrating external crystallization. Conversely, W/C=0.8 specimens' peak porosity in 0–100 nm pores promoted capillary-dominated solution ingress, where slow sustained evaporation enabled internal supersaturation and crystallization. Surface sealing reduced total crystallization mass (m_t) and m_e by 50% across all W/C ratios, while m_i remained stable, attributed to suppressed evaporation and salt migration. Chloride concentration mapping revealed unsealed specimens consistently displayed higher edge-versus-core Cl^- concentrations horizontally at all heights, whereas sealed specimens showed minimal horizontal variation—confirming evaporation dominance in lateral salt distribution. Although unsealed specimens maintained higher absolute Cl^- concentrations vertically, both types exhibited negligible vertical concentration gradients, indicating evaporation indirectly modulates vertical distribution. Ultimately, persistent NaCl crystallization with associated expansive stress constitutes the primary physical degradation mechanism, highlighting material densification and surface permeability reduction as critical pathways for minimizing salt deposition and enhancing structural durability.

4）Comparative capillary absorption experiments were conducted on three sets of specimens: First, between the salt-free, uncoated NOW group (tested in pure water) and NOS group (tested in saturated NaCl solution), the capillary absorption coefficient of the NOS group ($A_{cap,sol}$) was lower than that of the NOW group ($A_{cap,w}$). For specimens with water-cement ratios (W/C) of 0.4, 0.6, and 0.8, the scaling factors $A_{cap,sol}/A_{cap,w}$ were 0.79, 0.90, and 0.98, respectively. Second, when comparing the salt-free, uncoated NOS group and salt-laden, uncoated NSS group (both tested in saturated NaCl solution), salt crystal deposition on the material's pore walls reduced pore size, pore volume, and pore connectivity. This resulted in a 45.72% and 60.82% decrease in $A_{\mathrm{cap,w}}$ for NSS specimens with W/C of 0.6 and 0.8, respectively, alongside a 56.39% and 56.34% reduction in capillary moisture content ($w_{\mathrm{cap,w}}$) at the same W/C values. Third, when comparing the salt-laden, uncoated NSS group and salt-laden, coated CSS group (both tested in saturated NaCl solution), the CSS group exhibited reductions in $A_{\mathrm{cap,w}}$ of 22.92%, 36.13%, and 28.55% for W/C of 0.4, 0.6, and 0.8, respectively, with corresponding decreases in $w_{\mathrm{cap,w}}$ of 9.76%, 32.82%, and 27.52%. This reduction was attributed to the coating's inhibition of surface moisture evaporation and capillary action.

5）In a salt spray environment, salt crystals deposit within the pores of cement mortar, and by using a saturated NaCl solution instead of pure water in vacuum saturation and capillary absorption tests—coupled with subsequent result corrections—this approach effectively prevents salt crystal dissolution during water absorption, preserving the original pore structure under salt-laden conditions. As salt spray cycles increase, chloride ion content in specimens rises, while open porosity (P_{o}) and saturated moisture content (w_{sat}) gradually decrease and apparent density (ρ_{b}) increases; after 35 cycles, the average salt concentration reaches 1.99 wt.%, with P_{o} and w_{sat} each reduced by 18.7% and ρ_{b} increased by 3.85%. The ratio of capillary absorption coefficients ($A_{\mathrm{cap,sol}}/A_{\mathrm{cap,w}}$) in deionized water versus saturated NaCl solution is 0.871, used to correct coefficients across all cycles, and both $A_{\mathrm{cap,w}}$ and $w_{\mathrm{cap,w}}$ decrease gradually as cycles increase: after 35 cycles, $A_{\mathrm{cap,w}}$ drops by 30% and $w_{\mathrm{cap,w}}$ by 17.4%. The primary mechanism behind these reductions is the extensive filling of 0.02–0.12 μm pores by salt crystals, which reduces porosity and weakens capillary action and permeability—key drivers of the decreases—though NaCl's strong hygroscopicity partially offsets the reduction in $w_{\mathrm{cap,w}}$, resulting in a smaller decrease magnitude. By comparing with reference specimens, influence factors (η_{Acap} for absorption coefficient, η_{wcap} for moisture content) under different salt contents were calculated, plotted, and curve-fitted to polynomial equations, which enabled the establishment of corrected calculation formulas for $A_{\mathrm{cap,s}}$ and $w_{\mathrm{cap,s}}$ in salt spray-exposed cement mortar.

6) Salt spray deposition increases the equilibrium moisture content (u_{t}) of cement mortar and alters its moisture sorption isotherm: at relative humidity (φ) < 75%, the ut of salt-laden specimens is slightly higher than that of reference ones, while at $\varphi \geq 75\%$, the deliquescence of NaCl crystals causes the slope of the moisture sorption isotherm for salt-laden specimens to increase significantly, with u_{t} at each humidity level rising alongside increasing salt content. The u_{t} of salt-laden specimens is governed by the interactive effects of ambient humidity and

salt content; building on different fitting formulas for the moisture sorption isotherms of reference specimens, the calculation model for u_t below 0.75 RH was corrected via influence factor fitting equations, and conversely, leveraging the relationship between ambient humidity and salt solution concentration within porous materials—as elucidated by the Robinson-Stokes equation and Nielsen formula—the calculation model for u_t of salt-laden materials above 0.75 RH was corrected via the superposition method, leading to the development of three segmented fitting models (5-11a-b), (5-15), and (5-18) for the equilibrium moisture content (u_t) of cement mortar under salt spray deposition.

7) The influence of salt spray deposition on the water vapor permeability coefficient ($\delta_{v,s}$) of cement mortar varies with humidity: in wet-dry cup tests, when the humidity on the higher-humidity side (φ_1) is $< 75\%$, $\delta_{v,s}$ decreases with increasing salt content in the specimens; conversely, when $\varphi_1 \geq 75\%$, $\delta_{v,s}$ increases as salt content rises. This discrepancy arises because salt crystal clogging of pores reduces $\delta_{v,s}$, whereas when ambient humidity exceeds NaCl's deliquescence humidity, salt crystals in the material dissolve, accompanied by liquid water migration. Based on the fitting functions of the water vapor permeability influence factor ($\delta_{v,s}$) curves— which describe how $\eta_{\delta,v}$ varies with salt content under conditions of $\varphi_1 < 75\%$ and $\varphi_1 \geq 75\%$ respectively—segmented correction equations for $\delta_{v,s}$ of salt-laden cement mortar were established. Notably, salt crystal deposits formed in salt spray environments are primarily distributed on the surface and shallow layers of cement mortar, predominantly within pores with diameters ranging from 0.02 to 0.12 μm. Under conditions of $\varphi < 75\%$, the increased internal surface area of pores due to salt crystals enhances adsorptivity, leading to a rise in equilibrium moisture content (u_t); simultaneously, pore filling and clogging by salt crystals result in a reduction in $\delta_{v,s}$.

Key innovations

This study investigates the impact of coastal salt spray climates on moisture transport properties of porous building materials, with a focus on cement mortar—a commonly used material in building envelopes. By examining salt crystallization patterns, chloride ion migration, and capillary absorption characteristics under different water-cement ratios and surface evaporation conditions, the research establishes an accelerated salt spray testing methodology tailored for porous materials. The derived influence factors and correction equations for liquid and vapor transport properties under salt deposition provide a scientific basis for accurately determining moisture-related parameters of porous materials in salt-laden environments. The key innovations are as follows:

1）Improved Testing Methodology for Liquid Water Transport Properties

Traditional vacuum saturation and capillary absorption tests, while effective for measuring porosity and liquid transport in salt-free porous materials, are inadequate for coastal applications. When pure water is used as the absorption medium, it dissolves pre-existing salt crystals in the material, altering pore structures and distorting measurements. This study introduces a novel approach by replacing pure water with saturated NaCl solution in both vacuum saturation and capillary absorption tests. Through physical parameter conversion and corrections, this method accurately quantifies porosity, apparent density, saturated moisture content, capillary absorption coefficient, and capillary moisture content in salt-contaminated materials, significantly improving the reliability of liquid transport properties assessments.

2) Salt Spray-Specific Experimental Simulation

Previous research predominantly relied on salt solution immersion to introduce salts into porous materials—a method that poorly replicates real-world salt spray exposure conditions. This study develops an accelerated salt spray testing protocol that authentically simulates coastal climate effects. By systematically analyzing changes in fundamental pore characteristics and liquid transport properties under varying salt deposition levels, the research quantifies and models influence factors for capillary absorption parameters. The resulting correction equations for capillary absorption coefficient and moisture content provide the first dedicated predictive tools for salt spray-affected porous materials.

3) Humidity-Dependent Transport Mechanism Modeling

This study uncovers a critical phase-transition mechanism: NaCl crystals deliquesce into saturated solutions when ambient humidity exceeds their water activity (75% RH) and recrystallize below this threshold. Building on this foundational behavior, the research integrates the Robinson-Stokes equations and Nielsen's formula to establish both segmented models of equilibrium moisture content—incorporating humidity-driven salt phase transitions—and differentiated corrections for vapor permeability tailored to conditions above and below the deliquescence threshold. These methodological innovations enable the first-principles prediction of hygrothermal performance in salt-contaminated building envelopes across the full humidity spectrum.

The innovations collectively provide a comprehensive framework for assessing and predicting moisture transport behavior in coastal construction materials, overcoming longstanding limitations in both experimental methodologies and theoretical modeling approaches.

Shortcomings and limitations

While this study has achieved significant progress through extensive experimentation, several limitations warrant acknowledgment:

1) The research exclusively examined cement mortar as a representative porous building material. The experimental demands—including specimen preparation (multiple replicates per test condition), prolonged drying/equilibration protocols (requiring consecutive mass stability checks within 0.1% thresholds), and extended testing durations (e.g., 3-month sorption isotherm measurements)—necessitated this focused approach. Although cement mortar shares NaCl's non-reactive physical interaction with most porous materials (where salt effects manifest primarily through pore structure alteration), the findings' generalizability to other materials requires verification through future comparative studies.

2) The experiments utilized NaCl-only salt spray, despite seawater's complex ionic composition (2.39% NaCl, 0.52% $MgCl_2$, 0.41% Na_2SO_4, 0.12% $CaCl_2$, 0.07% KCl etc.). While NaCl dominates (69% of total salts) and aligns with standard corrosion testing protocols, the exclusion of sulfate interactions—particularly ettringite formation in cementitious systems—and potential multi-salt synergistic effects represents an oversimplification of real coastal exposures. This limitation underscores the need for follow-up studies on compound salt mixtures.

3) This research exclusively characterized adsorption isotherms, omitting desorption measurements due to methodological constraints. The initial high-moisture conditions required for desorption testing would dissolve and redistribute salt crystals, fundamentally altering the material's native microstructure. While adsorption testing across six specimen batches at five humidity levels adequately captured the influence of salt deposition on cement mortar's hygroscopic behavior, future studies should develop validated desorption protocols—despite the extended duration exceeding three months.

These limitations delineate clear pathways for advancing porous material research in marine environments while contextualizing the current findings' applicability.

Prospects for future work

Future research should focus on the following key directions to advance understanding of salt spray effects on porous building materials:

1） Conduct field investigations and laboratory studies to evaluate the influence of low-concentration salt components (beyond NaCl) commonly found in coastal environments on moisture transport mechanisms in porous building materials.

2）Refine experimental techniques and measurement systems for characterizing hygric properties of salt-contaminated porous materials and composite wall assemblies, enhancing data accuracy and analytical reliability.

3) Collaborate with research institutions across eastern and southeastern coastal China to systematically test moisture transport parameters of building materials under salt deposition, establishing a comprehensive reference database for common construction materials.

4) Develop material-specific strategies for managing internal salt crystallization and surface erosion protection, tailored to diverse coastal climate conditions based on experimental and theoretical findings.

5) Investigate how marine salt spray affects carbonation and CO_2 absorption in cementitious materials, providing critical data for lifecycle carbon balance predictions and carbon neutrality evaluations in coastal construction.

This research roadmap addresses current knowledge gaps while aligning with practical needs for durable, sustainable coastal infrastructure development.

References

[1] Lu Ming, Development issues of marine environmental science and marine monitoring technology in China, Journal of Yellow Sea and Bohai Sea (03) (2000) 96-100. (In Chinese)

[2] Wu Chuanjun, Yang Qinye, Lu Qi, 20th Century Chinese Academic Encyclopedia: Geography, Fujian Education Publishing House, Fuzhou, 2002. (In Chinese)

[3] Xu Guobao, Content and distribution of salt spray in coastal atmosphere in China, Environmental Technology (03) (1994) 1-7. (In Chinese)

[4] Zeng Juyao, On the salt spray content and distribution in the near-surface atmosphere in coastal areas of China, Special Electrical Engineering (04) (1982) 15-20. (In Chinese) [5] Z. Meng, M. Liu, C. Gao, Y. Zhang, Q. She, L. Long, Y. Tu, Y. Yang, Greening and browning of the coastal areas in mainland China: Spatial heterogeneity, seasonal variation and its influential factors, Ecological Indicators 110 (2020) 105888.

[6] X. Zhang, J. Ning, Land use change in coastal zones of China from 1985 to 2020, Frontiers in Marine Science 11 (2024).

[7] C. Cardell, F. Delalieux, K. Roumpopoulos, A. Moropoulou, F. Auger, R. Van Grieken, Salt-induced decay in calcareous stone monuments and buildings in a marine environment in SW France, Construction and Building Materials 17(3) (2003) 165-179.

[8] Z.S.G. Silva, J.A.R. Simão, The role of salt fog on alteration of dimension stone, Constr Build Mater 23(11) (2009) 3321-3327.

[9] H. Morillas, F.F. de Mendonça Filho, H. Derluyn, M. Maguregui, D. Grégoire, J.M. Madariaga, Decay processes in buildings close to the sea induced by marine aerosol: Salt depositions inside construction materials, Science of The Total Environment 721 (2020) 137687.

[10] A.E. Charola, Salts in the Deterioration of Porous Materials: An Overview, Journal of the American Institute for Conservation 39(3) (2000) 327.

[11] C. Rodriguez-Navarro, E. Doehne, Salt Weathering: Influence of Evaporation Rate, Supersaturation and Crystallization Pattern, Earth Surface Processes and Landforms 24 (1999) 191-209.

[12] A.A. Sawdy-Heritage, L. Pel, A review of salt transport in porous media : assessment methods and salt reduction treatments, 2008.

[13] M. Koniorczyk, D. Gawin, Heat and Moisture Transport in Porous Building Materials Containing Salt, Journal of Building Physics 31(4) (2008) 279-300.

[14] Zheng Shansuo, Ruan Sheng, Cao Chen, et al., Experimental study on compressive mechanical properties of brick masonry in offshore atmospheric chloride ion environment,

Journal of Functional Materials 49(1) (2018) 1127-1133. (In Chinese)
[15] H. Bravo A, R. Soto A, R. Sosa E, P. Sánchez A, A.L. Alarcón J, J. Kahl, J. Ruíz B, Effect of acid rain on building material of the El Tajín archaeological zone in Veracruz, Mexico, Environmental Pollution 144(2) (2006) 655-660.
[16] R. Hamilton, H. Crabbe, Environment, Pollution and EffectsEnvironment, Pollution and Effects, in: R. Hamilton, V. Kucera, J. Tidblad, J. Watt (Eds.), The Effects of Air Pollution on Cultural Heritage, Springer US, Boston, MA, 2009, pp. 1-27.
[17] M. Hori, H. Morihiro, Micromechanical analysis on deterioration due to freezing and thawing in porous brittle materials, International Journal of Engineering Science 36(4) (1998) 511-522.
[18] A. Jamshidi, Study of building stones durability against the freeze-thaw process: Current methods and recommendations for the future, Journal of Building Engineering 86 (2024) 108772.
[19] J.M.P.Q. Delgado, A.S. Guimarães, V.P. de Freitas, I. Antepara, V. Kočí, R. Černý, Salt Damage and Rising Damp Treatment in Building Structures, Advances in Materials Science and Engineering 2016 (2016) 1-13.
[20] M. Collepardi, Degradation and restoration of masonry walls of historical buildings, Materials and Structures 23(2) (1990) 81-102.
[21] Liu Cigui, Building a marine power with Chinese characteristics [N], Guangming Daily, 2012-11-26(013). (In Chinese)
[22] Wang Hong, Building a marine power boosts the realization of the Chinese Dream [N], People's Daily, 2017-11-20(007). (In Chinese)
[23] JGJ/T 70-2009, Test Methods for Basic Properties of Building Mortar, China Architecture & Building Press, 2009. (In Chinese)
[24] Bi Wanli, Building Materials (4th Edition), 2022. (In Chinese)
[25] BS EN 197-1: 2011(E) Cement Composition, specifications and conformity criteria for common cements.
[26] JGJ/T 220-2010, Technical Specification for Plastering Mortar, 2010. (In Chinese)
[27] BS EN 196-1:2016 Methods of testing cement Part 1: Determination of strength (2016).
[28] S.J.C. Granneman, B. Lubelli, R.P.J. van Hees, Effect of mixed in crystallization modifiers on the resistance of lime mortar against NaCl and Na2SO4 crystallization, Construction and Building Materials 194 (2019) 62-70.
[29] E. Franzoni, C. Gentilini, M. Santandrea, S. Zanotto, C. Carloni, Durability of steel FRCM-masonry joints: effect of water and salt crystallization, Materials and Structures 50(4) (2017).

[30] B. Lubelli, R.P.J. van Hees, H.P. Huinink, C.J.W.P. Groot, Irreversible dilation of NaCl contaminated lime–cement mortar due to crystallization cycles, Cement and Concrete Research 36(4) (2006) 678-687.

[31] R.M. Espinosa, L. Franke, G. Deckelmann, Model for the mechanical stress due to the salt crystallization in porous materials, Construction and Building Materials 22(7) (2008) 1350-1367.

[32] C. Gentilini, E. Franzoni, S. Bandini, L. Nobile, Effect of salt crystallisation on the shear behaviour of masonry walls: An experimental study, Construction and Building Materials 37 (2012) 181-189.

[33] E. Franzoni, M. Santandrea, C. Gentilini, A. Fregni, C. Carloni, The role of mortar matrix in the bond behavior and salt crystallization resistance of FRCM applied to masonry, Construction and Building Materials 209 (2019) 592-605.

[34] L. Su, D. Niu, D. Huang, Y. Luo, H. Qiao, Y. Zhang, Chloride diffusion behavior and microstructure of basalt-polypropylene hybrid fiber reinforced concrete in salt spray environment, Construction and Building Materials 324 (2022).

[35] A.R.G. Azevedo, J. Alexandre, G.C. Xavier, E.B. Zanelato, M.T. Marvila, N.A. Cerqueira, B.C. Mendes, S.N. Monteiro, Study of Durability of Mortars with Effluent Sludge from Paper Industry Exposed to Salt Spray, Characterization of Minerals, Metals, and Materials 20182018, pp. 669-676.

[36] L. Pel, H. Huinink, K. Kopinga, Ion transport and crystallization in inorganic building materials as studied by nuclear magnetic resonance, Applied Physics Letters 81(15) (2002) 2893-2895.

[37] Yang Xiaoquan, Qu Chunpu, Yang Fa, Li Chuang, Xiong Rui, Study on mechanical properties of cement mortar under sulfate/chloride attack, Qinghai Transportation Science and Technology 32(01) (2020) 88-92. (In Chinese)

[38] Su Yulong, Lai Weizhong, Chen Xiqiang, Wen Hongyu, Ling J., Journal of Guangxi University (Natural Science Edition), Changes in mechanical properties of cement mortar after sulfate attack, 35(4) (2010) 693-697. (In Chinese)

[39] Huang Qian, Wang Chong, Zhao Liang, Zhao Min, Effect of nano-SiO_2 on sulfate attack resistance of cement mortar under semi-immersion, Journal of Building Materials 22(06) (2019) 978-985. (In Chinese)

[40] Ma Kunlin, Xie Youjun, Long Guangcheng, Liu Yunhua, Physical erosion of sodium sulfate on cement mortar, Journal of the Chinese Ceramic Society (10) (2007) 1376-1381. (In Chinese)

[41] Chen Da, Liao Yingdi, Hou Lijun, Ouyang Feng, Mechanical properties and constitutive model of cement-based materials under sulfate attack, Journal of Building Materials 16(06) (2013) 936-941. (In Chinese)

[42] Qiao Hongxia, Zhang Lu, Feng Qiong, Shang Minggang, Wen Shaoyong, Study on corrosion characteristics of reinforced concrete under salt spray-drying cycles, Journal of Functional Materials 51(05) (2020) 5161-5167. (In Chinese)

[43] M. Koniorczyk, Salt transport and crystallization in non-isothermal, partially saturated porous materials considering ions interaction model, Int J Heat Mass Tran 55(4) (2012) 665-679.

[44] Zhu Jianjian, Gao Jianming, Chen Fei, He Zhizhang, Erosion mechanism of cement mortar semi-immersed in $NaCl\text{-}Na_2SO_4$ mixed solution, Journal of Southeast University (Natural Science Edition) 49(05) (2019) 964-972. (In Chinese)

[45] R.M. Espinosa-Marzal, G.W. Scherer, Impact of in-pore salt crystallization on transport properties, Environmental Earth Sciences 69(8) (2013) 2657-2669.

[46] Yang Quanbing, Zhu Beirong, Study on salt crystallization damage of concrete, 7th National Academic Conference on Concrete Durability, Yichang, Hubei, China, 2008, p. 7. (In Chinese)

[47] He Jing, Shen Xiangdong, Dong Wei, Study on dry-wet resistance of effective aeolian sand cement mortar under salt attack, Concrete (06) (2018) 105-107+111. (In Chinese)

[48] Zhao Lihua, Zeng Yongyin, Zhu Jichao, Study on the influence of salt spray-temperature coupling on the performance of asphalt mixture, Highway 63(06) (2018) 253-257. (In Chinese)

[49] Guo Jiwu (Ed.), Building Structures, China Architecture & Building Press, 2019. (In Chinese)

[50] Wu Wenjuan, Wang Ren, Zhu Changqi, Meng Qingshan, Tang Shengwen, Effect and mechanism of salt spray on the performance of coral aggregate concrete structures, Journal of Building Materials 21(04) (2018) 600-607. (In Chinese)

[51] M. Borges, J. Simão, Z. Silva, Artificial Weathering of Portuguese Granites Exposed to Salt Atmosphere: Variations of Physico-Mechanical Properties, 2011.

[52] G. Barone, P. Mazzoleni, G. Pappalardo, S. Raneri, Microtextural and microstructural influence on the changes of physical and mechanical proprieties related to salts crystallization weathering in natural building stones. The example of Sabucina stone (Sicily), Construction and Building Materials 95 (2015) 355-365.

[53] M. Ludovico-Marques, C. Chastre, Effect of salt crystallization ageing on the compressive behavior of sandstone blocks in historical buildings, Engineering Failure Analysis 26 (2012)

247-257.

[54] BS EN 14147: 2003(E) Natural stone test methods. Determination of resistance to ageing by salt mist.

[55] Zhang Ke, Zhang Zhengqi, Deterioration of mechanical properties of asphalt mixture in salt-containing high-humidity environment, Journal of South China University of Technology (Natural Science Edition) 43(08) (2015) 106-112. (In Chinese)

[56] Lü Lingyi, Lü Zihua, Building Mechanics, China Architecture & Building Press, 2018. (In Chinese)

[57] Yu Hongfa, Sun Wei, Ma Haiyan, Yan Lianghui, Chloride ion diffusion equation of concrete under multiple factors, Journal of Building Materials (03) (2002) 240-247. (In Chinese)

[58] Yu Hongfa, Sun Wei, Theoretical model of chloride ion diffusion in concrete, Journal of Southeast University (Natural Science Edition) (S2) (2006) 68-76. (In Chinese)

[59] L. Pel, H. Huinink, K. Kopinga, Salt transport and crystallization in porous building materials, Magnetic Resonance Imaging 21(3-4) (2003) 317-320.

[60] E. Ruiz-Agudo, F. Mees, P. Jacobs, C. Rodriguez-Navarro, The role of saline solution properties on porous limestone salt weathering by magnesium and sodium sulfates, Environmental Geology 52(2) (2007) 269-281.

[61] M. Angeli, D. Benavente, J.-P. Bigas, B. Menéndez, R. Hébert, C. David, Modification of the porous network by salt crystallization in experimentally weathered sedimentary stones, Materials and Structures 41(6) (2008) 1091-1108.

[62] B. Lubelli, R.P.J. van Hees, C.J.W.P. Groot, Sodium chloride crystallization in a “salt transporting” restoration plaster, Cement and Concrete Research 36(8) (2006) 1467-1474.

[63] R. Hendrickx, H.C.D. Clercq, S. Roels, Y. Vanhellemont, S. Herinckx, Experimental investigation of the influence of precipitated salts on the liquid transport properties of brick using an organic fluid, 2011.

[64] R. Hendrickx, H.D. Clercq, Y. Vanhellemont, Experimental determination of liquid transport parameters of salt-contaminated porous stone : uptake experiments using decane, in: XII DBMC - Int. Conf. Durab. Build. Mater. Components, 2011: pp. 1–9.

[65] C. Feng, H. Janssen, Y. Feng, Q. Meng, Hygric properties of porous building materials: Analysis of measurement repeatability and reproducibility, Building and Environment 85 (2015) 160-172.

[66] J. Carmeliet, O. Adan, H. Brocken, R. Cerny, S.J.J.o.B.P. Roels, Determination of the Liquid Water Diffusivity from Transient Moisture Transfer Experiments, 27(4) (2004).

[67] J. Todorović, H. Janssen, The impact of salt pore clogging on the hygric properties of bricks,

Construction and Building Materials 164 (2018) 850-863.

[68] D. Benavente, M.A.G. del Cura, x, Garcı, x, J. a-Guinea, S. Sánchez-Moral, S. Ordóñez, Role of pore structure in salt crystallisation in unsaturated porous stone, Journal of Crystal Growth 260(3) (2004) 532-544.

[69] L. Bai, J. Xie, J. Liu, Y. Xie, Effect of salt on hygroscopic properties of cement mortar, Construction and Building Materials 305 (2021).

[70] O. Kläusler, S. Clauß, L. Lübke, J. Trachsel, P. Niemz, Influence of moisture on stress-strain behaviour of adhesives used for structural bonding of wood, International Journal of Adhesion and Adhesives 44 (2013) 57-65.

[71] F. Larsen, S. Ormarsson, J.F. Olesen, Moisture-driven fracture in solid wood, Wood Material Science & Engineering 6(1-2) (2011) 49-57.

[72] M. Woloszyn, T. Kalamees, M.O. Abadie, M. Steeman, A. Sasic Kalagasidis, The effect of combining a relative-humidity-sensitive ventilation system with the moisture-buffering capacity of materials on indoor climate and energy efficiency of buildings, Building and Environment 44(3) (2009) 515-524.

[73] F. Zezza, F. Macrì, Marine aerosol and stone decay, Science of The Total Environment 167(1) (1995) 123-143.

[74] K. Sedlbauer, Prediction of Mould Fungus Formation on the Surface of and Inside Building Components, (2001).

[75] H. Viitanen, Factors affecting the development of biodeterioration in wooden constructions, Materials and Structures 27(8) (1994) 483-493.

[76] G.W. Scherer, Stress from crystallization of salt, Cement and Concrete Research 34(9) (2004) 1613-1624.

[77] M. Qin, R. Belarbi, A. Aït-Mokhtar, L.-O. Nilsson, Coupled heat and moisture transfer in multi-layer building materials, Construction and Building Materials 23(2) (2009) 967-975.

[78] H.M. Künzel, Simultaneous Heat and Moisture Transport in Building Components: One- and two-dimensional calculation, 1995.

[79] J. Carmeliet, F. Descamps, G. Houvenaghel, A Multiscale Network Model for Simulating Moisture Transfer Properties of Porous Media, Transport in Porous Media 35(1) (1999) 67-88.

[80] N.B. Vargaftik, B.N. Volkov, L.D. Voljak, International Tables of the Surface Tension of Water, Journal of Physical and Chemical Reference Data 12(3) (1983) 817-820.

[81] B. Li, Q. Meng, J.-M. Tulliani, R. Giordano, C. Li, J. Zhao, P. Ren, Salt migration and capillary absorption characteristics of cement mortar partially immersed in NaCl solution, Journal of Building Engineering 64 (2023).

[82] J. Zhao, H. Luo, Transport and crystallization of NaCl solution in porous silicate materials, Journal of Crystal Growth 519 (2019) 25-34.

[83] A. Arnold, K. Zehnder, Monitoring wall paintings affected by soluble salts, the conservation of wall paintings (1991).

[84] B. Lubelli, M.R. de Rooij, NaCl crystallization in restoration plasters, Construction and Building Materials 23(5) (2009) 1736-1742.

[85] R. Černý, L. Pel, R. Pishkari, O. Adan, J. Kočí, V. Kočí, Combined wicking and drying of a NaCl solution in porous building materials, MATEC Web of Conferences 282 (2019).

[86] R. Hendrickx, H.D. Clercq, Y. Vanhellemont, Experimental Determination of Liquid Transport Properties on Salt-Contaminated Porous Stone.

[87] J. Chwast, H. Janssen, J. Elsen, Gypsum efflorescence under laboratory conditions: preliminary study, 2014.

[88] N. Shahidzadeh, M.F.L. Schut, J. Desarnaud, M. Prat, D. Bonn, Salt stains from evaporating droplets, Scientific Reports 5(1) (2015) 10335.

[89] S. Gupta, H.P. Huinink, M. Prat, L. Pel, K. Kopinga, Paradoxical drying of a fired-clay brick due to salt crystallization, Chemical Engineering Science 109 (2014) 204-211.

[90] B. Lubelli, R.P.J. van Hees, H.J.P. Brocken, Experimental research on hygroscopic behaviour of porous specimens contaminated with salts, Construction and Building Materials 18(5) (2004) 339-348.

[91] L. Franke, J. Grabau, The influence of salt content on the drying behavior of bricks, Conserv. Hist. Brick Struct (1998) 59–68.

[92] J.F. Daan, Coupled salt and moisture transport in partially saturated porous media, Poromechanics II2020.

[93] P. Rovnanikova, Environmental pollution effects on other building materials, Trends in Genetics Tig 10(7) (2007) 225-6.

[94] Z. Pavlík, P. Michálek, M. Pavlíková, I. Kopecká, I. Maxová, R. Černý, Water and salt transport and storage properties of Mšené sandstone, Construction and Building Materials 22(8) (2008) 1736-1748.

[95] S. Sanchez-Moral, M. Cura, S. Ordonez, J. Garcia-Guinea, D. Benavente, Role of pore structure in salt crystallisation in unsaturated porous stone.

[96] George, W., Scherer, Stress from crystallization of salt, Cement & Concrete Research (2004).

[97] Putnis, Andrew, Prieto, Manuel, Fluid supersaturation and crystallization in porous media, Geological Magazine (1995).

[98] A.S. Guimarães, J.M.P.Q. Delgado, V.P. de Freitas, A.P. Albuquerque, The Effect of Salt Solutions and Absorption Cycles in the Capillary and Drying Coefficient of Red Brick Samples with Different Joints, Advances in Materials Science and Engineering 2016 (2016) 7868194.

[99] M. Pavlíková, Z. Pavlík, M. Keppert, R. Černý, Salt transport and storage parameters of renovation plasters and their possible effects on restored buildings' walls, Constr Build Mater 25(3) (2011) 1205-1212.

[100] Doehne, E., Salt weathering: a selective review, Geological Society London Special Publications 205(1) (2002) 51-64.

[101] M. Koniorczyk, M. Wojciechowski, Influence of salt on desorption isotherm and hygral state of cement mortar – Modelling using neural networks, Construction and Building Materials 23(9) (2009) 2988-2996.

[102] S.C. Pandey, A.M. Pollard, H.A. Viles, J.H. Tellam, Influence of ion exchange processes on salt transport and distribution in historic sandstone buildings, Applied Geochemistry 48 (2014) 176-183.

[103] S.C. Pandey, A.M. Pollard, H.A. Viles, A simulation study of capillary transport, preferential retention and distribution of salts in historic sandstone buildings, Environmental Earth Sciences 76(12) (2017).

[104] W. Brachaczek, Study of the Impact of Microstructure and Sorption Properties of the Renovation Plasters on the Wall Drying Rate, Periodica Polytechnica Civil Engineering (2018).

[105] W. Brachaczek, Microstructure of renovation plasters and their resistance to salt, Construction and Building Materials 182 (2018) 418-426.

[106] R. Bahadur, L.M. Russell, Water uptake coefficients and deliquescence of NaCl nanoparticles at atmospheric relative humidities from molecular dynamics simulations, Journal of Chemical Physics 129(9) (2008).

[107] J.G. Méndez-Bermúdez, H. Dominguez, L. Pusztai, S. Guba, B. Horváth, I. Szalai, Composition and temperature dependence of the dielectric constant of 1-propanol/water mixtures: Experiment and molecular dynamics simulations, Journal of Molecular Liquids 219 (2016) 354-358.

[108] S. Godts, R. Hayen, H.D. Clercq, Investigating salt decay of stone materials related to the environment, a case study in the St. James church in Liège, Belgium, Studies in Conservation 62(6) (2016) 1-14.

[109] Xu Yunfei, Experimental study on heat transfer coefficient of porous materials in summer environment of South China Sea islands [Dissertation], South China University of Technology, 2018. (In Chinese)

[110] Pan Zhenhao, Study on evaporative cooling of ceramic porous materials in extreme hot and humid climate [Dissertation], South China University of Technology, 2018. (In Chinese)

[111] Huang Ming, Technical research on creating a salt-containing atmospheric environment in the hot and humid climate wind tunnel for South China Sea islands [Dissertation], South China University of Technology, 2019. (In Chinese)

[112] Li Lingling, Research on wind tunnel test methods for complex heat transfer conditions on building surfaces [Dissertation], South China University of Technology, 2019. (In Chinese)

[113] Zhou Zhongrui, Study on the influence of salt spray corrosion on the surface thermal properties of building coatings [Dissertation], South China University of Technology, 2022. (In Chinese)

[114] Mao Huijun, Study on thermal and optical properties of building glass under salt deposition [Dissertation], South China University of Technology, 2022. (In Chinese)

[115] Zhao Heyang, Study on sampling methods for near-surface salt-containing air space [Dissertation], South China University of Technology, 2023. (In Chinese)

[116] Xiang Ling, New method for salt testing on coastal building surfaces and research on deposition characteristics [Dissertation], South China University of Technology, 2023. (In Chinese)

[117] Tang You, Study on measurement methods and distribution rules of salt spray concentration in outdoor environment of coastal buildings [Dissertation], South China University of Technology, 2023. (In Chinese)

[118] He Jian, Hygrophysical properties of salt-containing autoclaved aerated concrete [Dissertation], South China University of Technology, 2023. (In Chinese)

[119] H. Wang, Y. Wang, Z. Zhang, X. Liu, S. Xu, Cyclic behavior and hysteresis model of beam-column joint under salt spray corrosion environment, Journal of Constructional Steel Research 183 (2021).

[120] Zhong Lijuan, Huang Qinghua, Gu Xianglin, Zhang Weiping, Review of accelerated tests for chloride ion erosion in concrete under salt spray environment, Structural Engineers 25(3) (2009) 144-149. (In Chinese)

[121] Liu Jiduo, Duan Zhihao, Comparison of neutral salt spray test methods at home and abroad, Electroplating & Finishing 24(3) (2002) 39-40. (In Chinese)

[122] Zheng Chuntao, Overview of domestic and foreign salt spray test methods, Materials Protection (06) (1973) 15-25. (In Chinese)

[123] Su Linwang, Cai Jian, Liu Peige, Chen Qingjun, Wei Muyang, Rong Liangwan, Experimental study on concrete beams under salt spray environment and alternating load,

Journal of South China University of Technology (Natural Science Edition), 45(5) (2017) 97-104. (In Chinese)

[124] Wang Jianmin, Liu Guanguo, Lei Xiao, Li Di, Ma Hu, Experimental study on chloride ion resistance of concrete under salt spray environment, Industrial Construction 43(11) (2013) 89. (In Chinese)

[125] F. Auger, World limestone decay under marine spray conditions, The conservation of monuments in the Mediterranean Basin. International Symposium (I) = La conservazione dei monumenti nel bacino del Mediterraneo, simposio internazionale (I) (1990).

[126] T. Van, K. Beck, M.J.E.G. Al-Mukhtar, Accelerated weathering tests on two highly porous limestones, 52(2) (2007) 283-292.

[127] Liu Jianhua, Zhao Liang, Li Songmei, Hu Jianping, Gong Zhaohe, Influence of salt spray environment on mechanical properties of glass fiber reinforced resin matrix composites, Acta Materiae Compositae Sinica 024(003) (2007) 18-22. (In Chinese)

[128] Wang Qi, Tan Linlin, Wang Jie, Study on salt spray aging test of carbon fiber epoxy composites, Equipment Environmental Engineering 8(05) (2011) 39-42. (In Chinese)

[129] R.P.J.V. Hees, H.J.P. Brocken, Damage development to treated brick masonry in a long-term salt crystallisation test, Construction & Building Materials 18(5) (2004) 331-338.

[130] E. Franzoni, C. Gentilini, M. Santandrea, S. Zanotto, C. Carloni, Durability of steel FRCM-masonry joints: effect of water and salt crystallization, Materials and Structures 50(4) (2017) 1-16.

[131] Li Bing, Zhang Lianying, Qiu Peitao, Liu Ruixue, Yin Huiguang, Macro and micro study on uniaxial compression damage and fracture of concrete after salt spray action, Concrete (11) (2015) 27-30. (In Chinese)

[132] J. Dewanckele, M.A. Boone, T.D. Kock, W.D. Boever, L. Brabant, M.N. Boone, G. Fronteau, J. Dils, L.V. Hoorebeke, P. Jacobs, Holistic approach of pre-existing flaws on the decay of two limestones, Science of the Total Environment 447(mar.1) (2013) 403-414.

[133] T.D. Gonçalves, V. Brito, J. Musacchi, L. Pel, T. Saidov, Drying of porous building materials possibly contaminated with soluble salts: summary and findings of the DRYMASS research project, Swbss-international Conference on Salt Weathering of Buildings & Stone Sculptures, 2014.

[134] G. Li, F. Tian, C. Ren, Salt Spray Testing on the Chloride Resistance of Jointed Concrete, Journal of Asian Architecture and Building Engineering 17(1) (2018) 141-148.

[135] L. Xiang, Q. Meng, P. Ren, Effects of environmental and architectural factors on chloride-salt deposition on coastal building surfaces in the Zhujiang River Estuary, Building and

Environment 242 (2023).

[136] Yang Chun'er, Current status of salt spray test technology, Synthetic Materials Aging and Application 39(1) (2010) 43-47. (In Chinese)

[137] T. Zhao, H. Wang, Q. Luo, Q. Li, K. Wu, Rusting behavior of a deformed 450 MPa-grade weathering steel in 5 wt.% NaCl salt spray, Journal of Materials Research and Technology 21 (2022) 3181-3194.

[138] H. Zhang, W. Zhang, Y. Meng, H. Li, Deterioration of sea sand roller compacted concrete used in island reef airport runway under salt spray, Construction and Building Materials 322 (2022).

[139] M.I. Borges, J. Simão, Z. Silva, Artificial Weathering of Portuguese Granites Exposed to Salt Atmosphere: Variations of Physico-Mechanical Properties, Proceedings of Salt Weathering on Buildings and Stone Sculptures 2011. University of Cyprus., 2011.

[140] D. Huang, D. Niu, L. Su, Y. Liu, B. Guo, Q. Xia, G. Peng, Diffusion behavior of chloride in coral aggregate concrete in marine salt-spray environment, Construction and Building Materials 316 (2022).

[141] H. Mao, Q. Meng, J. Wang, Thermo-optical performance of building glass under salt sedimentation, Construction and Building Materials 408 (2023).

[142] Song Guanghui, Experimental study on salt spray dry-wet cycles of concrete for coastal structures, Concrete and Cement Products (11) (2016) 9-12. (In Chinese)

[143] P. López-Arce, M.J. Varas-Muriel, B. Fernández-Revuelta, M. Álvarez de Buergo, R. Fort, C. Pérez-Soba, Artificial weathering of Spanish granites subjected to salt crystallization tests: Surface roughness quantification, CATENA 83(2) (2010) 170-185.

[144] Chen Jiyong, Research and implementation of chloride ion concentration detection [Dissertation], Beijing University of Chemical Technology, 2016. (In Chinese)

[145] Wang Zongting, Chen Yong, Lan Quan, Zhao Yanfeng, Study on determination of chloride ions by test paper method, Concrete and Cement Products (01) (1998) 17-18. (In Chinese)

[146] An Taiying, Wen Qingzhen, Zhu Jinhua, Research progress in determination methods of chloride ions, Henan Chemical Industry 30(Z2) (2013) 8-11+24. (In Chinese)

[147] Song Mingyang, Li Min, Comparison and analysis of several spectrophotometric methods for determining chloride ion content in water, 2017, p. 4. (In Chinese)

[148] JTS/T 236-2019, Technical Specification for Testing of Hydraulic Engineering Concrete, 2019. (In Chinese)

[149] ISO 21466: 2019(E) Microbeam analysis — Scanning electron microscopy — Method

for evaluating critical dimensions by CD-SEM 2019

[150] ISO 15901-1: 2005(E) Evaluation of Pore Size Distribution and Porosimetry of Solid Materials by Mercury Porosimetry and Gas Adsorption 2005

[151] B117–2011(E) Standard Practice for Operating Salt Spray (Fog) Apparatus1.

[152] BS EN 13925-2:2003 Non-destructive testing. X-ray diffraction from polycrystalline and amorphous materials-Procedures 2003

[153] R. Fort, J. Feijoo, M.J. Varas–Muriel, M.A. Navacerrada, M.M. Barbero-Barrera, D. De la Prida, Appraisal of non-destructive in situ techniques to determine moisture- and salt crystallization-induced damage in dolostones, Journal of Building Engineering 53 (2022).

[154] H.J. Moon, S.H. Ryu, J.T. Kim, The effect of moisture transportation on energy efficiency and IAQ in residential buildings, Energy and Buildings 75 (2014) 439-446.

[155] M. Steeman, A. Janssens, H.J. Steeman, M. Van Belleghem, M. De Paepe, On coupling 1D non-isothermal heat and mass transfer in porous materials with a multizone building energy simulation model, Building and Environment 45(4) (2010) 865-877.

[156] J. Kwiatkowski, M. Woloszyn, J.J. Roux, Influence of sorption isotherm hysteresis effect on indoor climate and energy demand for heating, Applied Thermal Engineering 31(6-7) (2011) 1050-1057.

[157] S. Geving, J. Holme, Mean and diurnal indoor air humidity loads in residential buildings, Journal of Building Physics 35(4) (2011) 392-421.

[158] ISO 12570: 2000(E) Hygrothermal performance of building materials and products — Determination of moisture content by drying at elevated temperature.

[159] B. Lubelli, R. Hees, H.P. Huinink, C. Groot, Irreversible dilation of NaCl contaminated lime–cement mortar due to crystallization cycles, Cement & Concrete Research 36(4) (2006) 678-687.

[160] T. Bultreys, W. De Boever, V. Cnudde, Imaging and image-based fluid transport modeling at the pore scale in geological materials: A practical introduction to the current state-of-the-art, Earth-Science Reviews 155 (2016) 93-128.

[161] ISO 15148: 2002(E) Hygrothermal performance of building materials and products. Determination of water absorption coefficient by partial immersion 2002

[162] BS EN 1925, 1999 Natural stone test methods - Determination of water absorption coefficient by capillarity 1999

[163] C. Feng, H. Janssen, Hygric properties of porous building materials (III): Impact factors and data processing methods of the capillary absorption test, Building and Environment 134 (2018) 21-34.

[164] M. Angeli, D. Benavente, J.P. Bigas, B. Menendez, R. Hebert, C. David, Modification of the porous network by salt crystallization in experimentally weathered sedimentary stones, Materials & Structures 41(6) (2008) 1091-1108.

[165] A. Arnold, K. Zehnder, Crystallization and habits of salt efflorescences on walls. II. Conditions of crystallization, Ve congres international sur l'alteration et la conservation de la pierre. Actes. Vth international congress on deterioration and conservation of stone. Proceedings, lausanne, 25-27-9, 1985 (1985).

[166] L.G. Li, A.K.H. Kwan, Adding limestone fines as cementitious paste replacement to improve tensile strength, stiffness and durability of concrete, Cement and Concrete Composites 60 (2015) 17-24.

[167] Y.-Y. Kim, K.-M. Lee, J.-W. Bang, S.-J. Kwon, Effect of W/C Ratio on Durability and Porosity in Cement Mortar with Constant Cement Amount, Advances in Materials Science and Engineering 2014 (2014) 1-11.

[168] P. Grassl, H.S. Wong, N.R. Buenfeld, Influence of aggregate size and volume fraction on shrinkage induced micro-cracking of concrete and mortar, Cement and Concrete Research 40(1) (2010) 85-93.

[169] C. Andrade, L. Saucedo, N. Rebolledo, S. Cabeza, D. Meinel, X-Ray computed tomography and traditional analysis of a capillary absorption test in cement pastes, Cement and Concrete Composites 113 (2020) 103634.

[170] H. Derluyn, Salt transport and crystallization in porous limestone. Neutron-X-ray imaging and poromechanical modeling, ETH, 2012.

[171] M. Steiger, A.E. Charola, K. Sterflinger, Stone in Architecture, Stone in Architecture2011.

[172] B. Meng, 20. Characterization of pore structure for the interpretation of moisture transport 1993, pp. 155-162.

[173] B. Fitzner, R. Snethlage, Einfluss der porenradienverteilung auf das verwitter ungsverhalten ausgewaehlter sandsteine, Bautenschutz+ Bausanierung (1982).

[174] I. Sunagawa, Characteristics of Crystal Growth in Nature as Seen from the Morphology of Mineral Crystals, Bulletin de Mineralogie 104(2) (1981) 81-87.

[175] D. Benavente, M.A.G.d. Cura, J. Garcia-Guinea, S. Sanchez-Moral, S. Ordonez, Role of pore structure in salt crystallisation in unsaturated porous stone, Journal of Crystal Growth 260(3/4) (2004) 532-544.

[176] A.E. Charola, Salts in the Deterioration of Porous Materials: An Overview, Journal of the American Institute for Conservation 39(3) (2000) 327-343.

[177] M.A. Sanjuán, C. del Olmo, Carbonation resistance of one industrial mortar used as a

concrete coating, Building and Environment 36(8) (2001) 949-953.

[178] M. Khanzadeh Moradllo, M. Shekarchi, M. Hoseini, Time-dependent performance of concrete surface coatings in tidal zone of marine environment, Construction and Building Materials 30 (2012) 198-205.

[179] J. Liu, C. Vipulanandan, Evaluating a polymer concrete coating for protecting non-metallic underground facilities from sulfuric acid attack, Tunnelling and Underground Space Technology 16(4) (2001) 311-321.

[180] M.H.F. Medeiros, P. Helene, Surface treatment of reinforced concrete in marine environment: Influence on chloride diffusion coefficient and capillary water absorption, Construction and Building Materials 23(3) (2009) 1476-1484.

[181] H.Y. Moon, D.G. Shin, D.S. Choi, Evaluation of the durability of mortar and concrete applied with inorganic coating material and surface treatment system, Construction and Building Materials 21(2) (2007) 362-369.

[182] A.A. Almusallam, F.M. Khan, S.U. Dulaijan, O.S.B. Al-Amoudi, Effectiveness of surface coatings in improving concrete durability, Cement and Concrete Composites 25(4) (2003) 473-481.

[183] BS EN 1936-2006-- Natural stone test methods. Determination of real density and apparent density, and of total and open porosity (2006).

[184] C. Feng, A.S. Guimarães, N. Ramos, L. Sun, D. Gawin, P. Konca, C. Hall, J. Zhao, H. Hirsch, J. Grunewald, M. Fredriksson, K.K. Hansen, Z. Pavlík, A. Hamilton, H. Janssen, Hygric properties of porous building materials (VI): A round robin campaign, Building and Environment (2020).

[185] V. Soulios, E.J. Hansen, H. Janssen, Hygric properties of hydrophobized building materials, MATEC Web of Conferences 282 (2019) 02048.

[186] ASTM C1585-20 Standard Test Method for Measurement of Rate of Absorption of Water by Hydraulic-Cement Concretes, 2020.

[187] T/CECS 10203-2022, Test Methods for Hygrophysical Properties of Building Materials, 2022. (In Chinese)

[188] I. Ioannou, C. Charalambous, C. Hall, The temperature variation of the water sorptivity of construction materials, Materials and Structures/Materiaux et Constructions 50(5) (2017).

[189] V.I. Nikitsin, B. Backiel-Brzozowska, Determining hydraulic radii of construction wall materials in capillary moisture transfer, Int J Heat Mass Tran 88 (2015) 558-564.

[190] S. Roels, J. Carmeliet, H. Hens, O. Adan, H. Brocken, R. Cerny, Z. Pavlik, C. Hall, K. Kumaran, L. Pel, R. Plagge, Interlaboratory Comparison of Hygric Properties of Porous

Building Materials, Journal of Thermal Envelope and Building Science 27(4) (2004) 307-325.

[191] C. Feng, Study on the Test Methods for the Hygric Properties of Porous Building Materials, South China University of Technology, 2014.

[192] M.H. Hansen, Retention curves measured using pressure plate and pressure membrane apparatus: Description of method and interlaboratory comparison, 1998.

[193] ASTM C1699-09, Standard Test Method for Moisture Retention Curves of Porous Building Materials Using Pressure Plates 2009

[194] ISO 11274, 1998(E) Soil Quality - Determination of the Water Retention Characteristic - Laboratory Methods 1998

[195] R. Plagge, G.A. Scheffler, A. Nicolai, Experimental Methods to Derive Hygrothermal Material Functions for Numerical Simulation Tools, 1995.

[196] S. Roels, J. Elsen, J. Carmeliet, H. Hens, Characterisation of pore structure by combining mercury porosimetry and micrography, Materials and Structures/Materiaux et Constructions 34(2) (2001) 76-82.

[197] C. Feng, H. Janssen, Hygric properties of porous building materials (IV): Semi-permeable membrane and psychrometer methods for measuring moisture storage curves, Building and Environment 152 (2019) 39-49.

[198] T/CECS 10292-2023, Determination of Water Retention Curve of Porous Building Materials: Semipermeable Membrane Method, 2023. (In Chinese)

[199] R. Fuentes-Azcatl, M. Barbosa, Sodium Chloride, NaCl/ϵ: New Force Field, (2015).

[200] D. Czernia, B. Szyk, Air Density Calculator. Available at: https://www.omnicalculator.com/physics/air-density. Accessed: Mar 13, 2024.

[201] C. Hall, W.D. Hoff, Water Transport in Brick, Stone and Concrete (1st ed.). CRC Press. https://doi.org/10.4324/9780203301708, 2002.

[202] B. Lubelli, Sodium chloride damage to porous building materials, Architecture, 2006.

[203] ISO 9346: 2007(E) Hygrothermal performance of buildings and building materials — Physical quantities for mass transfer — Vocabulary 2007

[204] A. Brambilla, A. Sangiorgio, 5 - Moisture buffering of building materials, in: A. Brambilla, A. Sangiorgio (Eds.), Moisture and Buildings, Woodhead Publishing2021, pp. 99-128.

[205] ISO 12571: 2013(E) Hygrothermal performance of building materials and products — Determination of hygroscopic sorption properties.

[206] M.R. Hall, 14 - Hygrothermal materials for heat and moisture control in buildings, in: M.R. Hall (Ed.), Materials for Energy Efficiency and Thermal Comfort in Buildings, Woodhead Publishing2010, pp. 345-364.

[207] A. Brambilla, A. Sangiorgio, 2 - Principles of hygrothermal processes, in: A. Brambilla, A. Sangiorgio (Eds.), Moisture and Buildings, Woodhead Publishing2021, pp. 9-26.

[208] M. Khoukhi, The combined effect of heat and moisture transfer dependent thermal conductivity of polystyrene insulation material: Impact on building energy performance, Energy and Buildings 169 (2018) 228-235.

[209] J. Petković, H.P. Huinink, L. Pel, K. Kopinga, R.P.J. van Hees, Salt transport in plaster/substrate layers, Materials and Structures 40(5) (2006) 475.

[210] Xie Yue, Xie Jingchao, Bai Lu, Liu Jiaping, Experimental study on water vapor migration in cement mortar with salt, Building Energy Efficiency (Chinese and English) 49(12) (2021). (In Chinese)

[211] GB 50178-1993, Standard for Climatic Regionalization for Building, 1993. (In Chinese)

[212] GB 50176-2016, Code for Thermal Design of Civil Buildings, 2016. (In Chinese)

[213] S.B. Swami, S.K. Das, B. Maiti, Moisture sorption isotherms of black gram nuggets (bori) at varied temperatures, Journal of Food Engineering 67 (2005) 477-482.

[214] A. Jamali, M. Kouhila, L. Ait Mohamed, J.T. Jaouhari, A. Idlimam, N. Abdenouri, Sorption isotherms of Chenopodium ambrosioides leaves at three temperatures, Journal of Food Engineering 72(1) (2006) 77-84.

[215] R.H. Peuhkuri, C. Rode, K.K. Hansen, Effect of method, step size and drying temperature on sorption isotherms, 2005.

[216] ISO 12572: 2016(E) Hygrothermal performance of building materials and products — Determination of water vapour transmission properties — Cup method 2016

[217] ASTM C1498-04a(2016) Standard Test Method for Hygroscopic Sorption Isotherms of Building Materials 2016

[218] S. Brunauer, P.H. Emmett, E. Teller, Adsorption of Gases in Multimolecular Layers, Journal of the American Chemical Society 60(2) (1938) 309-319.

[219] C.R. Oswin, The kinetics of package life. III. The isotherm, Journal of the Society of Chemical Industry 65(12) (1946) 419-421.

[220] M. CAURIE, A new model equation for predicting safe storage moisture levels for optimum stability of dehydrated foods, International Journal of Food Science & Technology 5(3) (1970) 301-307.

[221] S.M. Henderson, Equilibrium moisture content of hops, Journal of Agricultural Engineering Research 18(1) (1973) 55-58.

[222] M. PELEG, Assessment of a semi-empirical four parameter general model for sigmoid moisture sorption isotherms, Journal of Food Process Engineering 16(1) (1993) 21-37.

[223] C.v.d. Berg, S.C. Bruin, Water activity and its estimation in food systems: theoretical aspects, 1978.

[224] C. Pade, M. Guimaraes, The CO2 uptake of concrete in a 100 year perspective, Cement and Concrete Research 37(9) (2007) 1348-1356.

[225] A. Dodoo, L. Gustavsson, R. Sathre, Carbon implications of end-of-life management of building materials, Resources, Conservation and Recycling 53(5) (2009) 276-286.

[226] J. He, Q. Li, Q. Meng, P. Ren, S. Li, H. Wu, Experimental investigation of the effect of salt on the hygroscopic properties of autoclaved aerated concrete, Construction and Building Materials 370 (2023).

[227] O. Koronthalyova, L. Bagel, M. Kuliffayova, T. Ifka, Effect of Presence of Salt on Hygric Performance of Ceramic Bricks, Transport in Porous Media 107(3) (2015) 667-682.

[228] A.L. Horvath, Handbook of aqueous electrolyte solutions : physical properties, estimation, and correlation methods, 1985.

[229] B. Li, Q. Meng, R. Giordano, J.-M. Tulliani, P. Ren, J. Wang, The hygric properties of cement mortar with salt spray deposition, Construction and Building Materials 449 (2024b).

[230] B. Sibiryakov, L.W.B. Leite, E. Sibiriakov, Porosity, specific surface area and permeability in porous media, Journal of Applied Geophysics 186 (2021) 104261.

[231] Y. Ghasemi, M. Emborg, A. Cwirzen, Exploring the relation between the flow of mortar and specific surface area of its constituents, Construction and Building Materials 211 (2019) 492-501.

Academic achievements during the PhD program

1、 **Published papers** **(only those relevant to the content of the dissertation):**

序号	Authors	Tittle	Journals	Volume, year, month and pages of publication	Chapter of the dissertation it relates to	Indexed database
1	Bing Li, Qinglin Meng	Review on the accelerated test methods for porous building materials in salt spray environment	Concrete	2021(11): 6-9.	Chapter 2	CCJ
2	Bing Li, Qinglin Meng, Qiong Li, Peng Ren	Study on the thermal comfort and energy efficiency in middle school under triple control mode in Guangzhou	Building Science	2021, 37(6):42-51.	Chapter 1	CCJ
3	Bing Li, Qinglin Meng , Jean-Marc Tulliani, Roberto Giordano, Chuanrui Li, Jing Zhao, Peng	Salt migration and capillary absorption characteristics of cement mortar	Journal of Building Engineering	Volume 64, 1 April 2023, 105605	Chapter 3	SCI
4	Bing Li, Roberto Giordano, Jean-Marc Tulliani, Qinglin Meng	Effect of sea salt on carbonation and CO_2 uptake in cement mortar	Construction and Building Materials	Volume 438,9 August 2024, 137212	Chapter 4	SCI

5	Bing Li, Qinglin Meng, Roberto Giordano, Jean-Marc Tulliani, Peng Ren, Junsong Wang	The hygric properties of cement mortar with salt spray deposition	Construction and Building Materials	Volume 449, 25 October 2024, 138438	Chapter 4	SCI
6	Bing Li, Qinglin Meng, Jean-Marc Tulliani, Roberto Giordano	Experimental study on the hygroscopic properties of cement-based building materials in a salt mist environment.	Proc. 11th SuDBE, Espoo, Finland	Aug. 2023, pp.116.	Chapter 5	—
7	Bing Li, Wanjiang Wang, Saierjiang Halike, Roberto Giordano, Jean-Marc Tulliani, Qinglin Meng	Water Vapor Permeability in Cement Mortar under Salt Spray Deposition	Journal of Cultural Heritage	Under review	Chapter 5	SCI
8	Bing Li, Roberto Giordano, Jean-Marc Tulliani, Saierjiang Halike,Wanjiang Wang, Qinglin Meng	Fitting Equations for the Sorption Isotherms of Cement Mortar with Salt Spray Deposition	Frontiers of Architecture research	Under review	Chapter 5	SCI